Christian Sippl

Shallow and deep structure of the Pamir-Hindu Kush region from local seismic data

---

Dissertation zur Erlangung des Doktorgrades im
Fachbereich Geowissenschaften
an der
Freien Universität Berlin

Berlin, 2013

Erstgutachter: Prof. Dr. Frederik Tilmann
Freie Universität Berlin, GeoForschungsZentrum Potsdam

Zweitgutachter: Prof. Dr. Lothar Ratschbacher
TU Bergakademie Freiberg

Tag der Disputation: 26.04.2013

"The rest of us, not chosen for enlightenment, left on the outside of Earth, at the mercy of a Gravity we have only begun to learn how to detect and measure, must go on blundering inside our front-brain faith in Kute Korrespondences, hoping that for each psi-synthetic taken from Earth's soul there is a molecule, secular, more or less ordinary and named, over here - kicking endlessly among the plastic trivia, finding in each Deeper Significance and trying to string them all together like terms of a power series hoping to zero in on the tremendous and secret Function whose name, like the permuted names of God, cannot be spoken... plastic saxophone reed *sounds of unnatural timbre*, shampoo bottle *ego-image*, Cracker Jack prize *one-shot amusement*, home appliance casing *fairing for winds of cognition*, baby bottles *tranquilization*, meat packages *disguise of slaughter*, dry-cleaning bags *infant strangulation*, garden hoses *feeding endlessly the desert*... but to bring them together, in their slick persistence and our preterition... to make sense out of, to find the meanest sharp sliver of truth in so much replication, so much waste..."

Thomas Pynchon, Gravity's Rainbow

Abstract

The Pamir-Hindu Kush region is one of the tectonically least well understood, and probably most exceptional, areas on earth. Vigorous intermediate-depth seismicity in a peculiar geometry featuring an along-strike change in dip polarity attests to the deep burial of lithospheric material in a continental collision zone. However, the provenance of involved structures, the precise geometry and regional kinematics as well as the processes responsible for the generation of these earthquakes are largely unknown.

In the framework of project TIPAGE, the aim of which is to investigate these open issues, a temporary network of seismic stations was operated in the Tajik Pamir and southern Kyrgyzstan from 2008 to 2010. The recorded data is analyzed within this study. Since encountered seismicity rates were significant, an automated processing chain for the retrieval of high-quality phase picks and hypocentral locations was implemented. Several tests and quality checks were performed in order to ascertain the precision of obtained phase arrivals and hypocentral locations. 9,530 earthquakes were identified and located with this method, with relative location errors that should be lower than 7.5 km thanks to the application of the double-difference method. The distribution of shallow seismicity shows a pronounced discrepancy between a largely aseismic eastern and a seismically active western Pamir, separated by a seismogenic, roughly north-south trending lineament. Intermediate-depth seismicity can be subdivided into the Pamir and Hindu Kush seismic zones, which are separated by a clear gap that widens with depth, due to a 90 ° discrepancy in strike and dip directions across it. Earthquakes in both structures outline narrow (10-15 km wide), rather steeply dipping planes resembling Wadati-Benioff zones. The Pamir deep seismicity describes an arc, with its strike changing from north-south to east-west and its dip evolving from eastwards to southwards from its southwestern to its eastern end. This geometry clearly implies a Eurasian origin. In contrast, the Hindu Kush seismicity defines a structure that subvertically dips northwards and strikes east-west, but shows considerable complexity, apparently being fragmented into several highly active clusters. While its provenance can not unequivocally be clarified from its geometry, the continuity of some observed features across the gap separating Pamir and Hindu Kush deep seismicity could hint at a common origin of the two.

For a selection of 359 earthquakes, moment tensor solutions were determined, either through the analysis of first-motion polarities or by waveform fitting. Obtained results show that deep seismicity in the Hindu Kush uniformly features downdip extensive mechanisms, hinting at primarily buoyancy-driven dynamics. Mechanisms for intermediate-depth events beneath the Pamir are significantly more variable, and show no uniformly oriented principal stress axes. However, the Pamir slab exhibits a tendency towards along-arc extension where it is curved and appears continuous along strike, which most likely is a consequence of active bending. Along-arc extension either means that the subduction zone experiences extensive hinge rollback or that a process of sheet-like delamination is active. Crustal earthquakes throughout the Pamir are dominated by

left-lateral strike-slip faulting along northeast-southwest striking rupture planes. An incremental rotation of P axes from purely north-south in most of the Pamir to purely east-west in the Tajik Depression is discernible, and the same pattern is retrieved from a spatially damped stress inversion on a regular grid. It can be interpreted to attest to the distributed accommodation of differential northward movement between Pamir and Tajik Depression throughout the western Pamir, possibly combined with radial overthrusting of the Pamir over the Tajik Depression, driven by gravity due to the large altitude difference. Focal mechanisms in the Tajik Depression feature westward slip along horizontal fault planes, which might attest to stick-slip behavior at gaps in the evaporite décollement, along which Tajik Depression sediments are gliding westward, pushed by the overriding Pamir.

Phase arrivals determined with the aforementioned automated processing chain are used for a local earthquake tomography study. A pronounced low-velocity zone in the middle crust is found in the southern Pamir, which coincides with a good electrical conductor at depth discovered with magnetotelluric deep sounding techniques. v_p/v_s values in this anomalous body are, rather surprisingly, relatively low. Nevertheless, the presence of partial melt or aqueous fluids in the southern Pamir middle crust seems likely. The slab outlined by the hypocenters of intermediate-depth earthquakes beneath the Pamir is imaged as a high-velocity anomaly about 3-5% faster than the surrounding mantle. Directly above this slab, anomalously slow P wave velocities (only about 7.1 km/s), coincident with elevated values of v_p/v_s, are present at uppermost mantle depths. The updip end of intermediate-depth seismicity coincides remarkably well with the onset of these anomalies. South of the Pamir slab, normal to slightly slow mantle velocities are found, no indication for the presence of underthrusted Indian material at depth is found.

Zusammenfassung

Die Pamir-Hindukusch-Region in Zentralasien ist, was ihre Tektonik anbelangt, eines der außergewöhnlichsten und am wenigsten verstandenen Gebiete der Erde. Sie ist gekennzeichnet durch das ungewöhnlich häufige Auftreten starker mitteltiefer Erdbeben, deren Hypozentren eine Struktur mit seltsamer Geometrie abbilden, die einen lateralen Wechsel in der Einfallsrichtung aufweist. Diese Konstellation deutet auf das tiefe Absinken lithosphärischen Materials innerhalb einer kontinentalen Kollisionszone hin. Jedoch sind der Ursprung des seismogenen Materials, die genaue geometrische Konfiguration, die regionale Kinematik sowie die Prozesse, die für die Erzeugung dieser Erdbeben verantwortlich sind, weitgehend unbekannt.

Im Rahmen des Projektes TIPAGE, das auf die Beantwortung dieser offenen Fragestellungen abzielt, wurde im tadschikischen Pamir und in Süd-Kirgisien in den Jahren 2008 bis 2010 ein temporäres seismisches Netzwerk betrieben. Die dort aufgezeichneten Daten werden in dieser Studie analysiert. Da die vorgefundenen Seismizitätsraten beträchtlich waren, wurde eine automatisierte Prozessierungskette zur Ermittlung von präzisen Phasenankunftszeiten und Hypozentral-Lokalisierungen implementiert. Mehrere Tests und Qualitätsproben zur Verifizierung der Genauigkeit der Prozedur wurden vorgenommen. Eine Gesamtzahl von 9.530 Erdbeben wurde mit besagter Methode im Datensatz identifiziert und lokalisiert. Die relativen Lokalisierungsfehlern sind durch die Anwendung der *double-difference*-Lokalisierungsmethode kleiner als 7.5 km. Die räumliche Verteilung der Flachbeben zeigt eine ausgeprägte Zweiteilung des Pamir in einen weitestgehend aseismischen Ostteil und einen seismisch aktiven Westteil, welche durch ein grob Nord-Süd verlaufendes Lineament voneinander getrennt sind. Die mitteltiefe Seismizität kann in die seismisch aktiven Zonen unterhalb von Pamir und Hindukusch aufgeteilt werden. Diese sind durch eine seismische Lücke voneinander getrennt, welche sich mit größerer Tiefe weitet. Die Beben zu beiden Seiten der Lücke unterscheiden sich des Weiteren durch die Streich- und Einfallsrichtungen der von ihnen beschriebenen Strukturen, die sich von einer auf die andere Seite um 90 ° ändert. Bebenlokationen in beiden Zonen definieren schmale (10-15 km breit), eher steil einfallende planare Strukturen, die an Wadati-Benioff-Zonen erinnern. Die Tiefseismizität im Pamir konturiert einen Bogen, von dessen südwestlichem Ende nach Osten hin sich die Streichrichtung von Nord-Süd zu Ost-West, die Einfallsrichtung von ostwärts nach südwärts ändert. Diese Bebengeometrie deutet klar auf einen eurasischen Ursprung des abtauchenden Materials hin. Im Kontrast dazu beschreibt die Seismizität unter dem Hindukusch eine subvertikal nordwärts einfallende, Ost-West streichende Struktur. Diese weist allerdings beträchtliche Komplexität auf und scheint aus mehreren sehr aktiven *Clustern* zu bestehen. Obwohl die Herkunft des Hindukusch nicht eindeutig geklärt werden kann, deutet die Kontinuität einiger gemeinsamer Merkmale über die sie trennende Lücke hinaus auf einen gemeinsamen Ursprung von Pamir und Hindukusch hin.

Für 359 der lokalisierten Erdbeben wurden Momententensoren ermittelt, entweder durch die Analyse der Polaritäten von Erstankünften oder durch Wellenforminversion. Tiefbeben unter dem

Hindukusch weisen durchweg Extension in Richtung des Abtauchens der Struktur auf, was auf primär gravitativ getriebene Prozesse hindeutet. Die Mechanismen der mitteltiefen Beben unter dem Pamir sind deutlich uneinheitlicher und zeigen keine eindeutige Orientierung ihrer Spannungsachsen. Jedoch ist in den Teilen der Struktur, die gebogen und entlang ihres Streiches kontinuierlich erscheinen, eine Tendenz zu Mechanismen zu beobachten, die horizontale Extension entlang des beschriebenen Bogens andeuten. Dies ist mit hoher Wahrscheinlichkeit eine Konsequenz von aktiver Verbiegung der Struktur. Die vorherrschenden extensiven Mechanismen mitteltiefer Beben unterhalb des Pamir könnten durch zwei Szenarien erklärt werden: entweder weicht die Scharnierlinie der Subduktionszone stark zurück, oder eine Schicht der Unterkruste und Mantellithosphäre wird delaminiert und sinkt in den Mantel. Krustenbeben im Pamir treten vornehmlich als sinistrale Blattverschiebungen entlang nordost-südwest verlaufender Bruchflächen auf. Des Weiteren ist eine kontinuierliche Rotation der Kompressionsachsen von einem reinen Nord-Süd-Trend zu einer Ost-West-Orientierung im tadschikischen Becken zu erkennen. Eine räumlich gedämpfte Spannungsinversion auf einem regulären Gitter ergab ein sehr ähnliches Muster. Diese Spannungsverteilung lässt sich als Konsequenz des räumlich verteilten Ausgleichs differentieller Nordwärtsbewegung zwischen Pamir und tadschikischem Becken im gesamten Westpamir verstehen, kombiniert mit gravitativ getriebener radialer Überschiebung des Pamir über das Becken durch die extreme Topographiedifferenz. Herdflächenlösungen im tadschikischen Becken zeigen westwärts gerichteten Versatz entlang horizontaler Bruchflächen, was auf *stick-slip*-Verhalten in Lücken im Evaporit-Décollement hindeuten mag. Entlang dieses Décollements werden die Sedimente des tadschikischen Beckens durch vom Pamir ausgeübten Schubkräften westwärts geschoben.

Die automatisch ermittelten Ankunftszeiten seismischer Phasen wurden für die Durchführung einer lokalen Erdbebentomographie-Studie genutzt. Ergebnisse zeigen eine ausgeprägte Niedriggeschwindigkeitszone in der mittleren Kruste des südlichen Pamir, die mit der Position eines guten elekrischen Leiters im Untergrund zusammenfällt, welcher mittels megnetotellurischer Methoden entdeckt wurde. Dies scheint auf das Vorhandensein partieller Schmelzen oder anderer Fluide in der mittleren Kruste des Pamir hinzudeuten. v_p/v_s-Verhältnisse innerhalb dieser Anomalie sind allerdings eher niedrig. Die abtauchende Platte unterhalb des Pamir, welche von den Bebenlokationen ersichtlich war, wird hier als Region anormal hoher P-Wellengeschwindigkeiten (3-5 % schneller als der umgebende Mantel) abgebildet. Direkt oberhalb dieser Platte werden extrem niedrige Geschwindigkeiten (nur ca. 7.1 km/s) und hohe v_p/v_s-Verhältnisse ermittelt. Das obere Ende der mitteltiefen Seismizität entspricht mit erstaunlicher Genauigkeit dem unteren Ende dieser Anomalie. Südlich der abtauchenden Platte unterhalb des Pamir werden normale bis leicht niedrigere Mantelgeschwindigkeiten abgebildet, kein Anzeichen des Vorhandenseins abgetauchten indischen Lithosphärenmaterials in der Tiefe wird beobachtet.

Contents

1. Introduction

Today's Himalaya-Tibet orogenic system is, to first order, the result of the ongoing indentation of a rigid cratonic block (India) into a mechanically weaker Eurasia (see analog experiments by *Tapponnier et al.*, 1982) following the closure of the Tethys ocean (*Patriat and Achache*, 1984; *Guillot*, 2003). The tectonic evolution of the collision is complex and involves subduction/underthrusting of (greater) Indian lithosphere, possible slab break-off(s), distributed lithospheric shortening of both Eurasia and India as well as possible lithospheric delamination and continental-scale escape along large strike-slip systems (e.g. *Molnar and Tapponnier*, 1975; *Tapponnier and Molnar*, 1979; *Avouac and Tapponnier*, 1993; *Yin and Harrison*, 2000; *Chemenda et al.*, 2000). The lateral edges (syntaxes) of this Indian indenter have since effected the creation of deformed regions of considerable complexity in their vicinity, which are less well understood than processes and structures along the indenter's front (Himalaya, Tibetan plateau). The ongoing convergence between India and Eurasia is currently to first order accommodated by continental underthrusting of Indian lithosphere (*Nábelek et al.*, 2009; *Kind and Yuan*, 2010) and possibly lower crust (*Hetényi et al.*, 2007; *Wittlinger et al.*, 2009) beneath Eurasia and the internal shortening of Eurasia further north. However, there is some indication that parts of the Eurasian continent might likewise locally subduct or underthrust (e.g *Burtman and Molnar*, 1993; *Kind et al.*, 2002; *Wittlinger et al.*, 2004; *Zhao et al.*, 2011). The Pamir-Hindu Kush region, which is situated north of the western Himalayan syntaxis, exhibits features that not only set it apart from the neighboring Himalaya-Tibet system, but are globally unique and thereby raise some fundamental issues in our understanding of geodynamic processes.

The western Himalaya-Hindu Kush-Pamir system accommodated a similar amount of Cenozoic convergence as the Himalaya-Tibet system, albeit over a much shorter meridional width, resulting in a higher amount of upper plate shortening (*van Hinsbergen et al.*, 2011, deduce 1050 km) as well as a probably higher amount of crust that vanished into the mantle. Travel time tomography studies for the Pamir and Hindu Kush (*Koulakov and Sobolev*, 2006; *Negredo et al.*, 2007; *Koulakov*, 2011) show pronounced high-wavespeed anomalies apparently extending all the way through the mantle transition zone, occasionally flanked by low-velocity regions. These are accompanied by vigorous intermediate-depth (up to nearly 300 km depth) earthquake activity (*Billington et al.*, 1977; *Pegler and Das*, 1998), which is, with the possible exception of Vrancea, Romania (*Ismail-Zadeh et al.*, 2012), globally unique within a continental collision zone far from any active oceanic subduction. Tibet, in comparison, is essentially aseismic at depths greater than 80 or 90 km (uppermost mantle). Intermediate-depth earthquakes in the Pamir-Hindu Kush stirred scientific curiosity since *Gutenberg and Richter* (1954) first reported their existence nearly six decades ago. Generally, the Pamir-Hindu Kush intermediate-depth seismicity is thought to attest to active mantle deformation at the edge of the India-Eurasia collision. The modes of deep lithospheric deformation during orogeny, however, are only poorly understood and a great variety of processes have been shown to be theoretically possible in a number of studies based on numeri-

cal or analog modeling (e.g. *Toussaint et al.*, 2004; *Burov and Yamato*, 2008; *Gray and Pysklywec*, 2012; *Chemenda et al.*, 2000).

These include, in addition to the scenarios resembling classic oceanic subduction, lithospheric and/or lower crustal delamination (*Bird*, 1979) or convective downwelling of a drop-like lithospheric body into the mantle (Rayleigh-Taylor instability, see *Houseman et al.*, 1981). However, comparison of these models to nature is difficult because of a lack of observations - not least because of the generally aseismic nature of orogenic mantle deformation, with the apparent exception of the Pamir-Hindu Kush. A variety of models attempting to explain the Pamir-Hindu Kush zone's peculiar geometry (along-strike overturning of dip) and dynamics have been proposed, but fundamental questions, e.g. whether it is related to subduction (e.g. *Billington et al.*, 1977) or exists due to a mantle drip (*Koulakov*, 2011), whether continental (*Roecker*, 1982; *Burtman and Molnar*, 1993) or oceanic material (*Chatelain et al.*, 1980; *Pegler and Das*, 1998) hosts these earthquakes or whether Pamir and Hindu Kush form one single (*Billington et al.*, 1977; *Pegler and Das*, 1998; *Pavlis and Das*, 2000) or two separate structures (*Chatelain et al.*, 1980; *Burtman and Molnar*, 1993; *Fan et al.*, 1994) outlined by seismic activity have not been conclusively solved. The similarity of the Pamir-Hindu Kush earthquakes to inclined Wadati-Benioff zones known from oceanic subduction and source mechanisms exhibiting down-dip extension (at least beneath the Hindu Kush), also a hallmark of intermediate-depth earthquakes in oceanic plates, early on led to the belief that they are the expression of subduction of a last piece of the Tethys ocean or another remnant ocean basin (*Chatelain et al.*, 1980). However, Pamir and Hindu Kush are far beyond the Indus-Yarlung suture where oceanic subduction is supposed to have stopped about 50 Ma ago. There is no indication of a possible land-locked or remnant ocean basin north of the suture in the regional rock record (*Burtman and Molnar*, 1993), and the absence of large-scale Cenozoic volcanism seems to confirm this (*Schwab et al.*, 2004). Subduction of continental plates, on the other hand, is not the typical mode of convergence in continental collision. Buoyancy and weakness of generic continental crust rather promotes pure shear thickening through distributed shortening. A further complication in a continental subduction scenario would be the occurrence of intermediate-depth earthquakes themselves. The most frequently invoked model for generation of intermediate-depth earthquakes is dehydration embrittlement (*Kirby et al.*, 1996; *Hacker*, 2003; *Hacker et al.*, 2003; *Jung et al.*, 2004), which allows rapid shear failure in a pressure and temperature regime where rocks would otherwise deform in a ductile manner. In this conceptual model, fluids released in prograde metamorphic reactions of hydrous minerals present in oceanic lithosphere lower the normal stress so that frictional sliding is enabled. Lower continental crust and upper mantle, however, are mostly dry (e.g. *Rudnick*, 1995; *Rudnick and Fountain*, 1995) and may not provide the water necessary for the dehydration mechanism to work. There are other concepts of intermediate-depth earthquake generation that do not require hydrated lithosphere (*Kelemen and Hirth*, 2007; *John et al.*, 2009), but those immediately raise the question why intermediate-depth earthquakes are not observed more often outside oceanic subduction zones.

Within this thesis, passive seismic data collected during the two-year TIPAGE deployment in Tajikistan and Kyrgyzstan from 2008 to 2010, are analyzed. This is the first modern digital seismological dataset for this politically unstable region, all previous studies either relied on globally recorded data or some short-term deployments of analog stations in Afghanistan during the late 1960s and 70s. Modern seismological techniques applied to the collected digital seismic data provide a wealth of new constraints on regional crustal and sub-crustal structure, leading to a better understanding of active tectonic processes.

After a summary of the tectonic and lithologic setting in the Pamir and its surroundings, which also briefly focusses on large-scale processes that have been established for the Himalaya-Tibet system, an overview over geodynamic models already proposed for the study area is given (Chapter 2). This is followed by a short description of the TIPAGE seismic deployment (Chapter 3).

In chapter 4, I present a detailed seismicity distribution derived from the two years of data by the application of an automated processing chain for the retrieval of exact seismic phase picks and high-fidelity hypocentral locations starting from the raw waveform data. With the application of an STA/LTA trigger algorithm with adaptive trigger threshold and a routine that groups trigger alerts to events based on a grid search of traveltimes on a rough orthorhombic grid, a first-break location of each earthquake is obtained. P picks are then refined and/or added by the use of a focussed P phase picking algorithm, S picks are added with a second algorithm. After each of these steps, earthquakes are relocated and picks obtaining too large residuals in this relocation process are weeded out. With this processing chain, 9,530 well-defined earthquake hypocenters are determined, which sharply outline structures at crustal and mantle depths. A slightly modified version of this chapter is currently in review in *Journal of Geophysical Research* (*Sippl et al.*, 2012, *in review*).

Focal mechanisms for 359 of these earthquakes are determined in Chapter 5. Events featuring large magnitudes are used for moment tensor retrieval by waveform inversion, whereas fault plane solutions for smaller events inside the network are determined from first motion polarities. The obtained distribution of fault plane solutions and principal stress axes is imaged and interpreted in detail for crustal earthquakes as well as deep seismicity below Pamir and Hindu Kushs. Stress inversions based on the determined moment tensors are performed, subdividing these three regions into areas of roughly homogeneous stress field. Alternatively, a single spatially damped inversion on a regular grid is obtained, which does not rely on an *a priori* subdivision of the study area.

The tomographic inversion of phase arrival times retrieved in Chapter 4 for the spatial distribution of v_p and v_p/v_s is described in Chapter 6. A declustered subset of earthquakes is used for this purpose, reducing data redundancy and the size of the problem. The definition of the utilized grid, the evaluation of the optimal damping parameter and a number of tests and procedures aimed at quantifiying the distribution of resolution capability (both exploiting the resolution matrix and performing synthetic tests) is presented, followed by the display of inversion results. These are then interpreted, attempting to combine obtained results with available evidence from other geophysical methods, like magnetotelluric deep sounding and receiver function analysis.

Chapter 7 is an attempt at integrating the findings of Chapters 4-6 into a single geodynamic model of the Pamir-Hindu Kush, briefly discussing potential implications. Finally, Chapter 8 features the conclusions of the present work and a brief outlook on future perspectives and possible research avenues.

2. Regional geological and tectonic setting

As described in the Introduction, the India-Eurasia collision and the position of the region of interest at the western syntaxis of the Indian indenter to first order define the conditions under which the observed conspicuous features at depth must have developed.

In this chapter, I intend to provide an overview on regional kinematics and tectonic evolution that will be the framework for the interpretation of the results presented in this thesis. After a synopsis of the India-Eurasia collision, the constituent parts of the western Himalayan syntaxis will be presented one at a time, and their key features and structural elements will be discussed. To conclude the chapter, a brief summary of geodynamic models potentially explaining intermediate-depth seismicity beneath Pamir and Hindu Kush will be provided.

2.1. The Indo-Eurasian collision and the large-scale structure of Tibet

Before the final closure of the Tethys Ocean and the onset of collision between India and Eurasia at about 50-55 Ma (*Patriat and Achache*, 1984; *Guillot*, 2003; *van Hinsbergen et al.*, 2011), Asia already consisted of a collage of continental blocks and terranes, scrapes of Gondwana that had successively collided and been amalgamated to continental Eurasia (e.g. *Mattauer*, 1986; *Yin and Harrison*, 2000). These continental fragments or terranes are today separated by narrow suture zones, where former ocean floor material outcrops at the surface (Figure 2.1 shows the constituent blocks and sutures of Tibet). There is still considerable debate about the exact timing of the collision onset (see e.g. discussions in *Yin*, 2010; *van Hinsbergen et al.*, 2011), but most authors nowadays assume a collision onset of 52-50 Ma, with a possible earlier collision of India with the Kohistan-Ladakh arc near the western Indian syntaxis (possibly as early as 65 Ma, see *Hildebrand et al.*, 2001; *Klootwijk et al.*, 1992). Unlike the drastic decrease in convergence velocity that has been postulated to have accompanied the collision onset (e.g. *Guillot*, 2003), the latest studies show a more gradual slowdown of India relative to Eurasia from roughly 11-12 cm/yr convergence before the collision to values between 34 and 44 mm/yr today for India's western and eastern syntaxis, respectively (*Molnar and Stock*, 2009; *DeMets et al.*, 2010).

Many authors have tried to estimate the total convergence between India and Eurasia since the initial contact, most of them arriving at values around 2400 km for western and 3200 km for eastern Tibet (*Molnar and Tapponnier*, 1975; *Patriat and Achache*, 1984; *Dewey et al.*, 1989; *Le Pichon et al.*, 1992; *Replumaz and Tapponnier*, 2003; *Guillot*, 2003; *van Hinsbergen et al.*, 2011). Although the collision has led to the uplift of the world's largest plateau (Tibet) and the formation of the world's highest mountain range (Himalaya), this amount of convergence could not have been accommodated by internal shortening and crustal thickening alone. In fact, the

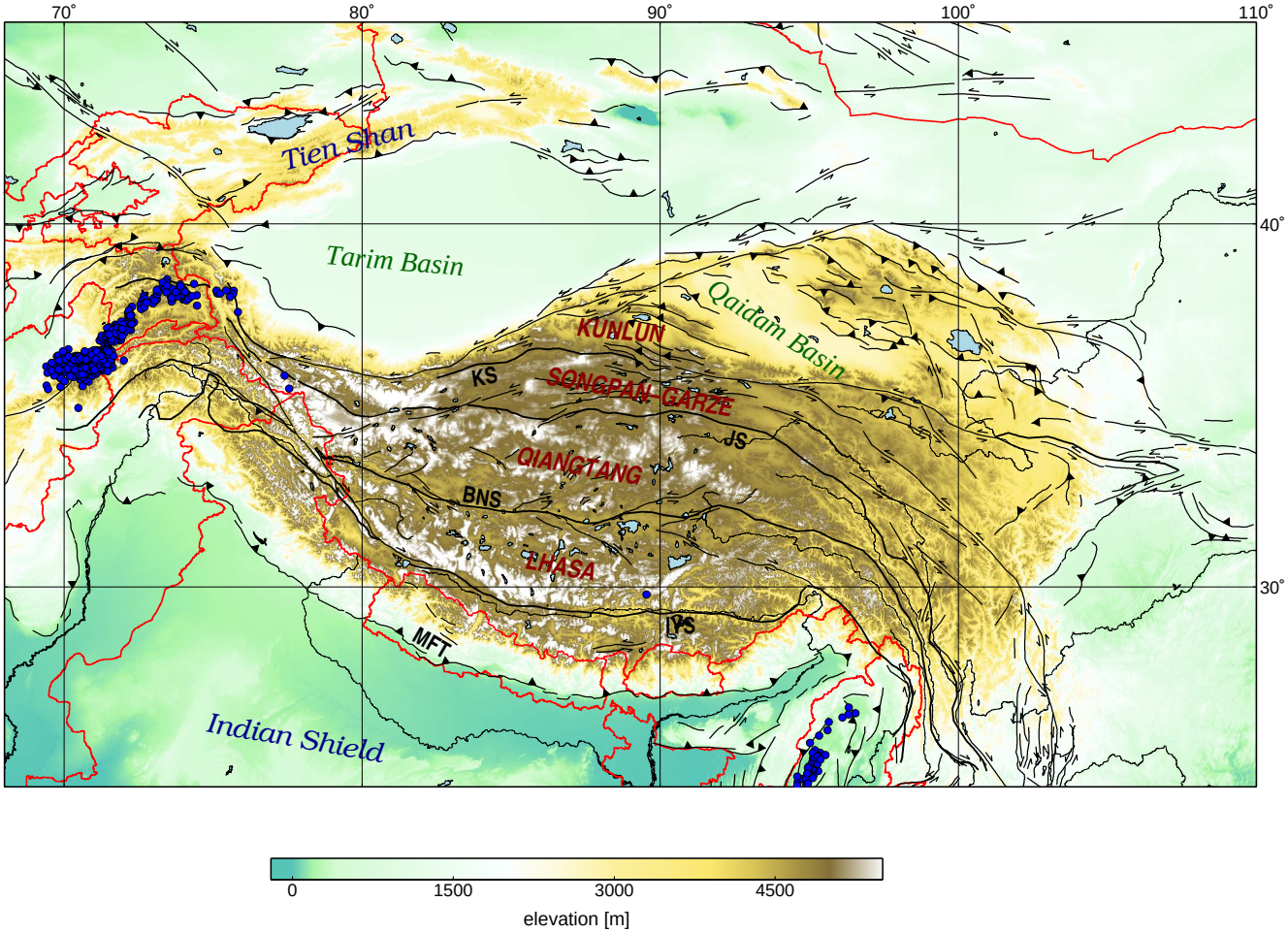

Figure 2.1.: Topographic map of Tibet, with main sutures and fault zones indicated by black lines. Earthquakes from the EHB catalog (*Engdahl et al.*, 1998) with hypocentral depths greater than 100 km are plotted as blue circles. These are clearly confined to the Himalayan syntaxes. KS = Kunlun Suture, JS = Jinsha Suture, BNS = Bangong-Nujiang Suture, IYS = Indus-Yarlung Suture, MFT = Main Frontal Thrust. Faults and sutures were taken from the HimaTibetMap compilation (*Styron et al.*, 2010)

amount of convergence accommodated by deformation inside the Asian plate is estimated by *van Hinsbergen et al.* (2011) to be 1050 km at the latitude of the Pamir-Hindu Kush and 600 km in eastern Tibet. Thus, the main part of the convergence must have been accommodated by another mechanism, namely the continental-scale underthrusting of the Indian plate beneath Asia (*Mattauer*, 1986; *Guillot*, 2003). Pre-collision India had a considerably greater northward extent, this "Greater India", whose size and shape is still widely debated (see e.g. *Ali and Aitchison*, 2005; *van Hinsbergen et al.*, 2012) was underthrust beneath Asia, whereupon the upper crust of the subducting Indian plate was scraped off and forms today's Himalayan mountain range (*van Hinsbergen et al.*, 2011). A third mechanism accommodating a, however comparatively small, part of the total convergence of India and Eurasia is lateral escape of Tibet to the east (*Gan et al.*, 2007; *Yin*, 2010; *Yin and Harrison*, 2000) along conjugate strike-slip systems (see Figure 2.1). *van Hinsbergen et al.* (2011) estimated the total amount of convergence taken up by this process to about 250 km.

The history of Tibet's development is complicated and far from unequivocally agreed upon. Today's extent of underthrust Indian lithosphere, as shown in Figure 2.2, is insufficient in the context of the total estimated convergence, so one or several episodes of slab breakoff and subsequent sinking of Indian lithosphere into the mantle must have occurred. Remnants of these detached slabs can be seen in global seismic tomography studies (*Van der Voo et al.*, 1999). *Chemenda et al.* (2000) show a tentative history of underthrusting and repeated lithospheric detachment based on analogue and numerical modeling. Around 25 Ma, the tectonic style of the collision zone underwent a major change, which might or might not be connected to the onset of the Arabian-Eurasian collision at very roughly this time (*Yin*, 2010; *Hatzfeld and Molnar*, 2010). This change effected the formation of large strike-slip faults along which the eastward extrusion of Indochina and the westward extrusion of the Afghan block took place, as well as, possibly, the jump of deformation northwards over the Tarim basin, leading to the formation and uplift of the Tien Shan (*Yin*, 2010; *Neil and Houseman*, 1997). The start of the southward progression of the main deformation front between India and Eurasia from the Indus-Tsangpo suture into the Indian plate is also attributed to this period (*Yin*, 2010). The temporally progressive movement of this thrust front from the Main Central Thrust (MCT) over the Main Boundary Thrust (MBT) to the Main Frontal Thrust (MFT), which represents the recent thrust front, can be deduced from Figure 2.2 (bottom right).

2.2. The Pamir and surroundings

2.2.1. Structure of the Pamir

The Pamir is an arcuate, northward convex mountain range, which acted and still acts as a rigid indenter penetrating northward into the Eurasian plate (*Sobel et al.*, 2012). As such, it overrode the Tajik-Yarkand Basin, which used to link today's Tajik Depression west of the Pamir to parts of the Tarim basin east of it (*Burtman and Molnar*, 1993). To the north, the Pamir is bounded by the Alai Valley, which represents the last remnant of this former basin (*Burtman and Molnar*, 1993; *Coutand et al.*, 2002), and where a substantial part of current north-south shortening is accommodated by thrust faulting along the Main Pamir Thrust (MPT) (*Arrowsmith and Strecker*, 1999; *Coutand et al.*, 2002; *Zubovich et al.*, 2010). The western flank of the Pamir is outlined by the left-lateral Darvaz strike-slip fault, which marks its demarcation to the Tajik Depression. To the east, the Karakorum Fault and the Kashgar-Yecheng transfer system (KYTS) mark the Pamir's boundary towards the westernmost Himalaya (Karakorum Range) and the Tarim Basin, respectively.

Lithologically, the Pamir can be subdivided into four roughly east-west striking, arcuate zones (see Figure 2.3). The north Pamir, which is bounded by the MPT in the north and by the Tanymas suture in the south, represents a terrane that collided with the Eurasian continent in early to middle Carboniferous (*Burtman and Molnar*, 1993). South of that, the Central Pamir mainly consists of shallow marine sediments (carbonates) and is thus believed to be a former continental margin or platform (*Burtman and Molnar*, 1993). The Rushan-Pshart zone is an extended region of ophiolite and limestone outcrops that represents the suture zone associated with a Mesozoic ocean basin that closed in late Jurassic or early Cretaceous. South of it, the southern Pamir is lithologically divided into its western and eastern parts. Whereas in the west, Carboniferous to Permian sand- and siltstones dominate, the east mainly consists of precambrian metamorphites

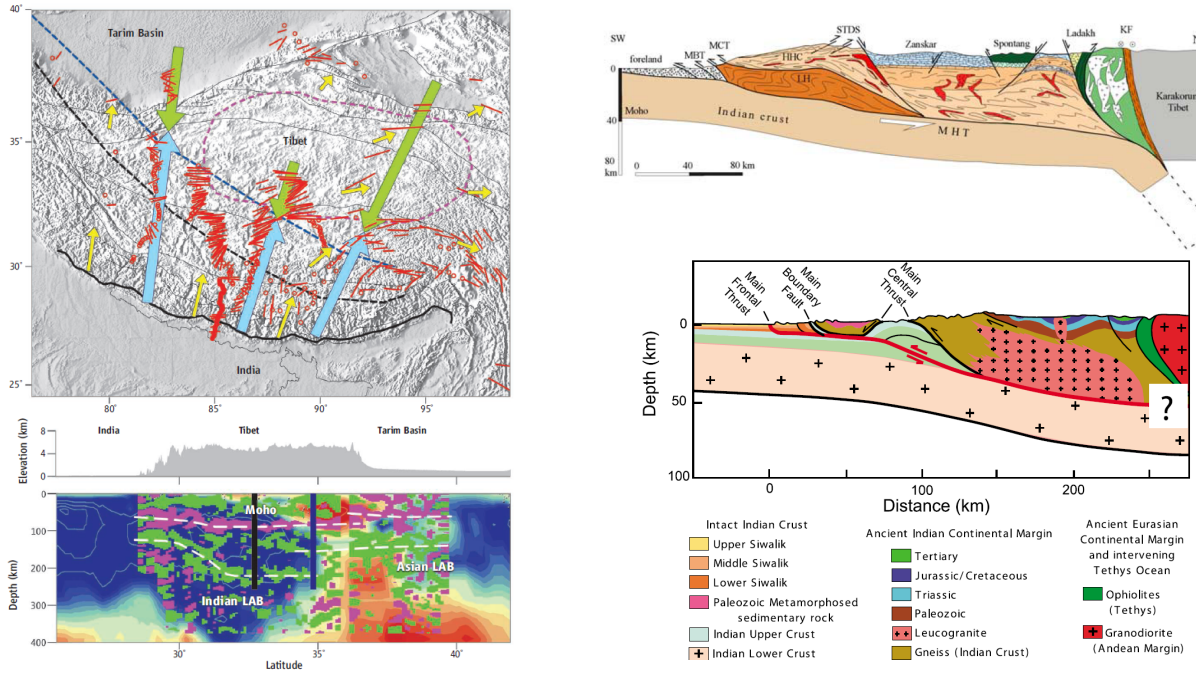

Figure 2.2.: Continental underthrusting of India beneath Eurasia explained in detail. *Left, top*: Summary of several seismological studies on the sub-Tibetan lithosphere; solid black line marks the boundary between India and Eurasia at the surface, dashed blue and black lines and the meeting points of the green and blue arrows outline the contact from Indian to Asian lithosphere at depth according to different studies (for details, refer to *Kind and Yuan*, 2010). Yellow arrows represent measured GPS velocities, the purple dashed line outlines a region of anomalously hot and ductile mantle underlying central Tibet. *Left, bottom*: Profile from India to Tarim Basin, showing an overlay of tomography and receiver function results (Both Figures taken from *Kind and Yuan*, 2010). *Right,top*: North-south profile through Himalaya-Tibet showing the continental-scale underthrusting of India beneath Asia along the MHT (Figure taken from *Guillot*, 2003). *Right, bottom*: Close-up view (schematical) of the Himalayan deformation front. The succession of active thrust fronts (MCT, MBT, MFT) can be seen, and their common rooting in the MHT detachment (imaged with seismicity by *Monsalve et al.*, 2006) is shown (Figure taken from *Hatzfeld and Molnar* (2010)

.

and some more recent granitic intrusions (*Burtman and Molnar*, 1993). One should keep in mind that all these units making up the Pamir are still "Eurasian" (referring to Eurasia as everything that was one block when India arrived), the continental suture marking the boundary of the Indian and Eurasian plates at the surface can be found several 100 km further south, forming an arc arround the Nanga Parbat massif and then continuing west into northern Pakistan and north-eastern Afghanistan (*Tahirkheli et al.*, 1979; *Crawford*, 1974).

The different suture zones and terranes that make up Tibet - and are well known and studied there - can be traced through the Pamir into NE Afghanistan. However, they are substantially deflected northwards in the Pamir (*Burtman and Molnar*, 1993, infer a value of about 300 km), and the correlation of the Pamir sutures with the Tibetan ones is far from obvious and still highly

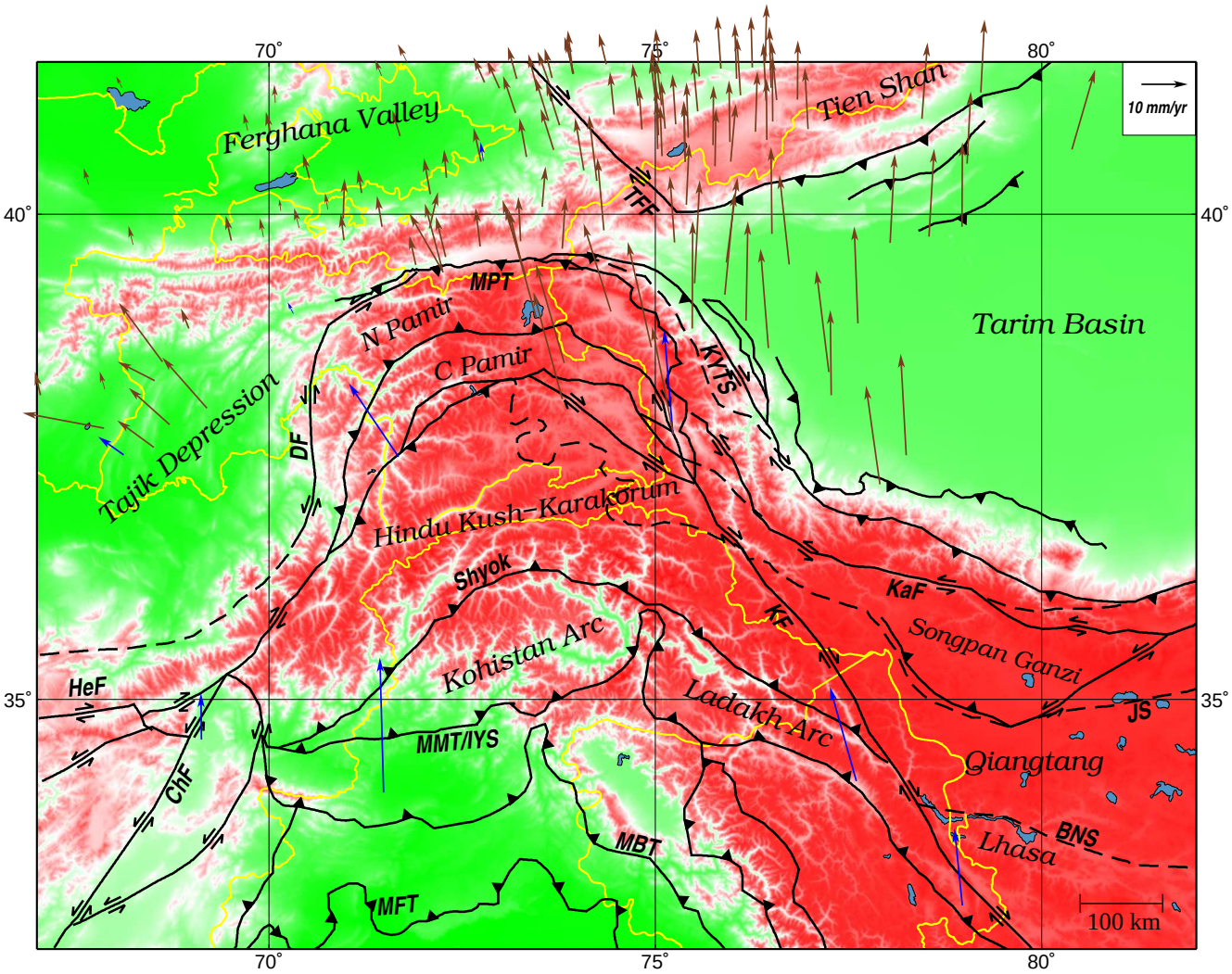

Figure 2.3.: Topographic map of the study region, showing GPS velocities relative to stable Eurasia (brown arrows from *Zubovich et al.* (2010), blue arrows from *Mohadjer et al.* (2010)) and tectonic features (faults and sutures), taken from *Robinson et al.* (2004) and *Mechie et al.* (2012). HeF = Herat Fault, ChF = Chaman Fault, MFT = Main Frontal Thrust, MBT = Main Boundary Thrust, MMT/IYS = Main Mantle Thrust/Indus-Yarlung Suture, DF = Darvaz Fault, MPT = Main Pamir Thrust, TFF = Talas-Ferghana Fault, KYTS = Kashgar-Yecheng Transfer System, KF = Karakorum Fault, KaF = Karakax Fault, BNS = Bangong-Nujiang Suture, JS = Jinsha Suture

debated. Two schools of correlating these sutures have emerged:

Burtman and Molnar (1993) and *Yin and Harrison* (2000) correlate the sutures in the following way:

- The northern Pamir is equivalent to the Kunlun terrane in Northern Tibet
- the central Pamir corresponds to the Songpan-Garzi terrane, which makes the Tanymas suture in the Pamir translate into the Ayimaqin-Kunlun-Mutztagh suture in Tibet
- the South Pamir-Karakorum-Hindu Kush terrane is equivalent to the Qiangtang terrane in Tibet, the suture separating them from the central Pamir/Kunlun terrane is called Rushan Pshart in the Pamir and Jinsha suture in Tibet
- The Lhasa terrane in Tibet might translate into the Kohistan sequence in Pakistan, or (more probably) both are different structures that might not have extended over the whole width of the convergence zone; the Shyok suture north of it in the Pamir translates into the Bangong-Nujiang suture in Tibet
- The Indus-Yarlung suture, boundary between continental domains of India and Eurasia, continues into Pakistan, circling the Nanga Parbat massif, as what was called the MMT (Main Mantle Thrust) by *Tahirkheli et al.* (1979)

In a paper by *Schwab et al.* (2004), the sutures are correlated in a different way (also advocated by *Lacassin et al.*, 2004): In their proposal, there is no equivalent to the Kunlun terrane in the Pamir, thus all correlations are shifted by one terrane/suture. Hence, the S Pamir corresponds to the Lhasa terrane, the Central Pamir to the Qiangtang terrane and the Northern Pamir to Songpan-Garze. The Tanymas suture translates into the Jinsha, the Rushan-Pshart suture into the Bangong-Nujiang suture. The Kohistan-Ladakh arc and the corresponding Shyok suture, which are without counterpart in Tibet, might represent a former magmatic arc with limited longitudinal extent.

The second of these models requires a substantially greater northward shift of the Pamir sutures, which must have taken place along the Chaman and Karakorum strike-slip faults. Thus, knowledge about their total slip amounts should constrain the suture correlations.

2.2.2. Active deformation in and around the Pamir

Figure 2.3 shows a compilation of GPS vectors from two studies (*Mohadjer et al.*, 2010; *Zubovich et al.*, 2010), which represent the entirety of available GPS data for the region. It is obvious that while most of Kyrgyzstan is adequately sampled, large parts of Tajikistan and, even more so, Afghanistan and Pakistan lack GPS sites, so that making quantitative statements about the current kinematics of the region is difficult.

From these data, it appears that recent kinematics of the Pamir are asymmetric between its western and eastern flanks. Whereas the northward relative movement of the Pamir to the Tajik Depression in the west features a substantial westward component of apparent convergence between Pamir and Tajik Depression, its eastern flank shows no such trend, rather the opposite: Pamir and Tarim Basin diverge, the resulting extension is accommodated by normal faulting along the Karakul and Kongur Shan rifts. This might attest to an anticlockwise rotation of the whole

Pamir block, leading to radial thrusting in the west and dextral strike-slip in the east (*Cowgill*, 2010), as shown in Figure 2.4.

In the following, a more detailed account of deformation loci and rates around the Pamir's bounds and in its interior are given.

Alai Valley

The Alai Valley represents the last remnant of a Mesozoic-early Cenozoic basin formerly linking the Tajik Depression and the Tarim Basin, which was subsequently annihilated by the advancing Pamir (*Coutand et al.*, 2002; *Burtman and Molnar*, 1993), probably by means of southward intracontinental subduction (*Sobel et al.*, 2012). Recent deformation in the Alai Valley, which is flanked by the Alai Range (Tien Shan) in the north and the Trans-Alai Range (Pamir) in the south, is concentrated at the MPT at the valley's southern rim. GPS studies infer a north-south convergence of 10-15 mm/yr across this thrust fault (*Reigber et al.*, 2001; *Mohadjer et al.*, 2010; *Zubovich et al.*, 2010), mainly based on values determined for its eastern part. Most authors place the onset of deformation at the MPT in the late Oligocene (*Thomas et al.*, 1994; *Sobel and Dumitru*, 1997; *Robinson et al.*, 2007), and deformation rates estimated from geological evidence are substantially lower than the ones determined from GPS. *Arrowsmith and Strecker* (1999) infer 6 mm/yr throughout the Holocene from the offset of fluvial terraces, *Burtman and Molnar* (1993) deduce 3.5 mm/yr from the summation of seismic moments, and *Coutand et al.* (2002) get an average of only 0.6-0.8 mm/yr from the reconstruction of balanced profiles. However, the last of these studies is probably strongly biased due to only taking into account the interior of the Alai Valley, and not the flank of the Trans Alai to the south of it, where most convergence probably ocurred. Based on geomorphological observations, *Coutand et al.* (2002) and *Strecker et al.* (2003) claim that active deformation at the MPT has already stopped at the easternmost segment of the MPT (east of about 73.5° E) and shifted south into the Pamir orogen to concentrate at the Markansu Fault. *Sobel et al.* (2011a) speculates that a transition from subduction to collision may already have happened at the MPT, due to the arrival of thicker and less dense Tien Shan crust from the north.

Tajik Depression and Darvaz Fault

The Tajik Depression is the remnant of a once larger basin being partly overridden by the Pamir indenter in its easternmost section. The eastern part of today's Tajik Depression is made up by a curved fold-and-thrust belt (FTB) extending to the western end of the Alai valley (*Leith and Alvarez*, 1985, e.g.). Crustal thicknesses throughout the Tajik Depression are thought to be 35 km or less (*Burtman and Molnar*, 1993), and seismic refraction profiles (*Kulagina et al.*, 1974; *Burtman and Molnar*, 1993) show sediment thicknesses of about 6 km in the northern part and up to 15 km in the southeastern part of the Tajik Depression. Thus, the crystalline basement would only have an average thickness of 20-25 km. A layer of Jurassic evaporites that is probably some 100 m thick is thought to act as a crustal-scale décollement throughout the basin, separating intact basement below it from folded sediments above (*Nikolaev*, 2002). In the southeast part of the basin, this layer reaches a depth of about 12 km below surface (*Burtman and Molnar*, 1993), and *Hamburger et al.* (1992) postulate a décollement at a depth of 12-15 km in the Peter I Range

(inside the FTB) based on the distribution of earthquake hypocenters and relate this décollement to the Jurassic evaporite horizon. Ongoing salt tectonics within the basin is evident from the presence of several salt domes.

As can be seen from the GPS vectors, there is a significant northward motion of the Pamir relative to the Tajik Depression as well as an east-west convergence (see Figure 2.3). Due to the scarcity of GPS sites, however, it is not feasible to deduce the exact loci of these deformation modes. The northward relative motion of the Pamir with respect to the Tajik Depression is thought to be accommodated by the left-lateral Darvaz Fault. However, evidence for the activity and estimates of slip rates for this fault are scarce, *Abers et al.* (1988) cites older work by *Kuchai and Trifonov* (1977) and *Trifonov* (1978), where 10-15 mm/yr of left-lateral slip were deduced from morphological analysis. However, in some publications, the Darvaz Fault is treated as a thrust fault (e.g. *Thomas et al.*, 1994); looking at the GPS vectors, it is possible that a combination of both is true. Taking a GPS vector from the western Pamir (Manem) and one in the Tajik Depression (Shaartuz), *Mohadjer et al.* (2010) inferred 11.4 mm/yr sinistral motion and 6.2 mm/yr east-west convergence between these two sites. However, since these localities are about 250 km apart, it is likewise possible that all of the 6.2 mm/yr east-west convergence measured between western Pamir and the Tajik Depression is taken up by folding inside the basin's sediments.

Two earthquake focal mechanisms from magnitude 6 events at the southeastern rim of the basin calculated by *Abers et al.* (1988) show thrust faulting in NW-SE direction. The authors related these events, that clearly occur within the basin's basement (depths between 20 and 25 km), to ongoing northward advance of the Hindu Kush slowly overriding the Tajik Depression from the south. This might corroborate a model proposed by *Reiter et al.* (2011), who could reconstruct the shape of the Tajik FTBs with analog modelling, using two northward propagating indenters with different indentation velocities (slow: Hindu Kush, fast: Pamir).

Karakorum Fault and Tarim Basin

Unlike the western boundary of the Pamir, where the Pamir is thought to at least partly overthrust the Tajik Basin in a westward direction (radial thrusting, see *Strecker et al.*, 1995; *Cowgill*, 2010), the eastern boundary of the Pamir features east-west extension accompanying dextral strike-slip. The Karakorum fault transfers right-lateral slip into the south and central Pamir, where it is distributed over a number of splay systems like the Aksu-Murghab, Aksu-Rangkul and Karasu faults (*Strecker et al.*, 1995; *Searle*, 1996; *Cowgill*, 2010; *Sobel et al.*, 2011a). North of the kink of the Karakorum Fault into these splay systems, active normal faulting in the Muji-Tashgorgan graben system attests to east-west extension. The relative motion between the Pamir and the western Kunlun range, both of which used to be a single linear belt before the Pamir's northward indentation according to *Cowgill* (2010), is not taken up by the Karakorum Fault (which then would have to transfer slip into the MPT), but by the Kashgar Yecheng transfer system (KYTS, see Figure 2.3) further east (*Cowgill*, 2010; *Sobel et al.*, 2011a), which is a 350 km long and 50 km wide complex zone of right-lateral faults that took up as much as 280 km of relative motion since its initiation (37 Ma or later, see *Cowgill*, 2010). This corresponds well to the estimated 300 km of northward displacement of the Pamir relative to the Tarim Basin based on the correlation of sutures from Pamir and Tibet in *Burtman and Molnar* (1993). A series of recent studies (*Searle*, 1996; *Robinson*, 2009) found relatively low total displacements for the Karakorum Fault (around 120-160 km), which would roughly comply with what is required by the correlation of sutures after

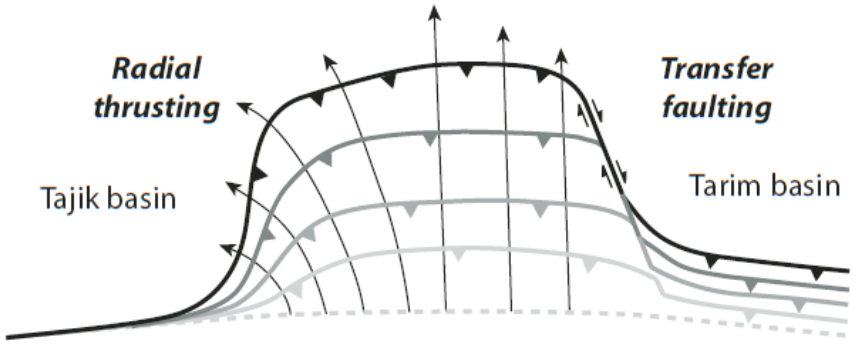

Figure 2.4.: Conceptual drawing of the different modes of northward displacement of the Pamir relative to its surroundings occurring along its western and eastern flank, respectively. Figure taken from *Cowgill* (2010).

Burtman and Molnar (1993) and *Yin and Harrison* (2000), but not suffice for the correlation after *Schwab et al.* (2004).

Recent deformation rates determined from GPS (see Figure 2.3), however, indicate that little or no differential motion between Pamir and Tarim Basin exists, i.e. that they move northwards with about the same velocity, whereas most convergence is accommodated in the central Tien Shan to the north (see *Zubovich et al.*, 2010; *Sobel et al.*, 2011a). This would mean that both Karakorum Fault and KYTS are largely inactive today. *Sobel et al.* (2011a) assumes that the significant increase in shortening observed for the central Tien Shan about 10-12 Ma ago (*Abdrakhmatov et al.*, 1996) correlates with a northward acceleration of the Tarim Basin, which lead to the rapid decrease in relative motion across the KYTS at that time. This would significantly reduce the total amount of time this system was active, and thus increase its overall slip rate to values around or above today's convergence rate at the MPT (about 10-15 mm/yr, see *Zubovich et al.*, 2010), indicating that the KYTS alone "fed" the thrusting (or intracontinental subduction) occurring at the MPT until about 10-12 Ma. Whereas deformation then jumped to the Tien Shan north of the Tarim Basin, convergence at the MPT seems to have stayed rather constant. East-west extension along the Muji-Tashgorgan graben system marking the Karakorum fault's northern termination is ongoing, as evident from the GPS velocity arrows (Figure 2.3).

Internal deformation in the Pamir

Internal deformation in the Pamir used to be focussed along the Tanymas and Rushan-Pshart sutures, where thrust faulting must have occurred, being transferred into the central Pamir from the Karakorum Fault by several dextral strike-slip systems including the Aksu-Murghab and Aksu-Rangkul systems and the East Pamir Fault. Looking at GPS data (Figure 2.3) and also field evidence (e.g. *Robinson et al.*, 2007; *Sobel et al.*, 2011a), the Karakorum Fault and thus also its splays show small to negligible amounts of slip today. Hence, not much slip can be transferred into the central Pamir to be taken up by the thrusts there.

East-west extension in the northern Pamir leads to normal faulting along north-south trending structures in the Karakul rift zone (*Strecker et al.*, 1995) and further east in the Kongur Shan (*Robinson et al.*, 2004, 2007). Fault plane solutions from globally recorded earthquakes indicate that the Karakul rift zone might have a continuation southwards all the way into Afghanistan, marked by earthquakes with normal faulting mechanisms (as also mentioned in *Strecker et al.*, 1995).

2.3. Hindu Kush and Afghanistan

To the southwest of the Pamir, the Hindu Kush mountain range and the northeastern part of Afghanistan exhibit a distinctly different style of tectonic activity. Although the collision history of these regions, with the aforementioned Tibetan and Pamir sutures finding their counterparts there, appears to have been roughly similar, recent and current behavior is not. Thrusting is, with the exception of the westward continuation of the MFT through the Salt Range and Sulaiman Range (*Bernard et al.*, 2000), largely absent, whereas the area is dominated by several large strike-slip faults. According to *Tapponnier et al.* (1981), these accommodated large-scale westward escape of the Afghan block in response to the northward indentation of the Pamir/India (see Figure 2.5). The crustal wedge between the dextral Herat Fault in the north and the sinsitral Chaman Fault to the south started moving westward in the Oligocene, roughly coincident with the start of the Pamir's northward advance (see estimated start of convergence at MPT, according to e.g. *Robinson et al.*, 2007) and with crustal melting in the eastern Hindu Kush and Karakorum Range (*Hildebrand et al.*, 1998). This westward extrusion is then supposed to have stopped in Miocene times (*Tapponnier et al.*, 1981), possibly due to collision of the central Afghan block with the Iranian Lut block, which began to be pushed eastwards after a major reorganization in the collision between Arabia and Eurasia around 12 Ma (*Hatzfeld and Molnar*, 2010). This scenario would require huge amounts of slip along the Chaman and Herat faults. *Tapponnier et al.* (1981) gives an estimate of total displacement along the Chaman fault of 500 to 1000 km, while *Prevot et al.* (1980) give an estimate of 300-500 km based on studies by *Auden* (1974) and *de Lapparent* (1972). As opposed to the nowadays supposedly inactive Herat Fault (*Tapponnier et al.*, 1981), which also shows no current slip in recent GPS data (*Mohadjer et al.*, 2010), the Chaman Fault today accommodates the northward movement of the Pamir with respect to eastern Afghanistan. *Mohadjer et al.* (2010) inferred an upper bound of 18.1±1 mm/yr of current displacement, however, considering they only utilized two permanent GPS sites several 100 km apart to retrieve this value, this may be significantly overestimated. Nevertheless, geologically derived values seem to confirm this high rate, with *Wellman* (1966) estimating 15 mm/yr and *Tapponnier et al.* (1981) finding 1-2 cm/yr for the last 100,000 years based on morphologic considerations.

There is evidence that the India-Eurasia collision occurred earlier along the western syntaxis of (then "Greater") India, possibly as early as 65 Ma (*Hildebrand et al.*, 2001; *Klootwijk et al.*, 1992). According to *Treloar and Coward* (1991), this might have led to a "pinning" at this location, with subsequent clockwise rotation of structures further east (NW Himalaya) and anticlockwise rotation of structures further west (northern Pakistan) and lateral extrusion happening in both directions. Unlike further east, the two southernmost sutures in Afghanistan, which mark the boundaries of the Kohistan Arc, have about the same age, and some authors even inferred that the southern one of the two subduction zones that must have been active there was the first to be

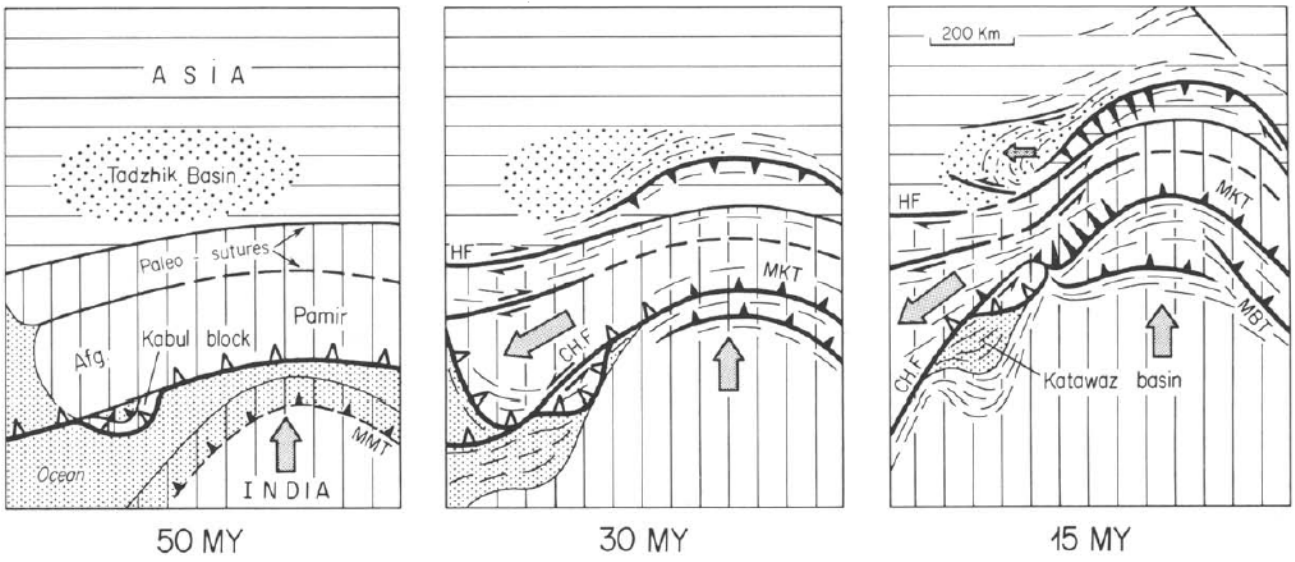

Figure 2.5.: Kinematics of westward extrusion of central Afghanistan due to the northward movements of India and the Pamir. Figure taken from *Tapponnier et al.* (1981). HF = Herat Fault, ChF = Chaman Fault

choked by the arrival of continental crust (*Tahirkheli et al.*, 1979; *Tapponnier et al.*, 1981; *Khan et al.*, 2009). Thus, the arriving Indian plate would first have collided with the Kohistan Arc before both together crashed into Eurasia.

2.4. Tien Shan

The Tien Shan mountain range marks the northern border of the presumably rigid Tarim Basin, which is being pushed north as a cause of the Indo-Eurasian collision and thus effects the uplift of a major mountain range more than 1500 km from the actual collision zone (*Tapponnier and Molnar*, 1979). Having formed at the locus of an upper Paleozoic-early Mesozoic suture (*Allen et al.*, 1993; *Sengör et al.*, 1993), the complex Tien Shan range can be subdivided into a number of distinct ridges separated by intermontane basins (see Figure 2.1). The E-W trending range is separated into an eastern and a western part by the lithospheric-scale, NW-SE striking, dextral Talas-Ferghana strike-slip fault, which after *Burtman et al.* (1996) has about 60 km post-Cretaceous offset. *Yin* (2010) identified the Talas-Ferghana fault as one of several parallel, homogeneously spaced right-lateral strike-slip faults that can be found from the Zagros mountains in Iran to the Altai Range in southern Siberia, and that he links to the collision of Arabia with Eurasia, which, although the propagation direction of Arabia is due north (*Hatzfeld and Molnar*, 2010), happens along a thrust front that has an orientation similar to those strike-slip faults. The Tien Shan mountains probably started to uplift around 23 Ma (*Hendrix et al.*, 1994; *Yin*, 2010; *van Hinsbergen et al.*, 2011, and references therein), although other studies give an even younger initiation age of about 10-12 Ma (e.g. *Abdrakhmatov et al.*, 1996), which coincides with the projected maximum elevation of Tibet at that time (*Molnar et al.*, 1993). This younger age probably corresponds to a significant acceleration in uplift of the Tien Shan (*Zubovich et al.*,

2010; *Yin*, 2010). Even so, the Tien Shan mountains formed considerably more recently than the India-Eurasia collision as consequence of which they supposedly came into existence. Presumably, active deformation shifted north at some point of the development of the whole collision zone and jumped across the rigid Tarim Basin to deform the much weaker region of today's Tien Shan (*Neil and Houseman*, 1997).

Total shortening estimates across the Tien Shan are around 200 km, with a higher value for the mountain range's western part (*Avouac and Tapponnier*, 1993), which can be either explained by the influence of the Arabian collision with Eurasia (*Yin*, 2010) or a clockwise rotation of the Tarim Basin (*Avouac and Tapponnier*, 1993), for which there is evidence in GPS velocities (*Gan et al.*, 2007).

Recently obtained GPS velocities (*Zubovich et al.*, 2010; *Reigber et al.*, 2001) show that the Tien Shan north of the Tarim Basin accommodates as much as 20±2 mm/yr of convergence, which is nearly two thirds of the total India-Eurasia convergence at this longitude. Thus, only little deformation nowadays is localized in western Tibet, but Tibet pushes the Tarim Basin into the Tien Shan, where active deformation occurs. The GPS arrows (see Figure 2.3) show a gradual decrease in velocity relative to stable Eurasia across the Tien Shan, hinting at rather distributed shortening across the whole range. In the western part of the Tien Shan, current total shortening is lower, because a big part of it is accommodated by the MPT immediately south. The Talas-Ferghana shows only small slip rates of <2 mm/yr and might either be inactive or locked today (*Zubovich et al.*, 2010).

The Ferghana Basin immediately west of the Talas-Ferghana fault, which subdivides the Tien Shan into two ridges (the Chatkal Range in the north and the Alai Range in the south) in its western part, behaves as another rigid block, being overthrust from both sides by aforementioned ridges (*Burtman et al.*, 1996; *Cobbold et al.*, 1993). *Thomas et al.* (1993) inferred a counterclockwise rotation of the Ferghana Basin of about 20° and a total shortening of 110 km for the Chatkal Range from paleomagnetic data.

2.5. Geodynamic models for the Pamir-Hindu Kush zone of intermediate-depth earthquakes

A wide variety of conceptual models attempting to interpret the occurrence of intermediate-depth seismicity beneath Pamir and Hindu Kush have been proposed in the last five decades. Since these models were nearly exclusively based upon studies of the seismicity distributions beneath Pamir and Hindu Kush, I will first give an overview over studies that presented local seismicity distributions, mentioning their data sources. Then, I will move on to give an overview of models that were proposed based on these seismicity distributions. This will be just a brief listing of studies and their main points, a discussion of these models will be presented, based on my own findings and published evidence, in Section 4.3.2.

Published studies showing seismicity distributions of the Pamir-Hindu Kush are few, and their data content mostly small. Owing to political reasons, studies of seismicity utilizing locally recorded data have been rare for this region. Especially the Pamir, probably owing to the smaller earthquake magnitudes compared to the Hindu Kush, has only been very sparsely imaged. *Nowroozi* (1971)

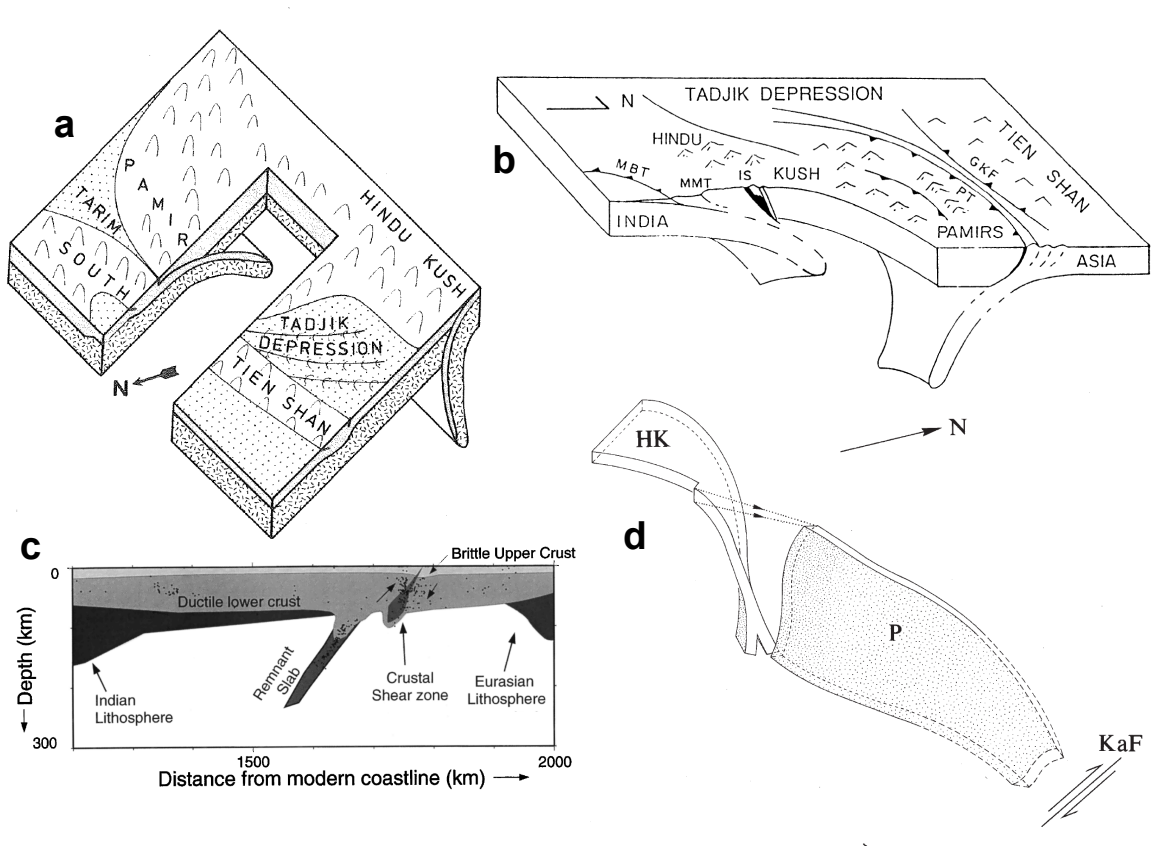

Figure 2.6.: Conceptual sketches of a selection of proposed models for the Pamir-Hindu Kush:
a) Two-plate model, featuring intracontinental southward subduction of Eurasia in the Pamir and northward subduction of Indian material in the Hindu Kush (Figure from *Burtman and Molnar*, 1993)
b) Model of southward subduction of Eurasia in the Pamir, steepened by the impingement of underthrusting India (Figure from *Fan et al.*, 1994)
c) A single, remnant slab of Indian provenance floating in the mantle due to neutral buoyancy, deformed as a consequence of mantle flow (Figure from *Pavlis and Das*, 2000)
d) Single, contorted slab of Indian provenance, contortion due to relative northward translation along the Karakorum Fault (Figure from *Pegler and Das*, 1998)

used recordings from a regional set of seismic stations to study seismic activity in southwestern and central Asia, and came up with a series of profiles through the Hindu Kush. A selection of these locations, together with ISC catalog events, were reprocessed by *Billington et al.* (1977). *Chatelain et al.* (1980) utilized data recorded by a two-month temporary deployment in Afghanistan in 1977, *Roecker et al.* (1980) analyzed recordings from stations of a local network in western Tajikistan (former USSR) and Afghanistan deployed from 1966-1967. All of these studies almost exclusively image seismicity in the Hindu Kush and have only very sparse or no coverage of the Pamir. *Fan et al.* (1994) showed some cross-sections through ISC bulletin earthquakes in the Pamir, and *Pegler and Das* (1998), in the most comprehensive study to date, relocated about 6,000 ISC earthquakes from the Pamir and Hindu Kush with a joint hypocenter determination technique.

A selection of proposed models is shown in Figure 2.6. Since intermediate-depth seismicity was found to outline planar zones resembling Wadati-Benioff zones in subduction zones, most models feature one or two subducting lithospheric slabs. Due to the observed along-strike change in dip polarity, two schools of subduction models, involving either two slabs subducting in opposite directions or a single, contorted slab, have emerged.

The first two-slab model was brought up by *Chatelain et al.* (1980), who invoked the subduction of a remnant basin of oceanic lithosphere (comparable to today's Caspian Sea) for the southward dipping eastern part of the zone. Based on a local earthquake tomography of the Hindu Kush, *Roecker et al.* (1982) first proposed that continental crustal material could be subducted there. In a monumental study reviewing a lot of Soviet literature, *Burtman and Molnar* (1993) proposed intracontinental southward subduction in the Pamir based on geological and geophysical arguments (Figure 2.6a). The idea that continental India, which underthrusts Eurasia further south, could be involved in the creation of seismicity in the Pamir-Hindu Kush, was first brought up by *Coward and Butler* (1985), who proposed that the Hindu Kush earthquakes may be occurring due to ramp faulting within the underthrusting lithospheric material. *Fan et al.* (1994) postulated an impingement of underthrusting India onto the continental, southward dipping Pamir slab as the reason for the steep dip angle of the latter (Figure 2.6b).

A model of a single, contorted slab was first invoked by *Billington et al.* (1977), who proposed the subduction of a last remnant of the Tethys Ocean as process responsible for intermediate-depth seismicity. This model was later expanded by *Pegler and Das* (1998), who proposed that the contortion of this oceanic slab of Indian provenance was due to a northward pull exerted on the eastern part of the slab by dextral relative motion along the Karakorum Fault (Figure 2.6d). Two years later, *Pavlis and Das* (2000) proposed a stagnant, contorted slab left over from the final closure of the Tethys as the source of intermediate-depth seismicity in the Pamir-Hindu Kush (Figure 2.6c). This remnant, consisting of oceanic material at depth and continental material at shallower levels (marking the transition of Indian material having arrived at the subduction zone), would have acquired neutral buoyancy at some point and since then have remained beneath the Pamir-Hindu Kush, being totally decoupled from surface tectonics. The active seismicity and contortion would be an effect of the mantle flow field on this slab remnant.

An entirely different class of models has been brought up rather recently. Based on the appearance of the Hindu Kush in seismic tomography, *Koulakov* (2011) interpreted it to be a mantle drip, i.e. a drop-like delamination of lithospheric material into the mantle. *Lister et al.* (2008) invoked a brittle process, analog to boudinage observed in smaller-scale structures, to effect a similar geometry. However, both of these concepts appear to not be compatible with the rather planar features outlined by earthquake locations, and fail to explain the Pamir seismic zone.

3. Field experiment/data

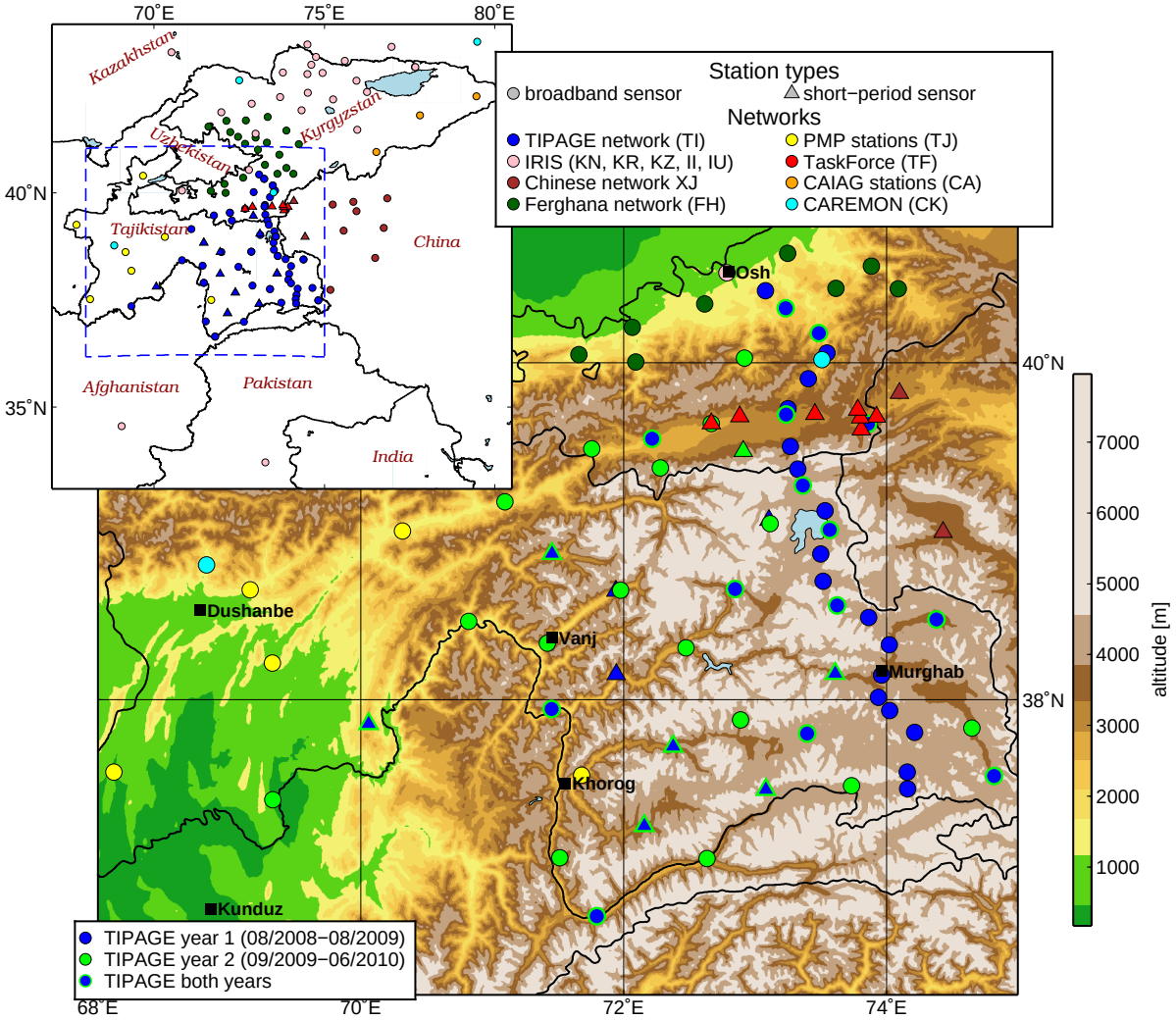

Figure 3.1.: Map showing the distribution of seismic stations during both periods of the TIPAGE deployment (main figure) and the auxiliary stations that were utilized (upper left subfigure). The blue dashed box in the upper left subfigure marks the area shown in the main figure.

As part of the TIPAGE (TIen Shan PAmir GEodynamic Program) project, a total of 40 seismic stations, 32 of them broadband sensors, were installed in southern Kyrgyzstan and eastern Tajikistan for a total duration of two years, from 08/2008 to 07/2010. The geometry of the array was changed in mid term, from a dense 24-station north-south profile with the other 16 stations distributed rather sparsely around it to a purely 2D geometry evenly covering the whole region of interest in the second term (see Figure 3.1).

This network was complemented by two further temporary deployments: 21 broadband stations distributed around the Ferghana Valley, south-western Kyrgyzstan, from 09/2009 to 09/2010 (*Haberland et al.*, 2011), and seven short-period stations in the Nura Valley deployed right after the 5 October 2008 Nura earthquake (Mw 6.6) for better coverage of the aftershock seismicity. Sampling frequencies for all temporary stations were 100 Hz. Data from several permanent networks in the region were retrieved through collaborations with the various institutes or from online resources (IRIS), further enlarging and partly densifying the network to cover all of Tajikistan and most of Kyrgyzstan.

Accuracy of GPS-derived timing was checked and, where necessary, adjusted (see Appendix A) for all stations of networks TI, TF, and FH.

4. Seismicity in the Pamir and Hindu Kush

4.1. Automatized seismogram picking, earthquake location and relocation

The rate of seismicity in the study region during the recording time was so high that conventional processing, i.e. locations based on manual phase picks, would only have allowed analysis of a subset of events. However, as one of the goals of this study is to present a realistic and as complete as possible image of the overall seismicity, I implemented an automated multi-stage processing chain for picking, locating and relocating earthquakes. Algorithms for the automated identification and onset time picking of seismic phases have been available for several decades (e.g. *Allen*, 1978), and their importance is rapidly increasing due to the growing amount of globally recorded seismic waveform data. However, their application in a continuous processing chain, leading from the continuous waveform data to a final, well-located set of earthquakes with high-quality, reliably classified arrival time picks, is still not a standard procedure. We used first detections from a short-term versus long-term average ratio (STA/LTA) trigger and a backprojection algorithm for event association and preliminary locations, then specialized P and S phase pick algorithms on targeted phase windows for an improved set of phase picks, which were jointly inverted for new hypocenters, station-phase-terms and a 1D velocity model. We finally calculated differential travel times based on waveform cross-correlation that were used together with phase picks in double-difference relocation. At each step, quality checks were implemented to weed out spurious picks, wrong associations and false and badly constrained events. Since the quality and reliability of the arrival time picks and ensuing hypocenters is the foundation of the geodynamic interpretation as well as for any future application of the data set, e.g. in tomography, this paper elaborates upon the applied processing chain and quality assessment in some detail.

4.1.1. Preliminary P-picks and locations

All vertical component waveform data were examined with a recursive STA/LTA trigger algorithm (as in *Withers et al.*, 1998) with an adaptive trigger threshold, i.e. the threshold was defined as the 99.9% quantile of the characteristic function. This ensures a roughly constant amount of alerts for each station and day, which was calibrated to capture all background seismicity. During seismicity swarms and aftershock series, this implementation leads to smaller events possibly being missed (depending on the activity level). Slightly more than $4 * 10^6$ trigger alerts were determined in this step, by far not all of them, however, related to actual earthquakes. The association of preliminary picks to preliminary events was performed using `Binder` (Rietbrock and Heath, pers. comm., 2010), a program which uses a migration approach on a rough orthorhombic grid of the region of interest, based on a preliminary 1D velocity model (used by *Mechie et al.*, 2012, as

starting model for 2D inversion in the eastern Pamir). Travel times from each station to each lattice node are calculated, subsequently a time window is propagated over the stack of trigger alert times, and consistent origin times at one node are searched for by back-propagating the travel times on the grid. An event is declared if origin times at one node are produced from the trigger alert stack within a user-defined error margin. Thus, most false trigger alerts are sorted out, whereas earthquakes consistently appearing in the seismic records of several stations at the right time are retained. The obtained events were finally relocated using Geiger's (*Geiger*, 1910) least squares inversion method (i.e. `HYPO71`; *Lee and Lahr*, 1975).

4.1.2. Repicking of P

Based on these preliminary locations and picks, P onsets were repicked with the `MPX` algorithm (*Aldersons*, 2004; *Di Stefano et al.*, 2006). This code performs a three-step procedure, consisting of the application of a Wiener filter (*Douglas*, 1997), running the picker of *Baer and Kradolfer* (1987) on the filtered data, and a quality weighting procedure relying on Fisher statistics. With the Wiener filter, the constituent noise frequency bands are suppressed in the signal. This has the advantage of not changing the characteristics (and thus also potentially the onset times) of the signal as e.g. a standard Butterworth bandpass filter would (*Douglas*, 1997), but it requires the input of two time windows, one in the noise and one in the signal, for spectral analysis to be applied in order to find these constituent frequencies of noise and signal. Hence, `MPX` can only be applied as a secondary picker, when a preliminary P pick around which these windows can be placed already exists (see Figure 5 in *Diehl et al.*, 2009a).

`MPX` was set up to classify onsets into four quality classes (0 to 3, see Table 4.1). The weighting scheme was calibrated with a hand-picked reference data set (see Section 4.1.5) following the procedure outlined in *Diehl and Kissling* (2008) (see Appendix B).

To exclude effects caused by the different frequency responses of the various sensor types, all vertical waveform data were converted to a Mark Products L4C seismometer response with 1 Hz eigenfrequency. For the local, mostly small to moderately sized earthquakes encountered here, this filter proved to be appropriate. In the next step, the STA/LTA arrival times were taken as the preliminary P estimate around which the time windows on the waveform data were placed. If a good pick (classes 0 or 1) was obtained with this configuration, it was accepted. In the other cases (classes 2 or 3), `MPX` was run multiple times with systematically varying window placements to account for the uncertainty in the preliminary onset estimates, and earlier and/or higher-quality arrivals were chosen to replace the initial pick.

In the case of no arrival being found for an STA/LTA-derived preliminary P estimate, the vicinity (6 seconds before until 2 seconds after the estimate, in steps of 0.5 seconds; asymmetry due to the tendency of STA/LTA picks being late) of this STA/LTA arrival was examined iteratively, and the highest-quality arrival obtained in this way was accepted. When two or more arrivals of the same quality class were found, the earliest one was accepted. If no arrival was found, the station with its STA/LTA pick was discarded for this event.

As the event association process with `Binder` (see Section 4.1.1) falsely discards a substantial amount of STA/LTA trigger alerts in the first step, stations with no STA/LTA pick were likewise iteratively examined with `MPX`. In this case, the first reference P estimate, around which the

search window was defined, came from raytracing (NonLinLoc package, *Lomax et al.*, 2000) based on the preliminary event location and the preliminary 1D velocity model. Since these locations are generally not very precise and the velocity model is not necessarily appropriate everywhere, the window in which the P arrival was searched for iteratively was doubled compared to the case where an STA/LTA pick existed.

Based on the refined P picks obtained in this manner, all events were relocated using an iterative procedure based on multiple `HYPO71` calls. For each event, a subset of picks which had the best quality classes and the shortest travel times was selected, and a first location was performed for these picks only. This first location, based solely on reliable picks, serves as reference against which the more dubious picks (lower quality classes, greater distance from event) were subsequently tested. In case the root mean square (RMS) residual of this location was higher than 1 second, different starting depths were tried. If this did not yield a location with acceptable RMS residual, the pick with the highest single residual was removed. This was repeated until a good location was found. In a second step, the picks with lower quality estimates and those from more distant stations were incorporated. This was done one pick at a time, and a pick was only kept if after relocation the single residual of the new pick fell below a distance-dependent goal residual (0.6s + (traveltime)*0.015). The rationale for performing this procedure is that a large amount of systematically shifted low-quality picks might, if added at the same time, dominate the location and thus effect a sorting out of the "better" (e.g. nearer and higher-quality) picks. All in all, 22,869 events, consisting of 380,626 P-picks, were obtained in this step.

4.1.3. S picking

Subsequently, S onsets were automatically determined using the software `spicker` (*Diehl et al.*, 2009b), which combines three different strategies of identifying S picks:

- The S-phase picker of *Cichowicz* (1993), which declares the S onset where the product of three parameters, i.e. deflection angle, degree of polarization and ratio of transverse to total energy, rises above a threshold.
- An STA/LTA detector applied to the horizontal components
- An autoregressive Akaike Information Criterion (AR-AIC) based predictive picking algorithm as described in *Takanami and Kitagawa* (1988).

With each of these single algorithms, an earliest and latest possible pick are determined, and the widths of these single "pick windows" as well as the consistency of the three methods yield quality classes of the picks. `spicker` hence requires a good P pick (needed for the polarization analysis and the choice of several time windows), an event location and a preliminary S pick.

We applied `spicker` to the stack of relocated events with `MPX` based P phases. The preliminary S arrivals were determined by raytracing. `spicker` was calibrated to rate picks into four quality classes as above (see Table 1).

After adding S arrivals, events were again relocated, using the same procedure as outlined for the P picks, only allowing for greater single residuals for the stations with low-quality arrivals and/or large hypocentral distances (cutoff value 1.0 s + (traveltime)*0.015). It should be mentioned that

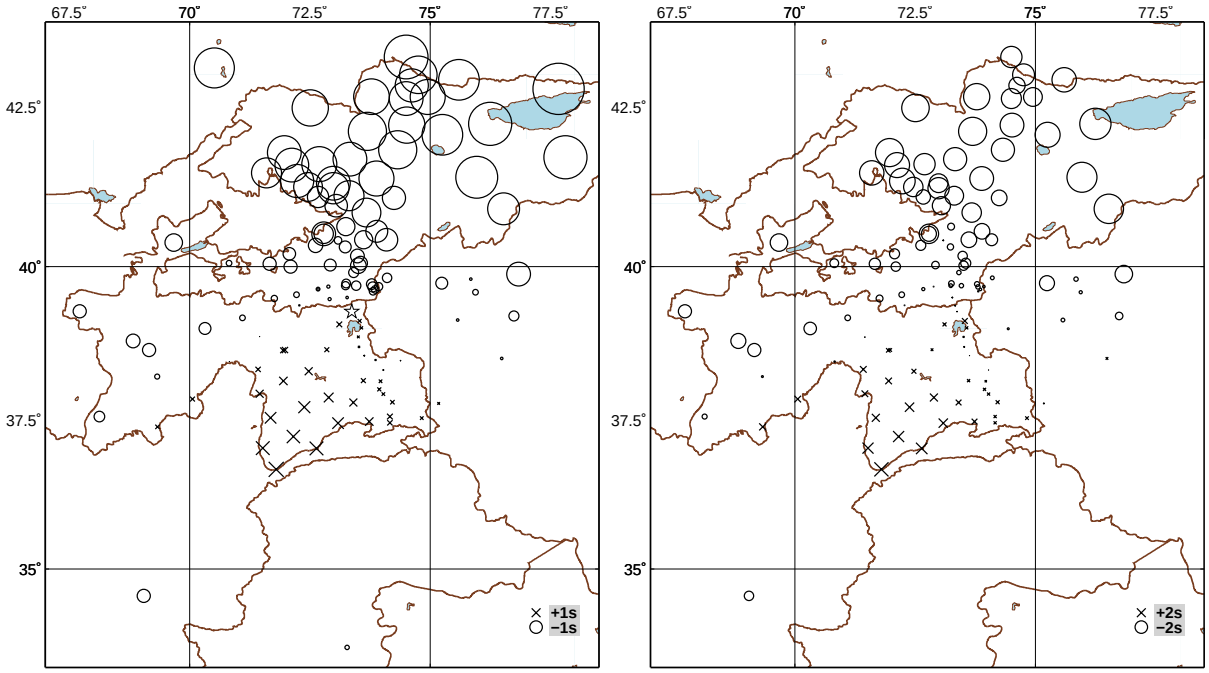

Figure 4.1.: Static station corrections for P (left) and S (right) phases determined from a joint inversion for 1D velocity model, hypocenters and station corrections for a reference data set of 1,780 automatically retrieved events consisting of 55,812 P and 30,699 S picks. Starting model and final 1D velocity model are shown in Figure 4.2. Only stations with at least 20 arrival times in the reference data set are shown. The reference station, constrained to have a P correction of zero, is shown with a star in the left subfigure.

Quality class	handpicking goal [s]	handpicking variance [s]	variance autopicker [s]
P_0	0.05	0.045	0.051
P_1	0.1	0.130	0.139
P_2	0.2	0.304	0.293
P_3	>0.2	0.669	0.914
S_0	0.1	0.162	0.173
S_1	0.2	0.712	0.252
S_2	0.4	0.775	0.408
S_3	>0.4	1.124	1.144

Table 4.1.: Uncertainties associated with the single picking quality classes for P and S onsets. Handpicking variance was defined as the average deviation between earliest and latest pick of four human analysts picking the same data set. Autopicking variance is the mean standard deviation of residuals between automatic pick and one (reference) human analyst (columns of the confusion matrices in Figure 4.3).

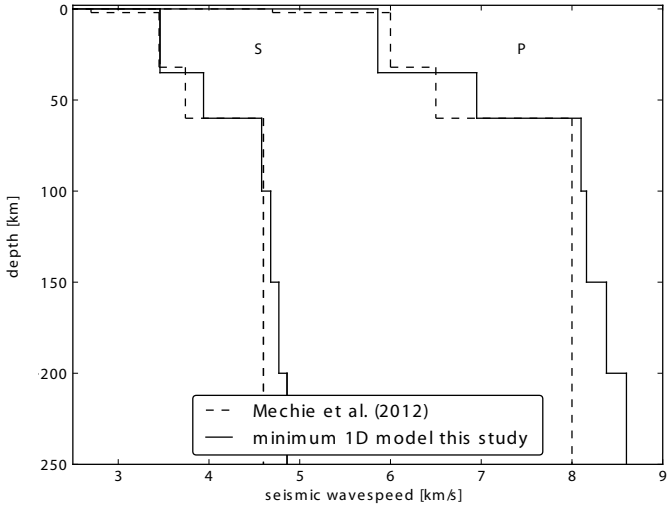

Figure 4.2.: Comparison of velocity models of *Mechie et al.* (2012) (initial model before 2D inversion; dashed lines) and the minimum 1D model obtained in this study (solid lines).

I allowed the possibility of further P picks being removed should they, and not the newly added S picks, have the greatest single residuals.

After this step, the catalog contained 22,858 events with 370,013 P and 149,332 S-picks. A selection procedure was applied subsequently in order to choose only the most robustly located earthquakes from the data set. A cumulative pick sum was calculated for each event in the following way: P and S picks of quality class 0, 1, 2 or 3 add 4, 3, 2 or 1 point(s) to this sum, and S picks count doubly. Only events which had a cumulative sum above 50, with at least 16 points coming from S arrivals, were selected. This second constraint was necessary to exclude some regional events that were falsely located into the region of interest based only on P picks (no S picks were determined for those events because of grossly false window placement within `spicker`). This resulted in the set of 9,530 well-located earthquakes comprising 197,951 P and 104,471 S picks that will be analyzed further below.

4.1.4. Determination of minimum 1D velocity model and relocation

Following the procedure outlined in *Kissling et al.* (1994), I simultaneously inverted for a minimum 1D velocity model, hypocentral parameters and static station corrections using the program `VELEST`. A declustered reference data set consisting of 1,780 events, comprising 55,812 P and 30,699 S picks, was selected by subdividing the study area into subregions and selecting only the best located events respectively. The 1D velocity model of *Mechie et al.* (2012) (their starting model for 2D inversion) was used as the initial model. A Wadati diagram for all available events yielded an average vp/vs ratio of approximately 1.74, which was used for the initial S model in the inversion procedure.

Due to the substantial extent and rampant geological heterogeneity of the study area, the retrieved 1D model (see Figure 4.2) is rather crude and only represents a large-scale average over the study region. A shallow sediment layer, present in the model of *Mechie et al.* (2012) derived for the eastern Pamir, could not be resolved. Thus, most of the travel time differences caused by the

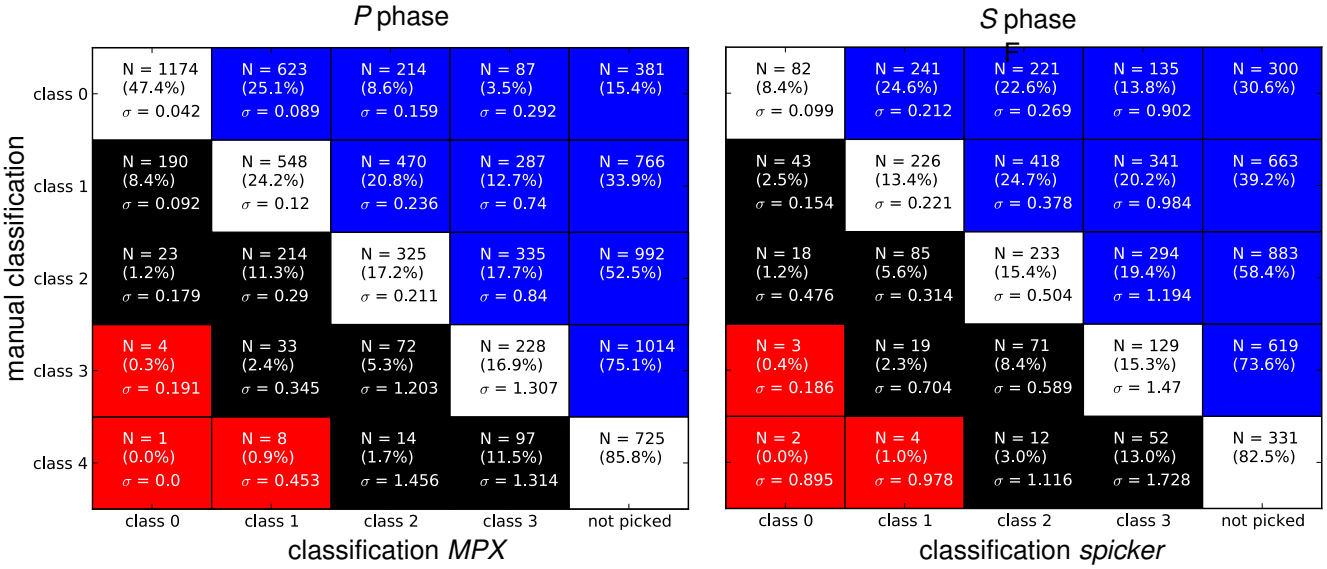

Figure 4.3.: Confusion matrices for P (left) and S (right) picks, comparing handpicks to the ones obtained by the automatic procedure described in the text. Columns refer to weighting classes as assigned by the two picking algorithms, rows represent the weighting scheme applied by the human analyst. The standard deviation of residuals between automatic and manual picks is given for each field (summed values for the columns are presented in Table 1). Percentages indicate the fraction of all manually determined arrivals of a certain quality class that are assigned a specific weight by the automatic procedure and sum up to 100% in each line of the confusion matrix. The conservative nature of quality weighting performed by the algorithms is discernible in the scarcity of picks falling into the black and red fields below the diagonal, which means that picks are rather downgraded than upgraded.

probably highly variable Moho depths and sediment thicknesses throughout the region of interest were mapped into the station corrections (see Figure 4.1). A trend from massively negative station corrections in northern Kyrgyzstan and around the Ferghana Valley and (to a lesser degree) in most parts of the Tajik Depression to positive values in and around the Pamir is discernible. This might, to first order, represent the misfit in the placement of the Moho in the 1D model. Moho depths in and around the Pamir plateau are significantly higher than 60 km (see *Mechie et al.*, 2012; *Beloussov et al.*, 1980), whereas they are substantially lower in the Tajik Depression (*Burtman and Molnar*, 1993) and the Ferghana Valley (*Steffen et al.*, 2011). Since seismicity is mainly concentrated in the southern and central part of the network, stations in the north have longer average path lengths, which presumably magnifies the error introduced by the assumption of a deep Moho; hence they acquire large negative station corrections.

All events in the catalog were re-located using the `VELEST`-derived 1D velocity model and station phase terms. Picks with residuals more than two standard deviations from the event's mean residual and with an absolute value above 1 second were removed, which led to a total reduction of 2.49% in P picks and 6.17% in S picks. Figure 4.4 shows the improvement in RMS residuals between locations using the preliminary velocity model and the minimum 1D model with station corrections. Obtained relocations not only show lower RMS residuals, but likewise define sharper structures compared to the preliminary ones, as illustrated in Figure 4.5 (subfigures A and B).

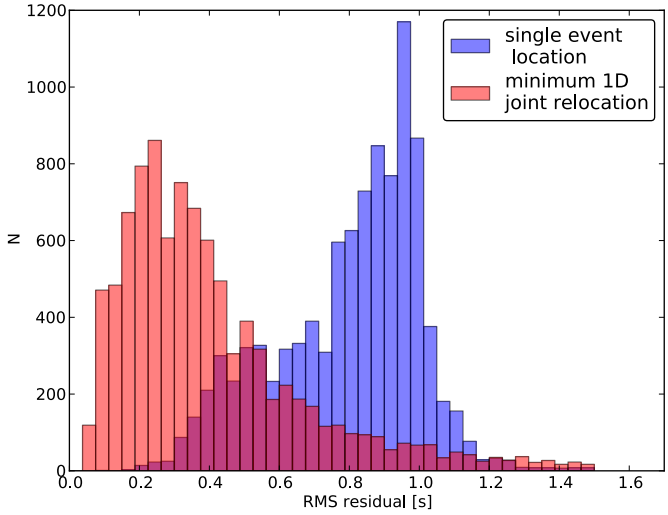

Figure 4.4.: Histograms of RMS travel time residuals obtained for the relocation of events after the S picking step, using the velocity model of *Mechie et al.* (2012) and single event location (blue) and after relocation with the minimum 1D model and station corrections (red).

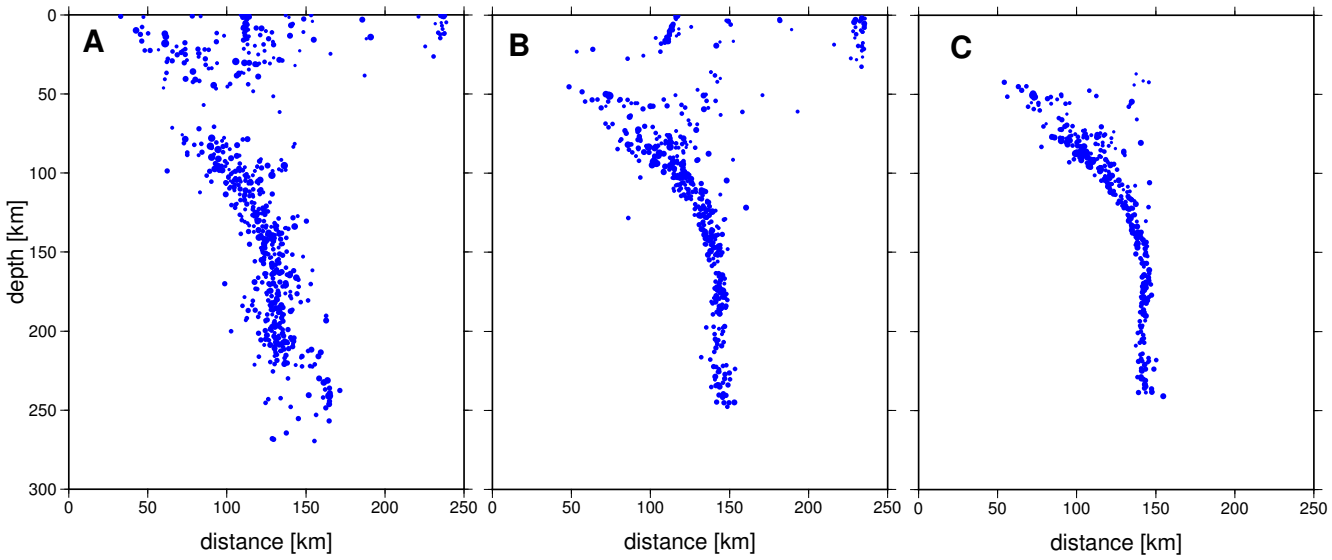

Figure 4.5.: Comparison of an example profile (equal to profile E-E' in Figure 4.14) through the obtained earthquake location processing chain. A: single-event relocation after S picking; B: Relocation with minimum 1D model and station corrections; C: Double-difference relocations with catalog and cross-correlation derived differential arrival times. Only deep events are shown in subfigure C, since not all distributed shallow events could be relocated with the double-difference method. Locations collapse to a more sharply defined structure from left to right.

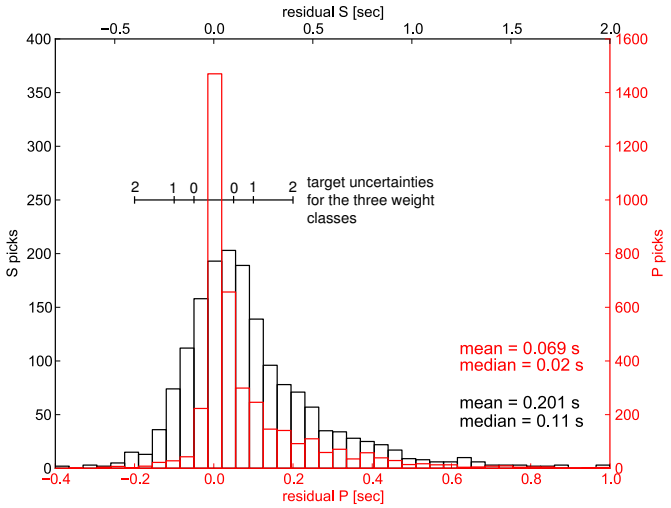

Figure 4.6.: Histograms of residuals between handpicks and automatic picks for P and S onsets, classes 0-2. Negative time values refer to the automatic pick being earlier than the handpick. Formal picking errors for classes 0, 1 and 2 are indicated by error bars around zero. Note that the horizontal axis is enlarged by a factor of 2 for S residuals.

4.1.5. Quality assessment

In order to assess the performance of the whole automated picking and location procedure, a reference data set consisting of 230 events was carefully handpicked (8,825 P and 5,538 S picks), guided by the weighting scheme shown in Table 1.

The picking and weighting performance of the whole automated procedure is compared to the human analysts' picks in two confusion matrices (Figure 4.3). The hit rates I obtain are relatively low (56.4% of the human analyst for P, 49.9% for S), which is not only due to the rather conservative nature of the two picking algorithms' weighting schemes (see *Di Stefano et al.*, 2006; *Diehl et al.*, 2009b), but also reflects the loss of some picks in the multiple relocations along the processing chain. Our automated classification is shown to be conservative, as nearly no picks being upgraded from the lowest visually assigned quality classes to the highest automatic ones are observed (red fields in the confusion matrices).

In order to evaluate the real uncertainties behind the automatically assigned weighting classes that were obtained for the data set, I have to evaluate the columns of the confusion matrices. Except for the lowest automatic class 3, the summed standard deviations of residuals are near the goal uncertainties for handpicking (see Table 1), and residuals are systematically smaller for higher quality classes. Histograms for residuals between handpicks and automatic picks, summed for quality classes 0 to 2 (i.e. the three leftmost columns in the confusion matrices in Figure 4.3), are shown in Figure 4.6.

Since the uncertainties listed in Table 1 are only goals, the implementation of which by human observers may substantially differ, I performed a test comparing four different analysts handpicking the same subset of the reference data set.

A comparison of the automated procedure's accuracy for each quality class is shown as a boxplot in Figure 4.7. The distribution of residuals (i.e. pick time difference human analyst - automatic pick)

is shown for each (automatic) quality class for P and S. Superimposed are the goal uncertainties (green bars) and the mean pick variability between the four human analysts. For the determination of this last quantity, each trace that was picked by at least two of the four analysts was evaluated, an average weighting class was determined (rounded mean of the assigned classes), and the absolute time difference between earliest and latest handpick was calculated. The means of all these differences, for each average weighting class, are displayed as red bars in Figure 4.7. It is evident that when picking S onsets, the human analysts do not reach the uncertainty goals of the quality classes.

Figure 4.7 and Table 1 show that, with the exception of the classes P_3 and S_3, the automatically obtained picks do not substantially deviate from what a human analyst would determine. In the case of S picks, the humans' performance may even be inferior to that of the algorithm. The retrieved quality classes scale with uncertainty (here taken as residual human-autopicker), and these uncertainties are not much higher (P) or even substantially lower (S) than the mean variance between different human analysts. The main caveats of the automatic procedure are the lower hit rate compared to handpicking and a slight tendency of automatic picks being later than manually determined ones (see Figure 4.6).

A final quality estimate for obtained picks that does not rely on any human reference analyst comes from the application of waveform cross-correlation (see also Section 4.1.8). Pairs of arrival times for clustered events at a single station were utilized and the optimum time lag, i.e. the amount of time one trace has to be shifted relative to the other in order to optimally align them, was determined. Results of this procedure are shown in Figure 4.8. It is observed that the lag times scale with quality class (larger lags for lower classes) and that the standard deviation of lags is comparable to (for P arrivals) or smaller than (for S arrivals) formal picking errors for each class.

4.1.6. Location uncertainty

To acquire a measure for the accuracy of the obtained locations, especially with respect to network geometry, I employed a probabilistic relocation scheme of the events (*Lomax et al.*, 2000). Here, a probability density function (PDF) for the location of each single event is retrieved, together with an error ellipse containing 68% of this PDF. To visualize location uncertainties for this large three-dimensional data set, the study region was subdivided into three depth layers (0-70 km, 70-150 km and >150 km), and each depth layer into $0.25° \times 0.25°$ bins. We then calculated the mean length of error ellipses for all events within each bin in longitudinal, latitudinal and vertical direction. If a bin contained less than five events, it was left blank. The results of this computation are shown in Figure 4.9. It is discernible that the vertical error is in all cases larger than the horizontal errors, and that shallow- and intermediate-depth events in the Hindu Kush have a rather bad depth resolution, whereas the deep ones are substantially better constrained. Throughout the Pamir, horizontal errors lower than 7.5 km and vertical errors lower than 15 km are found. Intermediate-depth events in the Pamir show better constrained focal depths than crustal events. It should be mentioned that there are secondary effects influencing the observed accuracy as displayed in Figure 4.9. If events in one bin, for example, are relatively small in magnitude, hence only have fewer constituent picks than events elsewhere, this will lead to a worse accuracy estimate than in a region which has comparable network geometry but larger (better picked) earthquakes.

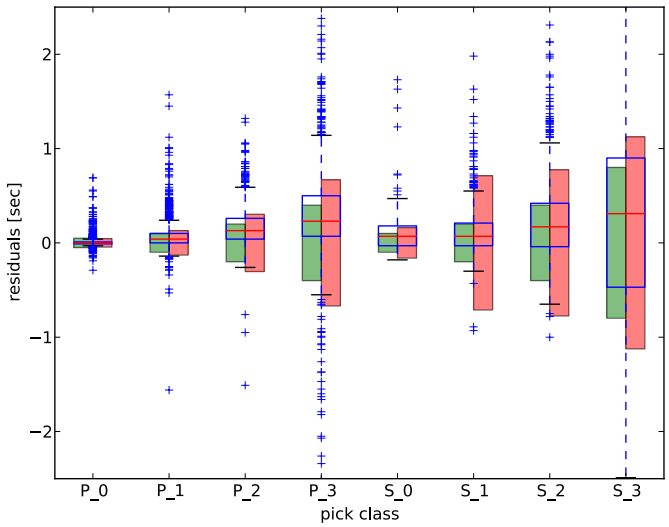

Figure 4.7.: Boxplot of the distributions of residuals between automatically and manually determined picks for P and S arrivals of a reference data set of 230 events, sorted by quality class. The red horizontal line in each boxplot is the median value, the blue box around it defines the inner quartile range, i.e. 50% of the data are within this box. The whiskers (dashed blue lines) extend to the furthest data point within another 1.5-times this inner quartile range, points outside this range are plotted as blue plus signs. Superimposed on this are the goal uncertainties for each quality class as listed in Table 1 (green bars) and the actual variability in handpicked arrival times obtained by four human analysts (red bars).

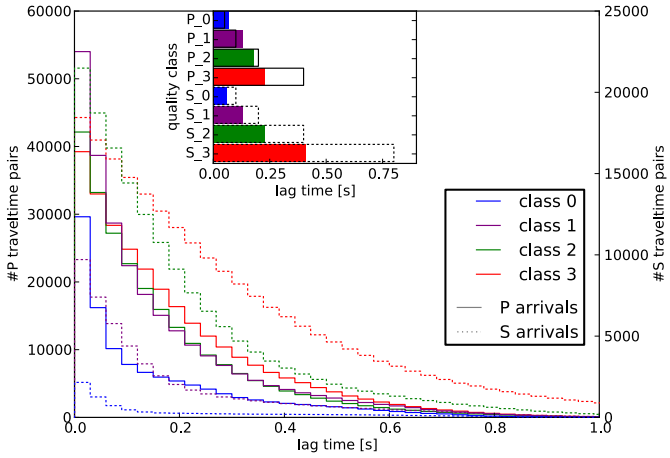

Figure 4.8.: Cumulative histogram of CC lag times, shown for all P and S quality classes. For each event pair at one station, the lower of the two picking quality classes was chosen to define overall quality. Differences between the quality classes are discernible, a greater proportion of small lags is observed for the higher quality classes. In the inset, the 68% quantile of the lag times for each quality class, taken as a proxy for standard deviation (which can not be determined for a one-sided distribution), shown as colored bars, is compared to the formal picking errors (black bar frames) defined in Table 4.1. Obtained lag values for P correspond well to formal errors, for S they are even substantially smaller.

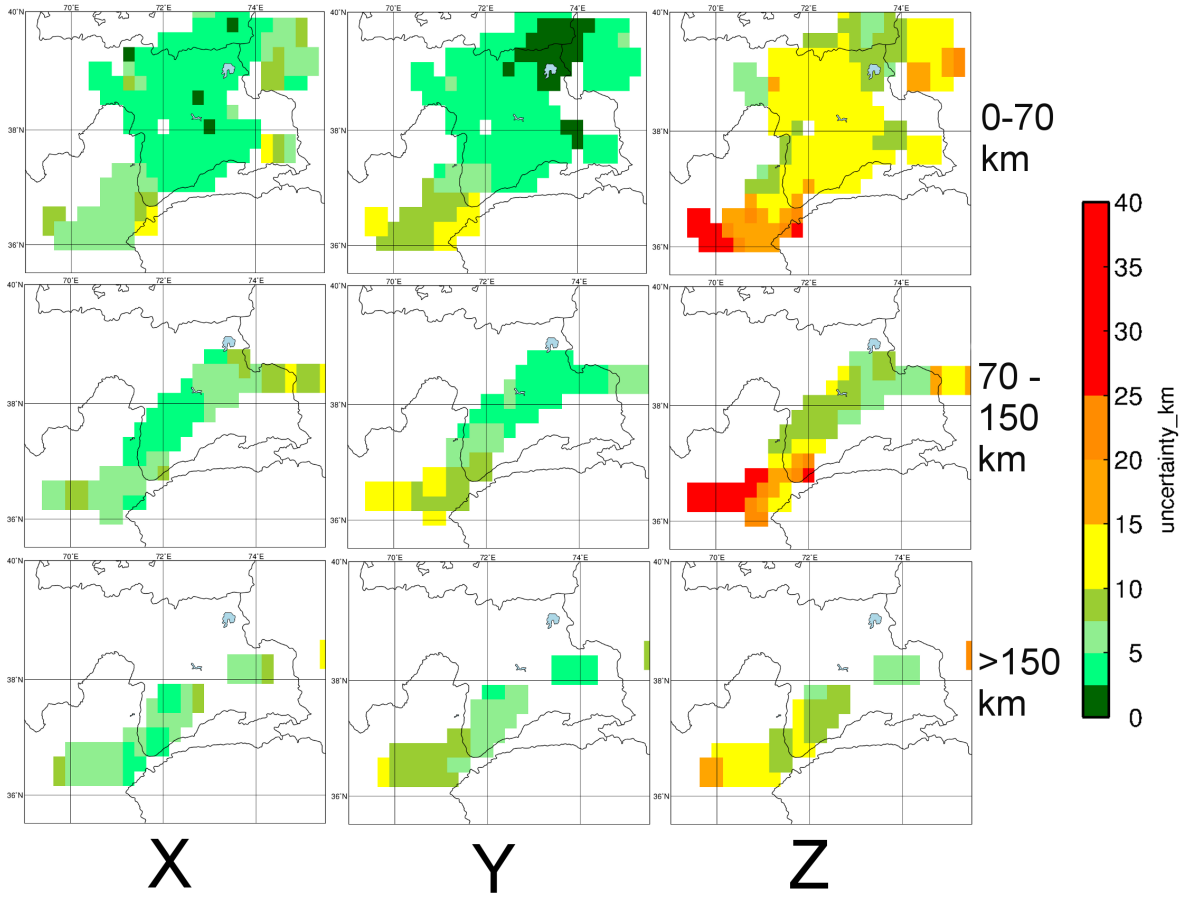

Figure 4.9.: Mean location uncertainty, i.e. extent of the error ellipsoid, in longitudinal, latitudinal and vertical direction calculated for 0.25°*0.25° bins in three depth layers, indicated at the right of the images. Bins containing less than five earthquakes are left blank.

4.1.7. Magnitudes

Local magnitudes (M_L) were calculated for all earthquakes using the approach of *Hutton and Boore* (1987). An alternative set of coefficients, distinguishing between shallow and deep seismicity in the calculation of the respective values of M_L (*Shin*, 1993) yielded comparable magnitudes. The distribution of magnitudes among all events is shown in Figure 4.10 (lower right). From the histogram, a magnitude of completeness of around 3 can be estimated, which is roughly where the histogram turns non-exponential from right to left. However, this is just a first-order estimate, and the value should vary substantially with region and time due to the heterogeneous and changing network geometry.

4.1.8. Double-difference relocations

To further refine the hypocenter locations, the catalog of earthquakes was relocated once more using a double-difference (DD) scheme (HypoDD, *Waldhauser and Ellsworth*, 2000). The DD method relates travel time differences of pairs of events to the same station to their spatial separations and therefore cancels out the correlated errors arising from unmodeled structure along

the segment of the path they share. It has been shown to be particularly effective if precise differential travel times from waveform cross-correlation are used. Cross correlation (CC) based travel time differences are often an order of magnitude more precise than the ones derived from phase picks. A further advantage of using CC travel time differences is that measurements are done algorithmically, not relying on analyst intervention, making it particularly suitable for large data sets. We calculated CC based differential travel times (for P and S) both for events with and without phase picks. In the latter case I used ray tracing to place the CC windows. In this way the data set is replenished with phase measurements that may have been missed due to the limited hit-rate in arrival time picking. Cross correlation measurements were done for events separated by not more than 15 km with windows of 2/4 seconds for P/S phases in the case that arrival time picks existed and longer 4/6 second windows in the case that theoretical arrival times were used, in order to compensate for the larger uncertainty in the window placements. Only measurements with a correlation coefficient >0.7 (see tests in *von Seggern*, 2009) were kept, with the correlation coefficient used as a weight in the hypocenter inversion.

In total, 8,207 earthquakes were relocated with hypoDD, utilizing 180,096 P and 130,134 S cross-correlation phase pairs as well as 1,013,650 P and 480,864 S differential arrival times from the catalog. A weighting scheme was implemented that starts the inversion exclusively with the catalog phase pairs, then successively down-weighs those and assigns higher weights to the cross-correlation phase pairs. The overall RMS residual was reduced from 0.239 to 0.184 seconds (-23.0%) for the catalog arrivals and from 0.332 to 0.026 seconds (-92.2%) for the cross-correlation phase pairs in the course of the relocation.

DD can only relocate events that have strongly linked measurements, i.e. that belong to spatial clusters. Hence, for events that could not be relocated by DD (e.g. because they are spatially isolated), I kept the locations derived in Section 4.1.4. The improvement in hypocenter locations through the different steps of the relocation scheme is impressively demonstrated in an exemplary cross-section in Figure 4.5. In this cross-section, structures are clearly sharpened and hypocenters at mantle depths collapse to a plane less than 10 km thick, first steeply dipping east and then dropping vertically down to a sharp cut-off at approximately 250 km depth. This further sharpening of imaged structures indicates that the final location uncertainties should, for the DD relocations, be smaller than the estimates shown in Figure 4.9.

4.2. Results

The seismicity in the earthquake catalog produced as described in Section 4.1 is shown in map view and two projections onto a single longitudinal and latitudinal plane, respectively, in Figure 4.10. An S-shaped belt of intermediate-depth seismicity from the Hindu Kush in the southwest into the Eastern Pamir is the most prominent feature in the study region. Most shallow earthquakes are located north of this structure, along the Pamir's northern perimeter and in several clusters in the western Pamir.

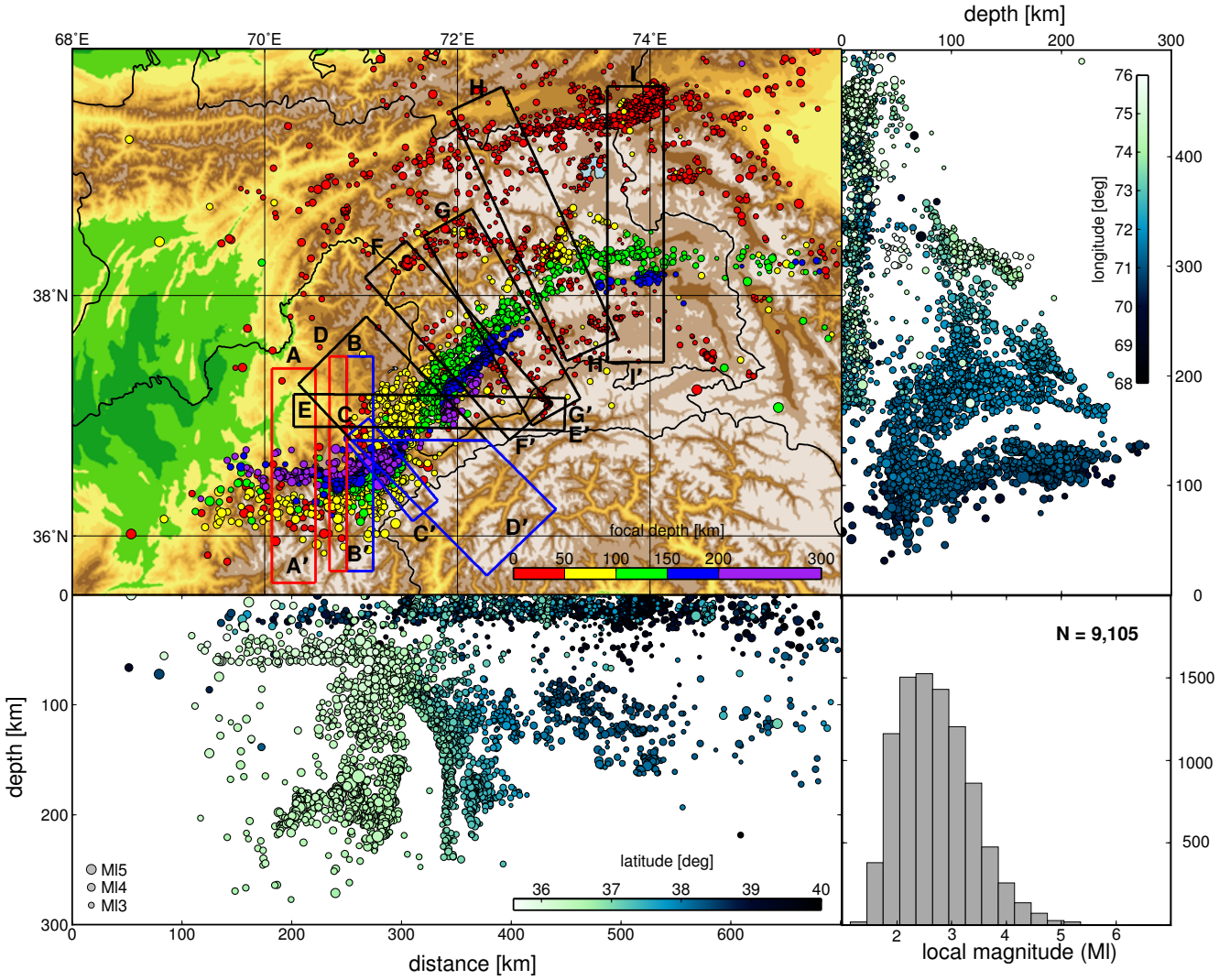

Figure 4.10.: Overall distribution of seismicity in the study area from 8/2008 to 6/2010 in map view (plotted onto a topographic map) and as projection of all events onto a longitudinal and latitudinal plane. Dot sizes denote different earthquake magnitudes, colors denote different depth levels (in the map view plot) and distance from the projection plane, respectively, as indicated in the color legends. Deeper events were plotted on top of shallower ones in the map view subplot, nearer events on top of farther ones in the projections. Boxes indicate the location and extent of the profiles shown in Figure 4.14, colors reflect a subdivision in western Hindu Kush (red), eastern Hindu Kush (blue) and Pamir (black) and is reflected in the colors in Figure 4.14. Lower right subfigure shows the distribution of local magnitudes in the data set. 9,105 of the total number of 9,530 earthquakes are shown here, the missing events are located north of the region shown in this plot.

4.2.1. Shallow seismicity

The distribution of seismicity with hypocentral depths shallower than 50 km (crustal) is shown in Figure 4.13A. Most shallow-focus earthquakes are located at the northern circumference of the Pamir, at or south of the southern margin of the Alai Valley, where the MPT surfaces. The strong cluster of seismicity in the eastern part of the Alai Valley originated mostly from the aftershock activity associated with the October 5, 2008 Nura earthquake (M_w 6.6). Shallow seismic activity within the Pamir is unevenly distributed: the eastern Pamir plateau appears to be largely aseismic, whereas several seismically active zones can be found in the deeply incised western Pamir. A northeast-southwest striking lineament passing lake Karakul in the north appears to separate these two regions. Crustal seismicity is concentrated in the uppermost 25 km (see Figure 4.10 and profiles in Figure 4.14), and mid- to lower crustal levels appear to be aseismic. Only a brief comparison of obtained earthquake locations with mapped surface structures is provided here, for a more detailed discussion of crustal tectonics in the Pamir refer to Section 5.5.1.

Correlation to mapped structures

Figure 4.11 shows a superposition of the epicenters of retrieved crustal earthquakes in the Pamir with mapped structures interpreted to be (geologically) recently active (*D. Rutte, pers. comm., 2012*). Geological and structural mapping of the Pamir Mountains is currently ongoing, so the compilation of features shown here is incomplete, and their spatial distribution also reflects heterogeneous progress in structural reconnoitering.

A correlation of the epicenters to mapped features is hard to infer. Numerous structures, especially in the eastern Pamir, show no earthquake activity at all, whereas many earthquakes occur far from any mapped fault (e.g. southwestern Pamir). The fact that the displayed lines indicate the surface outcrops of inclined structures, combined with the uncertainty to the depths of these earthquakes (see Figure 4.9), may allow for some scatter, but I do not dare to claim a general correlation here. Apart from the occurrence of a number of smaller earthquake clusters (both ends of the valley south of Vanj, east of Lake Sarez, south of Khorog), most seismicity appears to be diffusely distributed rather than outlining linear fault segments. An exception from this is the eastern MPT, directly west of the Nura aftershock sequence, where a clear lineament is defined by the epicenters.

Nura aftershock sequence

The by far largest number of shallow earthquakes recorded by the TIPAGE deployment belongs to the aftershock series of the October 5, 2008, M_w 6.6 Nura earthquake (*Krumbiegel*, 2011). Roughly 3,800 events, relocated with the double-difference technique, can be attributed to it, their spatial distribution is shown in Figure 4.12.

Epicenters of these aftershocks do not outline a simple planar fault, but define a rather complex L-shape, with an east-west trending segment along the border between Tajikistan and Kyrgyzstan that hosts the hypocenter of the main shock adjoining a second, NNE-SSW trending structure that was activated instantly after the main shock. Possibly, the main shock ruptured both sequences.

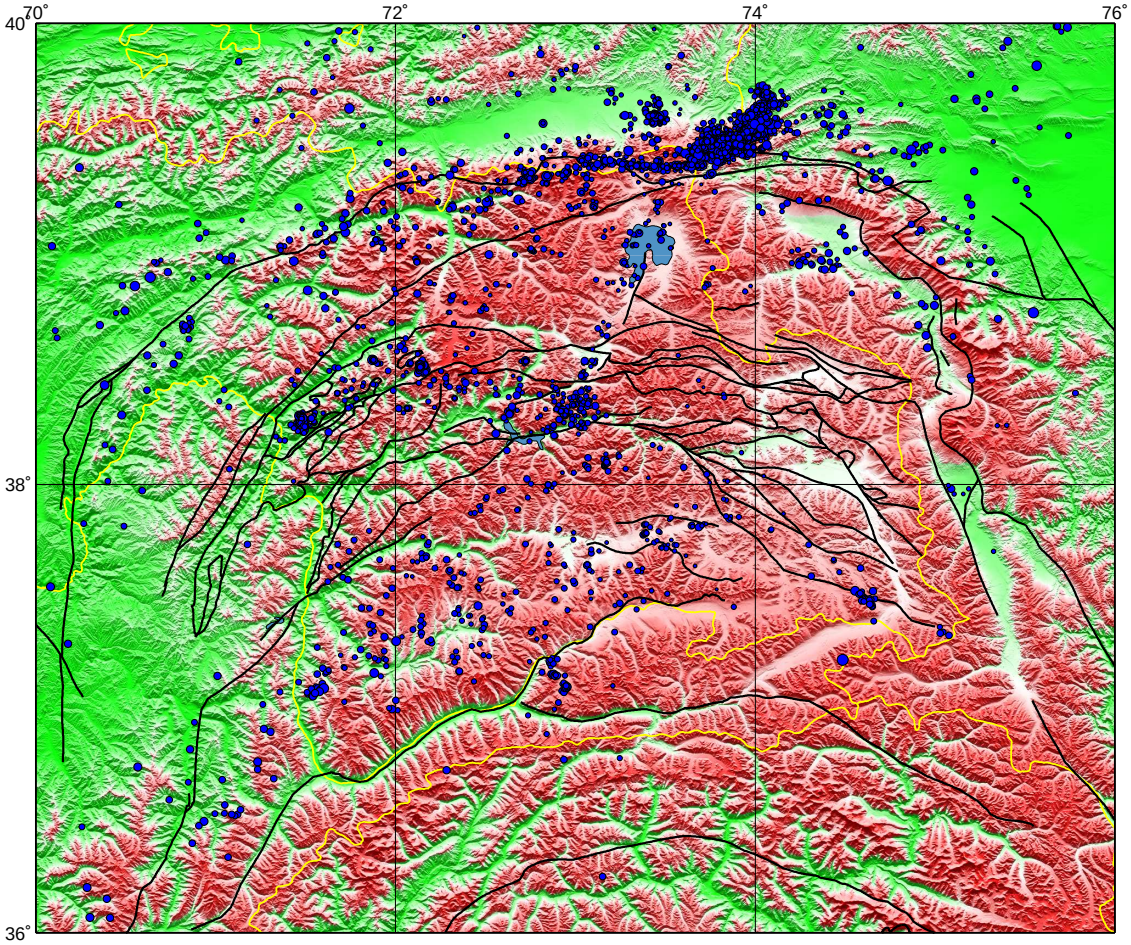

Figure 4.11.: Topographic map of the Pamir, with structures mapped as recently active shown by black lines (*D.Rutte, pers. comm. 2012*). Epicenters of shallow earthquakes are shown as blue circles.

A third, smaller subcluster can be identified further east, whose activity only began several weeks after the main shock.

The orientation of these features traces the predominant strike directions of mountain ridges in this area, which show a general change in orientation from east-west to NE-SW around the eastern end of the Alai Valley. The Nura aftershock series, albeit being an interesting study object, will not be investigated in detail in the framework of this thesis. It was examined in detail, using a smaller data set, by *Krumbiegel* (2011), and may be reinvestigated based on the shown locations in the future.

4.2.2. Intermediate-depth seismicity

The geometry of structures outlined by intermediate-depth earthquakes in the Pamir and Hindu Kush is shown in a series of representative profiles (Figure 4.14) and depth maps (Figure 4.13). We distinguish two distinct zones of seismicity - the Pamir and the Hindu Kush seismic zones -

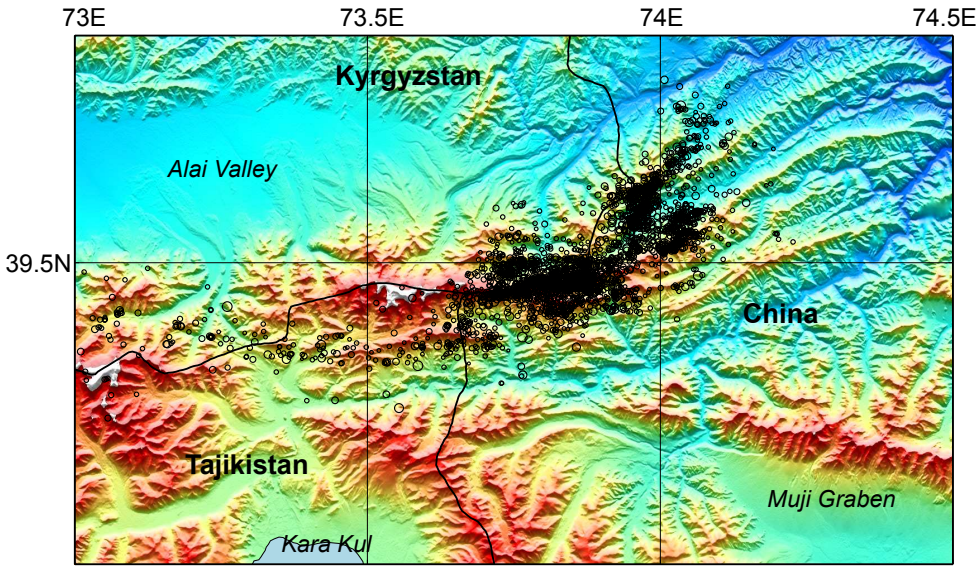

Figure 4.12.: Epicenters of Nura aftershocks, plotted onto a topographic map. The clustering of the events into three distinct groups is clearly discernible.

separated by a seismic gap and a 90 degree change in dip and strike directions around 36.8°N, 71.4°E, discussed in more detail below.

Pamir

The Pamir seismic zone begins at the boundary of the Pamir with the Tarim basin in the east and ends slightly northeast of the Hindu Kush zone's eastern termination, dipping due east (see cross-section E-E', Figure 4.14). Intermediate-depth earthquakes in this zone are confined to a thin (about 10-15 km thick), curviplanar structure outlining an arc, with its strike gradually changing from north-south to east-west and the dip changing from eastwards to southwards (see profiles E-E' through I-I' in Figure 4.14). All along this arc, the dip angle stays approximately constant at around 50°, except for depths greater than 150 km in the western part of the structure, where the dip steepens to become (sub)vertical (see profiles E-E' and F-F'). Some uppermost mantle earthquakes in these two profiles are located southeast or east of the curved plane defined by the majority of events. They appear to form a structure resembling a backthrust in the hanging wall (see profiles E-E' and F-F' in Figure 4.14).

Intermediate-depth seismicity in the Pamir is separated from shallow crustal activity by an apparently largely aseismic lower crust (depth region 25-70 km). Earthquakes in the Pamir deep seismic zone are located at depths greater than about 70 km. Their deepest extent is 140-170 km in the eastern part of the zone and 220-250 km in the zone's western part. These deepest earthquakes in the western Pamir form two subparallel, vertical "streaks" as evident from Figure 4.13E. A gap in seismicity at 150-200 km depth (Figure 4.13D) around 73°E marks a zone where the maximum depth and the density of earthquakes reaches a minimum; further east greater depths are reached again toward the zone's termination (see also color-coded stripes in Figure 4.10). Towards its southwestern end, the Pamir seismic zone abruptly changes its strike (best visible in Figure

4.13D), from NE-SW to due north-south. Local magnitudes in the Pamir seismic zone are generally moderate to low during the entire recording period, with only a handful of events stronger than M_L 4.5.

Hindu Kush

The Hindu Kush seismic zone is generally oriented east-west at roughly 36.4°N, with a sharply defined eastern end towards 71.4°E and a less clear western end somewhere between 69° and 69.5°E (see Figure 4.10). Hypocenters extend in depth from roughly 40 to 250 km, with only a few isolated earthquakes outside this depth range. Cross sections (Figure 4.14, profiles A-A' to D-D') and depth cuts (Figure 4.13) reveal significant geometric complexity.

In its westernmost part (Figure 4.14, profile A-A'), earthquakes in the Hindu Kush are confined to a tight cluster at 180-220 km depth that dips steeply southward. This cluster shows a northward convex curvature along strike, as visible in Figure 4.13D, and appears to be unconnected to some diffuse seismicity at lower crustal or uppermost mantle depths shown in the same profile. The termination of this part of the Hindu Kush can be seen in a change in strike and dip directions around 70.85°E, towards a more planar, WSW-ENE trending and steeply northward dipping structure east of this longitude (see Figure 4.14, profile B-B'). The transition between these two zones is apparent as a southward protruding "spur" in Figure 4.13D.

In the eastern part of profile B-B' (blue earthquakes), earthquake hypocenters outline a more planar structural entity extending from crustal depths to about 250 km depth. Most seismicity is concentrated between 160 and 210 km depth, whereas nearly no earthquakes are observed directly above this, around 150 km depth. For the whole structure a very slight northward dip is discernible, although this inference is less robust for its shallower part, due to the greater scatter in earthquake locations observed here, likely owing to lower location accuracy (see Section 4.1.6). Still further east (profile C-C'), the Hindu Kush seismic zone's strike progressively bends towards a NE-SW direction, aligning with the general strike of the Pamir seismic zone, and there is a clear segmentation into an upper and a lower part, separated by a seismic gap at 150 km depth. To the shallow side of this divide, hypocenters outline a planar feature dipping northwestward. Below the seismic gap at 150 km, a subdivision of the structure into three separate earthquake clusters is discernible. The exact geometric configuration of these clusters is complex and difficult to comprehend, and might thus not be obvious at first glance. The shallowest of these deep clusters extends from 150 to about 200 km depth and appears to be continuous with the shallower part both in dip direction and width. Below 180 km depth, two parallel striking clusters frame the first one on both sides, i.e. northwest and southeast of it. At depths greater than 200 km, where the uppermost of the three clusters is not observed any more, these parallel clusters are horizontally separated by about 15 km, which leads to the pattern of two parallel streaks in the depth map (see Figure 4.13E) and to an inverted-V or fork-like appearance in the profiles (Figure 4.14, profiles C-C' and D-D'). Whereas the two lowermost clusters are planar with a considerable horizontal extent, the shallowest of the three clusters is only present in the direct vicinity of the Hindu Kush zone's eastern termination, its shape resembling a narrow finger.

Profile D-D', which images earthquake hypocenters to both sides of the gap separating the Pamir and Hindu Kush seismic zones, shows the jump in dip occurring across this gap. Whereas there is a clear change in dip polarity at levels shallower than 150 km, the structures apparently align

in their lower parts, where both are sub-vertical. This alignment, however, can only be observed for the uppermost of the three deep clusters in the eastern Hindu Kush, whereas Hindu Kush and Pamir again diverge below 200 km depth. One should, however, look at this projection with some caution, since the southwesternmost Pamir is not projected onto a plane perpendicular to its strike (which is north-south). Hence, the discrepancy of dips imaged here appears to be smaller than it really is. Inspection of profiles E-E' and C-C' and their map view location gives a more accurate picture of the change in vergence across the gap.

Seismic moment release is significant in the Hindu Kush, with 81 earthquakes of $M_L > 4.5$ (of a total of 138 for the whole study area) present in the two years' data. A large majority of the bigger earthquakes occurs in the deeper clusters, i.e. below the vertical gap at approx. 150 km. The thickness of the planes defined by the hypocenters is around 15-20 km (see profiles in Figure 4.14), only slightly thicker than for the Pamir. Seismic activity in the Hindu Kush zone is confined to mantle and possibly (high location uncertainty for shallowest part, see Figure 4.9) lower crustal depths. No connection to shallow crustal activity is evident.

Summarizing the observations, one can identify a clear separation between intermediate-depth seismic activity in the Pamir and Hindu Kush by a seismic gap across which a clear jump in dip and strike of the structures occurs. However, a tendency towards an alignment of strike directions and dip (at least in the deeper part) is discernible towards their potential intersection. The Pamir seismicity outlines an arcuate, slab-like zone that extends from about 50 to 150 (east) or 240 (west) km depth and gradually changes its strike from east-west at its eastern end to north-south at its western end. The dip direction likewise changes from southwards to eastwards along the arc. The Hindu Kush seismic zone shows significant complexity, consisting of a number of discrete seismicity clusters with complicated geometrical relationships. To first order, the whole structure can be subdivided into a shallower and a deeper part, separated by a seismic gap around 150 km depth. Generally striking east-west, the Hindu Kush's strike direction becomes NE-SW towards its eastern termination, forming an alignment with the Pamir. The dip of the Hindu Kush is generally sub-vertically north- to northwestward, but the westernmost deep cluster shows a steep southward dip.

4.3. Discussion

4.3.1. Automatic processing of local seismicity - feasibility and quality

The automatic procedure implemented here demonstrates a way to produce a complete catalog of well-located earthquakes and reliable arrival time picks for P and S phases together with their quantitative quality classification starting from a large continuous set of offline passive seismic

Figure 4.13. *(following page)*: Depth cuts through the study region - all earthquakes from one depth bin (extent indicated at the lower right of each map view plot) are projected onto a horizontal (map view) plane. Color scheme identical to Figure 4.10, map view plot. Black lines indicate national boundaries.

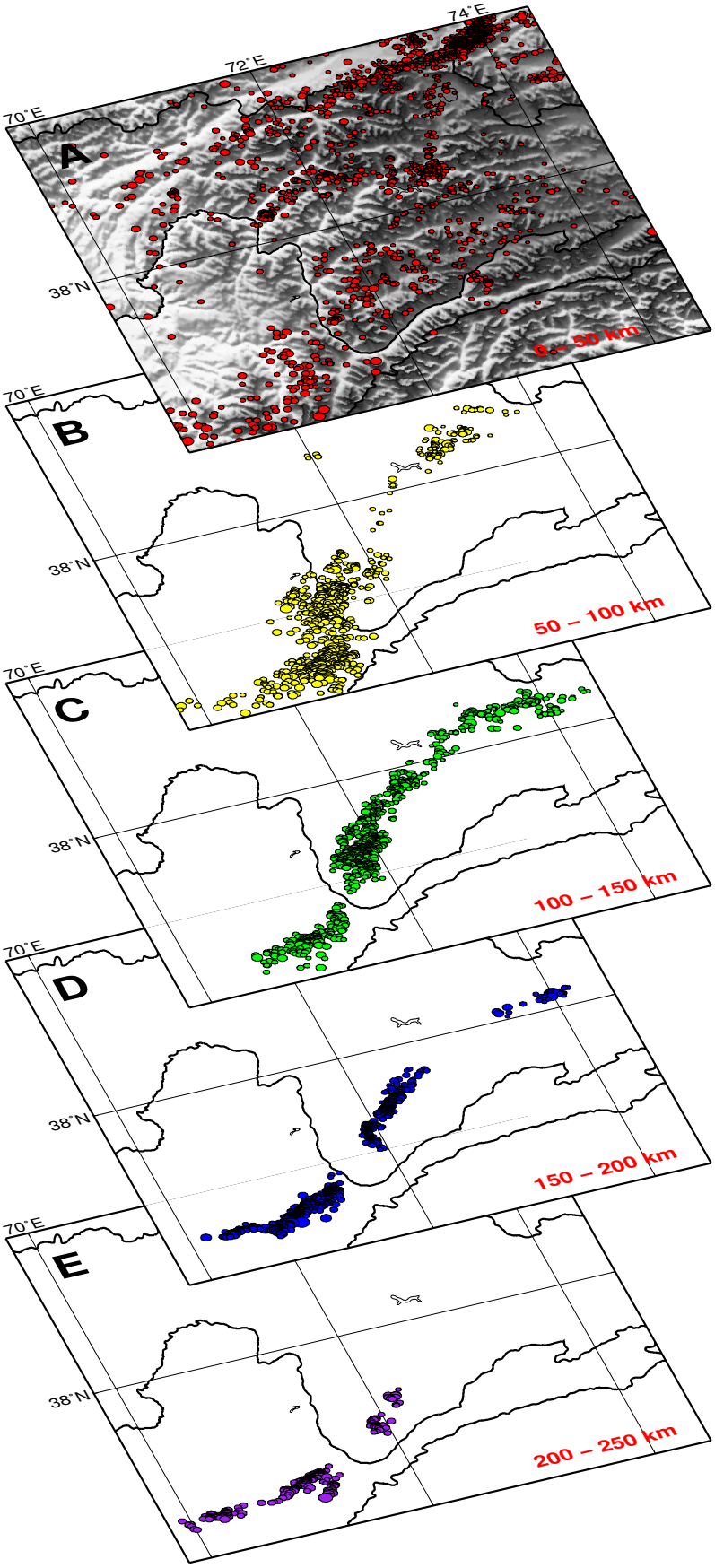
A
B
C
D
E
70°E
72°E
74°E
38°N
0 – 50 km
50 – 100 km
100 – 150 km
150 – 200 km
200 – 250 km

network data. While well-performing automatic triggers and targeted pickers for P and S phases have been available for some time (e.g. *Allen*, 1978; *Baer and Kradolfer*, 1987; *Cichowicz*, 1993; *Aldersons*, 2004; *Diehl*, 2008; *Küperkoch et al.*, 2010), they are only one cog in a bigger machine. Trigger algorithms produce interminable lists of possible phase onsets from which only a small minority can be associated to seismic events that can be located. Since targeted phase pickers depend on the correct placement of windows around the expected phase, for which either a good first detection or an accurate travel-time prediction (which depends on the event location) is needed, event association, location and phase-picking are highly inter-dependent. One bad or wrongly associated pick may deteriorate the event location such that other correct picks are not associated or dis-associated due to their residuals. Travel-time calculation for an erroneous location may place target phase windows such that they miss the phase. This interdependency can only be overcome by iteratively improving a location, and adding or improving phase picks based on the updated location in each step.

It is the calibration of the processing chain, i.e. testing when a pick should be considered a misspick and defining when a location can be considered "good", that is the most work-intensive part. It needs a carefully handpicked subset of events representative of the region's seismicity in order to calibrate parameters in the detection, association and phase-picking and to critically validate the whole procedure's performance. We have demonstrated that the accuracy of the automatically determined phase picks is comparable to manual picking (see Figures 4.7 and 4.8), which ensures high-quality locations and makes the picks also suitable for e.g. tomographic inversion. We tuned the phase-pick weighting to be conservative, i.e. to eliminate/downweigh picks rather than keep blunders (see confusion matrices, Figure 4.3). However, this resulted in a relatively low hit-rate for phase-picks compared to manual analysis. Then again, manually analyzing a large data set usually requires several analysts working on it. This introduces inconsistencies in both onset identification and weighting (Figure 4.7). An automatic picking system, on the other hand, is, by its very nature, consistent, since it applies the same set of criteria to the whole data set. The inherently lower hit-rate of successful phase picks may be at least partly compensated by additionally using differential phase arrival time measurements from waveform cross-correlation. This requires clustered seismicity, a prerequisite that is given, however, in many seismically active regions. The combination of an automatic phase picking engine with waveform cross-correlation and relocation algorithms that can make use of both types of data, like the double-difference algorithm, seems to me a promising avenue to analyze offline data sets containing a very large number of events. Event location and travel-time prediction by ray tracing also depend on the utilized velocity model, which may be unknown at the start of the analysis. An inadequate velocity model may impair the entire event association, phase picking and relocation procedure, which is why it might be advisable to invert for a velocity model, e.g. from a smaller reference hand-picked data set, at the very beginning of the procedure.

Formal location errors are variable throughout the study region, with small to moderate values for most of the Pamir (less than 10 km except for the depth of shallow events) and significantly higher values in the Hindu Kush, which is situated outside of the station network. However, the hypocenters outline crisp structures for the deeper parts of the Hindu Kush, which leads me to believe that relative location errors may be substantially smaller than what is shown in Figure 11. Double-difference relocations collapse to structures rarely exceeding a width of 10 km in the Pamir and 15 km in the Hindu Kush. If it is assumed that relative location errors are random and further assume that all events are situated along infinitely thin planes, relative location errors

could be estimated as the half-width of these structures, 5 and 7.5 km, respectively. The second assumption is probably incorrect and earthquakes most likely occur inside a volume of finite thickness. However, this would actually reduce the estimated errors, making the above estimates an upper bound. The highest uncertainties are present for relatively shallow-focus events in the (western) Hindu Kush, where even double-difference relocations do not outline sharply defined structures but a relatively diffuse cloud of hypocenters. Manually locating earthquakes in this region, I experienced highly volatile hypocentral depths. This is due to an unfavorable network geometry and makes these earthquakes difficult to interpret. The cloud of seismicity imaged at lower crustal depths in the western and central Hindu Kush most likely represents mislocated upper crustal seismicity. We believe that the obtained catalog is quite comprehensive for at least M>2.5 in the Pamir and M>3.5 in the Hindu Kush (varying with the station coverage), with the exception of western Tajikistan, where some crustal events are missed in the event association step, due to inappropriateness of the utilized averaged velocity model for the Tajik Depression with its thinner crust compared to the Pamir and its thick (up to 10 km) sedimentary layer. Hence crustal seismicity plotted in Figure 4.10 for western Tajikistan is most likely underestimated.

4.3.2. Interpretation of Results

A vast majority of the observed intermediate-depth seismicity occurs in clusters that reveal clearly planar structures of limited thickness (10-15 km) at suitable cross-section angles (see Figure 4.14). A schematical interpretation of the observed configuration of planes is sketched in Figure 4.15. The first-order division of seismicity into the Pamir and Hindu Kush seismic zones can be performed across a clear gap in seismicity coincident with a change in dip direction of the Benioff zone. This gap tapers off towards shallow depths, where both zones adjoin close to the presumed Moho position. The Pamir may be most straightforwardly interpreted as a single curved plane, with its curvature and vertical extent - both up- and downwards - increasing towards the southwest. Along with the change in strike from east-west to north-south, the dip direction changes from due south to due east at its south-westernmost termination where it meets the Hindu Kush. The Hindu Kush zone is much more compact compared to the Pamir zone. To first order, it strikes east-west and bends northward at its eastern end to converge with the general trend of the western Pamir zone. Hindu Kush seismicity appears to be separated into an upper and lower part by a vertical gap at approx. 150 km depth. The upper part of the Hindu Kush seismicity is quite sparsely sampled, yet reveals a steep north to north-westward dip. The lower part of the zone consists of a number of highly active clusters that form a complex mosaic of several steep planes of variable

Figure 4.14. *(following page)*: Series of profile projections perpendicular to the strike of the structure outlined by intermediate-depth earthquakes in Pamir and Hindu Kush. Locations of the profiles are indicated in Figure 4.10. Average topography across the swath widths is shown on top of the profiles. Circles denote earthquakes relocated with the double-difference method, crosses are events where this relocation was not performed. Colors of earthquake markers refer to different structural units (red: western Hindu Kush, blue: eastern Hindu Kush, black: Pamir) and are likewise indicated in Figure 4.10.

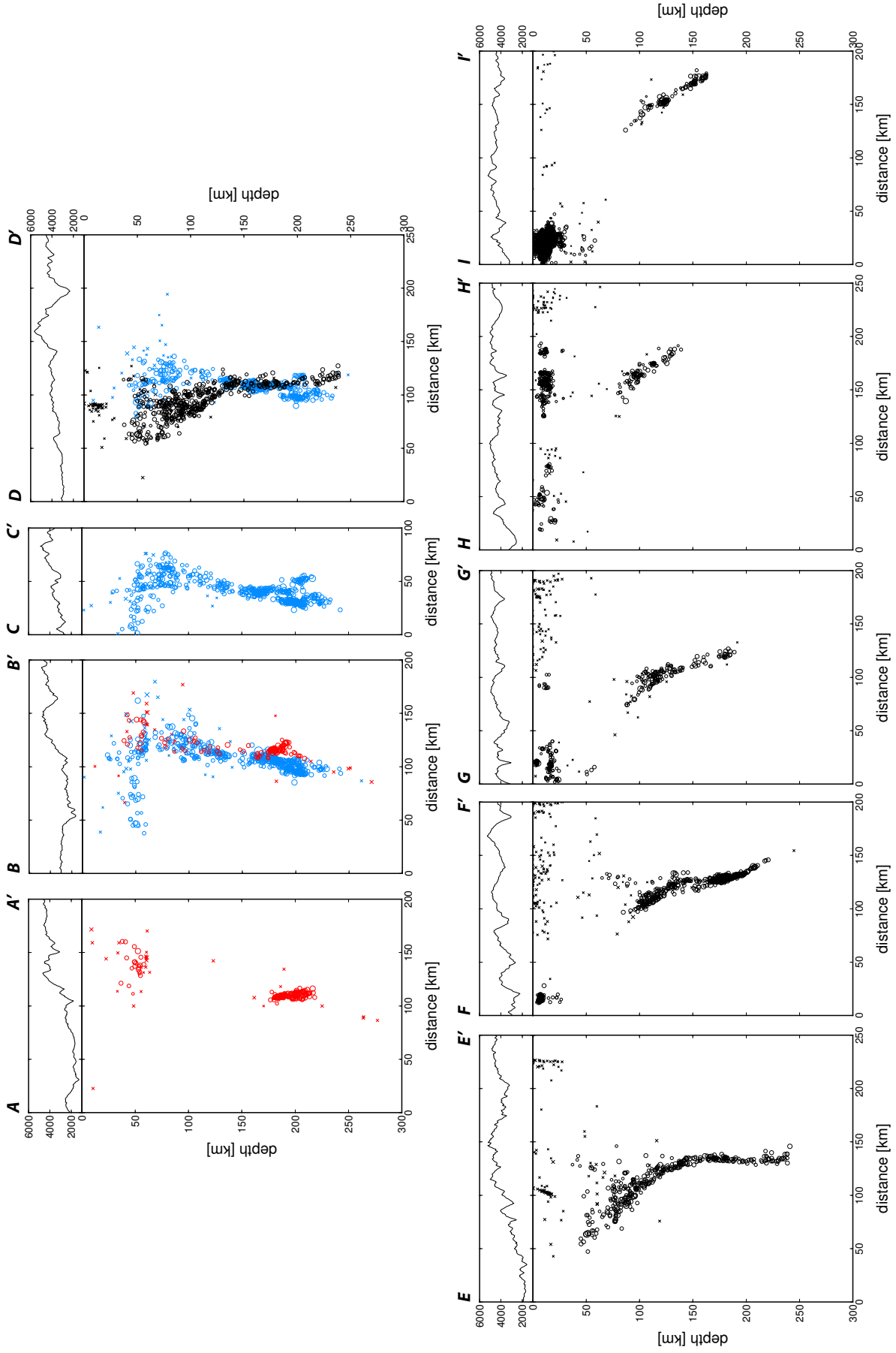
A
A′
B
B′
C
C′
D
D′
E
E′
F
F′
G
G′
H
H′
I
I′
depth [km]
distance [km]

size, strike, dip direction and curvature.

Processes responsible for intermediate-depth seismicity

It seems manifest that the intermediate-depth seismicity beneath one of the most active orogens on Earth attests to active deformation in the sub-crustal lithosphere. The mode of convergence and the resulting deformation pattern at depth as well as the ultimate fate of lithosphere in continental collision zones are not well understood. As crust is shortened and thickened, the underlying mantle lithosphere might either detach from the crust and subduct on one side of the orogen, or it might likewise thicken through simple shear underthrusting or pure shear shortening. During the latter process, thickened lithosphere might become gravitationally unstable (*Leech*, 2001) and delaminate as an intact sheet (*Bird*, 1979) or viscously drip into the underlying asthenosphere as a Rayleigh-Taylor instability (*Houseman et al.*, 1981). All these processes have been suggested to occur in the Indo-Eurasian collision zone (e.g. *Tilmann et al.*, 2003; *Koulakov*, 2011). It is not easy to distinguish between them, because mantle images from teleseismic waves are often too fuzzy and inferences from surface observations, like uplift history and magmatism, are non-unique. Based on the visual appearance of a drop-like high seismic velocity anomaly that reaches all the way into the mantle transition zone beneath the Hindu Kush, *Koulakov* (2011) suggested a lithospheric drip currently occurring there. It is not clear whether a Rayleigh-Taylor instability, which is a ductile process, would be capable of creating any seismicity at all. Indeed, well constrained mantle downwellings beneath Tibet (*Tilmann et al.*, 2003), the Andes (*Schurr et al.*, 2006), the Colorado plateau (*Levander et al.*, 2011) and the Sierra Nevada (*Zandt et al.*, 2004) take place aseismically. *Lorinczi and Houseman* (2009) could reproduce strain rates measured for the Vrancea intermediate-depth seismic zone by numerically simulating a narrow lithospheric downwelling. In their model, deformation is not localized, but distributed within the drip. Our observation that Pamir-Hindu Kush seismicity is highly localized along well-defined thin planar structures is difficult to reconcile with any such process, but rather evokes one that involves plunging plates like subduction or sheet-like delamination.

Intermediate-depth seismicity occurring dominantly in thin planes hints at the existence of a lithologically and/or rheologically distinct layer where conditions allow brittle material failure. In a chemically more or less homogeneous mantle, earthquake occurrence should be controlled by pressure and temperature alone, which would make it difficult to account for both the concentration of earthquakes in a thin layer and its depth span exceeding 200 km. The variability of source mechanisms in the Pamir and Hindu Kush zones (*Pegler and Das*, 1998; *Lister et al.*, 2008) also speaks against the possibility that earthquakes mark a localized mantle shear zone. Instead, I prefer the interpretation that earthquakes occur in a crustal layer that is entrained in the mantle. This is supported by the observation that intermediate-depth seismicity emanates near the presumed Moho depth, at least in the western Pamir and Hindu Kush. If the possibility of subduction of a remnant ocean basin beneath the Pamir is discarded due to the arguments presented earlier, then subduction of oceanic material from the south should have stopped with the final closure of the Tethys not later than 40 Ma ago (*Yin and Harrison*, 2000). This rules out the presence of oceanic material at depth. Even the scenario proposed by *van Hinsbergen et al.* (2012), in which Greater India was rifted on its path towards the collision with Eurasia, which could shift the final subduction of oceanic material to about 25 Ma, would not supply suitable oceanic material to host Pamir-Hindu Kush seismicity. If I rule out the presence of oceanic

crust on these arguments, earthquakes would hence trace continental crustal material on top of a mantle lithospheric "slab". *Roecker et al.* (1982) observed anomalously low seismic wavespeeds co-located with intermediate-depth seismicity in the Hindu Kush with local earthquake tomography and interpreted these findings with the presence of continental crustal material at depth. Such a presumably small-scale anomaly would likely not be resolved by the regional or global tomographic models of *Koulakov and Sobolev* (2006); *Koulakov* (2011) and *Negredo et al.* (2007), which only image the deeper, larger-scale structures. Presence of continental crust at mantle depths (65-110 km) is also supported by crustal xenoliths erupted at 11 Ma in the south-eastern Pamir (*Ducea et al.*, 2003; *Hacker*, 2005; *Gordon et al.*, 2012). The observed layer thicknesses of 10-15 km imply that only a part of the continental crust would be involved, which is consistent with the argumentation of *Molnar and Gray* (1979), that deep subduction of continental lithosphere, due to its higher buoyancy, should only be possible if the upper crust is scraped off and stays at the surface.

The inference that intermediate-depth earthquakes occur within subducting or delaminating continental lower crust, however, does not immediately solve the problem of seismogenesis. The most commonly evoked explanation for intermediate-depth seismicity in oceanic subduction zones is dehydration embrittlement (*Kirby et al.*, 1996; *Hacker et al.*, 2003). This hypothesis proposes that fluids released in prograde metamorphic reactions from hydrated minerals reduce normal stress and friction in the surrounding material and thereby enable brittle fracture and slip that would otherwise be inhibited by the high confining pressure at depth. However, lower continental crustal rocks do typically not contain any significant amount of hydrated minerals (*Rudnick*, 1995) and therefore deform dominantly in a ductile manner. In a delamination scenario for the Pamir, the southern and central Pamir's origin from accreted arcs (*Schwab et al.*, 2004) may provide preserved fluid reservoirs in hydrated rocks that are now released as these rocks are transported to greater depth. Alternatively, concepts of shear instabilities by thermal runaway (*Kelemen and Hirth*, 2007; *John et al.*, 2009) have been proposed for the generation of intermediate-depth earthquakes. Invoking this model, one could speculate that existing fine-grained shear zones in the lower crustal material, which are necessary for strain localization, might constrain earthquakes to the crustal layer. In any case, it remains an open question what the predisposing factors and specific processes are that cause the virile deep seismicity in an intra-continental setting that is observed almost nowhere else.

Provenance of imaged structures - Eurasia or India?

The peculiar geometry of the two Benioff zones apparently dipping in opposite directions invariably leads to the question of their provenance. There are essentially two prevailing lines of interpretation in literature: (1) Both Pamir and Hindu Kush slabs belong to a single slab of Indian origin which is torn, contorted and overturned in its south-dipping Pamir part (*Billington et al.*, 1977; *Pegler and Das*, 1998; *Pavlis and Das*, 2000). (2) Pamir and Hindu Kush are two distinct slabs subducting in opposite directions next to each other, where the Pamir slab is made up of Eurasian material and the Hindu Kush slab is of Indian provenance. (*Burtman and Molnar*, 1993; *Fan et al.*, 1994). Alternatively, a two-slab model involving the subduction of two remnant oceanic basins (which would have to be embedded in Eurasian lithosphere) in opposing directions has been proposed by *Chatelain et al.* (1980). This last possibility, however, appears to me highly ad hoc and not compatible with available surface evidence.

The geometry of the Pamir slab imaged here, with its clear separation from the Hindu Kush and general south- to southwestward dip, seems hard to reconcile with any process involving Indian material, instead strongly suggests to me a Eurasian origin. A hypothetical plane through the intermediate-depth seismicity below the eastern Pamir projected updip would emerge near the MPT (Figure 4.14, profile I-I'). The MPT separates the intermontane Alai valley, probably the last remnant of the Tajik-Yarkand basin, from the over 7000 m high Trans-Alai Range at the Pamir's northern deformation front. The MPT is seismically active (see Figure 4.13A) and a convergence rate of 10-15 mm/yr across it is constrained by GPS measurements (*Reigber et al.*, 2001; *Zubovich et al.*, 2010; *Mohadjer et al.*, 2010). The deep Pamir seismic zone could hence be seen as the continental analog to a highly arcuate, narrow subduction zone segment like the Caribbean or the Banda Arc ones (*Spakman and Hall*, 2010). In such a model, the arcuate shape of the Pamir seismic zone would be the consequence of the shape of the Indian indenter further south (western syntaxis), which led to the creation of northward-convex structural belts throughout the orogen and would have effected a likewise arcuate Pamir deformation front and slab. The prevalence of along-arc extensive mechanisms of intermediate-depth earthquakes beneath the Pamir, which *Pegler and Das* (1998) used as argument in favor of active contortion of a single seismic zone of Indian origin, could be reconciled with such a purely Eurasian Pamir seismic zone in combination with active slab rollback (*Sobel et al.*, 2011b). The MPT would mark the intersection of the plate interface with the surface and the strike-slip faults at the Pamir's edges (Darvaz/Chaman Fault and Karakorum Fault/KYTS) would accommodate northwards rollback of the whole system (STEP faults, see *Govers and Wortel*, 2005). Scraped-off upper crustal material from the downgoing slab would form the imbricate thrust sheets making up the Trans Alai. An alternative model resulting in a geometry like the one observed beneath the Pamir could be a delamination process. In that scenario, lithosphere beneath the Pamir would have thickened through its overthrusting onto the Tajik-Yarkand Basin to the point of becoming gravitationally unstable, and a sheet of lower crust and mantle lithosphere would now peel off in a manner similar to what is suggested by analogue (*Bajolet et al.*, 2012; *Chemenda et al.*, 2000) and numerical (*Bird*, 1979; *Göğüş and Pysklywec*, 2008) simulations. The clear gap between shallow seismicity at the MPT and subcrustal earthquakes would then separate different active processes. Lithosphere delaminating along an arcuate hinge would also naturally experience horizontal tensional stresses in accordance with observations. Such a scenario could as well lead to the temporal snapshot imaged today, but would have experienced a different evolutionary history.

The Hindu Kush seismic zone's general northward dip direction provokes an association with Indian material. Since the involved material is most likely of continental origin (see argumentation above), the underthrusting of continental India beneath Eurasia, occurring in along-strike continuity of active processes in the Himalayas and beneath the Tibetan Plateau (e.g. *Yuan et al.*, 1997; *Kosarev et al.*, 1999; *Kind et al.*, 2002; *Nábelek et al.*, 2009; *Kind and Yuan*, 2010), could provide the host material for Hindu Kush earthquakes (as first proposed by *Coward and Butler*, 1985). Since its onset, the deformation front of the India-Eurasia collision has propagated southwards from the Indus-Yarlung Suture (see Figure 2.3) to the MFT into the Indian plate. Thus, a substantial aseismic, subhorizontal northward underthrusting of Indian lithosphere and lower crust at depth (which is observed in Tibet, see e.g. *Nábelek et al.*, 2009) would be necessary for Indian material to reach the Hindu Kush, where seismicity and a seismic high velocity zone are observed today. Upon reaching the southern rim of the Tajik Depression, this lithospheric slab would have to steepen to near-vertical while starting to generate vigorous seismicity in its crustal part (as imaged by *Roecker et al.*, 1982). Further east, there is no continuation of Hindu

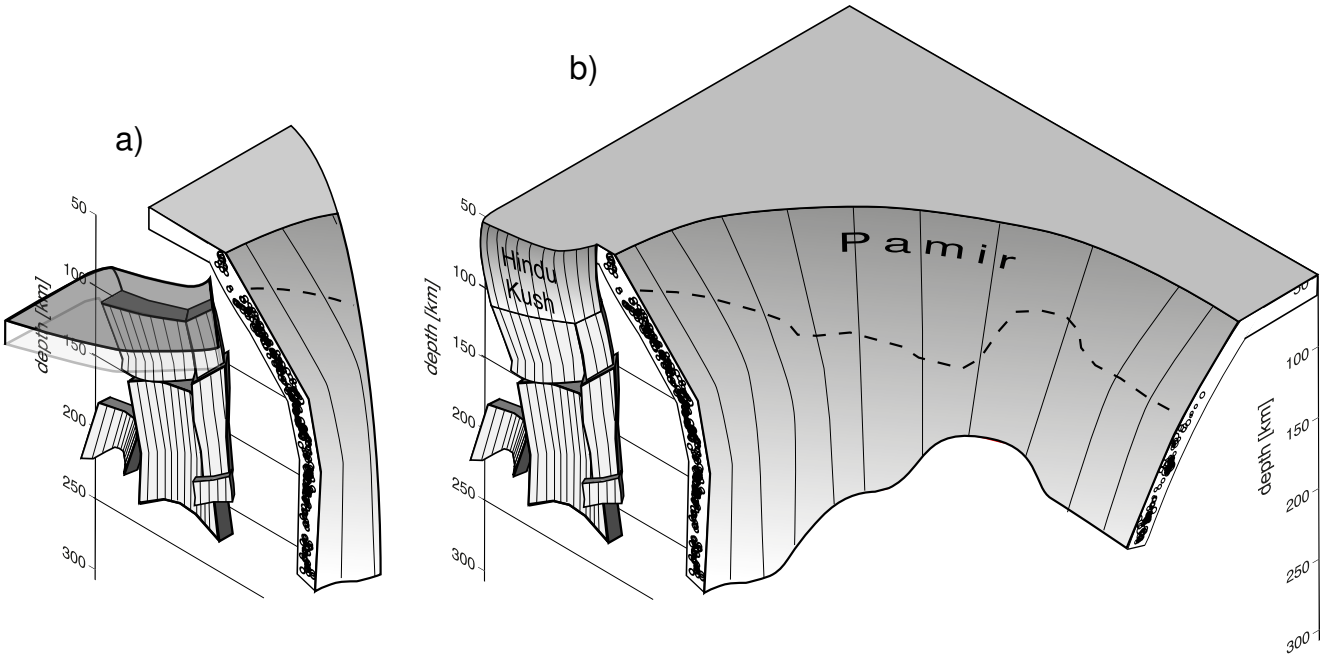

Figure 4.15.: Schematic representation of the geometry outlined by the earthquake locations presented in this study. The Pamir seismic zone defines an arc which incrementally changes its dip direction from southwards to eastwards and its strike direction from east-west to north-south from east to west. Dashed line corresponds to the upper limit of intermediate-depth seismicity along strike. The Pamir's dip angle stays constant along strike at depths shallower than 150 km. Southwest of the Pamir arc, clearly separated from it in terms of dip direction, is the Hindu Kush seismic zone, which strikes roughly east-west and generally dips nearly vertically northwards. A tendency towards a strike alignment with the western Pamir is discernible in its eastern part. Although significantly smaller in width, the Hindu Kush exhibits considerably more structural complexity than the Pamir, shown by its fragmentation in several (curvi)planar fragments. Its provenance is unclear, could be either Indian (scenario shown in subfigure a) or Eurasian (b).[1]

Kush seismicity, and an unimpeded northward propagation of underthrusting India would not be compatible with the presence of the Pamir slab. Hence, the deeper part of the Indian slab must have detached, whereas a remnant stub could still impinge onto the Pamir slab today, effecting its steep dip angle (*Fan et al.*, 1994). A schematic representation of this concept is shown in Figure 4.15a.

However, there is a number of observations that suggest to me that seismicity in the Pamir and Hindu Kush owes its existance to the same process under similar environmental conditions or even

[1]Figure not made by the author, but by B. Schurr

occurs in rocks of the same provenance. Several seismicity features are continuous across the gap separating the Hindu Kush and Pamir seismic zones, like the alignment of their strikes and their abutment at shallow level as well as the significance of the 150 km depth level, where a seismic gap is observed in the Hindu Kush zone and the Pamir zone shows a kink towards steeper dips. Moreover, the simple fact that this globally almost singular seismicity would hardly be occurring fortuitously in two distinct structures next to each other suggests to me a common origin.

An alternative model accounting for this objection could be one in which the Hindu Kush is interpreted as overturned and torn fragment belonging to a formerly larger southward-subducting Eurasian slab (see Figure 4.15b). In such a model, Eurasian subduction might have commenced after a major break-off event of the Indian slab (*Chemenda et al.*, 2000; *DeCelles et al.*, 2002) which is supposed to have occurred 10-20 Ma ago. The western demarcation of the Pamir in all likelihood reflects the westward extent of the Indian indenter, which is evident from the predominance of strike-slip faulting throughout Afghanistan (*Tapponnier et al.*, 1981). The Hindu Kush part of this former slab might have been pinned against the southern rim of Tajik Depression lithosphere, whereas the Pamir part has been torn away, where the seismic gap between Hindu Kush and Pamir can be seen today, by the advancement of the Indian indenter. The imaged bends of both structures towards each other near their intersection (see Figure 4.13D) would reflect processes directly before the tear took place, when the slab must have been stretched and contorted in the region around the locus of the final tear. With ongoing northward indentation of the Pamir, its deformation front and hence the hinge point of the subducting slab propagated north, developing an arcuate shape that probably mimics the outline of the Indian salient further south. The intriguing alignment of intermediate-depth seismicity with surface features, with the Pamir deep seismic zone tracing the curvature of structural belts in the shallow Pamir and the Hindu Kush seismicity situated at the southern rim of the Tajik Depression, would be a consequence of this scenario. Moreover, the location of the seismic gap separating Pamir and Hindu Kush deep seismicity at the point where Pamir, Hindu Kush and Tajik Depression meet, corresponds to what this model would predict. This model would advocate that shallow and deep processes are coupled (in contrast to the model suggested by *Pavlis and Das*, 2000).

In summary, based on the presented observations, I associate the Pamir zone of intermediate-depth earthquakes with a continental slab of Eurasian provenance, where the thin planar structure outlined by seismicity most likely represents lower crustal material. This inference leads me to exclude a one-plate model featuring a purely Indian slab. While a two-plate scenario in which the Hindu Kush represents underthrusted continental Indian material can not be ruled out, I currently prefer a one-plate model in which both Pamir and Hindu Kush deep seismic zones derive from a single Eurasian slab that is torn and overturned in its Hindu Kush part. Given that the occurrence of intermediate-depth seismicity in continental material in the Pamir-Hindu Kush is globally unique (see Introduction), it appears to me rather unlikely that two independent processes active next to each other by pure coincidence would both create these special earthquakes. However, only additional data, e.g. on stresses inside the seismic zones from earthquake mechanisms and possibly a three-dimensional seismic velocity model may allow to better understand the geodynamic processes acting in this intriguing part of the world.

5. Earthquake mechanisms and state of stress

In addition to the hypocentral locations of earthquakes, which accurately define the geometry of structures at depth and the loci of active faulting at the surface, their mechanisms, i.e. the orientation of their fault planes and the direction of motion along them, provide valuable information about the active stress field causing the earthquakes. Earthquake mechanisms can be retrieved by inverting either first motion polarities or entire displacement traces of an earthquake at an array of stations. Following a brief review of the theory of seismic moment tensors and moment tensor inversion, I present focal mechanisms for shallow and intermediate-depth earthquakes in the Pamir and Hindu Kush, obtained with both aforementioned approaches (see Section 5.2). These fault plane solutions are then used to invert for a best-fitting regional stress field, followed by a detailed discussion of possible implications and interpretations of obtained results.

5.1. Theory

Only parameters and formulae that are of importance to the utilized methods will be presented here. For a more complete overview of the theoretical background of moment tensors, refer to *Jost and Herrmann* (1989) or textbooks (e.g. *Aki and Richards*, 1980; *Stein and Wysession*, 2003).

A seismic moment tensor represents the mathematical description of forces equivalent to those acting at the earthquake source, which is assumed to be a point (*Jost and Herrmann*, 1989). Equivalent here means that they produce the same surface displacement, which is what can be measured with seismometers. Provided the response of the seismograph has already been removed, surface displacement can be expressed as (*Stump and Johnson*, 1977)

$$u_k(\mathbf{x}', t') = \int_{-\infty}^{\infty} \int_{V_0} G_{ki}(\mathbf{x}', t', \mathbf{x}, t) f_i(\mathbf{x}, t) dx^3 dt \tag{5.1}$$

wherein u_k is the k-component of displacement at the receiver position $\mathbf{x}'$ and arrival time t', G_{ki} represents the Green's Function of the medium between earthquake source $(\mathbf{x}, t)$ and receiver $(\mathbf{x}', t')$, f_i the sum of real and equivalent body forces and V_0 is the source volume (which will be reduced to a point). A term relating the recorded displacement to the elements of the moment tensor can be derived from this expression (for the derivation refer to *Stump and Johnson*, 1977):

$$u_k(\mathbf{x}', t') = G_{ki,j}(\mathbf{x}', t', \mathbf{0}, 0) \star M_{ij}(\mathbf{0}, t') \tag{5.2}$$

where $\star$ denotes the convolution and the terms M_{ij} are the elements of the moment tensor. Hence, the surface displacement is the convolution of the moment tensor elements that represent the earthquake source with a Green's Function G. This Green's Function is the impulse reponse of the medium between source and receiver, thus depends on the Earth model as well as on source and receiver positions.

A Moment Tensor M is a symmetric second-rank 3×3 tensor, thus contains 6 independent elements. The symmetry is a consequence of the conservation of angular momentum.

$$M = \begin{pmatrix} M_{11} & M_{12} & M_{13} \\ M_{12} & M_{22} & M_{23} \\ M_{13} & M_{23} & M_{33} \end{pmatrix} \tag{5.3}$$

The moments M_{jk} define the excitation of nine generalized force couples (see Figure 4.4-4 in *Stein and Wysession*, 2003), and can be derived as

$$M_{jk} = \mu A(u_j v_k + u_k v_j) \tag{5.4}$$

with a slip vector $\vec{u}$ and a vector $\vec{v}$ normal to the fault plane. A denotes the fault area, μ is the shear modulus. An interchange of the vectors $\vec{u}$ and $\vec{v}$ in Formula 5.4 has no effect on the moment M_{jk}, which leads to an identical radiation pattern for rupture occurring along the actual fault plane and an auxiliary plane perpendicular to it. Hence, it is not possible to determine along which of these two planes the earthquake occurred without further information like surface geology, aftershock distributions etc.

A description of equivalent forces can be gleaned from the analysis of the eigenvalues and -vectors of the moment tensor. The sum of the eigenvalues corresponds to the volume change of the source, it is positive for an explosive source, negative for an implosion and zero for a purely deviatoric moment tensor typical for shear failure.

The deviatoric part of the moment tensor can be decomposed, i.e. subdivided into contributions from different conceptual source models, in different ways (see e.g. *Randall and Knopoff*, 1970; *Jost and Herrmann*, 1989), the most common of which is into pure double-couple and CLVD (Compensated Linear Vector Dipole, see *Knopoff and Randall*, 1970). A deviatoric moment tensor is pure double-couple when one eigenvalue equals zero, can then be parameterized as a set of three angles (strike, dip and rake) indicating the orientation of one of the nodal planes and the direction of slip along it (as done in Appendix D).

It is debated whether varying proportions of CLVD in routinely obtained moment tensors reflect different earthquake physics (e.g. deviation from planar fault geometry). While some processes generating non-double couple earthquakes have been postulated (*Julian et al.*, 1998) and corresponding observations have been made (*Kuge and Kawakatsu*, 1993; *Miller et al.*, 1998), it is possible that for most "ordinary" earthquakes the CLVD part of the moment tensor simply reflects some part of the misfit of the best-fitting double couple that is being mapped into the CLVD contribution by the inversion algorithm.

The eigenvectors of the moment tensor define three orthogonal axes named P, B and T axes, representing the principal directions of maximum, intermediate and minimum tension. P and T axes of earthquakes are often used as an indicator for the regional tectonic stress field (*Stein and*

Wysession, 2003, e.g.). However, the presence of pre-existing fault planes in a region can effect a systematic shift of these axes away from the background stress field orientation (*McKenzie*, 1969).

Earthquake normal modes as well as surface or body waves can be used to invert for a moment tensor from seismogram data (e.g. *Gilbert*, 1973; *Stump and Johnson*, 1977; *Nábelek*, 1984). The location of the earthquake has to be known in order to compute synthetic Green's Functions from the source to each receiver. The general inverse problem can be stated as

$$\vec{d} = \mathbf{G}\vec{m} \tag{5.5}$$

where $\vec{d}$ is the data vector containing ground displacement seismograms or displacement spectra for n stations. $\mathbf{G}$ is a $n\times$ 6 matrix with the synthetic Green's Functions calculated using source and receiver coordinates and earth model. The vector $\vec{m}$, finally, contains the 6 moment tensor elements to be inverted for.

Modern algorithms simultaneously invert for moment tensor and the source time function, i.e. the function of the energy radiation of the point source with time, most often utilizing least squares minimization schemes (see Section 5.2.1).

5.2. Utilized methods

Focal mechanisms of local or regional earthquakes can be determined by fitting a double-couple mechanism to first-motion P polarity readings mapped onto a focal sphere (e.g. *Reasenberg and Oppenheimer*, 1985) or by waveform inversion based on the calculation of synthetic seismograms (see Section 5.1). Both of these principal methods have advantages and drawbacks. Waveform inversion results should be comparatively robust, provided that a certain number of stations with readings of good signal-to-noise ratio are present. The quality of inverted mechanisms depends on the validity of the used earth model as well as on a good event-station geometry. Events outside the network can still be used as long as a sufficient number of good signals at stations of variable distance and backazimuth is provided. However, since the comparison of observed seismograms with synthetics is normally done at low frequencies, where seismograms are comparatively simple, earthquakes beneath a certain magnitude threshold can not be inverted because they do not radiate above noise level at these frequencies. Solutions from first motion polarities, on the other hand, can even be retrieved for small local earthquakes when a number of clear polarity readings is present. This technique is, however, critically dependent on a good distribution of readings on the focal sphere (i.e. good variation both in azimuth and takeoff angle), is hence limited to the analysis of earthquakes well within the network.

Considering the geometry of the network with respect to the observed seismicity (see Figures 3.1 and 4.10), I chose a combination of both approaches as the optimal strategy. For the Hindu Kush seismicity, outside the network but featuring enough strong events, waveform inversion proved appropriate, whereas the number of obtained focal mechanisms could be significantly increased for the Pamir, where earthquakes are mostly smaller, by using first motion polarities.

5.2.1. Regional Moment Tensor Inversion

An inversion procedure for focal mechanisms of earthquakes at local and regional distances (*Nábelek and Xia*, 1995) was applied to the largest earthquakes in the data set. The relation between the moment tensor elements and the displacement observed at seismic stations for a layered medium can be expressed as

$$\begin{aligned}\mathbf{u}_{PSV}(\phi,\Delta,t) = [\mathbf{H}_{PSV2}(\Delta,h,t)(\frac{1}{2}(M_{22}+M_{11}) - \frac{1}{2}(M_{22}-M_{11})cos2\phi + M_{12}sin2\phi) \\ +\mathbf{H}_{PSV1}(\Delta,h,t)(M_{23}sin\phi + M_{13}cos\phi) + \mathbf{H}_{PSV0}(\Delta,h,t)M_{33}] * \Omega(t)\end{aligned} \tag{5.6}$$

$$\begin{aligned}\mathbf{u}_{SH}(\phi,\Delta,t) = [\mathbf{H}_{SH2}(\Delta,h,t)(\frac{1}{2}(M_{22}-M_{11})sin2\phi + M_{12}cos2\phi) \\ +\mathbf{H}_{SH1}(\Delta,h,t)(M_{23}cos\phi - M_{13}sin\phi)] * \Omega(t)\end{aligned} \tag{5.7}$$

where $\mathbf{u}_{PSV}$ and $\mathbf{u}_{SH}$ denote the displacement from P-SV and SH coupled seismic waves, respectively. Δ and ϕ stand for epicentral distance and azimuth, $\mathbf{H}$ represent unit-step excitation functions (Green's Functions) for a source depth h. Moment tensor components 1, 2 and 3 are here oriented in the x, y and z coordinate directions. The far-field source time function is parameterized as (*Nábelek*, 1984; *Nábelek and Xia*, 1995)

$$\Omega(t) = \sum_{k=1}^{n} a_k T_{2\tau}(t-(k-1)\tau) \tag{5.8}$$

i.e. as a series $T_{2\tau}$ of n isosceles-triangle functions of unit area, duration 2τ and overlap τ, with amplitude weights a_k. Here, I chose n=5 and τ=1 s. At the start of the procedure, a_1 was chosen to be 1 and all other weights were set to zero. For the derivation and applicability of these formulae, refer to *Nábelek* (1984).

The best-fitting focal mechanism and source-time function was retrieved by fitting synthetic full 3-component waveforms to the observed seismograms with a least squares minimization scheme, keeping the hypocentral coordinates of the event (as determined in Chapter 4) fixed.

Seismograms were downsampled to 0.5 or 1 Hz sampling frequency, depending on their epicentral distances (Δ > 400 km: 0.5 Hz, else 1 Hz), bandpass pre-filtered to 10-100 s, 10-60 s or 5-50 s (for magnitudes M>4.5, 4<M<4.5 and M<4), rotated into the RTZ coordinate system as well as cut to 256 data points trace length. Waveforms were then inspected visually and traces obviously dominated by noise were discarded. Additional bandpass filtering, usually with corner frequencies at 10 and 35 seconds and a 10 second taper, was subsequently applied.

Synthetic seismograms were calculated as the convolution of the assumed source term, Green's Functions calculated based on the used Earth Model (see Figure 4.2) as well as the source and receiver positions with the method of *Bouchon* (1982), and the instrument responses in each step. The iterative least-squares fitting of synthetics to observations was initiated with an arbitrary first-guess mechanism and was performed with an interactive procedure, offering the possibility

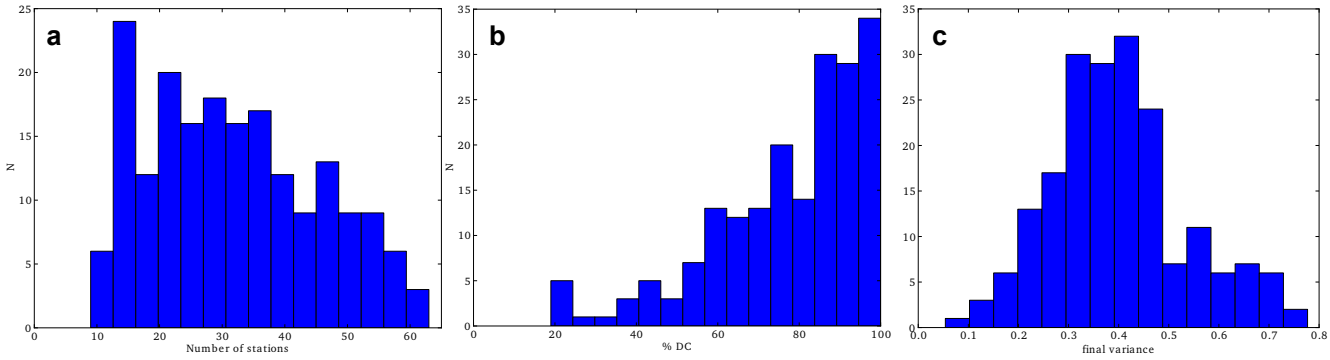

Figure 5.1.: Statistics for the 190 fault plane solutions obtained with regional moment tensor inversion: histograms of number of utilized stations (a), proportion of double-couple in the resulting moment tensor (b) and final variance (c).

to eliminate noisy or otherwise problematic traces in the process. Time shifts between observations and sythetics due to deviations of local subsurface structure from the utilized earth model were compensated by shifting the synthetics to best fit the observations (as determined by cross-correlation of waveforms). Moment tensors were constrained to be deviatoric, i.e. the isotropic part was not inverted for. Obtained waveform fits and variance values were inspected visually, followed by a decision whether further elimination of traces/time shift etc. was necessary or if the inversion should be stopped. This whole procedure was then, automatically, repeated for a range of depths around the initially chosen one, the centroid depth was chosen as the trial depth value that yielded the lowest variance (see examples in Figures 5.2 and 5.3).

All intermediate-depth earthquakes with local magnitudes larger than 4 and all shallow earthquakes with $M_L > 3.5$ were tried for inversion, a total of 190 regional moment tensor solutions was obtained[2] (see summary table in Appendix D). At least 10, sometimes up to 60 stations were used for the inversion of each moment tensor, most obtained solutions show a dominance of the double-couple part and final variance values center at around 0.3 to 0.4 (Figure 5.1). For 29 of these earthquakes, a CMT solution (www.globalcmt.org) was available. A comparison of the obtained results to these (see Figure 5.4) shows very similar mechanisms throughout the different regions, giving me high confidence in the obtained fault plane solutions.

Retrieved centroid depths for intermediate-depth earthquakes, especially for the ones in the Hindu Kush, were systematically deeper than the hypocentral depths from event locations. Since the centroid depth mainly depends on the alignment of seismograms, the arrival time difference between P and S should play an important role here. A too low v_p/v_s ratio used for the inversion could have such an effect, which would imply that the values from the 1D model (Figure 4.2), which are around 1.75 for mantle depths, are not applicable to the Hindu Kush. For a further elaboration upon this issue, refer to Section 6.3.

[2]Only about 60% of these were inverted by the author. B. Schurr did a large part of the shallow events, and some mechanisms inverted in the works of *Krumbiegel* (2011) and *Feld* (2011) were used

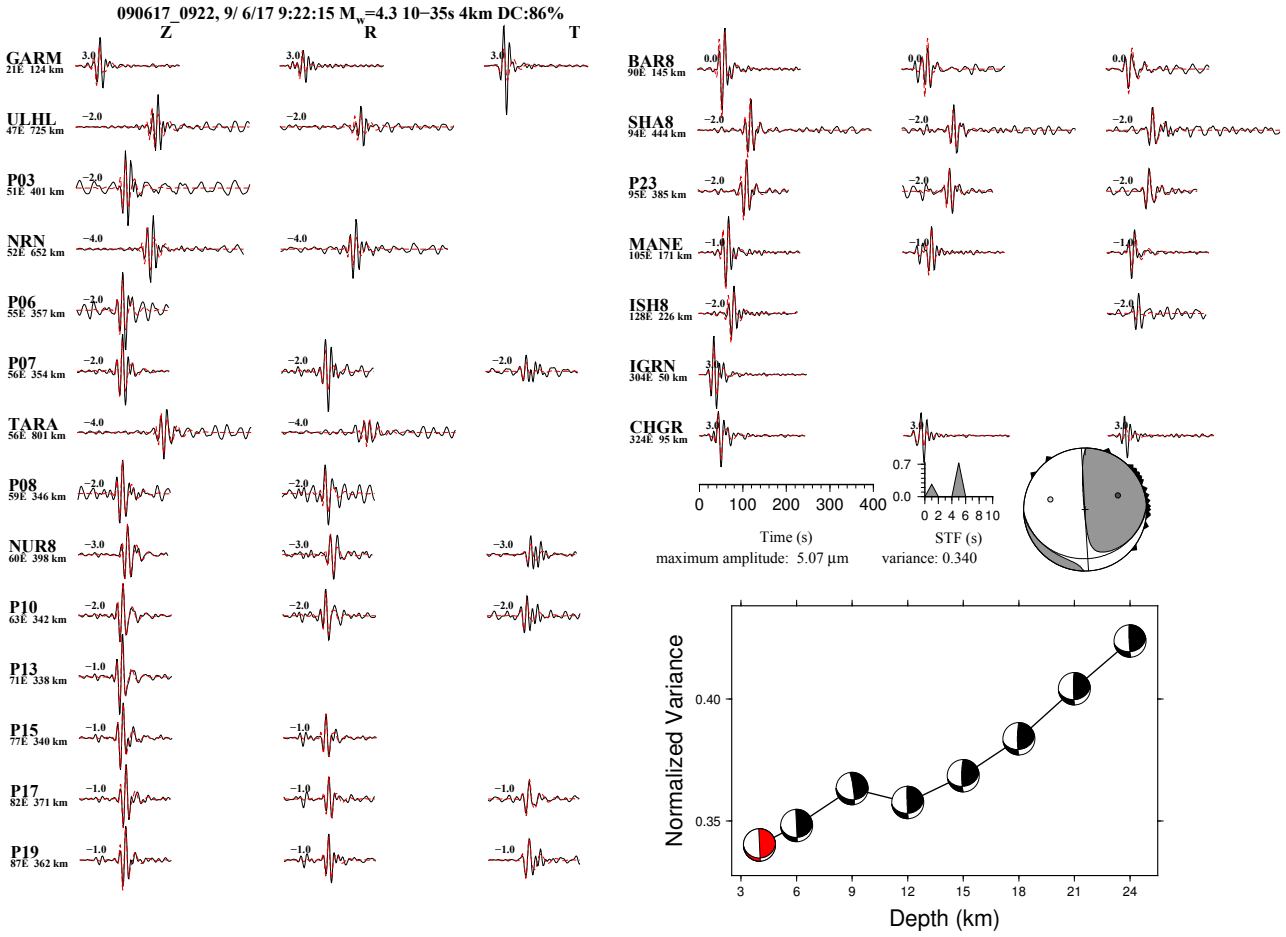

Figure 5.2.: Summary plot for an arbitrarily chosen shallow event inverted with RMT. Observed (black) and synthetic (red) waveforms for all utilized stations, sorted by backazimuth, are displayed along with the retrieved source time function. Lower right subplot shows inversion results for different trial depths, the lowest variance value (here: 4 km) marks the chosen centroid depth.

5.2.2. First motion polarities

In order to further expand the set of fault plane solutions, 241 intermediate-depth earthquakes and 36 shallow events in the Pamir were chosen for first motion polarity analysis. Only earthquakes from the second year of the TIPAGE deployment, with a hypocentral location inside the network (gap<180°), were judged suitable. The network geometry of the first year, with the dominating north-south profile and only some distributed stations around it, would have yielded a bad coverage of azimuths and takeoff angles. P phase first motion polarities determined automatically (`MPX`, see Section 4.1.2) were checked visually and, if necessary, changed or deleted. `MPX` assigns a polarity ("Up" or "Down") to each P phase pick, but gives no quantification of the uncertainty in this assignment, which were found to be considerable. Generally, picks with better arrival time quality classes also have higher-confidence polarities, but only utilizing class 0 P arrivals would have drastically reduced the available first motion data and hence the set of earthquakes for which a

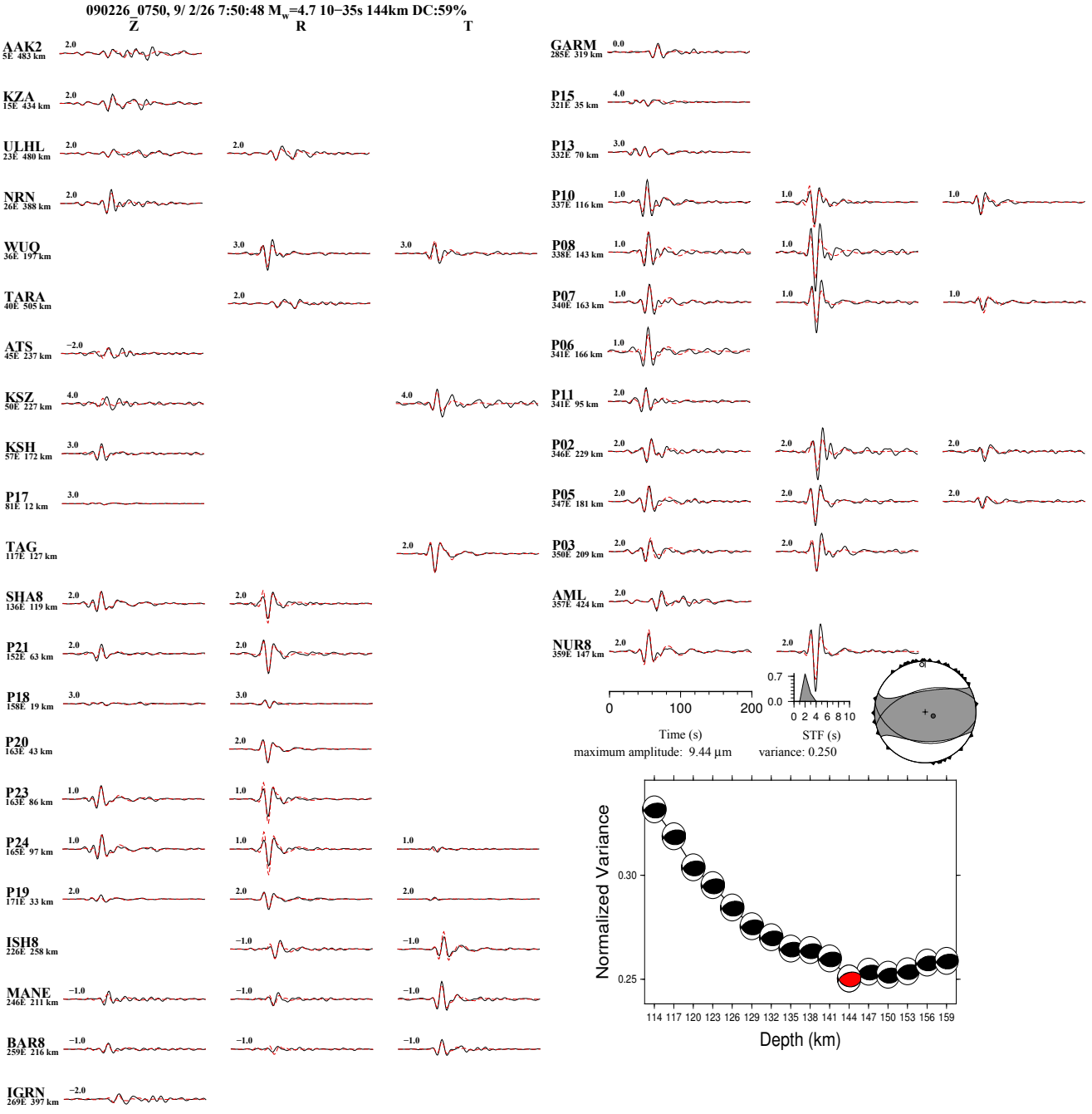

Figure 5.3.: Summary plot for an arbitrarily chosen deep event inverted with RMT. For plot details, refer to caption of Figure 5.2.

reliable fault plane solution can be found.

On average, a shallow earthquake of the data set comprised 23.61 polarity picks, an intermediate-depth one 32.28. Azimuths and takeoff angles were retrieved from a local raytracing routine (NonLinLoc), based on the best available hypocentral location of the event.

The program `HASH` (*Hardebeck and Shearer*, 2002) was subsequently utilized to determine fault plane solutions from the obtained sets of takeoff angles, azimuths and first motion polarities. `HASH` not only performs a grid search over strike, dip and rake angles to retrieve a preferred solution, but performs multiple trial runs of this, varying the source location in a chosen volume as well as flipping a pre-defined proportion of the polarity readings (I assumed that 5% would be erroneous) in order to evaluate the influence of possible uncertainties. A set of acceptable solutions is retrieved, a preferred one selected, and a quality estimate is given based on the variability among the acceptable mechanisms. Based on these quality estimates, earthquakes are partitioned into four quality classes, A to D. I limited analysis to events with azimuthal gaps smaller than 150 ° and a maximum gap in takeoff angles of 60 °.

From the inversion results, I only selected events with quality classes A and B for the intermediate-depth earthquakes (reducing their number to 167 events), whereas classes A through C for the shallow earthquakes (then 18 events) were kept.

Eight earthquakes in this set (five deep, three shallow) likewise have an RMT-derived fault plane solution. The comparison of retrieved mechanisms with the two different methods (see Figure 5.5) shows that some discrepancy between the results of both methods exist. The retrieved mechanism types are the same (no thrusting event turns into a normal fault or strike-slip or vice versa), but a moderate rotation of fault plane orientations is observed in most cases. Due to the high similarity of RMT solutions to what is obtained with global data (Figure 5.4 and because the RMT method is less critically depended on network geometry, we assume RMT solutions to be more robust than the ones obtained from first motion polarities.

5.3. Results

5.3.1. Crustal earthquakes

All focal mechanisms for crustal earthquakes (i.e. hypocentral depths less than 50 km) are shown as lower hemispheric projections in Figure 5.6. Except for events related to the Nura aftershock series (cluster of events at 39.4°N, 73.7°E) and some events near the Peter I Range, there is a suprising lack of thrust events considering the clear north-south compressive tectonics of the region (Figure 2.3). Instead, most mechanisms throughout the western Pamir exhibit strike-slip mechanisms, sinistral slip along northeast-southwest trending fault planes is my preferred

Figure 5.4. *(following page)*: Comparison of earthquake fault plane solutions obtained with regional moment tensor inversion (blue) to available CMT solutions (red) for the 29 earthquakes where the latter was available. Only the double couple part of the moment tensors are shown.

08/09/05 4:57:51
36.538N 71.260E 240.0
08/09/06 5:47:38
36.490N 70.854E 204.0
08/09/20 2:54:35
38.251N 73.267E 129.0
08/09/24 17:59:30
36.030N 71.140E 78.0
08/10/05 15:52:44
39.535N 73.817E 4.0
08/10/13 9:23:28
39.528N 73.868E 9.0
08/10/13 16:05:19
39.506N 73.840E 9.0
08/10/13 17:16:09
38.645N 70.328E 6.0
08/10/23 5:50:43
39.563N 74.018E 9.0
08/10/26 1:28:53
36.490N 70.705E 216.0
08/12/21 22:38:32
36.095N 71.405E 87.0
08/12/29 3:37:41
36.495N 71.063E 147.0
09/01/04 23:12:59
36.538N 70.962E 204.0
09/01/25 21:16:16
38.524N 72.174E 9.0
09/03/03 14:22:12
38.137N 71.566E 6.0
09/05/10 17:34:05
38.197N 67.567E 12.0
09/07/01 0:29:21
39.630N 73.456E 6.0
09/07/02 23:50:49
37.404N 71.703E 120.0
09/07/05 9:45:46
36.445N 71.188E 249.0
09/08/26 7:26:38
38.962N 70.581E 6.0
09/08/26 7:26:38
38.962N 70.581E 6.0
09/09/19 4:17:56
36.461N 70.724E 213.0
09/10/13 12:47:15
38.681N 70.848E 15.0
09/10/22 19:51:24
36.443N 70.966E 189.0
09/10/29 17:44:32
36.407N 70.772E 222.0
10/01/02 2:15:04
38.288N 71.445E 6.0
10/03/23 15:51:18
37.507N 74.606E 6.0
10/06/04 11:49:41
36.526N 70.165E 216.0
10/06/10 6:38:10
40.064N 74.464E 21.0

interpretation here (ambiguity fault plane-auxiliary plane). Into the Tajik Depression, mechanisms featuring slip along either purely vertical or purely horizontal rupture planes situated at centroid depths of 6-8 km (see Appendix E) become more common. It should be noted that even the Main Pamir Thrust, for which significant current convergence rates have been determined from GPS measurements (10-15 mm/yr, see *Zubovich et al.*, 2010), exclusively shows minor strike-slip events along most of its length in the observation period.

The overall distribution of P and T axes for shallow events (Figures 5.7 and 5.8) shows a prevalence of north-south to northwest-southeast trending, shallow dipping or (sub)horizontal P axes and east-west trending T axes with rather variable dips. Several trends are discernible from the spatial distribution of principal axis orientations shown in Figure 5.7. Whereas events in the central and eastern part of the Pamir, both at its northern circumference and further south, show perfectly north-south trending P axes and exactly east-west trending T axes, this picture gradually changes towards the Pamir's northwestern part. There, P axes acquire an east-west component which becomes more pronounced the further west into the foreland fold-and-thrust belts the event is situated. In the eastern Tajik Depression, P axes trend east-west. The T axes of earthquakes apparently do not show such a systematic development, they deviate from the uniform east-west trend observed for the eastern and central Pamir and acquire steeper dips.

5.3.2. Intermediate-depth seismicity

Hindu Kush

Fifty fault plane solutions for earthquakes in the Hindu Kush were retrieved in total, all of them by RMT (see Section 5.2.1), because their location outside the seismic network does not allow for the utilization of first motion polarities. Only earthquakes with magnitudes $M > 4$ could be inverted, and not all of these had a good enough low-frequency signal either. The obtained mechanisms are shown as beachballs plotted into different depth sections in Figure 5.9 and in a series of projections of P and T axes in Figures 5.10, 5.11 and 5.12. Whereas mechanisms display some variety at shallower depth, they appear strikingly uniform at depths greater than 150 km (see Figures 5.9 and 5.10), showing downdip extensive mechanisms with near-vertical T axes and P axes that are oriented subhorizontally, perpendicular to the strike of the structure outlined by Hindu Kush seismicity. No systematic difference in mechanisms between earthquakes situated in the different subclusters making up the Hindu Kush (see Section 4.2) could be identified. Increased variability of mechanisms in the shallower part of the Hindu Kush could be due to lower location accuracy of earthquakes there (see Figure 4.9). A higly uncertain hypocenter used as input for the inversion for a focal mechanism could effect a large error in the orientation of the mechanism, and if I assume location errors to be randomly distributed, this would increase the variability of obtained mechanisms without changing the general trend.

Figure 5.5. *(following page)*: Comparison of `HASH` fault plane solutions (green) with RMT solutions (blue) for earthquakes where both were available, five deep events (left side) and three shallow ones (right side). Picked first motion polarities and sets of possible planes are shown for the `HASH` solutions.

2009/11/15 01:56:19.80
39.31233N 72.81900E
depth 4.87 km
ML=4.6 Mw=4.45
2010/03/17 11:06:58.22
38.53383N 72.73859E
depth 3.47 km
ML=3.8 Mw=3.54
2010/04/20 19:07:42.24
39.21050N 72.47850E
depth 2.0 km
ML=4.1 Mw=3.93
2009/11/27 14:16:51.38
38.09933N 73.87250E
depth 158.68 km
ML=4.8 Mw=4.21
2010/01/08 13:23:49.20
38.41350N 73.80717E
depth 105.12 km
ML=4.5 Mw=4.09
2010/03/11 07:24:26.30
37.42100N 72.16967E
depth 178.84 km
ML=4.8 Mw=4.05
2010/05/13 04:36:20.80
38.30500N 73.77800E
depth 127.11 km
ML=5.3 Mw=4.59
2010/06/10 10:22:33.39
38.31167N 73.11500E
depth 101.78 km
ML=4.7 Mw=4.12

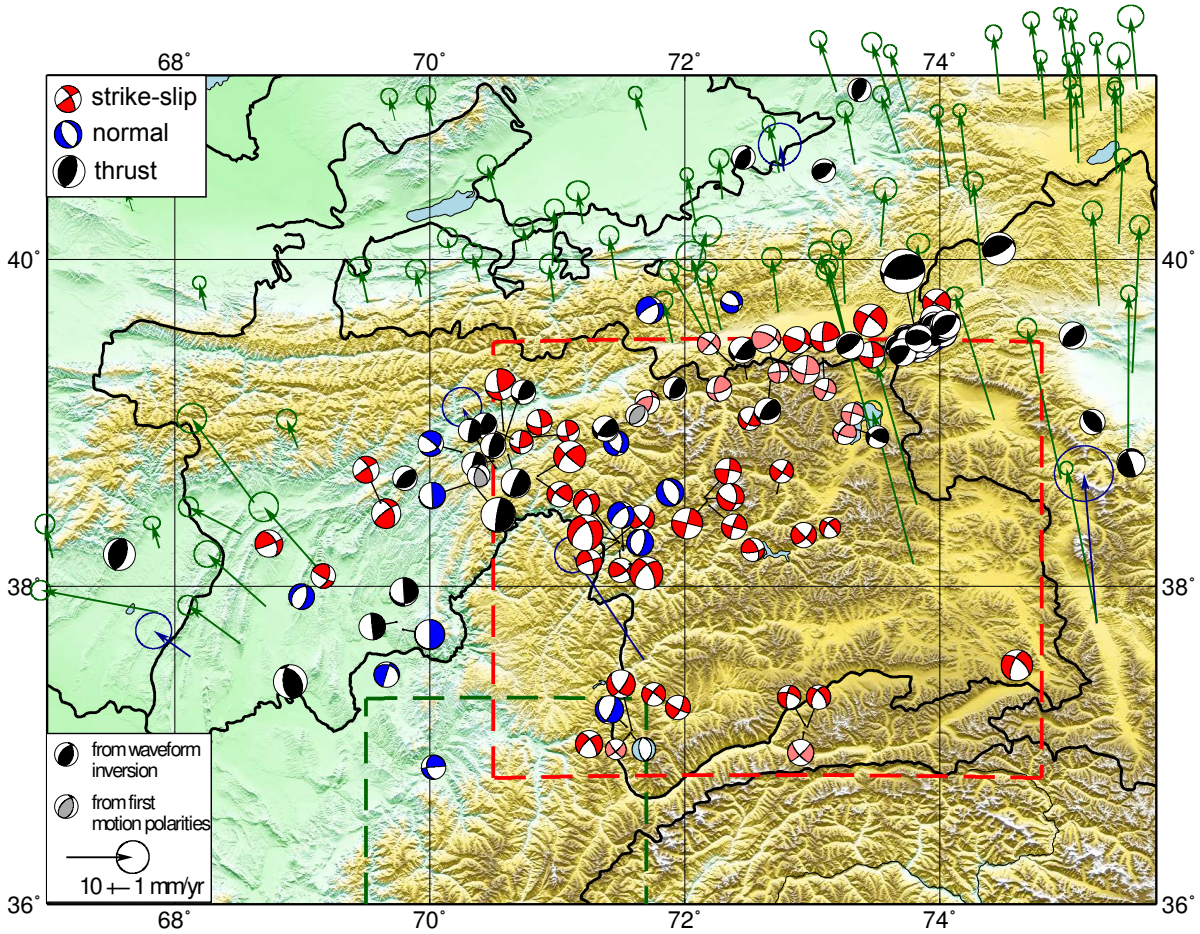

Figure 5.6.: Distribution of earthquake mechanisms for crustal seismicity, i.e. focal depths of less than 50 km. All beachballs show lower hemispheric projections of the fault plane solutions, the color of the beachballs refers to the mechanism type as indicated in the figure legend. Light colors denote mechanisms retrieved from first motion polarities, strong colors show RMT results. The beachball size corresponds to earthquake magnitude. Superimposed are GPS vectors from *Mohadjer et al.* (2010) (blue) and *Zubovich et al.* (2010) (green). Green and red dashed frames indicate the regions shown in the depth cuts in Figures 5.10 and 5.15, respectively.

The uniformity in axis orientations is emphasized by Figure 5.13, where the distribution of strike and dip angles of P and T axes is plotted in polar histograms. P axes plunge shallowly without exception, only 6 events out of 50 show a P axis dip angle between 30 and 45 degrees, the rest is shallower. Strike directions of P axes are mainly north-south and northwest-southeast, perpendicular to the east-west (western part) and southwest-northeast (eastern part, see Figures 4.10 and 4.13) strike of the Hindu Kush seismic zone. The depth sections (Figure 5.10) nicely show that P axes cut the seismcally active structure at about right angles, especially below 150 km depth. Note that this is likewise true for the small subcluster of earthquakes to the southeast of the main Hindu Kush seismically active plane.

T axes are all steeply plunging to subvertical, but show no clearly preferred strike direction, which could be interpreted as random fluctuations around a perfectly vertical orientation. However, a preferred strike perpendicular to the strike of the seismic zone seems to be discernible in the depth

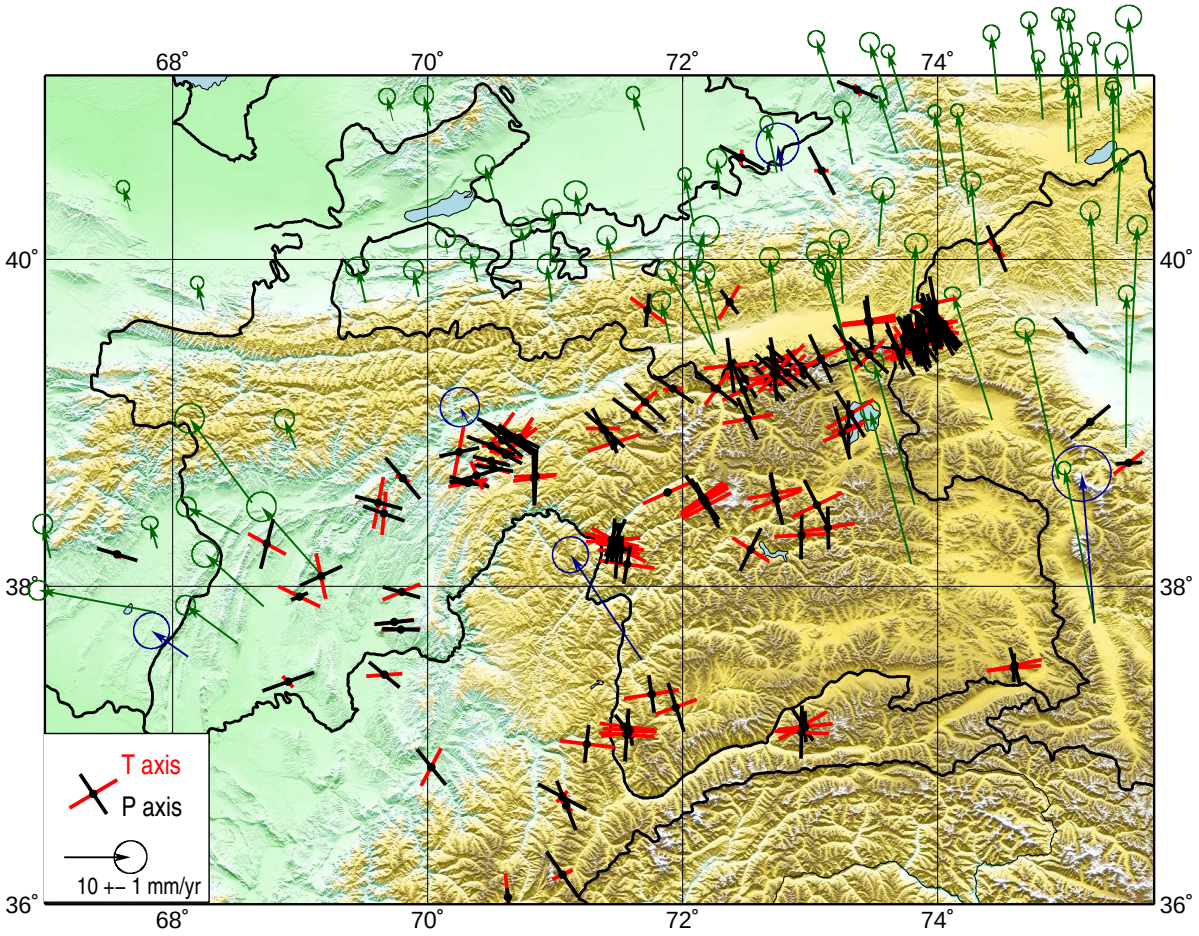

Figure 5.7.: Principal axes of compression (P axes, black) and extension (T axes, red) for shallow earthquakes. A projection of the three-dimensional axes onto the horizontal plane is shown. 3D vector lengths are normed to 1, so the length of 2D vectors gives an idea about their dips. Retrieved P and T axes show a consistent picture of north-south compression and east-west extension in the Pamir, whereas P axes turn to an east-west orientation towards the Tajik Depression.

interval 180-210 km in Figure 5.10. An east-west profile of the entire Hindu Kush (Figure 5.11) and the three strike-perpendiclar profiles in Figure 5.12 (locations shown in Figure 4.10) show that the dip of the T axes clearly follows the dip of the seismogenic planes. A notable exception to this behavior is shown by two events situated right above the seismic gap at 150 km, which show relatively shallowly plunging T axes (see Figure 5.11).

Pamir

For the Pamir zone of intermediate-depth earthquakes, 186 focal mechanisms were obtained, by far the most of these from first motion polarities due to the predominantly small to moderate magnitudes there (see Appendix D). Since the southwesternmost part of the Pamir seismic zone is situated outside the network, no focal mechanisms are available for this area (see Figure 5.16). Mechanisms of intermediate-depth events beneath the Pamir do not exhibit a single, coherently

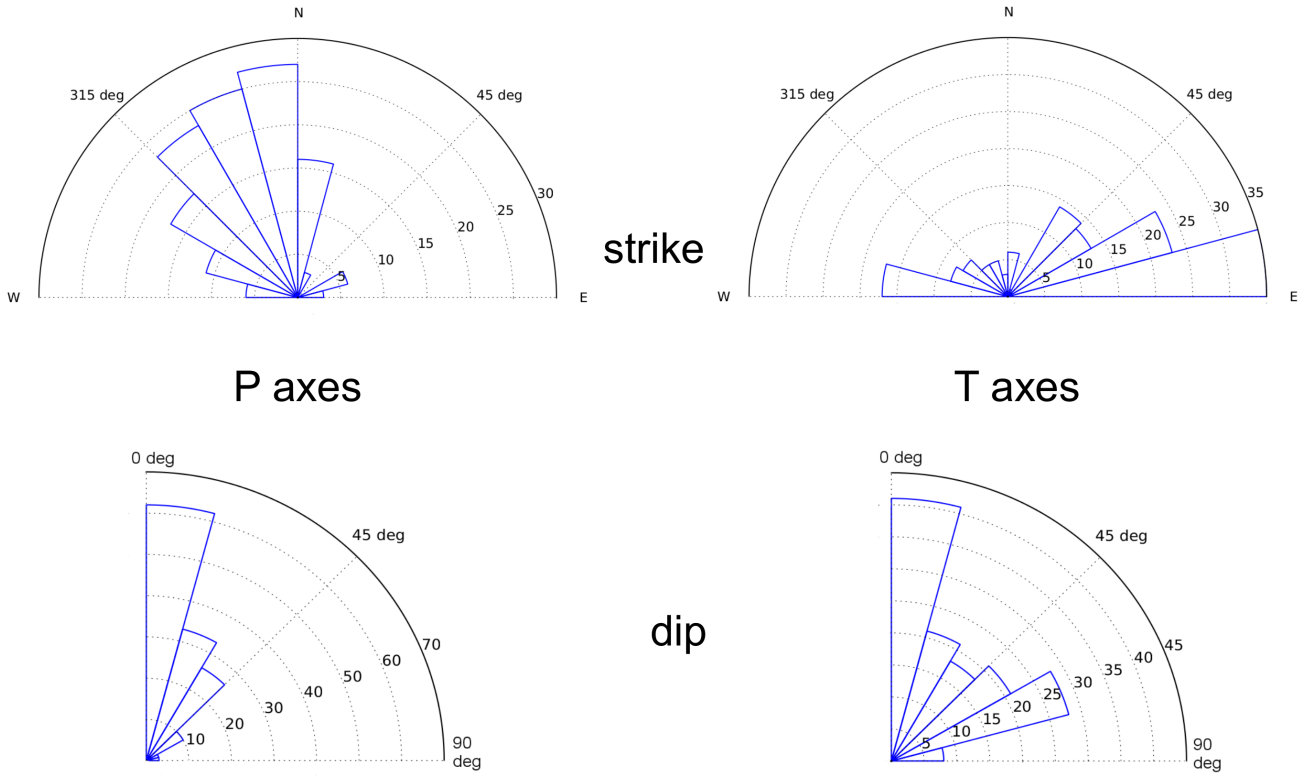

Figure 5.8.: Orientations of P and T axes for shallow earthquakes

occurring preferred orientation, but appear to possess significant variability. Whether this is entirely due to a more variable stress field or if this at least partly reflects the probably higher uncertainties inherent in focal mechanisms obtained from first motion polarities (see Figure 5.5) can not be discriminated.

The distribution of P and T axis orientations (Figure 5.17) shows no clearly preferred strike directions for both, P axes generally plunge shallowly, T axes show a prevalence of intermediate dips (around 45 °). However, some tendencies are discernible in the spatial distribution of axis orientations (Figures 5.15 and 5.16). P axes show a preferred orientation perpendicular to the strike of the structure outlined by intermediate-depth seismicity (Figure 5.15, right column). Due to the Pamir's arcuate geometry, implying a 90 ° change in strike from one end of the structure to the other, a broad range of strike directions is observed. In the depth sections between 50 and 125 km depth, T axes appear to be oriented along-strike of the arc in its eastern part. This prevalence is, however, lost at greater depths and towards the Pamir's west. There is a general trend that principal axes orientations appear more random in the west of the deep Pamir seismic zone. This might be an effect of the network geometry (see Figure 3.1), since earthquakes in this region are situated beneath the fringes of the network, thus the distribution of stations on the focal sphere is not ideal for the recovery of fault plane solutions through first motion polarities.

A subdivision into three domains with distinct prevalent T axis orientations was undertaken based on an along-strike cross section through the whole Pamir zone of intermediate-depth seismicity (Figure 5.16). Subregion 1, which encompasses the shallow (i.e. hypocentral depths <150 km) Pamir seismic zone from its western end until 73.3 °E, shows a dominance of shallowly plunging T

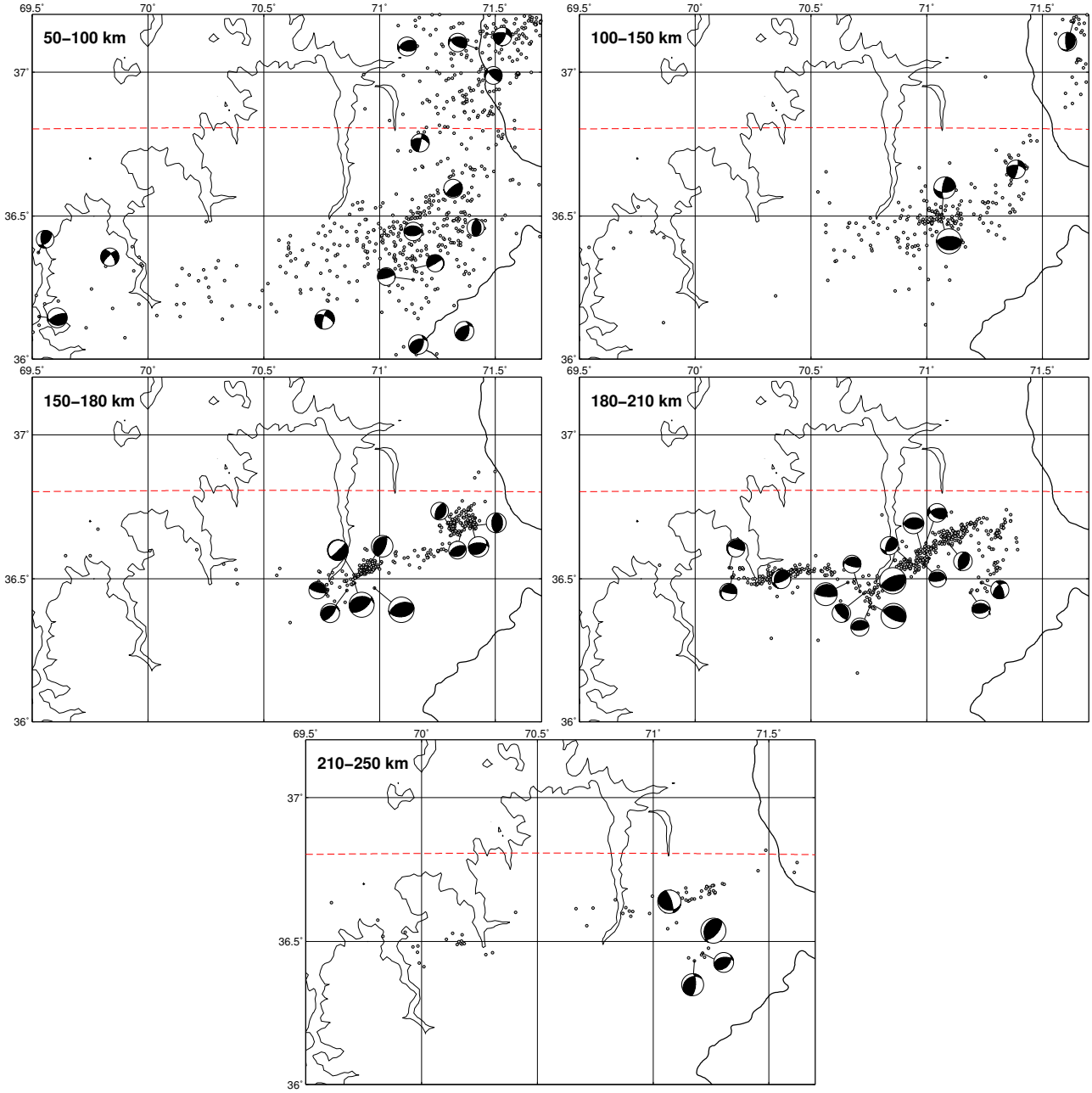

Figure 5.9.: Fault plane solutions obtained for Hindu Kush intermediate-depth seismicity, shown as lower hemispheric map view projections for different depth levels. Thick black line marks the national boundary between Tajikistan and Afghanistan, thin black line delineates the 2000 m altitude contour. Dashed red line marks the approximate boundary between Pamir and Hindu Kush seismic zones at 36.8 °N (Section 4.2.2).

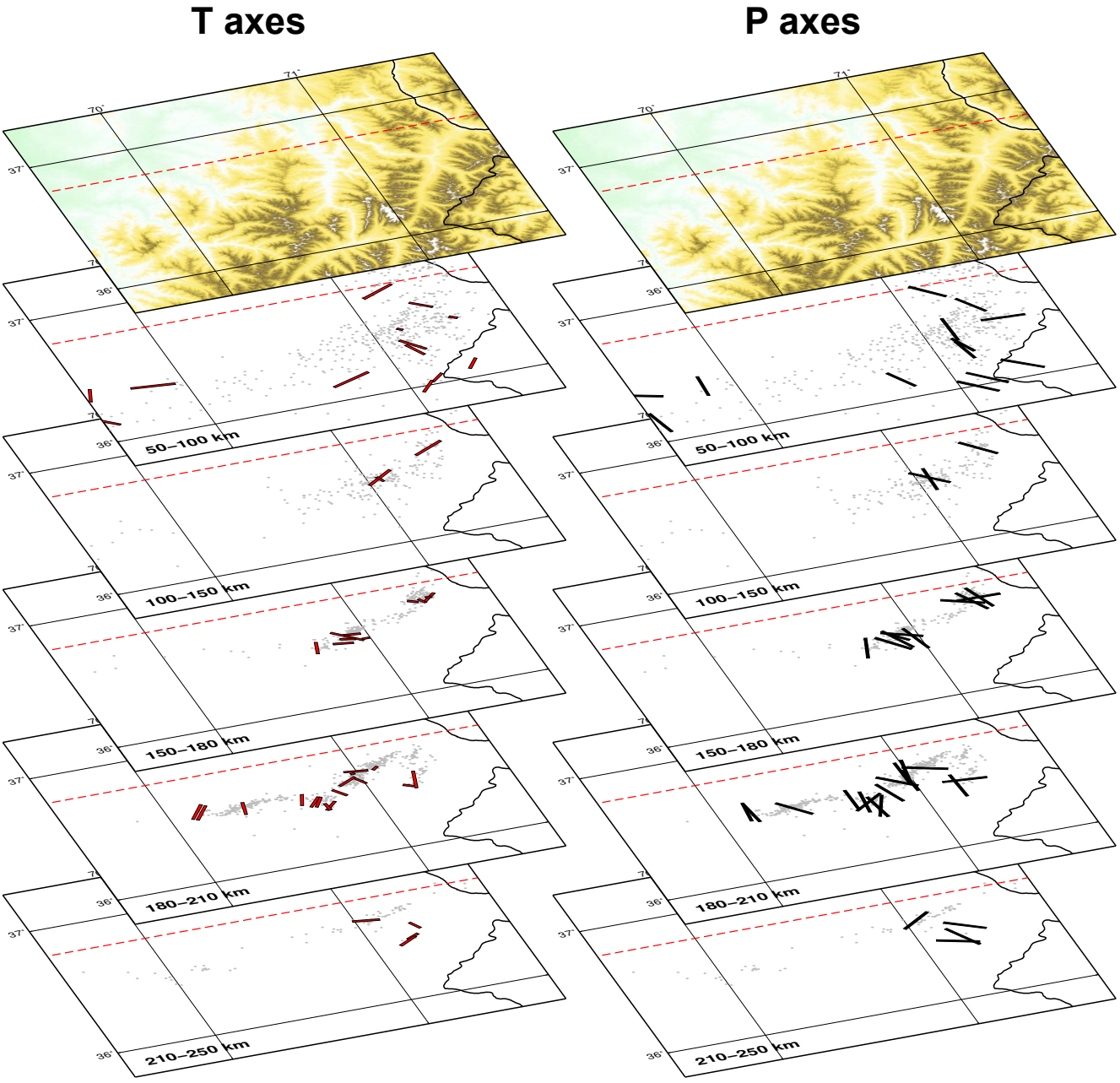

Figure 5.10.: Principal directions of extension (red, left column) and compression (black, right column) for different depth levels, plotted as 2D map view projection (location of displayed region is shown in Figure 5.6). Length of each vector correlates with its dip, i.e. the shorter a vector the more steeply it plunges. Superimposed are the earthquake hypocenters for each depth bin (small grey circles). It is evident that T axes throughout the Hindu Kush plunge steeply (hence the short vector lengths; see also Figure 5.13), whereas P axes are subhorizontal and seem to generally trend perpendicular to the strike of the structure outlined by seismicity. The dashed red line marks the latitude of 36.8°, which is the dividing line between the Pamir and Hindu Kush seismic zones (Section 4.2.2).

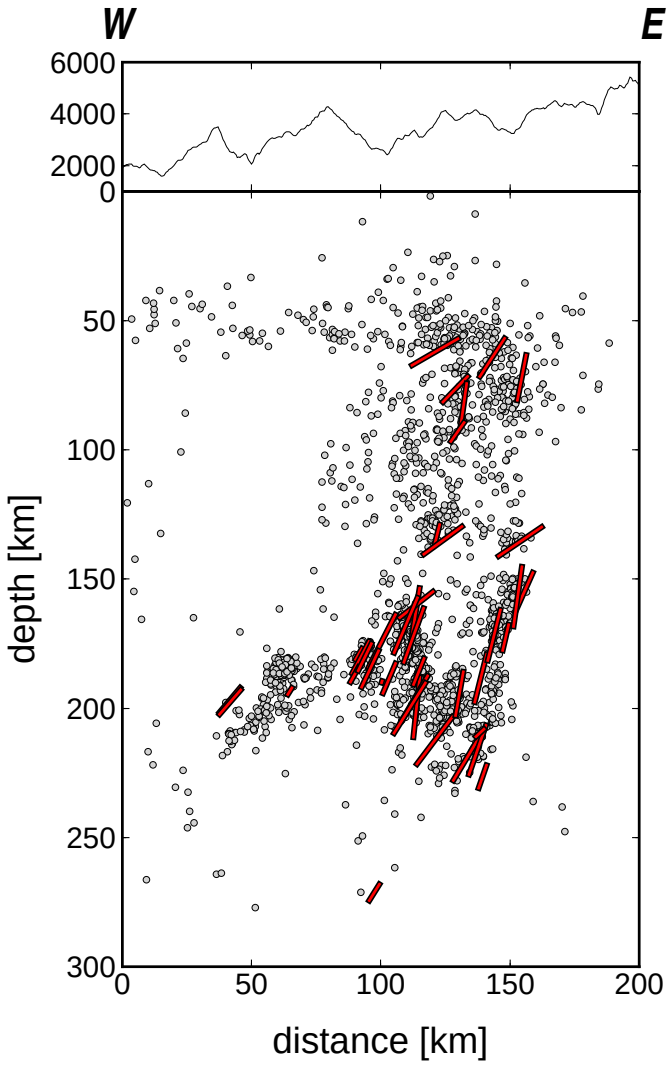

Figure 5.11.: East-west cross section through the Hindu Kush, showing T axes projected into this plane.

axes (see also red histogram in Figure 5.17), most of them following the strike of the arc described by the deep seismic zone. Subregions 2 and 3, making up the easternmost Pamir seismic zone and the deep part of the western Pamir zone, respectively, show substantially steeper inclined T axes.

5.4. Stress inversion

Earthquakes are shear failure processes occurring in response to stresses imposed by plate tectonics. Laboratory experiments on rocks have shown that failure in previously unfractured rock occurs along a plane at an angle of 30° relative to the direction of maximum compression (*Engelder*, 1987). Hence, the orientation of earthquake fault planes and the directivity of motion occurring along them are a proxy for local stress conditions. However, the ambiguity of focal mechanisms as to which plane is the actual rupture plane complicates inversions (*Gephart and Forsyth*, 1984).

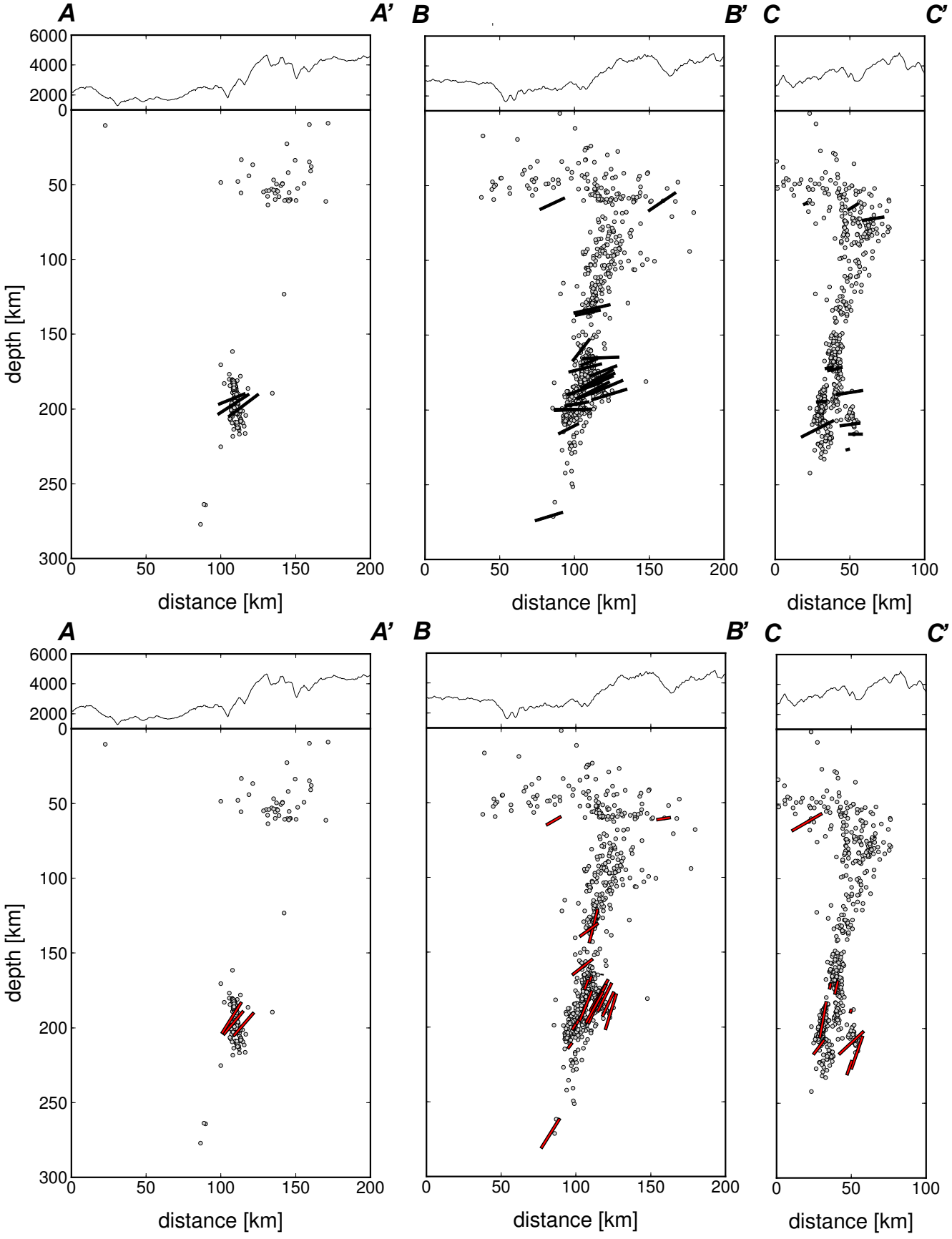

Figure 5.12.: Strike-perpendicular profiles through the Hindu Kush seismic zone, showing the projections of P (top) and T (bottom) axes into the projection planes. For the positioning of the profiles, refer to Figure 4.10.

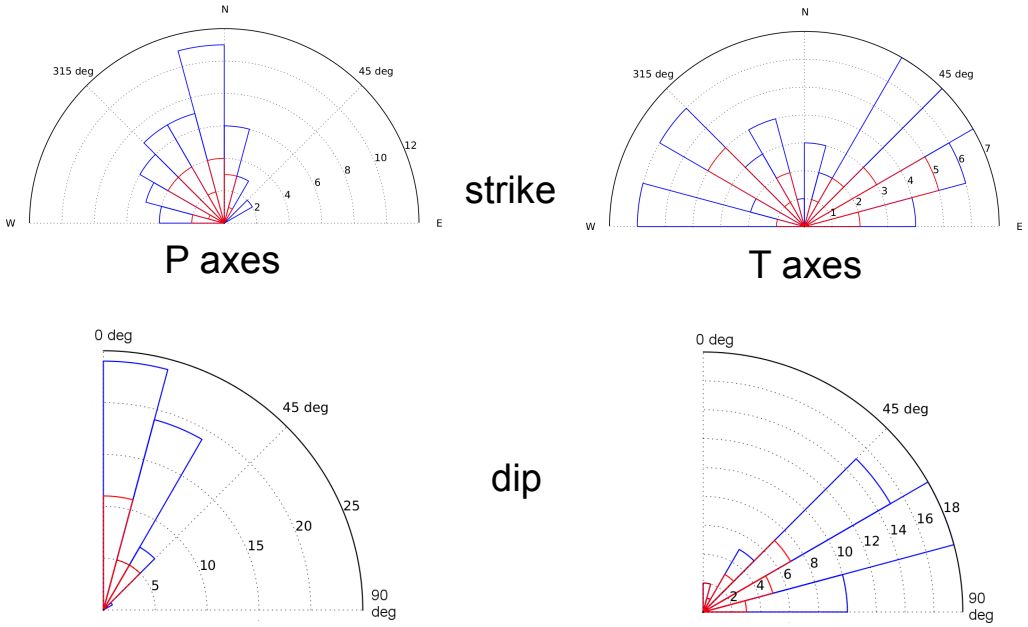

Figure 5.13.: Rose diagrams showing the distribution of the strikes (upper row) and dips (lower row) of P (left) and T axes (right) of earthquakes in the Hindu Kush. Blue histograms are for all Hindu Kush events, red histograms only for events shallower than 150 km. A clear prevalence of horizontal, roughly north-south plunging P axes and steeply plunging, randomly trending T axes is discernible.

Earthquakes in nature rarely occur in unfractured rock, but in pre-fractured material, which can lead to larger deviations of fault plane orientations from the ambient stress field. The inversion of a sufficiently large number of focal mechanisms should, however, eliminate these to first order randomly distributed deviations and yield a good estimate of the average background stress field (*McKenzie*, 1969)

Inverting the set of fault plane solutions for stress field conditions, I started out with a very coarse separation of events into three principal structures (crustal, deep Hindu Kush, deep Pamir) that were individually inverted and subdivided into regions of apparently homogeneous stress field where necessary (see Section 5.4.1). Since this prescription of subareas may be somewhat subjective, I went on to perform a single, spatially damped inversion of all crustal mechanisms (only those offered a decent spatial distribution) on a regular grid without imposing a regional subdivision (see Section 5.4.2).

5.4.1. Individual inversions of regions

The program `slick` (*Michael*, 1984, 1987) inverts for the four parameters σ_1, σ_2, σ_3 (maximum, intermediate and minimum compressive stress direction) and $\phi = \frac{\sigma_2 - \sigma_1}{\sigma_3 - \sigma_1}$ (relative stress magnitudes) with a linear approach, minimizing the total amount of rotation around an arbitrary axis necessary to rotate the focal mechanisms to fit the stress model. The algorithm determines the more likely fault plane of each input focal mechanism, thus requiring no additional geologic information on the target area besides the set of mechanisms to be inverted.

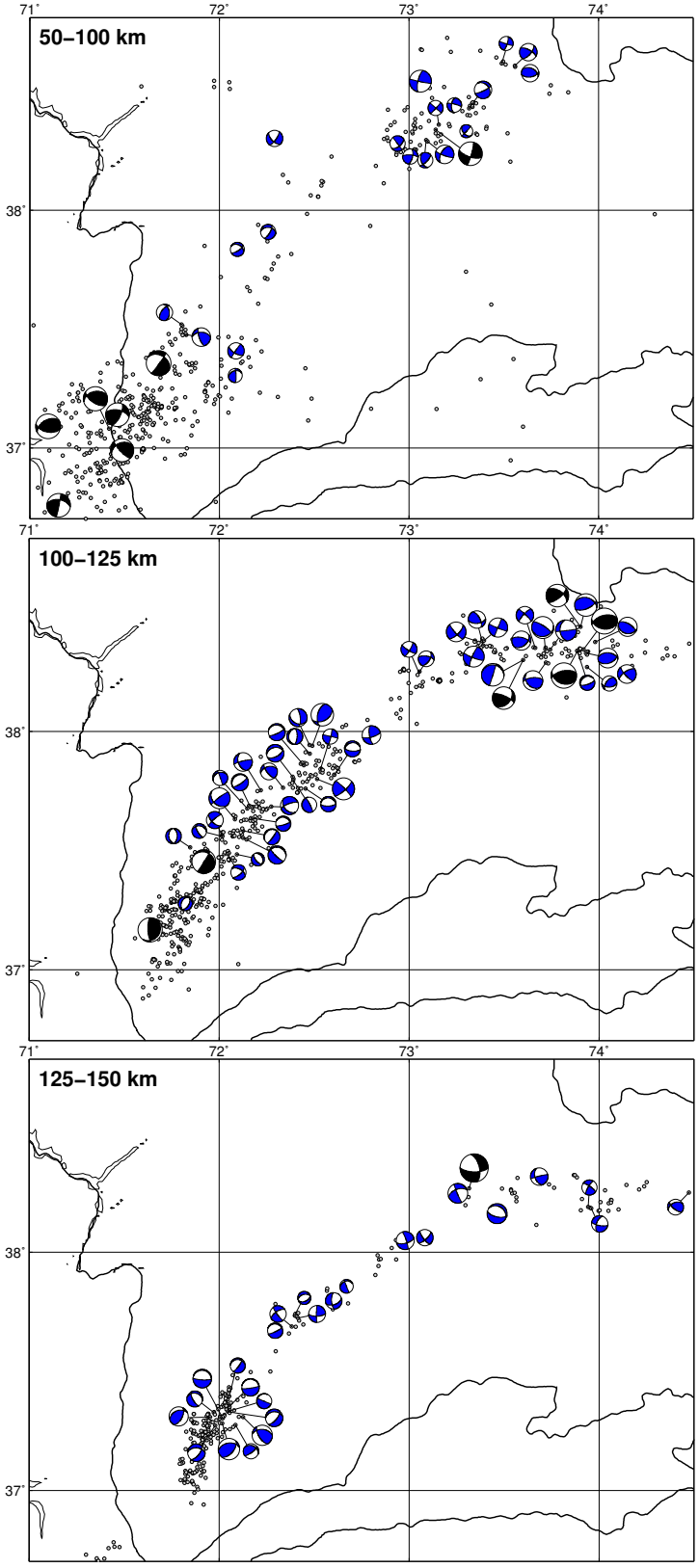

Figure 5.14.: Focal mechanisms determined for Pamir intermediate-depth earthquakes, shown as lower hemispheric map view projections for different depth levels. Blue beachballs denote mechanisms retrieved from first motion polarities (see Section 5.2.2), black beachballs mark focal mechanisms from waveform inversion (see Section 5.2.1). Heavy black lines are national boundaries.

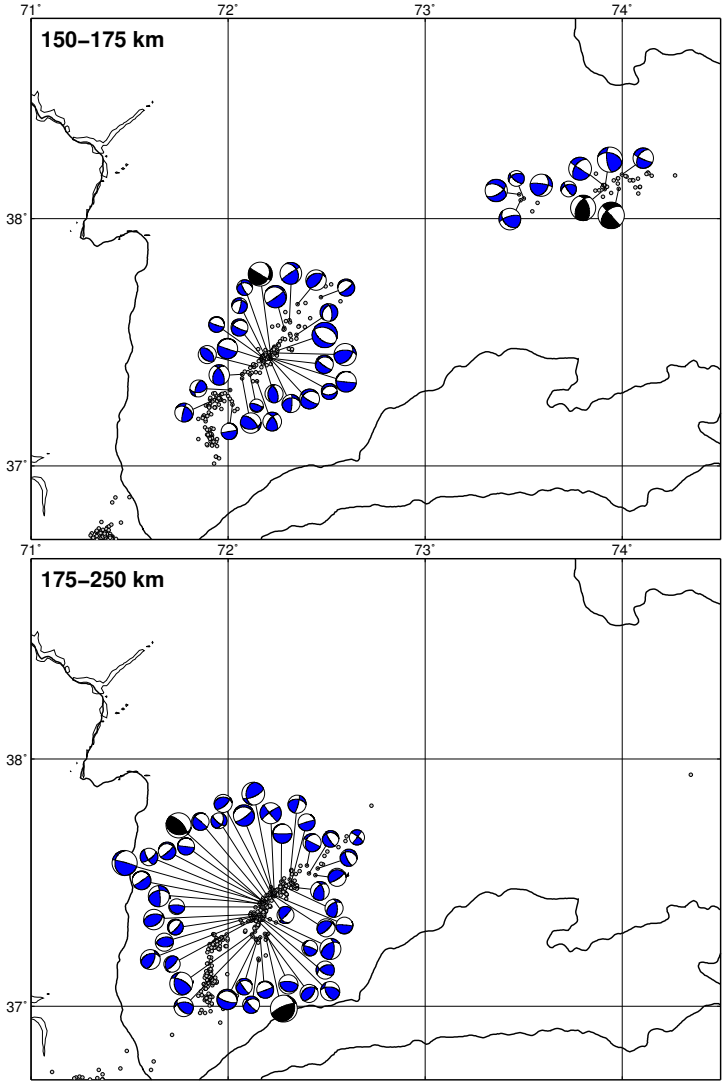

Figure 5.14.: Focal mechanisms of intermediate-depth Pamir earthquakes (*continued*)

The stress tensor is an analog to the moment tensor presented in Section 5.1, and the principal stress directions σ_1, σ_2 and σ_3 correspond to the P, B and T axes in that they are the eigenvectors of the smallest, intermediate and largest eigenvalue, respectively. An important assumption when inverting a set of focal mechanisms for a single stress tensor is that the stress field that effected them is uniform. Parameters that quantify the quality of the obtained fit of the retrieved stress tensor to the set of mechanisms are the average rotation angle β and the variance. However, these values only yield a measure of the goodness of fit of the determined stress tensor to the input data, but give no indication about the robustness of the inversion with respect to, e.g., single erroneous input mechanisms. Confidence intervals obtained with the methods of *Gephart and Forsyth* (1984) and *Michael* (1984) differ substantially when the same dataset is used, and no superiority of one scheme over the other can be universally assigned (*Hardebeck and Hauksson*, 2001). Hence, a bootstrap method as described in *Michael* (1987) was applied to glean some idea on solution robustness. 2,000 inversions with randomly resampled subsets of the input dataset were carried out for each region, the obtained spread of axis orientations give a good solution stability estimate.

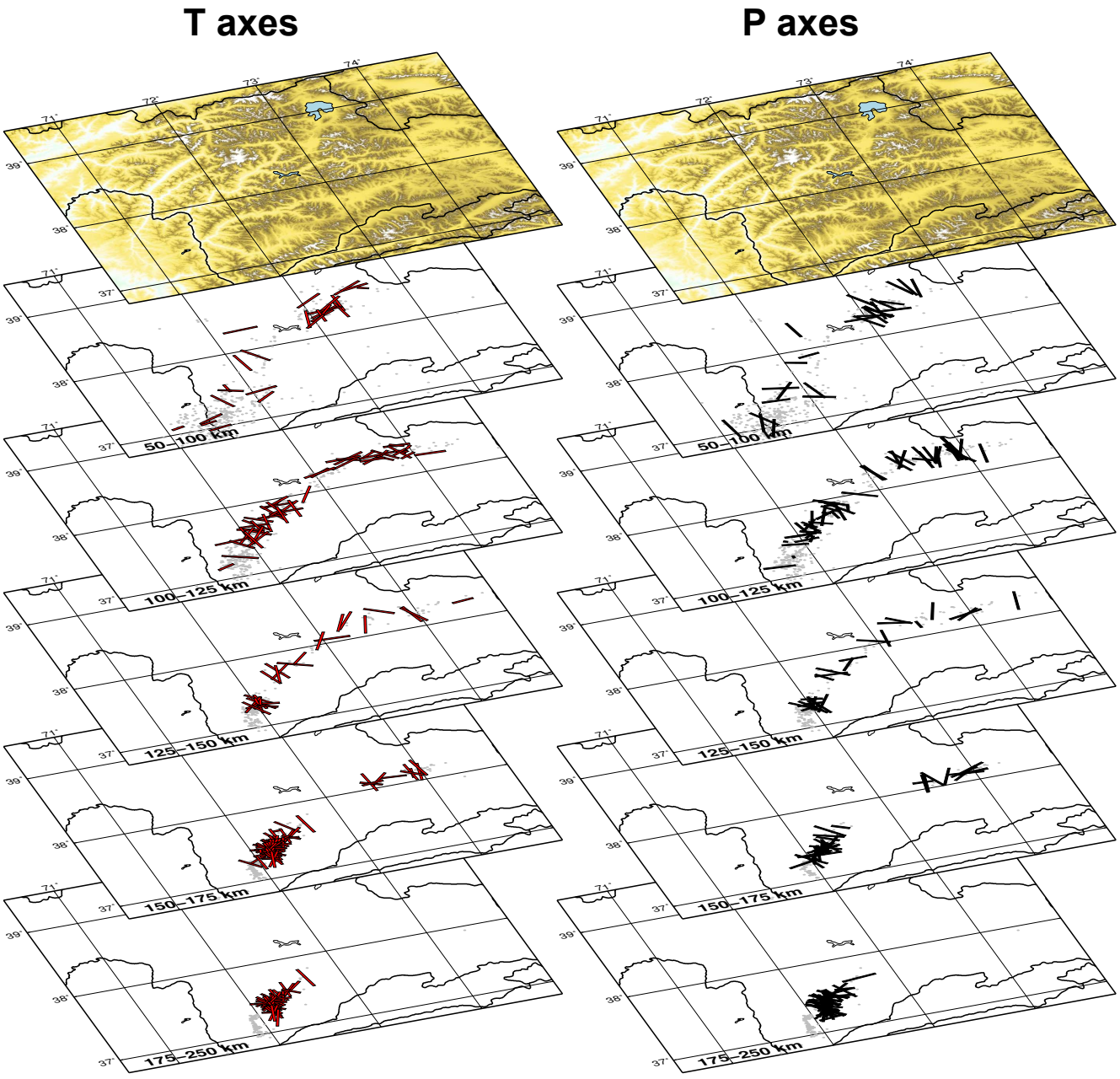

Figure 5.15.: Depth sections through the Pamir, with T axes (left, red) and P axes (right, black) plotted on top of the distribution of seismicity within each depth bin. Black lines indicate national boundaries. Location of the plotted region is shown in Figure 5.6.

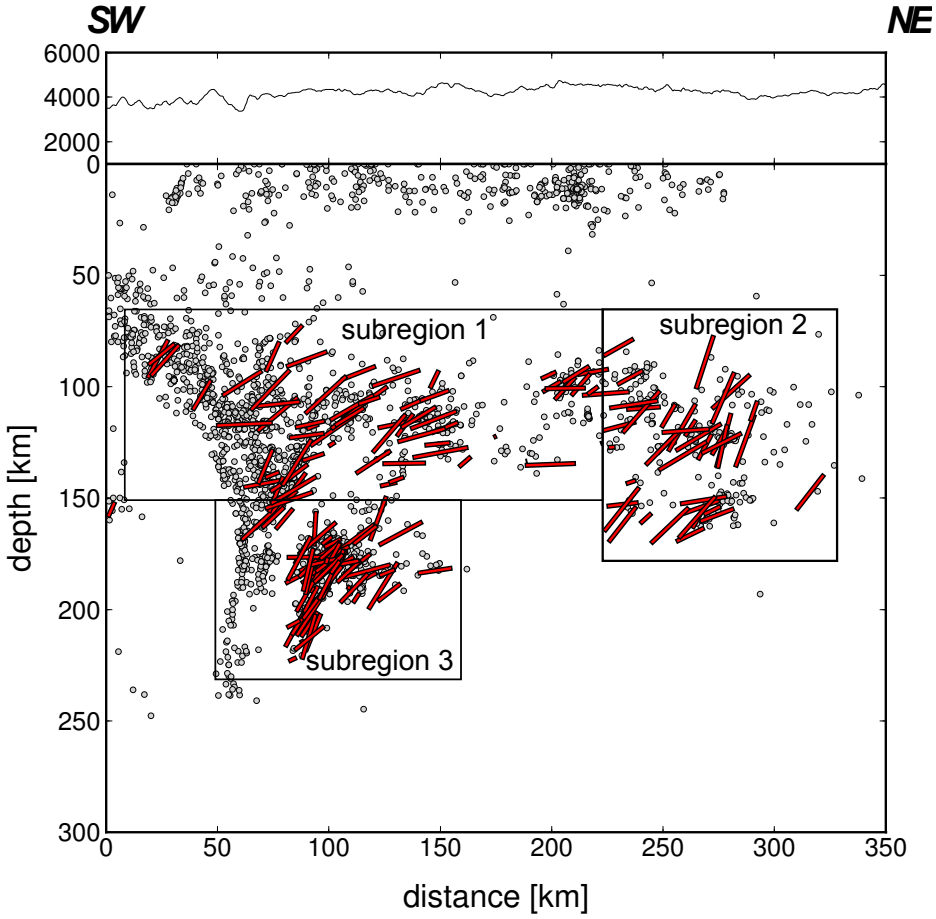

Figure 5.16.: Along-strike profile (oriented 60°E) through the entire Pamir deep seismic zone, showing a projection of T axis orientations into this plane. Length of displayed vectors scales with in-plane proportion of their amplitudes (longest possible vector is 100% in-plane, point means 100% perpendicular to the plane). Based on the prevalence of different general orientations of the T axes, three subregions of Pamir deep seismicity are defined (black frames) for later use in stress inversion (see Section 5.4).

An inversion of all crustal seismicity (as shown in Figure 5.6) yields an oblique thrust mechanism with NNW-SSE trending, horizontal P axis and rather steeply plunging, ENE-WSW trending T axis (Figure 5.18, upper left). Obtained values for β and variance indicate that there are significant deviations from this optimum stress tensor in the focal mechanism data, although the bootstrap results (colored symbols confined to narrow region on the focal sphere) indicate that the inversion is stable. The distribution of P and T axes in Figure 5.7 hints at the presence of distinct zones with different preferred focal mechanisms, rendering the assumption of a single, homogeneous stress field implicit in the inversion of all shallow earthquakes unlikely. Hence, I further subdivided shallow earthquakes into three regions and performed an inversion for each of these alone. The first group of these is the aftershock sequence of the Nura earthquake. Inversion of these events (Figure 5.18, lower left) yields a pure thrust mechanism with very stable P axis orientation and a somewhat more variable T axis, which oscillates around purely vertical. This makes sense considering that aftershocks showed both thrust and strike-slip mechanisms. Lower values for β (23.41 ° instead of 43.63 °) and variance (0.089 instead of 0.202) indicate a significantly

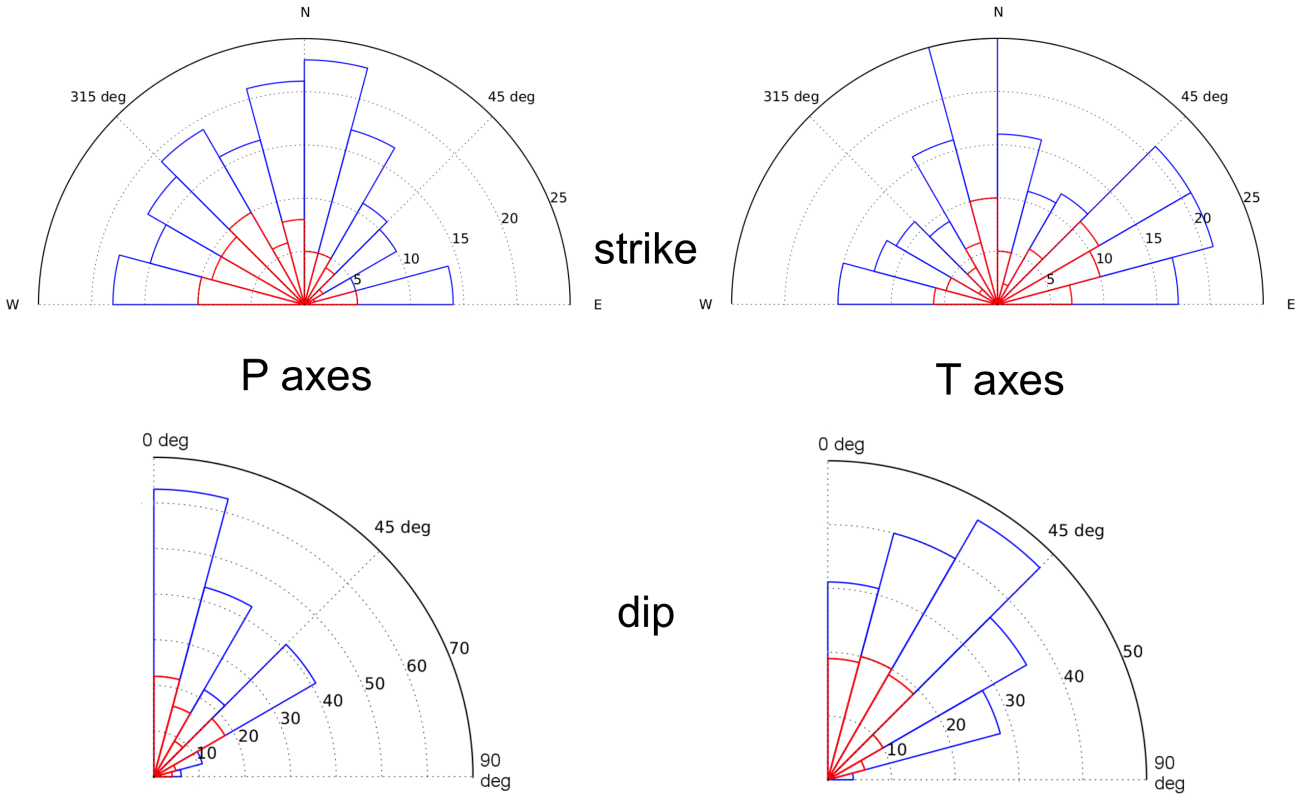

Figure 5.17.: Polar histograms of strike and dip of P and T axes obtained for intermediate-depth seismicity in the Pamir. Red bars show distributions only for events located in subregion 1 (as shown in Figure 5.16).

better fit than for the overall inversion. Events throughout the western and central Pamir formed the second group for a separate inversion, here the obtained best-fit stress tensor is indicative of strike-slip motion along a NE-SW or NW-SE oriented fault plane, which is consistent with most mechanisms in this region (Figure 5.6). Results for events located within the Tajik Depression (Figure 5.18, lower right) are less robust than the other inversions, which is due to the lower amount of fault plane solutions obtained for this region. However, the obtained fit is still better than for the overall solution. The best-fit mechanism indicates slip along a subhorizontal or subvertical rupture plane, which means that both P and T axes plunge roughly 45 °. However, the orientation of the P axis is not stably resolved.

Focal mechanisms for the Hindu Kush (see Figure 5.19) yield a well-defined stress tensor with low variance and an average rotation angle β of 19.6°. This is only slightly higher than angles routinely obtained for aftershock series (*Michael*, 1984, 1987, 1991). I presume that the inversion of focal mechanisms for a large-scale tectonic structure (roughly 100×200 km in the case of the Hindu Kush) should yield a stress tensor with worse fit parameters than the inversion of a dataset focussed on a single fault plane (aftershock series). The best-fit stress tensor for the Hindu Kush is a pure thrust (when seen in map view), with a nearly vertical σ_3-direction or T-axis and σ_1 (or P axis) horizontally trending NNW-SSE. This is in visual agreement with beachballs and principal axes seen in Figures 5.9 and 5.10. Resampled bootstrap inversions (colored symbols in Figure 5.19) show that the orientation of σ_3 is remarkably stable, whereas there is some variability in the

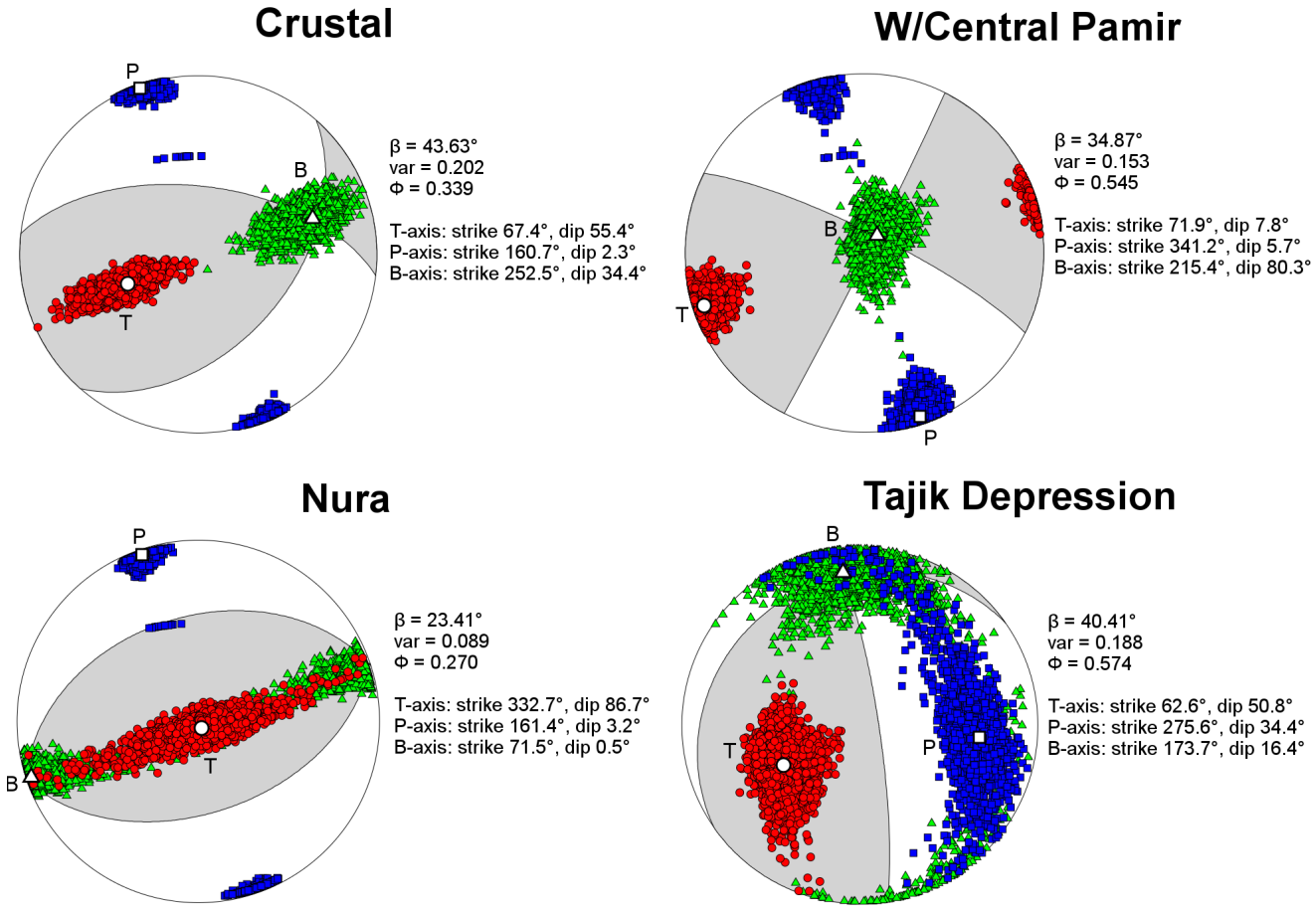

Figure 5.18.: Stress inversion results for crustal earthquakes: the obtained stress tensor is indicated as the background beachball and its principal axes are denoted by big square (P), circle (T) and triangle (B) symbols. Smaller, colored symbols indicate results of 2,000 bootstrap inversions with randomly resampled data, which provide a measure of inversion robustness for the retrieved stress tensor. In addition to a single inversion using all shallow earthquakes, inversions of three subregions (Nura region, western/central Pamir and Tajik Depression) were undertaken.

other two axes which are, however, both clearly confined to the horizontal plane. This instability the orientation of σ_1 and σ_2 might be due to the strike variation of the Hindu Kush structure, a trend that is apparently followed by the orientation of the earthquakes' principal axes (Figure 5.10).

As already evident from comparing the along-strike profiles (Figures 5.11 and 5.16), mechanisms of intermediate-depth earthquakes in the Pamir seismic zone exhibit a significantly higher degree of variability than in the Hindu Kush. This is reflected in the stress inversion results (see Figure 5.20), where obtained variance and β values are clearly larger than for the Hindu Kush. A single inversion for the entirety of mechanisms in the Pamir (186 events) yielded an oblique thrusting mechanism, with a relatively steeply plunging T-axis (56.8 ° NNE-SSW) and a P-axis trending roughly perpendicular to the average strike of the Pamir seismic zone. As argued in Section 5.3.2, a subdivision of the Pamir into three regions based on the average orientation of T axes in an

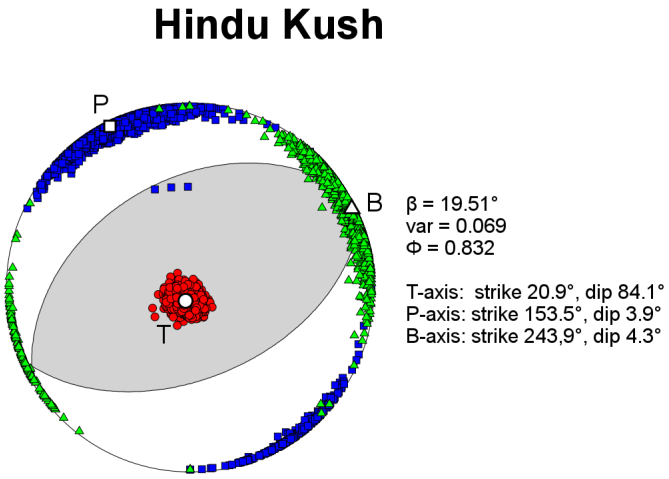

Figure 5.19.: Stress inversion result for the Hindu Kush: notation identical to Figure 5.18. Obtained results show a nearly vertically oriented T-axis and a horizontal P-axis roughly pointing north-south, i.e. perpendicular to the strike of structures outlined by seismicity (see Figure 4.14).

along-strike cross section seems evident. I thus carried out separate inversions for each of these regions (Figure 5.20). Subregions 2 and 3 have optimum stress tensors closely resembling the inversion result for all Pamir earthquakes, with steeply plunging T axes (as evident from Figure 5.11) and rather shallow P axes oriented roughly north-south. Subregion 1, however, exhibits a perfectly horizontal T axis oriented NE-SW, along-strike of the Pamir seismic zone. However, this inversion appears to be rather unstable with respect to the orientation of the preferred B and T axes (whereas P seems rather robust).

5.4.2. Damped stress inversion on a regular grid

Independent regional inversion for the stress field in a set of subregions naturally introduces subjectivity in the choise of these subregions. Moreover, the presence of noisy data in some of these subregions may introduce an apparent heterogeneity in the stress field not strongly required by the focal mechanism data (*Hardebeck and Michael*, 2006). For this reason, and to retain meaningful sample sizes, I there have only subdivided the study region into a handful of fairly large provinces (Section 5.4.1).
A spatially damped stress inversion scheme that searches for the regional stress model with the minimum inherent complexity has been proposed by *Hardebeck and Michael* (2006). Their program `SATSI` inverts for stress orientations in each predefined 2D or 3D subregion along with a minimization of the differences between adjacent subareas. Only heterogeneity strongly required by the data is retained. This approach, which is similar to seismic tomography (see Chapter 6), requires the choice of an optimal damping parameter ϵ from a tradeoff-curve between data and model variance (see e.g. *Eberhart-Phillips*, 1986). The strength of this method is that it does not rely on a prescribed subdivision of the study area into regions with presumably homogeneous stress field, but is able to obtain this subdivision, if it is really required by the data, by inverting

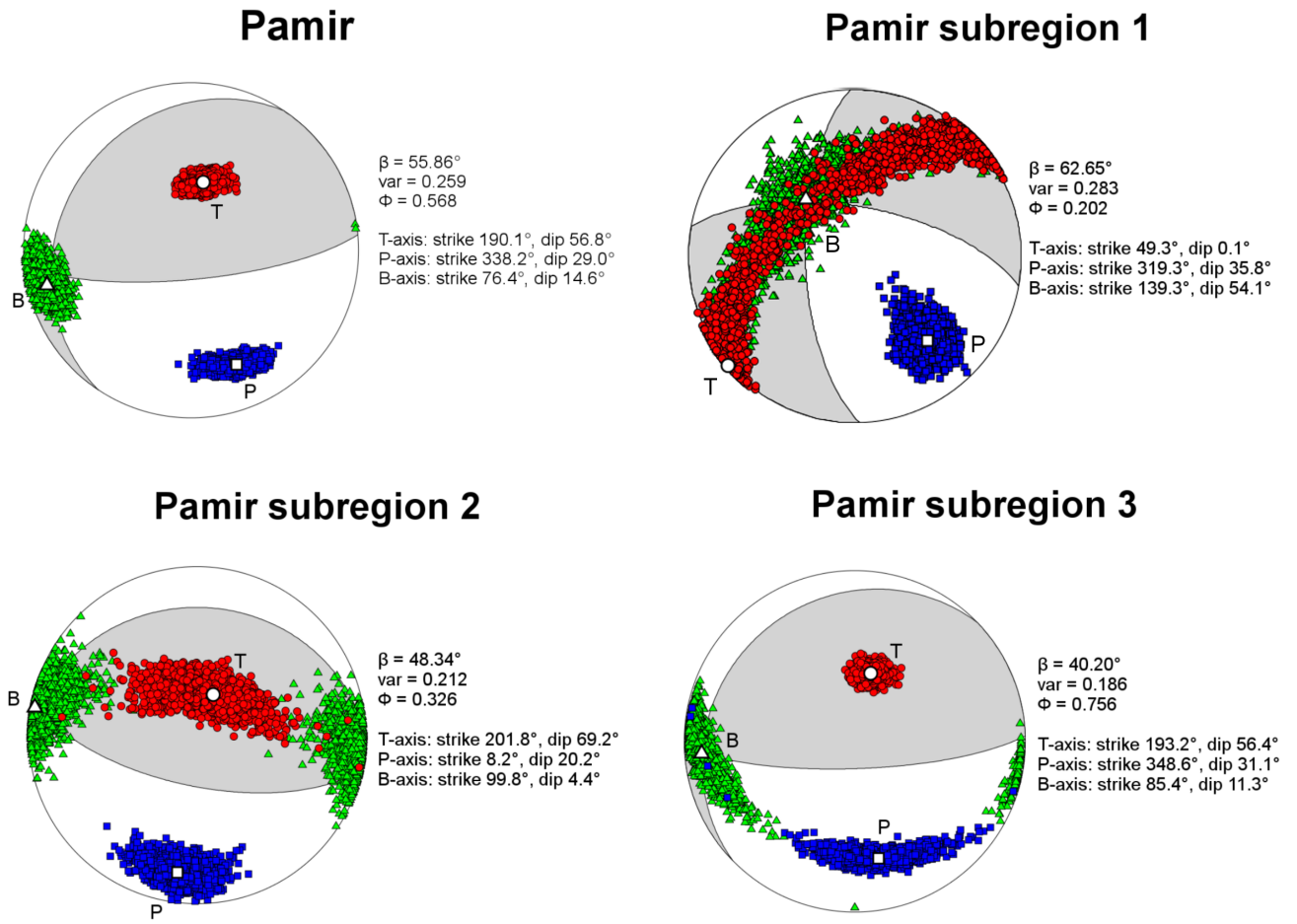

Figure 5.20.: Stress inversion results using `slick` for all intermediate-depth focal mechanisms in the Pamir (186 events, upper left) and independent inversions inside the three subregions defined in Figure 5.16. Notation same as in Figure 5.18.

on a regular grid. However, there is some influence of the grid choice onto the obtained results. I thus tried out various grid cell sizes.

`SATSI` was only applied to shallow seismicity, since only there spatially extended and, very roughly, homogeneous distribution of earthquake focal mechanisms is obtained. Inversion on a regular grid for the strongly clustered deep events is not easily feasible. Focal mechanism data were inverted for stress field on a regular grid with 0.5° grid spacing, which was densified to a grid spacing of 0.33° where a sufficient number of focal mechanisms were available. This proved to be the densest grid spacing that does not lead to too many grid nodes just being constrained by one or two mechanisms. The damping value was chosen as $\epsilon = 0.6$ based on the tradeoff curve shown in Figure 5.21. Obtained σ_1 and σ_3 axes are plotted in the center of each grid cell in Figure 5.22. The continuous trend from north-south trending principal compression in the southern, central and eastern Pamir to northwest-southeast compression in the northwestern Pamir and east-west compression in the Tajik Depression, already evident from Figure 5.7, is clearly imaged. The obtained mean rotation angle $\beta = 12.56°$ is substantially smaller than for the `slick` inversions (Section 5.4.1), which is hardly surprising considering that the fitting algorithm here has a lot

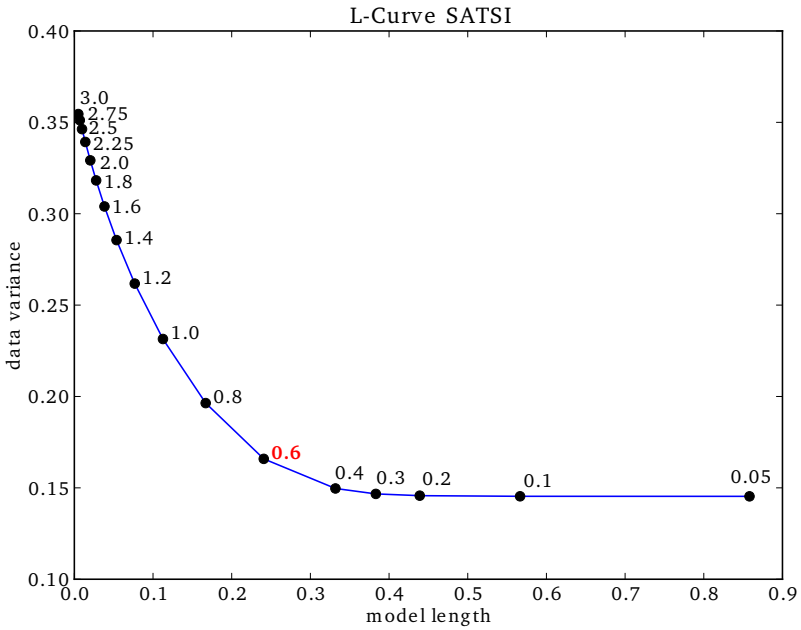

Figure 5.21.: Tradeoff curve for choice of damping parameter in `SATSI` stress inversion. The damping value $\epsilon = 0.6$ that best minimizes both model length and data variance is marked in red.

more degrees of freedom (i.e. orientation of many more single stress tensors) that can be adjusted to fit the observation data.

5.5. Interpretation and Discussion

5.5.1. Shallow processes

Radial thrusting of Pamir over Tajik Depression and distributed deformation in the western Pamir

Our set of crustal focal mechanisms for the Pamir and surroundings (Figure 5.6) shows a widespread absence of thrusting events along east-west trending rupture planes, which would be expected considering the regional deformation field (*Zubovich et al.*, 2010; *Mohadjer et al.*, 2010). The Main Pamir Thrust, which represents the main orogenic front of the Pamir and where 10-15 mm/yr of convergence have been deduced by the aforementioned studies, exhibits nearly no activity (except for the Nura earthquakes and aftershocks in its eastern part), some rather minor strike-slip events are situated somewhat to its south. This may indicate that the largest part of the MPT is currently locked and accumulates stress that might be released in a future big earthquake. This aspect will be further discussed below.

In the Pamir, a roughly north-south trending seismically active lineament from the eastern MPT, across Lake Karakul to the Wachan corridor, Afghanistan, seems to separate an actively deforming western Pamir from a largely aseismic eastern Pamir. Focal mechanisms in the western Pamir are mainly sinistral strike-slip along northeast-southwest striking fault planes (see Figure 5.18, upper

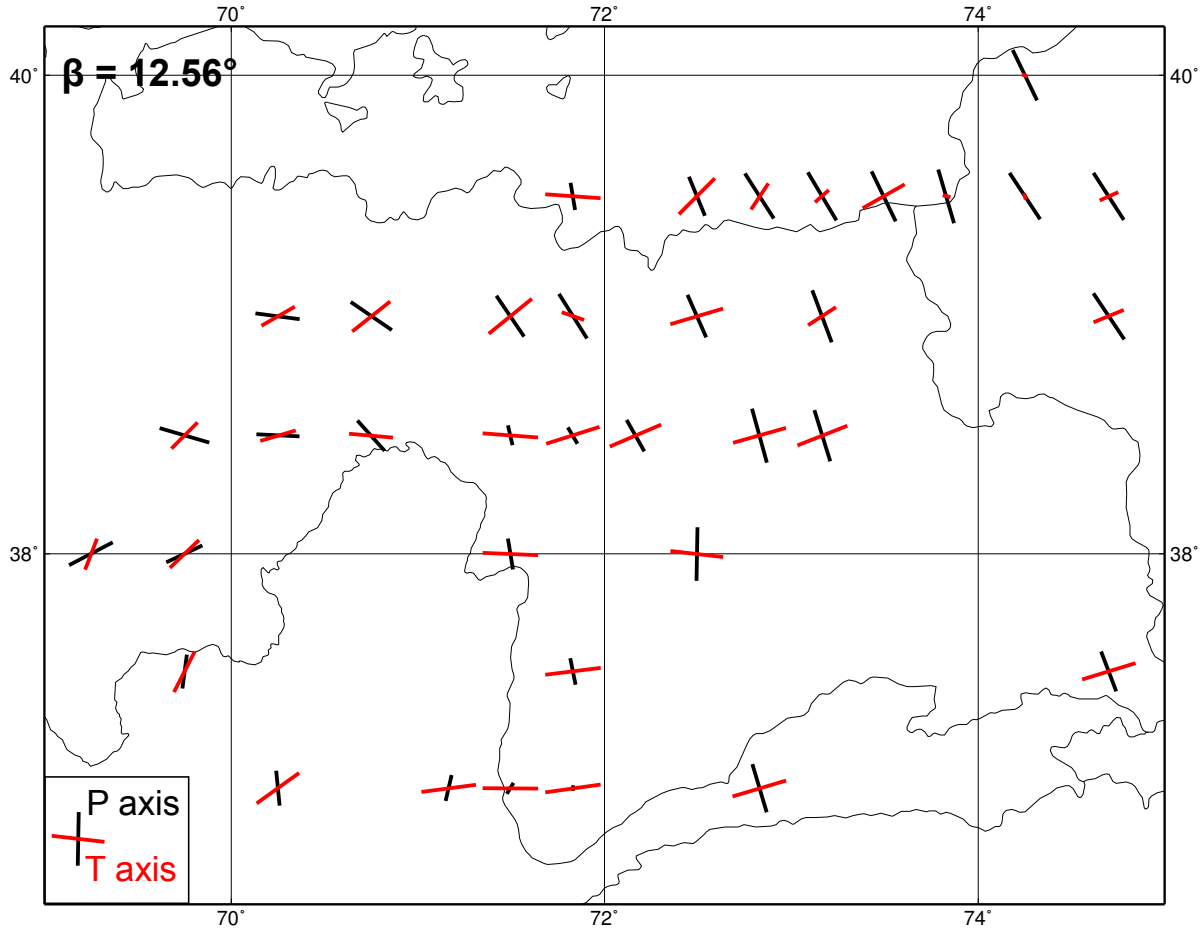

Figure 5.22.: Results of 2D spatially damped stress inversion on regular grid with gridsize 0.5° (densified to 0.33° in some areas). Shown are obtained σ_1 (P) and σ_3 (T) axes at the center of each grid cell. Axes are shown as 2D projection in map view, i.e. the length of the vector scales with dip (the shorter the steeper). A clear trend consisting of a rotation of P axes from a north-south orientation in the eastern, southern and central Pamir through a northwest-southeast strike in the northwest Pamir to a pure east-west orientation in the Tajik Depression is discernible.

right). A few distributed normal faulting mechanisms are observed, but no large-scale east-west extensional systems like in Tibet (*Murphy et al.*, 2010) appear to be active. The retrieved pattern of stress orientations (Figures 5.7 and 5.22) indicates a rotation of compressive axes from north-south in most of the Pamir to a northwest-southeast trend at the northwestern rim of the Pamir and to a pure east-west orientation in the Tajik Depression. A prevalence of northwest-southeast compression in the region around Garm, oblique to the general convergence direction of India and Eurasia (which is purely north-south, see e.g. *DeMets et al.*, 2010) and similar to what I retrieve, has been found by *Hamburger et al.* (1992) and *Lukk et al.* (1995). Another independent indication of the emergence of an east-west compressive component in the northwest Pamir is the direction of the GPS vector for the station in Khorog in *Mohadjer et al.* (2010), which shows about 6-7 mm/yr westward motion that is not observed further south (see also Figure 2.3).

Before attempting to interpret the obtained observations in a geodynamic context, i.e. finding a dynamic model for processes currently ocurring in the northwestern Pamir, I will give a brief

overview of "boundary conditions", i.e. try to work out important preconditions possible models have to be based on. Then, several models are proposed, their implications explained and their applicability to the Pamir is assessed.

The Pamir, having migrated northwards since about 25 Ma (*Sobel and Dumitru*, 1997), nowadays features considerably thickened (Moho depth 60-70 km, see *Mechie et al.*, 2012), weak felsic crust. Being flanked by basins to the east and west, the high average elevation of about 4 km of the Pamir plateau stands in contrast to substantially lower relief surrounding it.

To the north, the Pamir has nearly completely overridden the former Tajik-Yarkand Basin, the last remnant of which can be found in the Alai Valley (*Burtman and Molnar*, 1993). Further north, the southern Tien Shan probably acts as a backstop, upon which the Pamir possibly already impinges in its eastern part (*Sobel et al.*, 2011a). To its east, the Tarim Basin, a supposedly cratonic block with rigid, thick crust and lithosphere (*Yang and Liu*, 2002), resists internal deformation as well as subduction, and hence acts as "secondary indenter", being pushed north as a whole and transferring deformation into the Tien Shan north of it, promoting its uplift. No radially outward component of Pamir motion into the Tarim Basin, analog to what is seen in the northwest Pamir, has been found at its boundary to the Tarim Basin. Instead, the Pamir is guided in its northward movement by the rigid Tarim block, relative motion used to be accommodated across the KYTS (see Figure 2.4, *Cowgill*, 2010; *Robinson et al.*, 2004), today Tarim Basin and Pamir move northwards parallel to each other (*Zubovich et al.*, 2010; *Sobel et al.*, 2011a). Thus, the Pamir is currently being pushed against a backstop to the north (Tien Shan), and an eastward motion is hindered by the rigid Tarim Basin. The only possible escape direction left is westwards, into the Tajik Depression.

Although Tarim Basin and Tajik Depression used to be connected prior to the Pamir's northward indentation, they comprise fundamentally different material (*Leith*, 1982; *Yang and Liu*, 2002) and thus show distinct tectonic behavior. The architecture of the Tajik Depression should resemble the basin that has been overridden by the Pamir. The simple fact that this overriding was possible already shows that it must have comprised material distinct from the Tarim Basin. Indeed, a major dividing line between tectonic units may once have existed at the western edge of the Tarim Basin, which might have had a connection to the dextral Talas-Ferghana Fault further north (as suggested by *Sobel*, 1999).

The nature of the Tajik Depression basement, lying beneath up to 12 km of sediment cover, is not well known. *Burtman and Molnar* (1993) summarize Russian literature and active seismic data to conclude that crustal thickness in the Tajik Depression is around 35-40 km in total, implying a basement thickness of 22-30 km, which hints at thinned continental crust. *Leith* (1982) proposes Paleozoic forearc material as the most likely basement composition based on the surrounding rock assemblages and sutures. The surface morphology of the Tajik Depression, which shows westward convex fold belts (*Nikolaev*, 2002), attests to westward displacement of the sedimentary cover, probably by gliding over an evaporite detachment (see below).

Four different scenarios could potentially explain my observations from focal mechanisms, the distribution of stress axes and stress modelling (see Figure 5.23):

1. *En-block westward escape of the northwestern Pamir*
   The observed principal stress axes and focal mechanisms could be indicative of a westward escape motion of a crustal block in the northwest Pamir. Lateral motion of blocks is one

principal mode of how plate convergence can be accommodated in an orogen, and has been shown to be an important mechanism throughout Tibet (*Molnar and Tapponnier*, 1975; *Tapponnier et al.*, 1982, 2001) as well as in the Hindu Kush (*Tapponnier et al.*, 1981). A crustal block delineated by the MPT in the north, the Darvaz Fault in the west and the identified lineament from Lake Karakul to the Wachan corridor in the east (southern boundary unclear) could hence be pushed westward by the ongoing northward indentation of the Pamir.

2. *Gravity-driven outflow of crustal material*
   The rampant topography gradient between Pamir and Tajik Depression could lead to a compensatory outflow of ductile lower crustal material like proposed, on a much larger scale, for eastern Tibet (*Clark and Royden*, 2000). Possible evidence for this "channel flow" in eastern Tibet has been obtained by magnetotelluric studies around the Eastern Himalayan Syntaxis (*Bai et al.*, 2010). Flow of crustal material is apparently restricted to regions of limited crustal strength, whereas strong, rigid basins (like the Tarim) act as obstacles (this is imaged by GPS vectors, see e.g. *Gan et al.*, 2007). However, it is questionable how ductile, deep crustal deformation couples to the shallow, brittle deformation field imaged with surface observations. Nevertheless, this model could potentially explain the asymmetric deformation at the Pamir's edges (see Figures 2.4).

3. *Accommodation of differential motion between Pamir and Tajik Depression*
   The preferred occurrence of left-lateral strike-slip events in the northwestern Pamir could represent distributed accommodation of the relative northward motion of the Pamir with respect to the Tajik Depression. *Mohadjer et al.* (2010) derive a slip rate of 11.4 mm/yr for the Darvaz Fault that separates Tajik Depression and Pamir. However, they do so by evaluating the vectors of a station near Khorog and one at Shaartuz, in southwesternmost Tajikistan. These stations are separated by approximately 250 km, hence the obtained relative motion could occur anywhere between these two stations. Field evidence for slip rates and recent activity of the Darvaz Fault are sparse (*Trifonov*, 1978; *Burtman and Molnar*, 1993), and recent field campaigns came to the interpretation that the Darvaz Fault might be largely inactive today (*L. Gagala, pers. comm., 2012*). This could be corroborated by an absence of major seismicity along its length in the data (see Figure 4.13A). Hence, the accommodation of this relative motion could have jumped from the Darvaz Fault to a more distributed deformation of the whole (north)western Pamir (effecting the focal mechanisms shown in Figure 5.6).

4. *Radial overthrusting of the Pamir over Tajik Depression and Alai Valley*
   Strecker et al. (1995) proposed that the Pamir could, driven by the difference in topography compared to the Tajik Depression, radially overthrust the Tajik Depression. This would lead to compression axes pointing perpendicular to the Pamir's outline along it entire western flank. While exactly this behavior is seen in the northwest, I have no evidence for a similar stress orientation along the remainder of its western flank (Figure 5.6), as not much seismicity can be seen throughout the Afghan Badakhshan. This could, however, be an artifact of the station distribution (Figure 3.1), since there is a lack of stations in Afghanistan. A radially directed overthrusting along the whole western flank of the Pamir could effect a push onto the Tajik Depression's sediment cover, leading to westward slip over the evaporite horizon, effecting the observed fold belts.

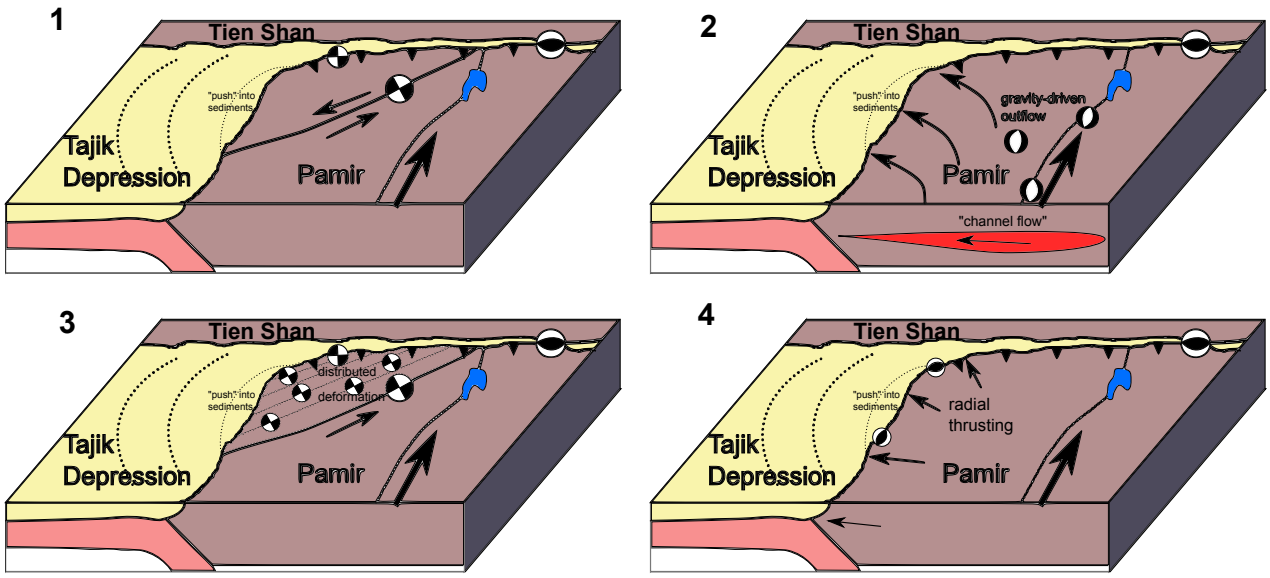

Figure 5.23.: Conceptual models for crustal processes in the northwest Pamir: (1) Block escape into Tajik Depression, (2) Gravity-driven outflow as consequence of lower crustal mass movement, (3) Distributed strike-slip deformation throughout the northwest Pamir to accommodate differential northward movement between Pamir and Tajik Depression, (4) Radial thrusting of the Pamir over its surroundings. For detailed descriptions of the models refer to the text.

Our observations of widely diffuse strike-slip seismicity in the western and northwestern Pamir (Figure 5.6) and incremental rotation of compressive axes in the northwest (Figures 5.7 and 5.22) appears to be not compatible with model 1, where slip should localize on major strike-slip faults (as in the cited examples). No such clear lineaments can be seen in the seismicity data, and digital elevation models as well as field studies attest to their absence. Crustal outflow due to lower crustal channel flow (model 2) should generate shallow east-west oriented normal faulting in the uppermost crust, as observed in Tibet (*Blisniuk et al.*, 2001), not a dominance of strike-slip faulting. However, a superposition of channel flow with a second process could effect the observed patterns. While some extensive mechanisms are observed, no clear prevalence of those, possibly occurring along major rift structures, is discernible. I hence prefer an interpretation that consists of a combination of the models 3 and 4. The western Pamir accommodates northward motion of the orogen relative to the Tajik Depression by diffuse sinistral strike-slip faulting, at the same time radially overthrusts the Tajik Depression and Alai Valley. This creates a westward push against the sedimentary cover of the Tajik Depression as well as reduces the amount of convergence along most of the MPT (except the eastern part). The Darvaz Fault should currently show a diminished or even totally absent sinistral strike-slip componenet of motion, but could exhibit thrust faulting due to radial thrusting.

Horizontal gliding over an evaporite décollement in the Tajik Depression

Obtained P and T axes from single earthquakes (Figure 5.7) as well as from regional stress inversion (Figure 5.22) show principal east-west compression in the Tajik Depression. The best-fit stress

tensor indicates slip along near-horizontal or near-vertical fault planes as the preferred mechanism (Figure 5.18, lower right), which is reflected in the appearance of several focal mechanisms for earthquakes in that region (Figure 5.6).

Throughout the Tajik Depression, paleozoic crystalline basement rocks are overlain by sedimentary cover up to 10-12 km thick in its eastern part (*Nikolaev*, 2002). A Jurassic evaporite horizon of several hundred meters average thickness, separated from the basement by maybe a kilometer of limestones, is thought to underlie the entire Tajik Depression at average depths of 7 to 10 km (*Burtman and Molnar*, 1993; *Nikolaev*, 2002; *Bourgeois et al.*, 1997). This layer is thought to form, due to its weakness, a major basal detachment decoupling the sedimentary cover from the basement (*Nikolaev*, 2002; *Reiter et al.*, 2011).

The centroid depths I obtained for earthquakes with the aforementioned mechanism type (6-9 km) agree well with the assumed position of said detachment, which makes me favor (sub)horizontal slip as the process generating them. Seismic deformation within a salt horizon should, however, not be possible, since evaporites are extremely weak even under shallow crustal conditions. They would hence promote ductile gliding over this basal décollement (*Davis and Engelder*, 1985).

Possibly, these earthquakes occur at a local depletion of the salt décollement, where the shallow sediments are welded to the crystalline basement, allowing stick-slip motion to take place. Such a mechanism was invoked to explain a M_w 6 event in the Kohat Plateau, Pakistan, in 1992, which exhibited a similar mechanism and likewise occurred at a depth comparable to that of an evaporite detachment in this basin (*Satyabala et al.*, 2012). Should this mechanism apply here, the distribution of these "detachment events" in the Tajik Depression would, over time, map patches where the salt horizon is absent. Everywhere else, deformation would occur in the ductile regime. This would imply sediments welded directly to the basement in the area around the city of Kulob and at the northeastern rim of the Tajik Depression, in the fold-and-thrust belt adjacent to the Peter I Range. The three "detachment events" near Kulob fall into an area where *Leith and Simpson* (1986a) identified a concentration of crustal seismicity they attributed to active salt doming (a giant salt dome exists in the vicinity of this city). However, they did not show fault plane solutions or exact hypocentral depths for their events, hence the question whether this observed concentration entirely features events occurring along a locally pinched out salt detachment can not be answered. A local depletion of salt near an active salt dome could be the consequence of salt diapirism (*Schultz-Ela et al.*, 1993), whereby most salt penetrated the sediment cover to form the dome at the surface, leaving a thinned out and possibly discontinuous salt layer at depth behind.

Ridges present throughout the Tajik Depression show a westward convex, arcuate outline (see *Nikolaev*, 2002), vaguely resembling giant glacier tongues. Radial overthrusting of the Pamir over the Tajik Depression could induce east-west compression in the sediment cover, effecting this geometry by introducing horizontal gliding over the décollement as well as internal folding of the sediments. The shape of fold-and-thrust belts in the Garm region does not resemble what would be expected if sediment outflow solely from the Alai Valley into the Tajik Depression would be the origin of these westward convex ridge structures. Moreover, it is unclear how far into the eastward thinning FTBs towards the Alai Valley the salt detachment, on top of which this outflow would have to occur, is present. *Leith and Alvarez* (1985) report its presence in the Vakhsh fold belt, whereas it is apparently absent in the Alai Valley (*Coutand et al.*, 2002). Hence, an outflow of sediments originating from the advancing Pamir front on top of a salt décollement is probably

not a valid model here. The process of radial thrusting invoked above could explain the present morphology as well as observations of Cenozoic counterclockwise block rotations in the Tajik Depression (*Bazhenov*, 1986; *Thomas et al.*, 1994), stronger towards the orogen, from the study of paleomagnetic properties of Red Beds.

The sense of slip of retrieved "detachment event" earthquakes is purely westward in the southeast Tajik Depression and west- to northwestward along the Peter I Range, i.e. roughly perpendicular to the outline of the Pamir Mountains, which is what would be expected from sediment gliding induced by radial overthrusting (as proposed in *Brookfield*, 2001, and shown in Section 5.5.1). Different earthquake mechanisms present within the Tajik Depression (several strike-slip, one normal faulting event, see Figure 5.6) would then attest to active deformation within the sedimentary cover. The exception to this is one event in the southeastern Tajik Depression, just across the border to Afghanistan, which shows horizontal slip with a vergence opposite to the other such events. This earthquake, however, is located at a much greater depth of about 23 km, hence is indicative of deformation within the basement.

Apparent aseismicity of the Main Pamir Thrust

Our observations that large parts of the Main Pamir Thrust (MPT) are apparently aseismic stand in contrast to high GPS-derived convergence rates across it (*Zubovich et al.*, 2010; *Reigber et al.*, 2001; *Mohadjer et al.*, 2010). This discrepancy could be resolved when the MPT is assumed to be currently locked in most of its western part, i.e. accumulating stress to be released in a future earthquake, or if it is currently slipping aseismically. However, GPS stations in the Pamir are sparsely distributed, so that the 10-15 mm/yr given by *Zubovich et al.* (2010) are just a rough estimate, and they were obtained for a profile in the east of the MPT, roughly through where major thrusting activity due to the Nura earthquake and its aftershock sequence can be seen. The historical record of large earthquakes at the northern circumference of the Pamir (see *Burtman and Molnar*, 1993) likewise shows a concentration of major thrust events in this region and considerably less activity further west. *Arrowsmith and Strecker* (1999) obtain an average convergence rate of 6 mm/yr throughout the Holocene for the central MPT from fluvial terrace dating, investigating an area west of the point where the north-south lineament through the Pamir meets the MPT. If one or several of processes 1 to 3 in Figure 5.23 is actually active in the northwestern Pamir, it should reduce north-south convergence across the MPT everywhere but in its easternmost part, where the Nura earthquake and its "predecessors" took place. Hence, it is possible that both the convergence estimates of *Arrowsmith and Strecker* (1999) and the ones from GPS are correct. The apparent higher seismic moment release in the eastern part of the MPT could thus be explained.

However, since my observations only span two years, and even the historical record of earthquakes does not reach back more than 100 years, what is imaged could easily be biased by a longer recurrence interval of large earthquakes in the western part of the MPT. It is entirely possible that the mode of deformation I obtain with two years of data represents the interseismic period of the MPT, when it accumulates stress.

A detailed GPS study of the northern Pamir and the Alai Valley would be necessary to determine the state of the MPT and the precise amount of convergence (i.e. whether there is a discrepany along strike), and whether the fault is currently locked or creeping.

5.5.2. Deep processes

Buoyancy-driven sinking of a possibly broken slab beneath the Hindu Kush

Focal mechanisms in the Hindu Kush uniformly exhibit downdip extension (see e.g. Figures 5.11 and 5.12), which is also reflected in the stress inversion results (Figure 5.19) and confirms the findings of several earlier seismological studies (*Nowroozi*, 1971; *Billington et al.*, 1977; *Roecker et al.*, 1980; *Pegler and Das*, 1998). Downdip extensive focal mechanisms are routinely observed for intermediate-depth earthquakes in oceanic subduction zones (*Isacks and Molnar*, 1969) and are thought to reflect stretching of the slab due to its negative buoyancy. Since I assume that the Hindu Kush slab consists of continental material (Section 4.3.2), which is normally less dense than asthenosphere, a prominent phase change (e.g. eclogitization) that increases the density of the slab material is required to effect the retrieved stress orientation. Eclogitization, however, can only take place in the presence of mafic material that is not routinely associated with continents (*Rudnick and Fountain*, 1995). However, *Hetényi et al.* (2007) have shown active eclogitization ocurring in underthrusted Indian material beneath Tibet, which is likewise of continental origin. This might indicate the presence of mafic material in continental lower crust. Inverted mechanisms (Figure 5.9) imply rupture planes with about 45° inclination, which stand in contrast to the horizontal rupture planes for large Hindu Kush events identified by *Kiser et al.* (2011) with an energy backprojection technique.

Together with the subvertical orientation of the whole seismically active structure in the Hindu Kush, T axis orientations hint at a process of passive sinking of the Hindu Kush slab into the mantle, apparently major horizontal forces are absent in this setting. No mechanisms attesting to an active tearing or contortion process, i.e. principal axes rotated into more horizontal directions in a specific part of the slab, were found, the different planar zones of seismicity possibly representing plate fragments (see Figure 4.14) show no differences in focal mechanisms. Most seismicity occurs below the seismic gap at 150 km depth which might represent a slab break-off, and no significant change of stress axis orientation is discernible across it. In this context, the two events exhibiting shallow dips of T axes directly above this seismic gap are intriguing, but probably not enough to base any interpretation on.

The most vigorous seismicity occurs at depths between 180 and 210 km, and the events with the largest magnitudes seem to focus at the intersection of the curved, southward dipping, isolated plane of western Hindu Kush deep seismicity with the more continuous structure immediately east of it (see Figures 5.9, 4.14 and 4.13). The increased moment release at this depth might hint at pressure and temperature conditions especially favorable for earthquake creation, or maybe represents a local heterogeneity in the slab composition or the stress field.

Active contortion of a sinking slab beneath the Pamir

The state of stress in the Pamir deep seismic zone appears to be fundamentally different from what is observed beneath the Hindu Kush. Here, principal axes orientations show substantially more scatter (Figure 5.17), some of which, however, may derive from higher uncertainties in focal mechanisms (Figure 5.5). The presence of more steeply plunging T axes is confined to regions where the Pamir slab appears discontinuous along strike (subregion 3 in Figure 5.16) and steepens

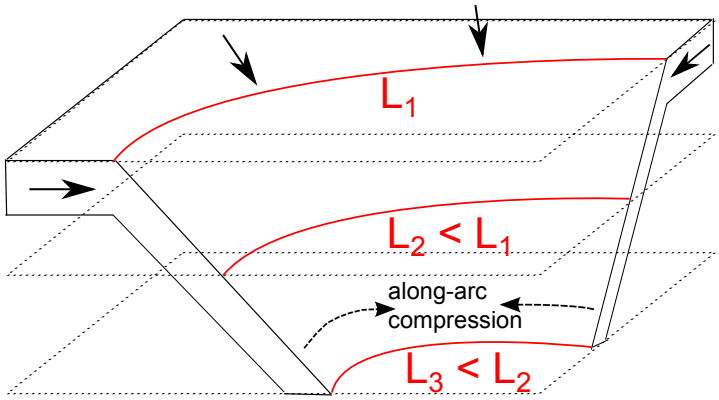

Figure 5.24.: Conceptual sketch visualizing that subduction along a fixed, arcuate hingeline causes along-arc compression at depth, since the contour lines of the slab are shortened.

its dip to become vertical (as can be seen in Figure 4.14, profiles E-E' and F-F') or where the Pamir slab possesses a roughly linear east-west strike and is not bent any more (subregion 2). In areas with an along-strike continuous, arcuate slab, along-arc extension, as already shown by *Fan et al.* (1994) and *Pegler and Das* (1998), dominates (subregion 1). This is reflected in the stress inversion results for these separate subregions (Figure 5.20). The strong contrast to the Hindu Kush, which appears to be entirely dominated by gravity forces, indicates that there is no mechanical coupling between these two slabs at present.

Obtained findings indicate that bending forces effected by the strongly arcuate geometry of the Pamir slab dominate over bouyancy-induced drag forces pulling the whole structure down. Bending forces would be largely absent where the slab is straight or where the slab loses its structural integrity along strike. There are examples of "classical" oceanic subduction zones exhibiting along-arc extension (Aleutians, e.g. *Stauder*, 1968; *Ekström and Engdahl*, 1989; *Creager and Boyd*, 1991) or compression (Hellenic Arc, e.g. *Benetatos et al.*, 2004) in strongly arcuate segments. Apparently, a strongly arcuate slab has horizontally oriented principal stress axes, but their actual orientation (extension or compression along the arc) depends on the presence and amount of hinge rollback. Subduction with a spatially fixed hingepoint in an arcuate geometry would have to effect along-arc compression, since the along-circle length of slab contour lines would diminish with depth (see Figure 5.24). Substantial hinge rollback could overcompensate this tendency, which would lead to along-arc extension as observed for the Pamir slab. The generally steep dip angle of the Pamir slab (about 50° in the upper part) could be explained with gravity-driven rollback. However, such a geometry would not be stable with time, but would eventually lead to a vertically oriented slab tear, propagating from the surface downwards.

Alternatively, if one assumes sheet-like delamination instead of active subduction as the process responsible for the creation of the Pamir slab (see Section 4.3), along-arc extension would be the expected mode of deformation at depth. A continuous layer of constant thickness that delaminates along an arcuate geometry will experience a lengthening of contour lines, i.e. along-arc extension, increasing with depth. This should lead to the eventual development of a vertical tear in the slab, initiating at its lower end and propagating upward. The decrease in seismicity rate and maximum hypocentral depth of earthquakes around 73 °E (visible as gap in Figure 4.13D) could be evidence for such a process.

6. Local earthquake tomography

6.1. Theory and Method

Seismic tomography is an inversion technique to retrieve the 3D subsurface velocity structure of a region from the information contained in seismic waveforms. The still most commonly used tomographic scheme is traveltime tomography (*Aki et al.*, 1977), where the arrival times of body waves or other phases are used to calculate the distribution of P and S-wave velocities (v_p, v_s) and their ratio (v_p/v_s) in the earth.

Stated as a linear inverse problem, seismic tomography can be described by the formula (compare Section 5.1)

$$\vec{d} = \mathbf{G}\vec{m} \tag{6.1}$$

The inherent task is to find, starting from an initial model $\vec{m}_0$, a model $\vec{m}$ (spatial distribution of seismic velocities) that optimally fits the observations $\vec{d}_{obs}$ (body wave travel time residuals). $\mathbf{G}$ is the Jacobian matrix defined below. The residuals contained in $\vec{d}_{obs}$ are the differences between observed (T_{ij}) and calculated (T_{ij}^{cal}) travel times (using model $\vec{m}_0$)

$$r_{ij} = T_{ij} - T_{ij}^{cal} \tag{6.2}$$

However, not travel times but phase arrival times are routinely observed at seismic stations. Those are the sum of the travel times T_{ij}, which can be expressed as line intergrals along the seismic ray path in a slowness field u, and the earthquake origin times τ_i,

$$t_{ij} = T_{ij} + \tau_i = \int_{source}^{receiver} u \; ds + \tau_i \tag{6.3}$$

Both the origin time τ_i and the source-side integration boundary depend on the earthquake location, which again depends on the slowness field, making the problem non-linear. For a velocity model parameterization consisting of L elements (for possible parameterization schemes, see Section 6.1.1), the travel time residual can be linearized to (Taylor expansion, see *Thurber*, 1993)

$$r_{ij} = \sum_{k=1}^{3} \frac{\partial T_{ij}}{\partial x_k} \Delta x_k + \Delta\tau_j + \sum_{l=1}^{L} \frac{\partial T_{ij}}{\partial m_l} \Delta m_l \tag{6.4}$$

The expressions Δx_k, $\Delta\tau_j$ and Δm_l represent the perturbation of earthquake hypocenters, origin times and the velocity model parameters from their values in the original model $\vec{m}_0$. They make up the model vector $\vec{m}$ in equation 6.1, the derivative terms define the Jacobian matrix $\mathbf{G}$ and

the residuals r_{ij} comprise the observation vector $\vec{d}_{obs}$. The linearization performed here allows the formulation of seismic tomography as a linear problem (see Equation 6.1).

Seismic traveltime tomography can be subdivided into three separate problems (*Rawlinson and Sambridge*, 2003): (1) choice of a decent model parameterization, (2) the forward problem of calculating travel times through a heterogeneous velocity model (retrieving T_{ij}^{cal}) and (3) the inverse problem of perturbing the velocity model to better fit the observed travel times. Since the linear representation of a non-linear problem (Equation 6.4) is utilized, several iterations of the two latter steps have to be performed in order to achieve convergence to a optimal model. Local earthquake tomography (*Aki and Lee*, 1976; *Kissling*, 1988) or LET, the technique applied in the following, represents the special case where the utilized earthquake hypocenters lie inside the perturbed velocity model, i.e. a change in the velocity model effects a change in the hypocentral locations of the earthquakes. Hence, unlike for non-global teleseismic tomographic inversion, earthquakes have to be relocated after each inversion step.

The following three sections briefly summarize basic concepts of implementing the aforementioned three basic steps of LET, and show which of the possible approaches are used in the code `simulps` (*Thurber*, 1983, 1993; *Eberhart-Phillips*, 1993; *Evans et al.*, 1994) that was used for tomographic inversion in this study.

6.1.1. Model parameterization

Only a finite number of discrete seismic velocities, which are for local studies usually defined for points or volumes in space, can be inverted for using seismic tomography. At the same time, the solution of the forward problem, which is the calculation of travel times through the velocity model, requires that a continuous velocity field is known. There are a number of different approaches for addressing this discrepancy:

Standard parameterization schemes include the use of constant velocity blocks (as in *Aki et al.*, 1977), the definition of velocity on discrete nodes connected by an interpolation function, definition of cells with constant velocity gradients or the discretization of the problem in the wavenumber domain (for examples for each scheme, refer to *Rawlinson et al.*, 2010). For modern LET schemes, the definition of velocities on grid nodes, together with an interpolation function (e.g. spline functions, see *Sambridge*, 1990; *Michelini and McEvilly*, 1991) that allows the calculation of velocities for arbitrary points between nodes, is probably most common.

`simulps` uses a rectangular grid with variable spacing between rows and columns, and tri-linear interpolation (*Thurber*, 1983) provides velocities between grid nodes:

$$V(x,y,z) = \sum_{i=1}^{2}\sum_{j=1}^{2}\sum_{k=1}^{2} V(x_i,y_j,z_k)\left[\left(1-\left|\frac{x-x_i}{x_2-x_1}\right|\right)\left(1-\left|\frac{y-y_j}{y_2-y_1}\right|\right)\left(1-\left|\frac{z-z_k}{z_2-z_1}\right|\right)\right] \quad (6.5)$$

The velocity at the arbitrary point (x, y, z) is thus calculated from the velocities defined at the eight grid nodes surrounding this point, weighted by their respective distances to the point. For badly resolved regions in the grid, it is possible to link adjacent nodes (*Thurber and Eberhart-Phillips*, 1999), i.e. to coarsen the grid.

6.1.2. Forward problem

The forward problem is defined as the determination of the data vector $\vec{d}$ of Equation 6.1 for a given velocity model, through the calculation of path integrals (Equation 6.3) through a heterogeneous velocity model. With large modern deployments and datasets, the number of travel paths that have to be recalculated in each iteration step can easily exceed 100,000, so that computational efficiency is still an important aspect.

Traditionally, ray tracing methods utilizing the principles of geometrical optics (high-frequency approximation) were used for this task. Approximate ray tracing (*Thurber and Ellsworth*, 1980), which avoids the direct solution of the ray equations implicit in shooting or bending schemes, became popular due to being computationally inexpensive and obtaining a good estimate of the "true" ray for most problems. Recently, the use of direct raytracers or the computation of the whole wavefront on a finite-difference grid (Eikonal solvers, see e.g. *Rawlinson et al.*, 2010) have become more popular due to the fast-growing available computing power.

A combination of an approximate raytracer with a pseudo-bending method (*Um and Thurber*, 1987) is implemented in `simulps`. In a first step, an approximation of the "true" ray is gained by calculating the travel times for a set of circular arcs between source and receiver with different curvatures and takeoff angles, picking the one with the fastest travel time as initial ray estimate (*Thurber*, 1983). Segments of this ray are then iteratively perturbed until it satisfies Fermat's principle within a defined error margin. This scheme has been shown to converge to paths very close to the ones obtained with direct solvers for a variety of test cases (*Um and Thurber*, 1987), but may become inaccurate for ray lengths exceeding 80 km (*Haslinger and Kissling*, 2001). Modifications to the original ray tracing scheme (described in *Schurr et al.*, 2006), implemented in the version of `simulps` that was used in this study, largely compensate this weakness.

6.1.3. Inverse problem

The inverse problem can be described as the search for a best-fitting model $\vec{m}$ in Equation 6.1. Directly solving this equation by inverting $\mathbf{G}$ is only possible in the unlikely case that $\mathbf{G}$ is a square matrix. This would mean that there are precisely as many observations (arrival times) as there are unknowns (grid nodes and station corrections), which is usually not the case. Hence, only an estimate $\vec{m}_{est}$ of the optimal model can be retrieved. A variety of different strategies for finding such an estimate have been used by different authors (for a more detailed description, refer to *Rawlinson and Sambridge*, 2003; *Rawlinson et al.*, 2010):

Backprojection methods, normally used for constant velocity block parameterizations, perturb the model by distributing each retrieved residual along the respective ray path. This can either be done ray path by ray path (Algebraic Reconstruction Technique) or by averaging over all rays (Simultaneous Iterative Reconstruction Technique).

The most commonly applied group of inversion techniques are gradient methods, where the inverse problem is formulated as the minimization of a function consisting of the data residual term and one or several regularization term(s). One gradient method, damped least-squares minimization, will be presented in some detail in the following, since it represents the technique used in this study (implemented in `simulps`).

Both backprojection and gradient methods do not necessarily converge to a global minimum, i.e. the actual best-fit model, which is why the choice of a starting model "close" to the best-fit model (*Kissling et al.*, 1994) is so important. A third group of inversion strategies, global optimization methods, represent the approach of searching the whole model space for a global minimum, e.g. by the use of random processes. Their significant computational expense has, to date, hindered more widespread usage.

The least-squares solution of the tomographic inverse problem (Equation 6.1) is retrieved by minimizing the square length of the residual vector $|\vec{r}| = |\vec{d}_{obs} - \vec{d}_{pre}| = |\vec{d}_{obs} - \mathbf{G}\vec{m}|$, assuming a normal distribution of data errors (*Nolet*, 2008; *Schurr*, 2000). The maximum likelihood solution can be written as (for a derivation, refer to *Rawlinson and Sambridge*, 2003)

$$\vec{m}_{est} = [\mathbf{G}^T\mathbf{C}_d^{-1}\mathbf{G} + \epsilon\mathbf{C}_m^{-1}]^{-1}\mathbf{G}^T\mathbf{C}_d^{-1}\vec{d} \tag{6.6}$$

where the matrices $\mathbf{C}_m$ and $\mathbf{C}_d$ are the *a priori* model and data covariances, which can be defined from standard deviations σ as

$$\mathbf{C}_m = \delta_{ij}(\sigma_m^j)^2 \tag{6.7}$$

$$\mathbf{C}_d = \delta_{ij}(\sigma_d^j)^2 \tag{6.8}$$

if errors in data and model are assumed to be uncorrelated. These *a priori* covariances can be considered weighting matrices for the initial model and the data. Due to a lack of knowledge of these, the covariance matrices are often set to the unity matrix $\mathbf{I}$, which simplifies the so-called stochastic inverse (*Aki et al.*, 1977) written in Equation 6.6 to (*Schurr*, 2000)

$$\vec{m}_{est} = [\mathbf{G}^T\mathbf{G} + \epsilon\mathbf{I}]^{-1}\mathbf{G}^T\vec{d} \tag{6.9}$$

The matrix that now has to be inverted is the multiplication of $\mathbf{G}$ with its transposed, thus has to be square. The ϵ in this equation represents a damping parameter, which regulates the tradeoff between prediction error and solution length and is commonly chosen based on the analysis of a tradeoff curve between data and model variance (*Thurber*, 1993; *Eberhart-Phillips*, 1986), as shown in Section 6.1.4.

`simulps` makes use of the method of parameter separation (*Pavlis and Booker*, 1980) for the inversion procedure, which involves a direct matrix inversion and yields, unlike approximate strategies like LSQR (*Paige and Saunders*, 1982), a full resolution matrix, the use of which will be discussed in Section 6.2.1.

6.1.4. Application

Data selection

The distribution of regional seismicity determined in Chapter 4 is not ideal as input for tomographic inversion, as it is strongly spatially clustered. The goal of setting up the automatized

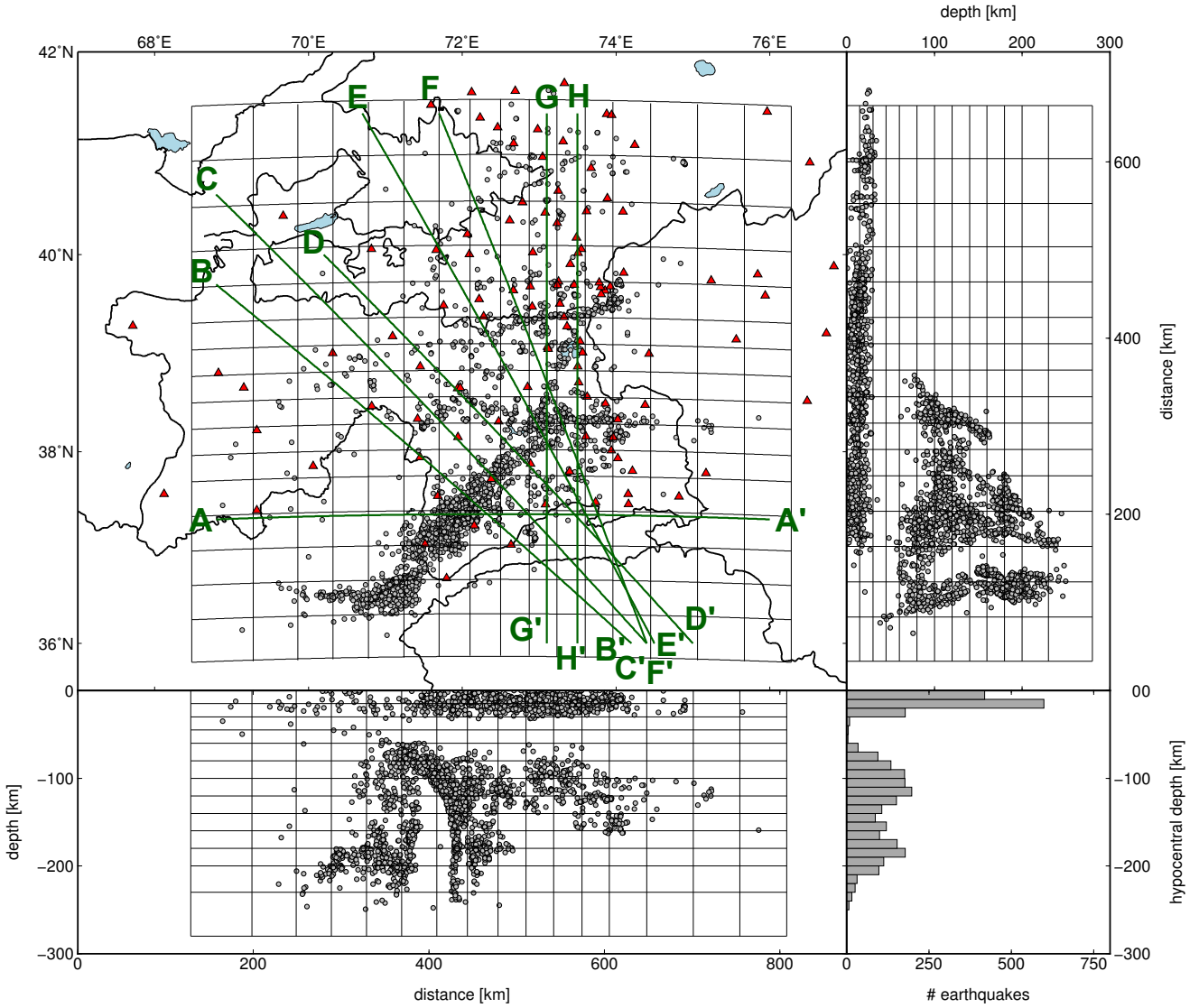

Figure 6.1.: Map view, longitudinal and latitudinal projection of the hypocenters of the utilized dataset and the grid. Horizontal grid spacing is between 30 and 40 km in the central part of the study area, grid cells are larger at its fringes. Vertical spacing is 15 km in the crust and 20 km at mantle depths. Stations whose arrival times were used for the tomographic inversion are shown as red triangles. Whereas shallow hypocenters are distributed over most of the grid area, deep earthquakes are confined to the southern part, which strongly affects ray geometries. Two thirds of all earthquakes in this set occur at mantle depths, one third is crustal (see histogram at lower right). Green lines mark the profiles shown in Figures 6.18, 6.19 and E.1.

picking and event location chain described there was to obtain a highly complete earthquake catalog in order to be able to meaningfully interpret imaged structures. Seismicity in this catalog clearly is inhomogeneously distributed in space, featuring prominent earthquake clusters and large quiescent regions. For tomography, however, an evenly distributed set of earthquakes is desirable.

The wealth of available travel times allows for discarding a substantial amount of events without suffering from a scarcity of phase picks. Hence, a data selection procedure was applied in order to eliminate redundant information (declustering), and limit the total size of the data set.

First, P and $(S - P)$ phase arrivals with quality class 3 were removed from the data set, since the picking uncertainties for this class has been shown to be significantly higher than its nominal values (see Table 4.1). In order to retain a manageable grid size, some of the more distant stations shown in Figure 3.1 were not used (see Figure 6.1).

The rejection of all data with an azimuthal gap of >180° is widespread in LET studies (e.g. *Haslinger et al.*, 1999; *Husen et al.*, 2000; *Arroyo et al.*, 2009), since hypocenters outside the seismic network are generally thought to be less well defined (*Kissling*, 1988). However, the dogmatic use of this gap criterion has been shown to not always represent the optimal strategy (*Koulakov*, 2009). For this experiment, a large and important part of the seismicity (Hindu Kush) is located outside of the network, thus would be left out with a strict application of this gap criterion. The sharpness of retrieved structures outlined by the Hindu Kush hypocenters (see Figures 4.13 and 4.14) implies that event locations there are well defined despite being located outside the network. We hence relaxed the gap criterion to only exclude events with an azimuthal gap >240°.

Next, a target number N of earthquakes for each grid cell was defined, and an algorithm was set up that chooses the N "best" events if the grid cell contains more, or simply takes what there is if it contains less. This choice was based on cumulative sums, as defined in Section 4.1.3, adapted to not count class 3 picks and only incorporate arrivals at stations finally used for the inversion. A minimum cumulative sum (both total and for S) was defined below which events were always rejected, thus enforcing a minimum quality standard for inversion events. This approach provided a well-balanced distribution of earthquakes for shallow events, which are widely distributed throughout the study region (see Figure 4.13A), but only led to a selection of comparatively few intermediate-depth events. The reason for this is their tight spatial clustering, so they only occupy a small number of grid cells, whereas most other deep cells do not contain any events. Since most of the volume I seek to illuminate in terms of seismic velocities has to be covered by rays coming from deep earthquakes, a proportion of two thirds of the total amount of events were forced to be deep (i.e. hypocentral depth >50 km). Finally, handpicks from a study by *Feld* (2011), in which crustal tectonics around the Ferghana Basin are investigated, were added to get a better coverage of the northern part of the study area. The spatial distribution of selected earthquakes, together with the utilized stations, can be seen in Figure 6.1.

In total, 56,229 P and 25,221 S phase arrivals from 3,299 earthquakes, recorded at 110 stations, were used for tomographic inversion, the distribution of utilized arrivals between the stations is shown in Figure 6.2.

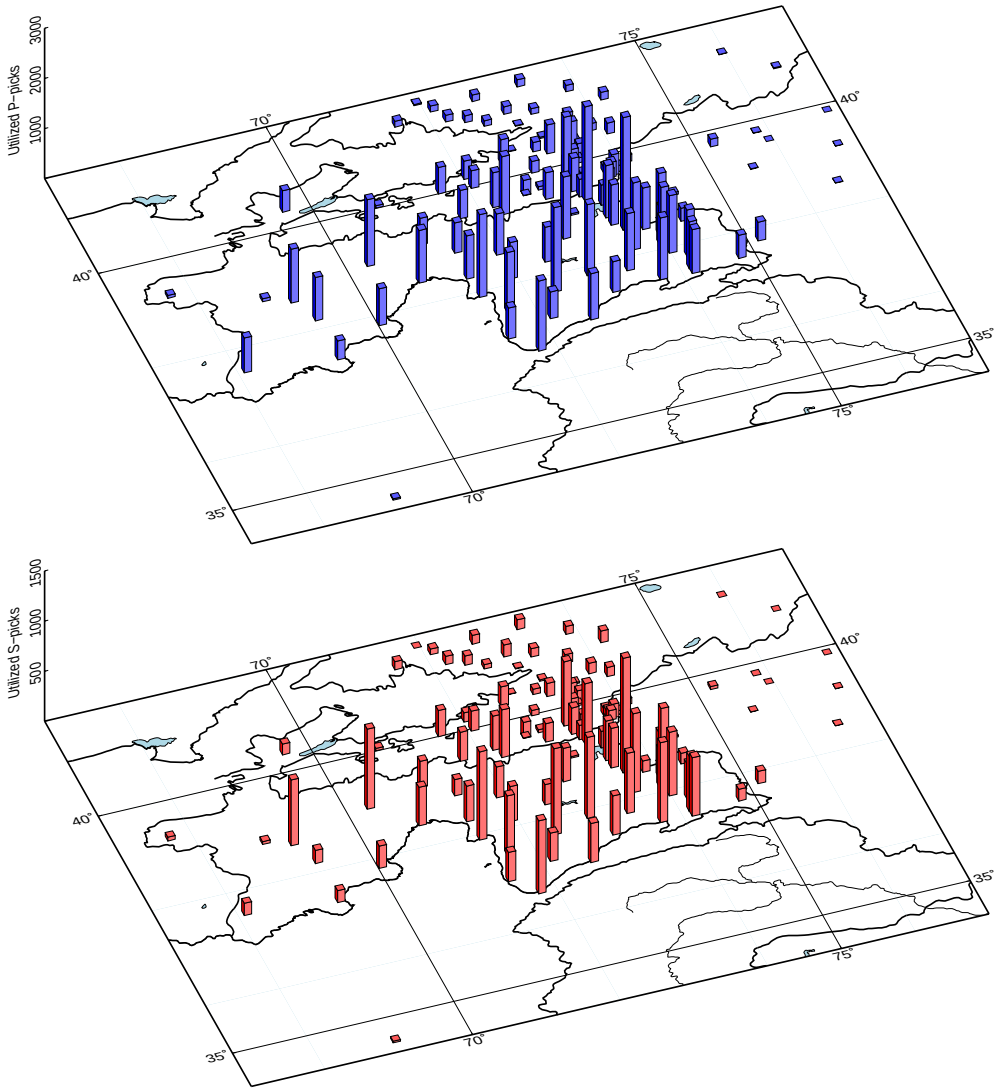

Figure 6.2.: 3D histograms showing the distribution of utilized P (blue) and S (red) arrival picks among the different stations.

Choice of grid

The grid on which the tomographic inversion was performed is shown in Figure 6.1. It features a horizontal node spacing of 30-40 km in most parts of the study region, reflecting the density of stations and earthquakes. Grid cell sizes increase at the fringes of the study area. At depth, nodes are 15 km apart for the first 60 km (crust), then have a spacing of 20 km throughout most of the imaged mantle depths.

This choice of grid parameterization was obtained by trying to somewhat balance ray coverage, i.e. achieve comparable values of derivative weight sum (DWS, see *Toomey and Foulger*, 1989; *Thurber and Eberhart-Phillips*, 1999), a measure of ray coverage that is defined as

$$DWS_j = \sum_{i=1}^{N} \sum_{l=1}^{L} \frac{\partial T_{ij}}{\partial m_l} \tag{6.10}$$

and can be seen as count of rays travelling through each cell weighted by the (relative) distance the ray traverses inside this cell, throughout the studied region. Even though DWS gives no indication about the variety in orientation of the different rays (cross-firing), it provides a more meaningful tool for evaluating the distribution of ray coverage than a simple hitcount does.

The utilized grid obviously pre-defines the maximum spatial resolution that can be achieved in this study. Depending on their velocity contrast with the surroundings, small-scale heterogeneities (few km) can normally not be resolved, but major tectonic structures in crust and mantle should robustly be retrieved with the chosen parameterization.

Starting model and v_p/v_s inversion

The definition of an appropriate initial velocity model to be perturbed in the course of tomographic inversion marks an important choice with possibly large influence on solution quality. As mentioned in Section 6.1.3, there is no guarantee that the least-squares minimization method converges to the global minimum, i.e. the model that optimally fits the data, instead of only obtaining a local minimum. Hence, a starting model "close" to the true model is an important prerequisite for a successful inversion process (*Kissling et al.*, 1994). I chose the minimum 1D P-velocity model determined in Section 4.1.4, which should constitute an average over the 3D structure of the study region, as starting model for v_p inversion.

Due to the routinely higher uncertainty of S arrival times, tomography studies generally utilize a smaller number of S picks (here: about half as much, see numbers above) with larger uncertainties compared to P arrivals. Hence, the resolution capability when inverting for S velocity is reduced, necessitating a coarser inversion grid. Instead of choosing this approach, v_p/v_s is directly inverted for in `simulps`, and the v_s model is derived from the result. The inherent uncertainty and expected variations in v_p/v_s are smaller than for v_s, making the inversion on the same grid as for v_p possible.

Input parameters for v_p/v_s inversion are $(S-P)$ travel time differences that were calculated from the P and S arrivals. We chose the conservative approach of assigning the lesser quality class between P and S picks to the $(S-P)$ differential arrival times.

`simulps` was applied to invert for v_p and v_p/v_s in a two-step procedure, i.e. first finding a best-fit P velocity model while keeping v_p/v_s fixed, then inverting for v_p/v_s in a second step, whereby v_p was kept fixed at the model determined in step one. The initial model here was a homogeneous half-space with $v_p/v_s = 1.74$, as determined from a Wadati diagram. This approach was chosen because it showed overall better stability and data fit than a simultaneous inversion, which can suffer from tradeoffs between v_p and v_p/v_s models.

Damping

The choice of the damping parameter ϵ in Equation 6.9 greatly influences the roughness of the resulting velocity model. While a too low ϵ (underdamped model) will lead to a rough model since data noise is fitted by model adjustments, too high damping effects an overly smooth model which does not fit well to the observed data. A tradeoff curve or L curve (*Eberhart-Phillips*, 1986), where data variance is plotted against model variance for different values of ϵ, is routinely

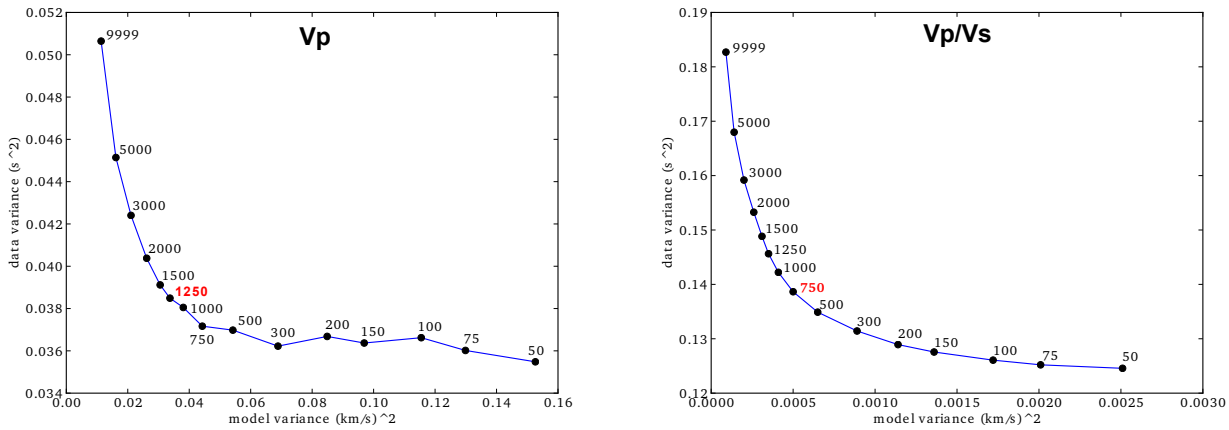

Figure 6.3.: Tradeoff curves for the determination of the optimal damping parameter ϵ for v_p (left) and v_p/v_s (right) inversion, computed for the fifth iteration step.

used to evaluate the optimal damping parameter, which should yield low data variance with still moderate model variance (i.e. lie in the "bow" of the L). Tradeoff curves for v_p and v_p/v_s inversion, computed for the fifth iteration step (as in *Schurr*, 2000), are shown in Figure 6.3, where the values that were finally chosen are indicated.

6.2. Resolution estimates and tests

The assessment of resolution capability is an important part of seismic tomography. Smearing of anomalies due to unfavorable ray geometry or the mapping of travel time residuals into sparsely illuminated regions can severely contort a tomographically retrieved velocity model. In order to interpret observed anomalies, a measure of their robustness and reliability is essential. There are two principal avenues towards an assessment of the spatial distribution of resolution capability, the direct evaluation of the resolution matrix and testing the retrieval of synthetic anomalies. Both of these will be applied in the following.

6.2.1. Direct estimation of resolution - RDEs and Spread

Using Equations 6.9 and 6.1, I can write

$$\vec{m}_{est} = [\mathbf{G}^T\mathbf{G} + \epsilon\mathbf{I}]^{-1}\mathbf{G}^T\vec{d} = [\mathbf{G}^T\mathbf{G} + \epsilon\mathbf{I}]^{-1}\mathbf{G}^T[\mathbf{G}\vec{m}_{true}] = \mathbf{R}_m\vec{m}_{true} \tag{6.11}$$

where $\mathbf{R}_m$ is the model resolution matrix that relates the solution model for the forward problem, $\vec{m}_{true}$, to the estimated model $\vec{m}_{est}$.

The resolution matrix $\mathbf{R}_m$ is an $m \times m$ matrix, where m is the number of parameters in the model, each of its rows represents the "averaging vector" for one inverted parameter (i.e. one velocity value on a grid node), which contains the relative contributions of all inversion parameters (grid nodes and station corrections) to the row parameter. Ideally, all off-diagonal elements of the

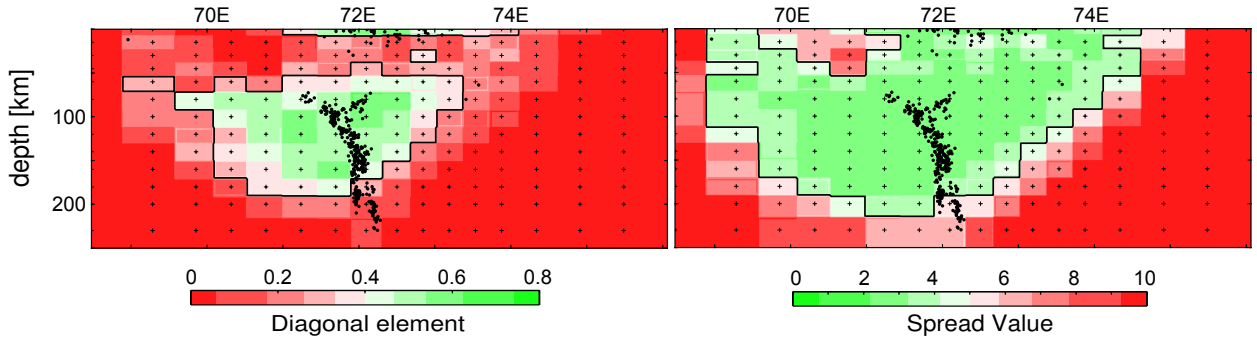

Figure 6.4.: Spatial distribution of RDE (left) and spread (right) values for an example cross section. Here, a significant number of grid nodes show low RDE but still acceptable spread values. This means that they show some smearing, which is, however, spatially tightly confined. The chosen critical values for spread and RDE (refer to the text for further information), the former of which is utilized in the results (see contour lines in Figures 6.14 to 6.19), are indicated by the heavy black contour lines.

resolution matrix would be zero, so that each inversion parameter were completely independent of all the others.

Detailed analysis of the averaging vector, by imaging the spatial distribution of the contributing nodes (e.g. *Toomey and Foulger*, 1989; *Husen et al.*, 2000), would yield the best attainable information about actual resolution capability, but is hardly feasible if nearly 9,000 parameters are inverted for (as in this study). Hence, it is necessary to reduce the averaging vector to scalar quantities whose distribution in space can be imaged along the same projections as the retrieved models.

One set of scalar quantities that can be used in such a way are the diagonal elements of the resolution matrix (Resolution Diagonal Elements or RDEs). Imaging RDEs reduces the provided information to the height of the central peak of the averaging vector. High RDE values indicate well resolved nodes, since they imply that the inverted parameter is highly independent.

The spread value (*Michelini and McEvilly*, 1991) quantifies the amount of smearing, i.e. the contributions of the non-diagonal elements of the resolution matrix weighted by their distance from the respective grid node. It is defined as

$$S_j = \log\left[||r_j||^{-1} \sum_{k=1}^{L} \left(\frac{r_{kj}}{||r_j||}\right)^2 D_{jk}\right] \tag{6.12}$$

where $||r_j||$ denotes the total length of the averaging vector, r_{kj} represents an off-diagonal element from a node separated from r_{jj} (the node for which the spread value is calculated) by D_{jk} km. Small spread values mean that the node is well resolved, in the sense that the relative contributions of off-diagonal elements are small and come from nearby nodes.

Both of these parameters, however, are greatly influenced by the chosen damping parameter and also by the model parameterization, i.e. grid node spacing (*Eberhart-Phillips and Reyners*, 1997). Hence, the definition of a critical spread or RDE value by comparison with other studies is not possible. Based on the computation of plots visualizing the spatial distribution of spread and

RDEs (see example in Figure 6.4), I finally chose the spread value to be more representative of resolving power, and defined critical values of spread for v_p and v_p/v_s inversion that will be used in the visualization of the obtained inversion results (heavy black contour lines). This choice, always somewhat arbitrary, was also guided by the resolution estimates obtained from synthetic tests (see Section 6.2.2).

6.2.2. Synthetic tests

The ability of the travel time data, together with the chosen set of parameters, to resolve subsurface structures is assessed with synthetic tests, where the retrieval of an artificial "true" velocity model is attempted (*Kissling*, 1988). For this purpose, the existing set of stations and earthquakes is kept, with earthquake locations spatially fixed, and travel times are recalculated by ray tracing through the synthetic input velocity model. Gaussian noise is added to these synthetic picks, the standard deviation of the normal distribution is set to the nominal uncertainties of the respective pick quality classes (see Table 4.1), in order to simulate the noise content of the data. Starting from the minimum 1D model (see Section 4.1.4), a tomographic inversion using these data is performed, and the result is compared to the input model.

The probably most widely used synthetic test is the checkerboard test, where the input model features alternating high- and low-velocity anomalies, usually of the size of a grid cell. The advantage of this setup is that it can image resolution or the lack thereof for the whole grid area, since amplitude and size of anomalies are the same everywhere. However, it has been shown that, rather counterintuitively, the good retrieval of small structures does not mean that larger structures likewise have to be well resolved (*Lévěque et al.*, 1993). Hence, it has become common practice to try out anomalies resembling the imaged structures. Since the utilized data set is rather large, a third type of test was performed in order to evaluate the importance of data selection for the obtained results. In this "odd-even test", to arbitrarily chosen halves of the dataset (events with odd and even numbers) are inverted separately, and results are compared. Highly different inversion results for the two subsets imply that anomalies critically depend on few earthquakes, whereas highly similar images attest to some robustness with respect to event selection.

Checkerboard test

Results of the checkerboard test for retrieving synthetic patterns of v_p and v_p/v_s are shown in Figures 6.5 and 6.6, respectively. Velocity (or ratio) variations of $\pm 15\%$ were alternatingly superposed onto the grid nodes of the 1D starting model. Depth sections for v_p (Figure 6.5) show good resolution throughout the Pamir for crustal depths, with somewhat less well-constrained areas in the northwest and southwest Pamir at upper and lower crustal depths, respectively. Significant smearing can be detected for the Tajik Depression and the northernmost part of the study area (southern Tien Shan and Ferghana Valley), where the majority of incoming rays are (sub)parallel. At mantle depths, well-resolved areas are confined to the vicinity of intermediate-depth seismicity, which is a consequence of ray geometry. Amplitudes of retrieved anomalies are generally lower than in the input model, which is a common feature of seismic tomography.

For v_p/v_s, the checkerboard test shows a generally weak ability to reconstruct such small-scale features. Only in the upper crust and in the direct vicinity of mantle earthquakes, the input

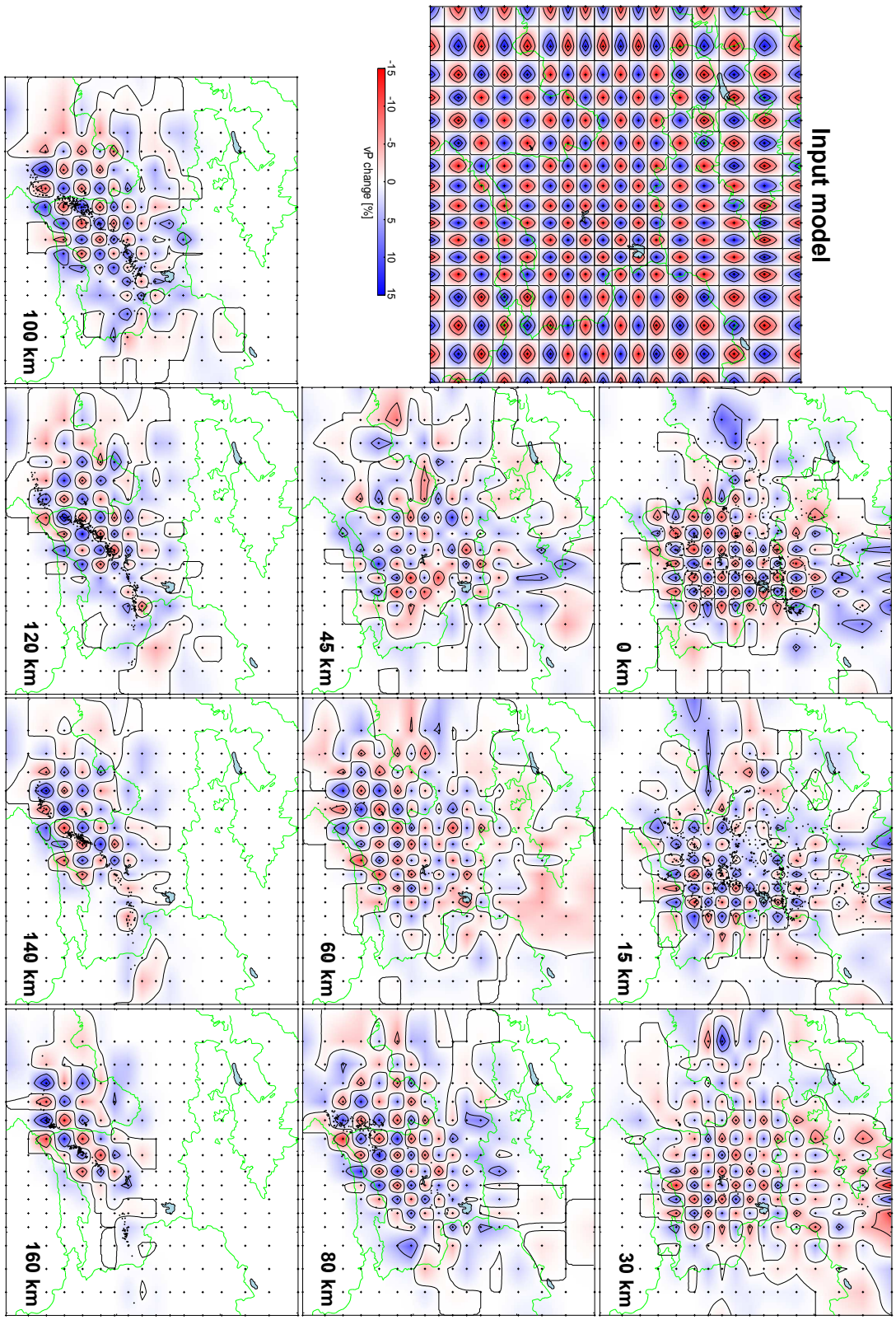

Figure 6.5.: Results of checkerboard test for v_p inversion. Reconstructions of synthetic input model (see left) are shown for different depth levels. Note that the sign of the anomaly at each node alternates in depth.

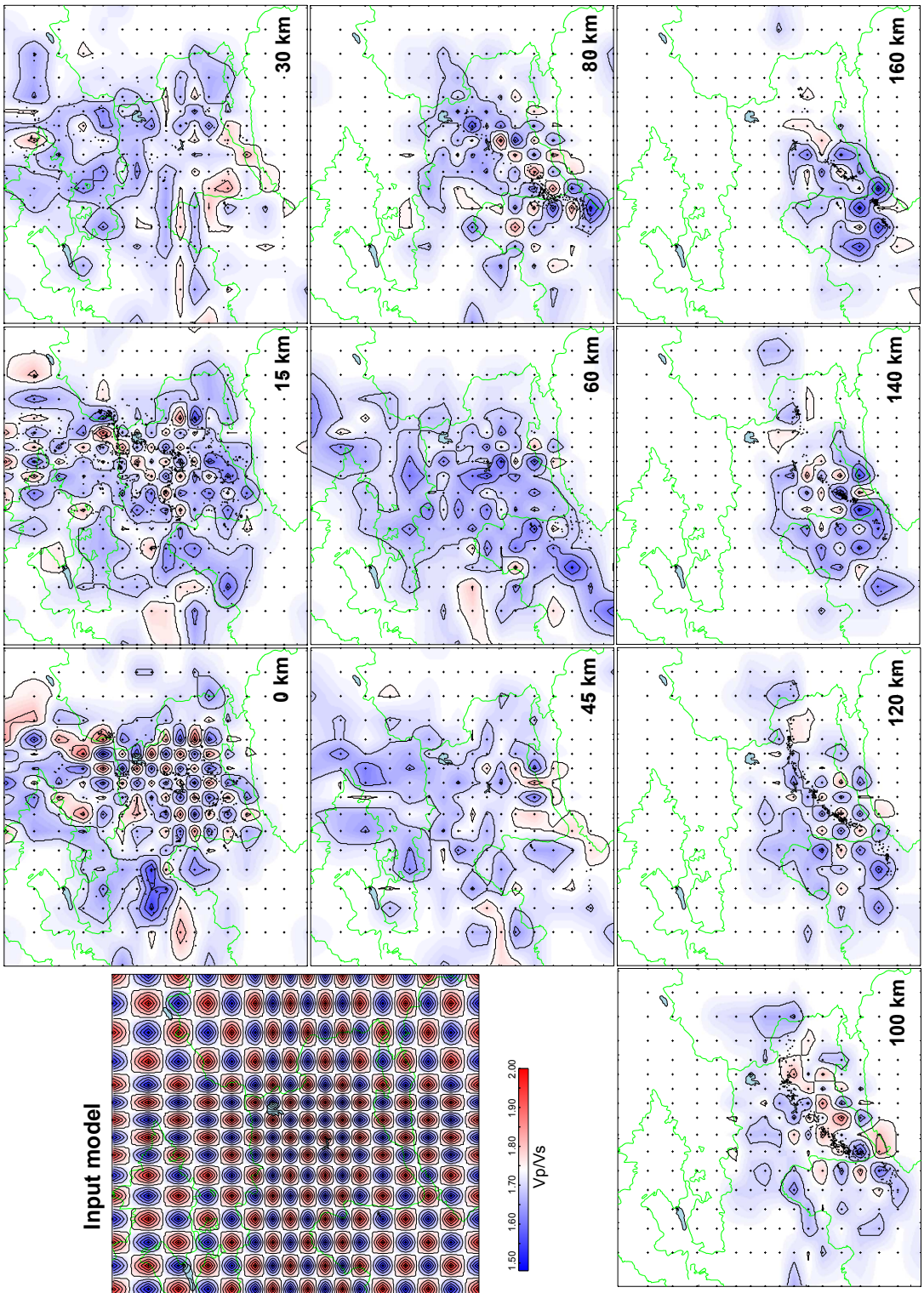

Figure 6.6.: Results of checkerboard test for v_p/v_s inversion. Reconstructions of synthetic input model (see left) are shown for different depth levels. Note that the sign of the anomaly at each node alternates with depth.

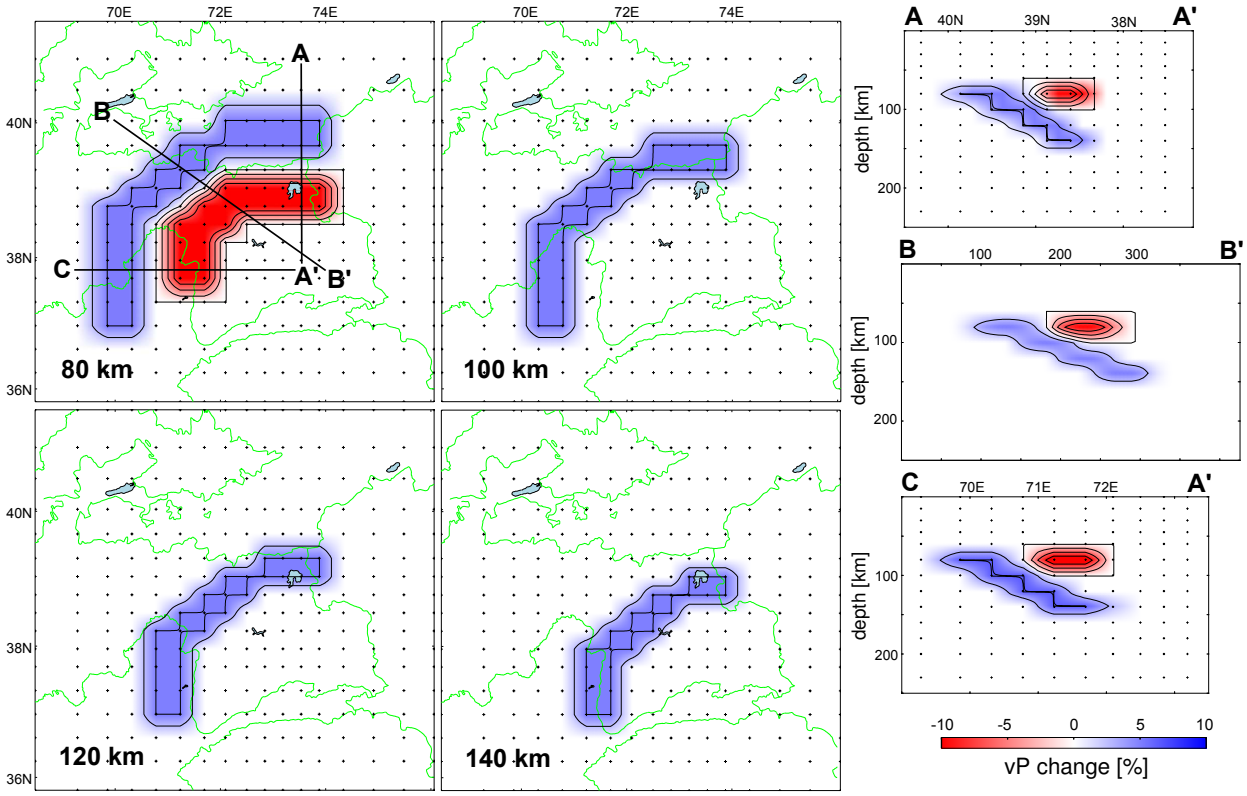

Figure 6.7.: Input model for v_p synthetic test, featuring a strong (-10%) low-velocity anomaly at 80 km depth and a fast (+5%) arcuate slab roughly resembling the Pamir slab of Figure 4.15.

anomalies can be retrieved, and they show severely decreased amplitudes. At lower crustal depths, structures of this scale can not be resolved at all.

Synthetic block structures

The retrieval of larger-scale synthetic anomalies, roughly representing observations shown in Section 6.3, is validated with synthetic test scenarios. For the v_p test, a subducting slab with high velocities (+5%) featuring a geometry resembling what is deduced from the earthquake locations (Figure 4.15) is used as input model, together with a strong (-10%) low-velocity anomaly at 80 km depth, right above the slab (see Figure 6.7). This geometry is robustly retrieved (Figure 6.8), smearing of the anomalies is weak and no major artifacts are produced by this geometric setting. Recovered amplitudes of the anomalies are nearly as high as the input model in the western Pamir (cross section B-B' in Figure 6.8), whereas they are significantly decreased further east. In the eastern Pamir, the high-velocity slab can not be retrieved at depth in excess of 120 km (cross section A-A').

The same type of test is carried out for the v_p/v_s inversion, where a different input model geometry is used. A layer of low values (1.63) at 0 km, underlain by high values (1.85) at depths of 30 and 45 km is introduced throughout the eastern Pamir. Additionally, a high-v_p/v_s anomaly is assumed at the position of the low-velocity anomaly in the v_p synthetic test. Results confirm the findings

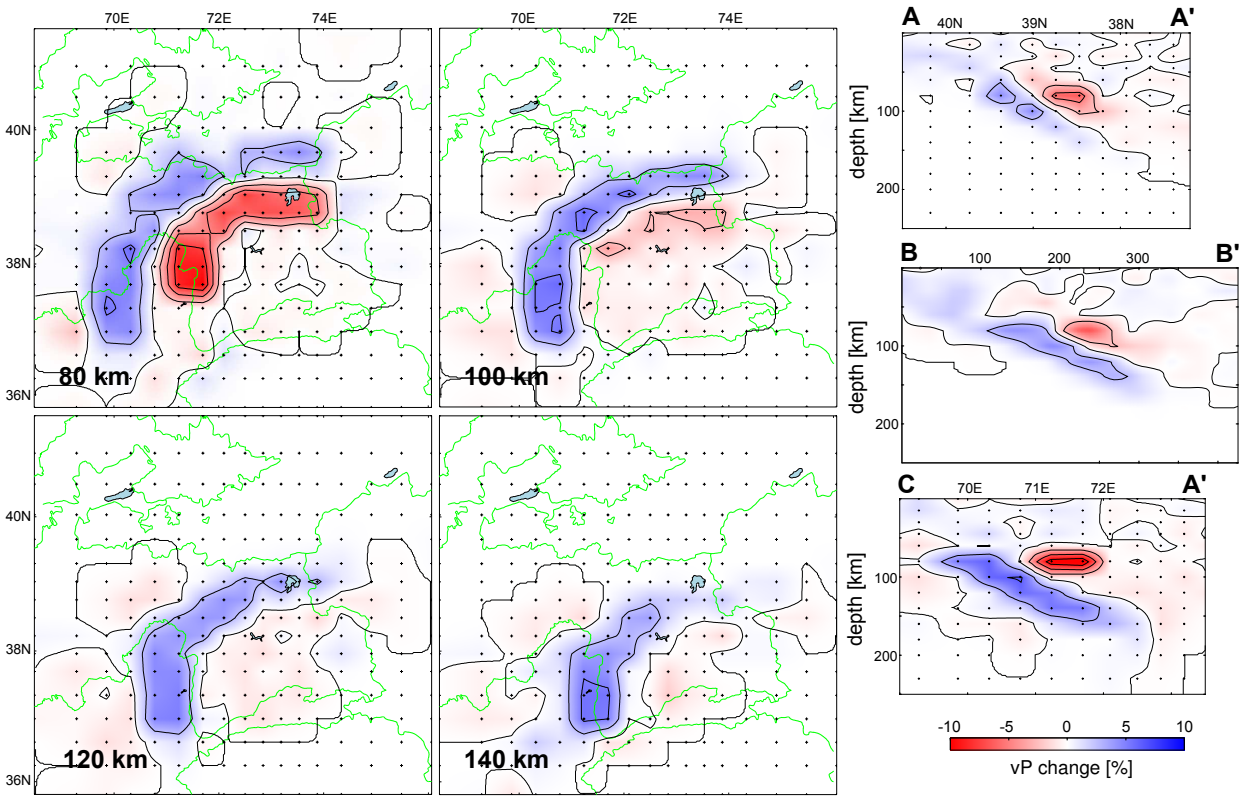

Figure 6.8.: Output of v_p synthetic test: overall, input anomalies from Figure 6.7 are well retrieved, some lack of resolving power is observed for the eastern Pamir at depths exceeding 120 km. Observed depth smearing is generally rather weak, amplitudes of anomalies are reduced by the tomographic inversion, in the east more than in the west. For the location of the three profile lines, refer to Figure 6.7.

of the checkerboard test (Figure 6.6): the anomaly in the shallow crust is robustly retrieved, without any depth smearing or amplitude decrease. Structures in the lower crust and upper mantle, however, experience significant smearing, both laterally and to greater depths. Only in the western Pamir, some resolving power at depth can be seen. Note, however, that no smearing of the lower crustal high-v_p/v_s values to the layer of nodes at 15 km depth occurs. Obtained test results imply that v_p/v_s anomalies not situated in the upper crust or near the mantle-depth earthquakes have to be very carefully interpreted.

Odd/even test

Results of the odd/even test are shown in Figures 6.11 and 6.12. v_p inversion using the two subsets yields highly similar results, all major anomalies are consistently retrieved, minor differences only exist for their detailed shape or amplitudes. The only exception to this is the westernmost part of the shallow depth cut (Tajik Depression), where high velocities are obtained with the odd-numbered events only. Due to the very limited number of events in this part of the study area (see Figure 4.10), the selection or non-selection of a small number of earthquakes there can make a big difference in the obtained inversion results. For v_p/v_s inversion, odd and even-numbered events yield comparable values throughout the shallow Pamir, but they show some differences

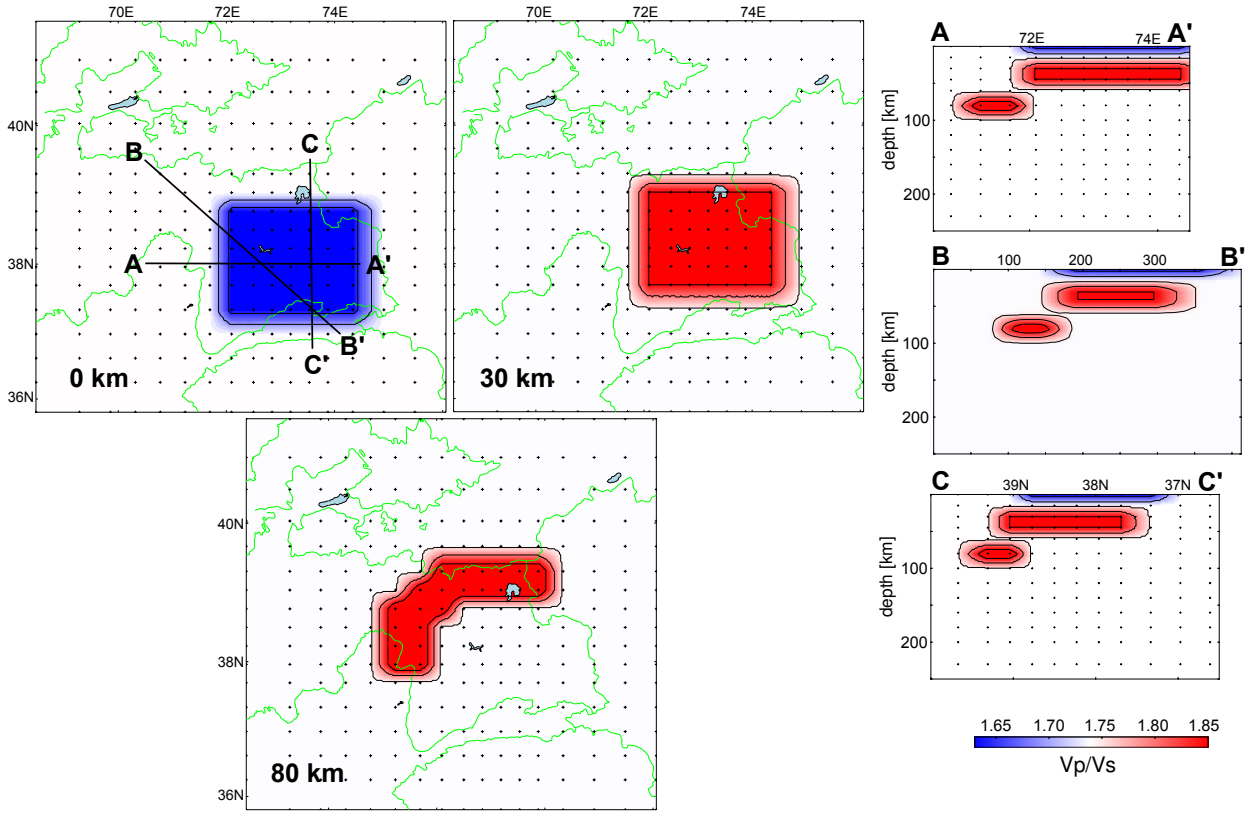

Figure 6.9.: Input model for v_p/v_s synthetic test, with anomalously low values in the uppermost crust of the eastern Pamir, underlain by a middle to lower crustal high-v_p/v_s anomaly. An L-shaped zone of high v_p/v_s was introduced in the upper mantle, at a depth of 80 km.

north of this. The prominent anomaly featuring high v_p/v_s values in the Garm region is only retrieved with the odd-numbered subset of data. At mantle depth, obtained v_p/v_s distributions appear to first order similar.

6.3. Results

The reduction of travel time residuals for the inverted 3D models compared to the 1D starting model (see Figure 6.13) indicates that models well expressing the structural information contained in the travel time data have been found. For both P and (S-P) arrivals, a high scatter in travel time residuals is observed for the 1D model, which clearly shows that this rough average model does not well represent the structural heterogeneity of the region (as argued in Section 4.1.4). With the 3D model, residuals lowered dramatically (93.8% variance decrease for P, 70.0% for (S-P) arrivals), their distributions are centered around zero, significantly narrower than for the 1D case, and exhibit less skew (i.e. are more symmetric around zero) than in the starting model.

Obtained velocity distributions are shown as map view sections of v_p perturbations (Figures 6.14 and 6.15) and absolute v_p/v_s (Figures 6.16 and 6.17) and a series of cross sections of absolute v_p (Figure 6.18) and v_p/v_s (Figure 6.19). As the provenance of material, i.e. whether it belongs

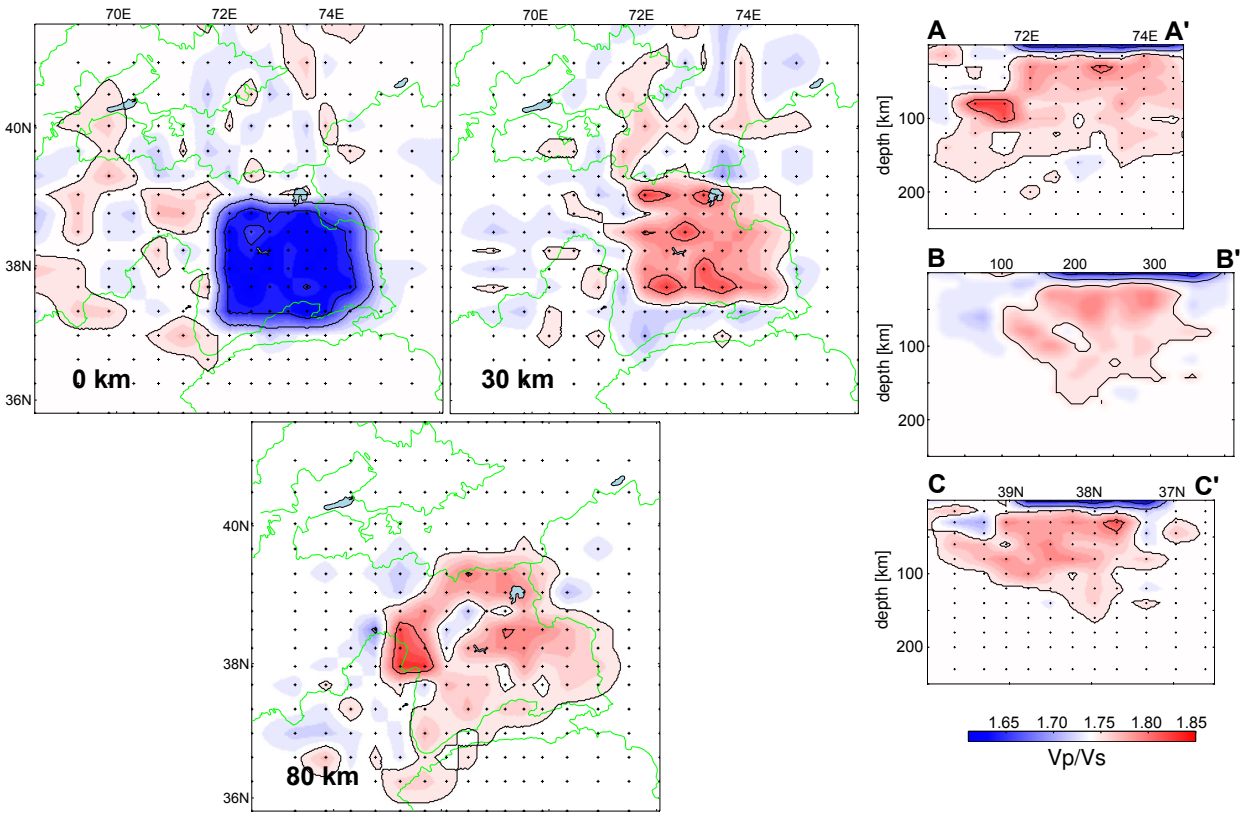

Figure 6.10.: Output of synthetic test for v_p/v_s: Only the low-v_p/v_s anomaly in the uppermost crust is decently retrieved, without smearing and amplitude decrease. Anomalies in lower crust and upper mantle are smeared significantly, to the degree that their original placement is hard to infer.

to the crust or mantle, will play a key role in the interpretation of obtained structures, I chose to image absolute v_p and not perturbations from the background model in the cross sections. Profiles of relative v_p can be found in Appendix E, both relative and absolute velocities will be discussed.

6.3.1. Crustal depths

In the uppermost crust, P wavespeeds slightly faster than the starting model (Figure 4.2), i.e. around 6 km/s, in combination with low values of v_p/v_s (<1.70), are observed throughout the Pamir. The Pamir orogen is outlined by the transition to significantly lower velocities in the surrounding sedimentary basins (Tajik Depression, Ferghana Valley, Alai Valley), where v_p values as low as 5.0 km/s are observed. The basins feature systematically higher v_p/v_s ratios than the Pamir. The Alai Valley appears exaggerated in size and slightly shifted northward, which is probably due to the utilized node spacing and the fact that a large number of stations were situated inside it. Like the Pamir, the Southern Tien Shan shows v_p values of slightly above 6 km/s and rather low v_p/v_s ratios, whereas parts of the Gissar Range show rather low P wavespeeds (however, the latter is rather badly resolved).

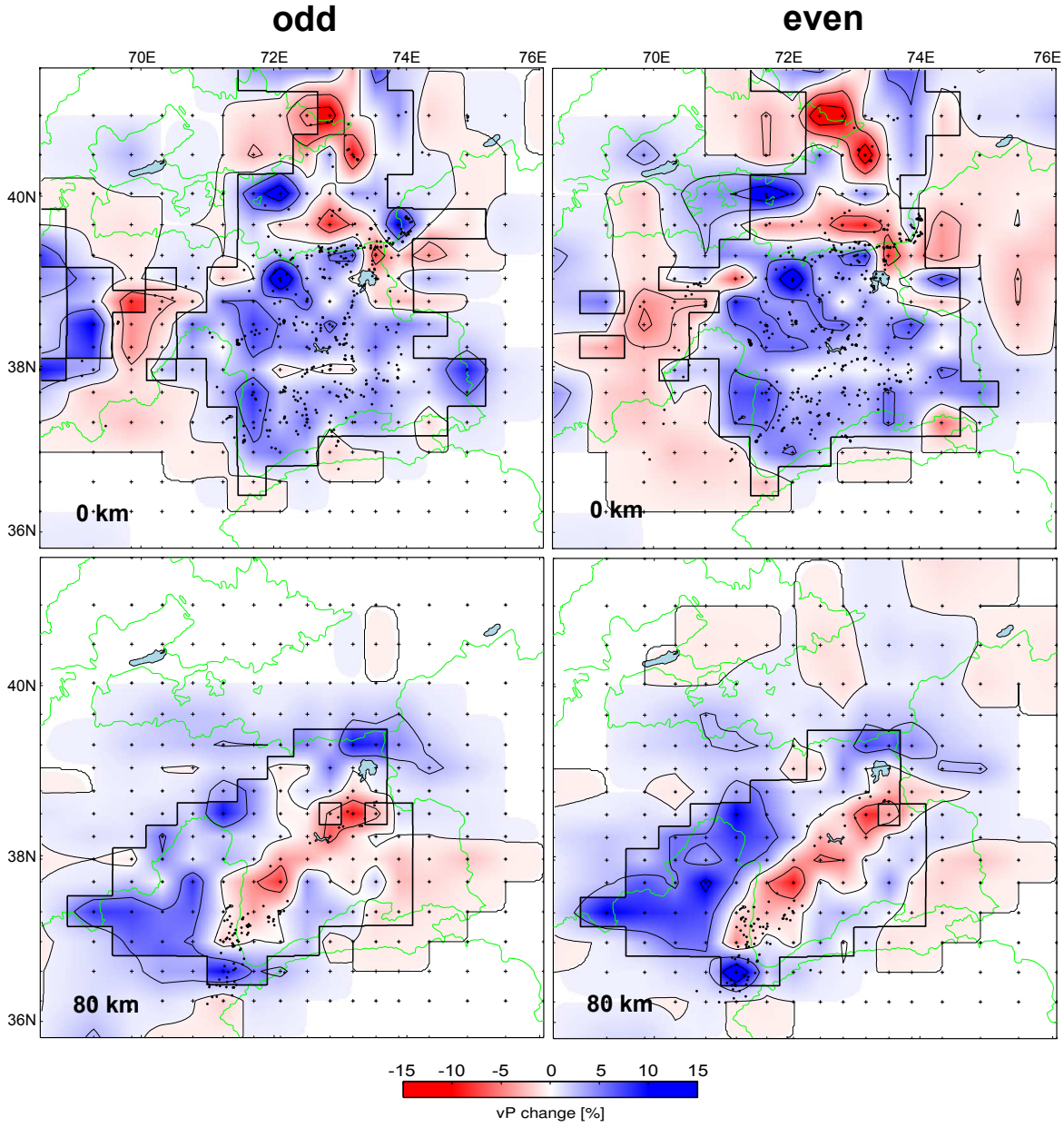

Figure 6.11.: Results of the odd/even test: Two depth cuts of separate v_p inversions using only the odd-numbered or even-numbered events in the original data set. Retrieved anomalies differ in detail, but their general pattern is consistently retrieved.

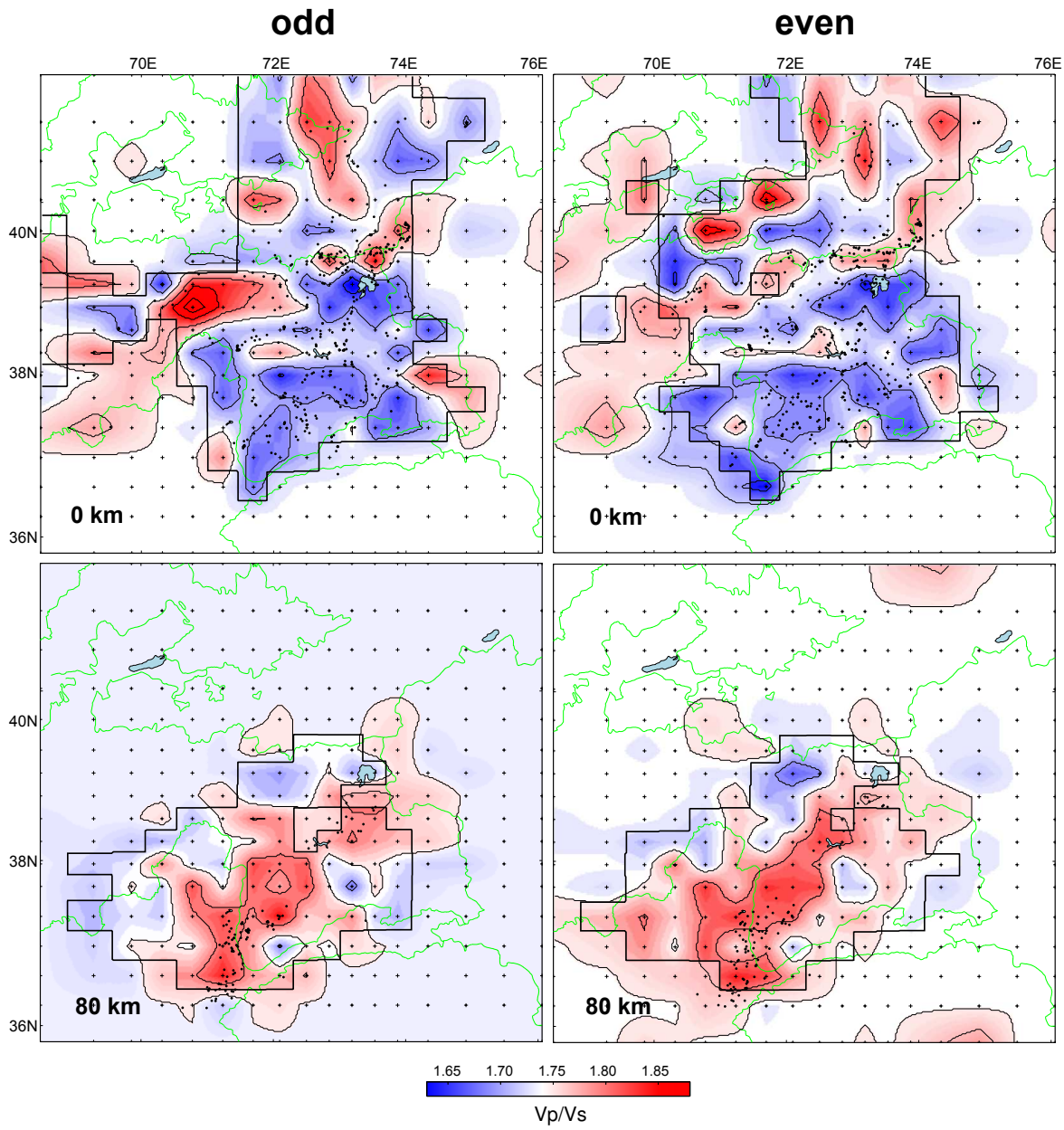

Figure 6.12.: Results of the odd/even test for v_p/v_s

Beginning at 15 km depth, a north-south division of the Pamir is discernible, with lower P velocities dominating the southern part, in contrast to a faster northern Pamir. A middle crustal low-velocity zone is observed throughout the Pamir's south, with v_p as low as 5.6-5.7 km/s (Figure 6.18). Crustal seismicity appears to be confined to depths above its upper end. No systematic north-south differences in v_p/v_s mirroring the observed v_p separation of the Pamir are found, low values (<1.70) prevail at 15 km depth, whereas generally higher values of slightly above 1.75 are observed from a depth of 30 km downwards. As shown in the synthetic test (Figure 6.10), significant smearing of v_p/v_s at lower crustal depths is observed. However, the test likewise shows that no upward smearing occurs, and low v_p/v_s values in the uppermost crust are not smeared downwards. Hence, the general observation of low v_p/v_s in 15 km depth as well as the presence of higher values at middle to lower crustal depths should be robust, although true values could

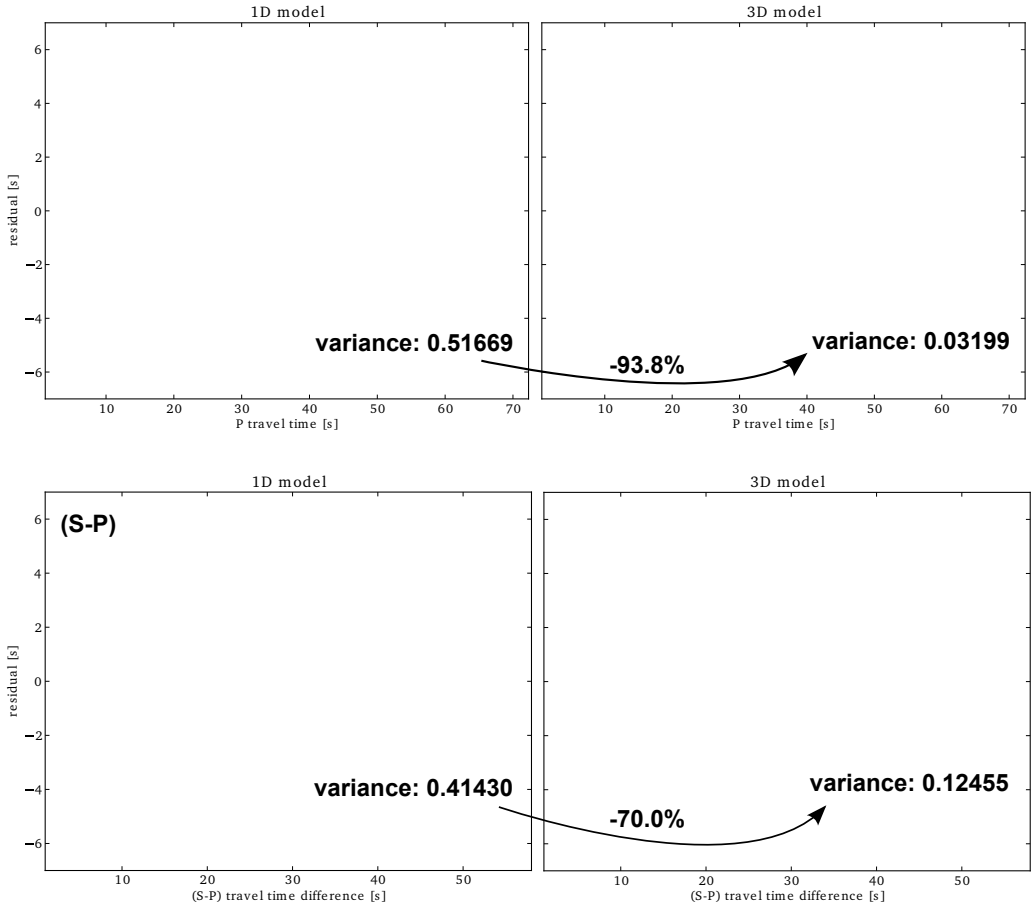

Figure 6.13.: Logarithmic density plot of travel time residuals against travel time for locations with the 1D velocity model (left column) and final relocations with the retrieved 3D model (right), shown for P arrivals (upper row) and (S-P) travel time differences (lower row). A substantial variance decrease is obtained with the 3D model in both cases.

deviate substantially more from the homogeneous starting model as found here. The slowest P velocities in the middle crust are found in the southwest Pamir, where the giant Shakhdara gneiss dome is located (*Stübner et al.*, 2012). Exceptionally high P velocities of around 6.4 km/s and v_p/v_s values of ≥ 1.80 characterize the basement of the Tajik Depression, which appears to be distinct not only from the Pamir, but also from the Ferghana Valley, where no such clear trends are seen. At middle to lower crustal depths, the separation between northern and southern Pamir is not visible any more, velocities lower than the background model prevail throughout the Pamir, with anomalously slow wavespeeds below Lake Karakul. The Tajik Depression as well as the southernmost Tien Shan consistently exhibit faster wavespeeds than the Pamir at these depths, whereas they are not systematically distinguishable by v_p/v_s ratios any more (which might, however, be due to poor lateral resolution). Average crustal velocities in the eastern Pamir agree well with values determined by *Mechie et al.* (2012), but significantly greater variations from the average are obtained here.

At a depth of 45 km, the Ferghana Valley and the Tajik Depression feature v_p values of ≥ 7.6 km/s, indicating the presence of mantle material. This is in accordance with crustal thickness estimates

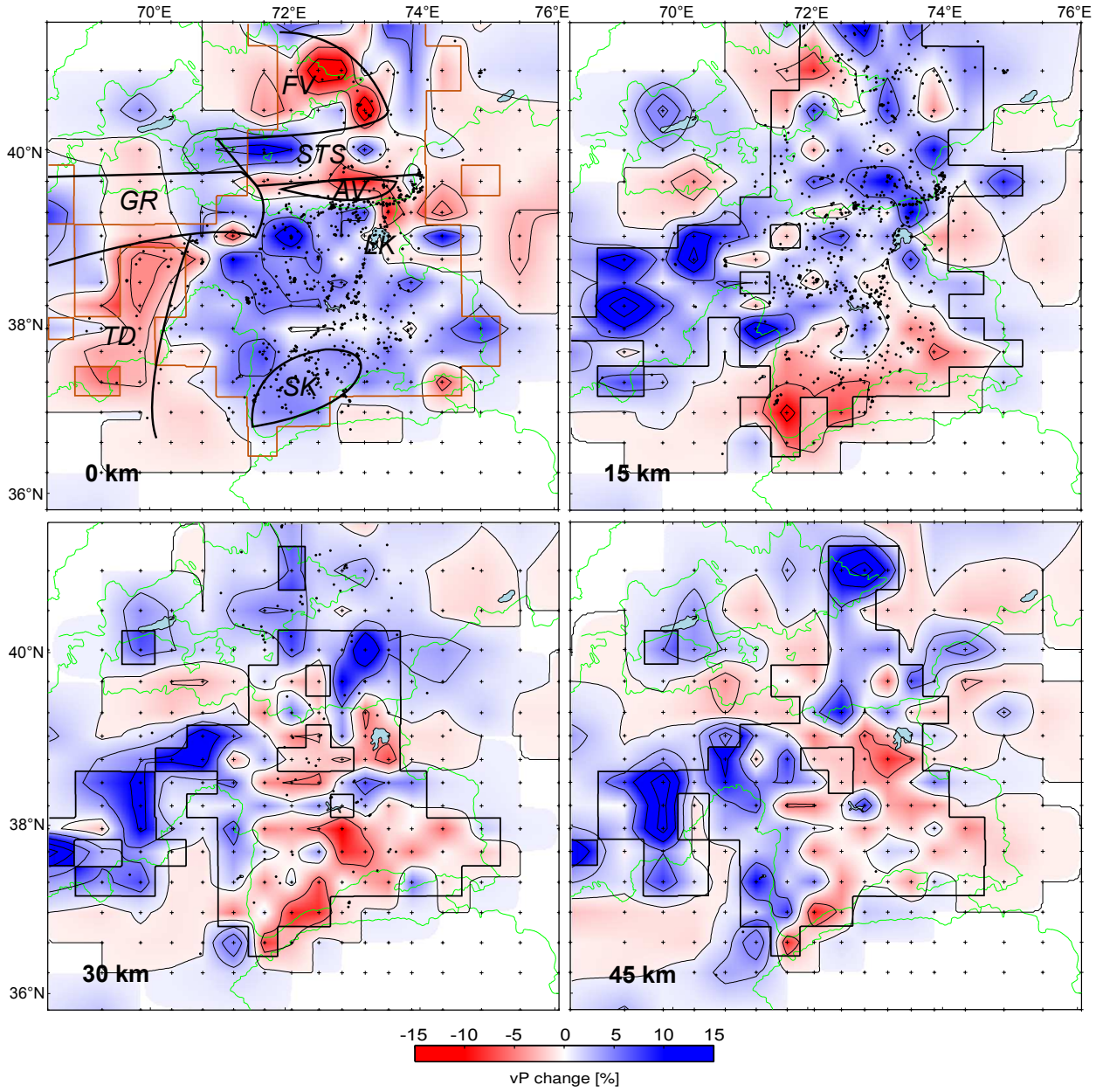

Figure 6.14.: Map view sections of relative P-velocity change compared to the starting model (see Figure 4.2) at crustal depths. Chosen depth levels correspond to the location of grid nodes at depth. Regions inferred to have good resolution (see Section 6.2.1) are encircled by the heavy black spread contour line, regions with presumably bad resolution are shown with weaker colors. Earthquake locations (relocated in the 3D model) from 10 km above to 10 km below the shown depth level are displayed as black dots, green lines depict national boundaries. In upper left depth section, spread contour are shown in brown, and rough outlines of geographic or structural features referred to in the text are shown in black. FV= Ferghana Valley, TD = Tajik Depression, STS = South Tien Shan, AV = Alai Valley, SK = Shakhdara Dome, LK = Lake Karakul, GR = Gissar Range

of *Burtman and Molnar* (1993) and *Steffen et al.* (2011) as well as with Moho depth values obtained from the TIPAGE data set by *F. Schneider (pers. comm., 2012)* with receiver function analysis (see Figure 6.21). The north-south oriented boundary between high velocities in the Tajik Depression and low wavespeeds in the Pamir appears to migrate eastwards, into the Pamir, from 30 to 45 km depth (Figure 6.14).

6.3.2. Mantle depths

The depth of 60 km marks the transition to mantle velocities in the background model. Low-velocity anomalies in the central and western Pamir and southern Tien Shan indicate larger Moho depths there. The front of fast velocities that migrated into the Pamir at crustal depths here acquires an arcuate outline, resembling the curvature outlined by hypocentral locations of earthquakes at greater depths (see Figure 4.13). The low velocities under most of the Pamir contain two stronger anomalies, one under the western Pamir, the other more northeast, that remain visible to at least 80 km depth (the latter one can still be faintly recognized at 100 km). Velocities in these "slow spots" are as low as 7.1-7.2 km/s, which strongly suggests that they are of crustal origin. These spots are situated directly south to southeast of a high-velocity region, which outlines an arcuately south- to eastward subducting slab (see Figure 6.18) with P wave velocities of 8.2-8.4 km/s. Westwards, this slab is clearly connected to the fast lithospheric material underlying the Tajik Depression (best visible in Figure E.1, Appendix E, profile A-A'). Elevated values of v_p/v_s ($\geq$1.80) are obtained for the slow spots, whereas values in the slab do not seem to systematically deviate much from the background value of 1.74.

Results of synthetic tests (Figures 6.8 and 6.10), in which the retrieval of anomalies with comparable geometry was simulated, show that the obtained distribution of v_p should be robustly retrieved, although with decreased amplitudes of the anomalies. This implies that the slow spots might in reality be even slower than found here. The resolution of v_p/v_s inversion, however, is strongly limited at mantle depths, anomalies are smeared out and drastically decreased in amplitude. This implies that significantly higher values of v_p/v_s may be present in the slow spots. Higher values of v_p/v_s in these depths could also provide an explanation for the systematically too deep centroid depths for intermediate-depth earthquakes retrieved with regional moment tensor inversion (Section 5.2.1). A larger time difference between P and S arrivals can either be explained with a deeper location (chosen in the case of RMT, since v_p/v_s was fixed to the values of the background model) or higher v_p/v_s along the ray path.

There is considerable along-strike variability in the described geometric setup (see Figure 6.15, depth map at 80 km depth): While the low-velocity zone at 60-100 km depth appears like a depression in a continuous Moho in the western cross sections (A-A' through E-E'), it looks like an isolated spot of very low velocities overlain by faster material, possibly even detached from the crust, further east (profiles F-F' through G-G'). These faster velocities at 60 km depth can also be seen in the corresponding depth section as a north-south trending fast anomaly in the eastern Pamir. In profiles C-C' and D-D', i.e. laterally between the two slow spots, moderately

Figure 6.15. *(following page)*: Map view sections of relative v_p at mantle depths. For an explanation of the different plot features, refer to Figure 6.14.

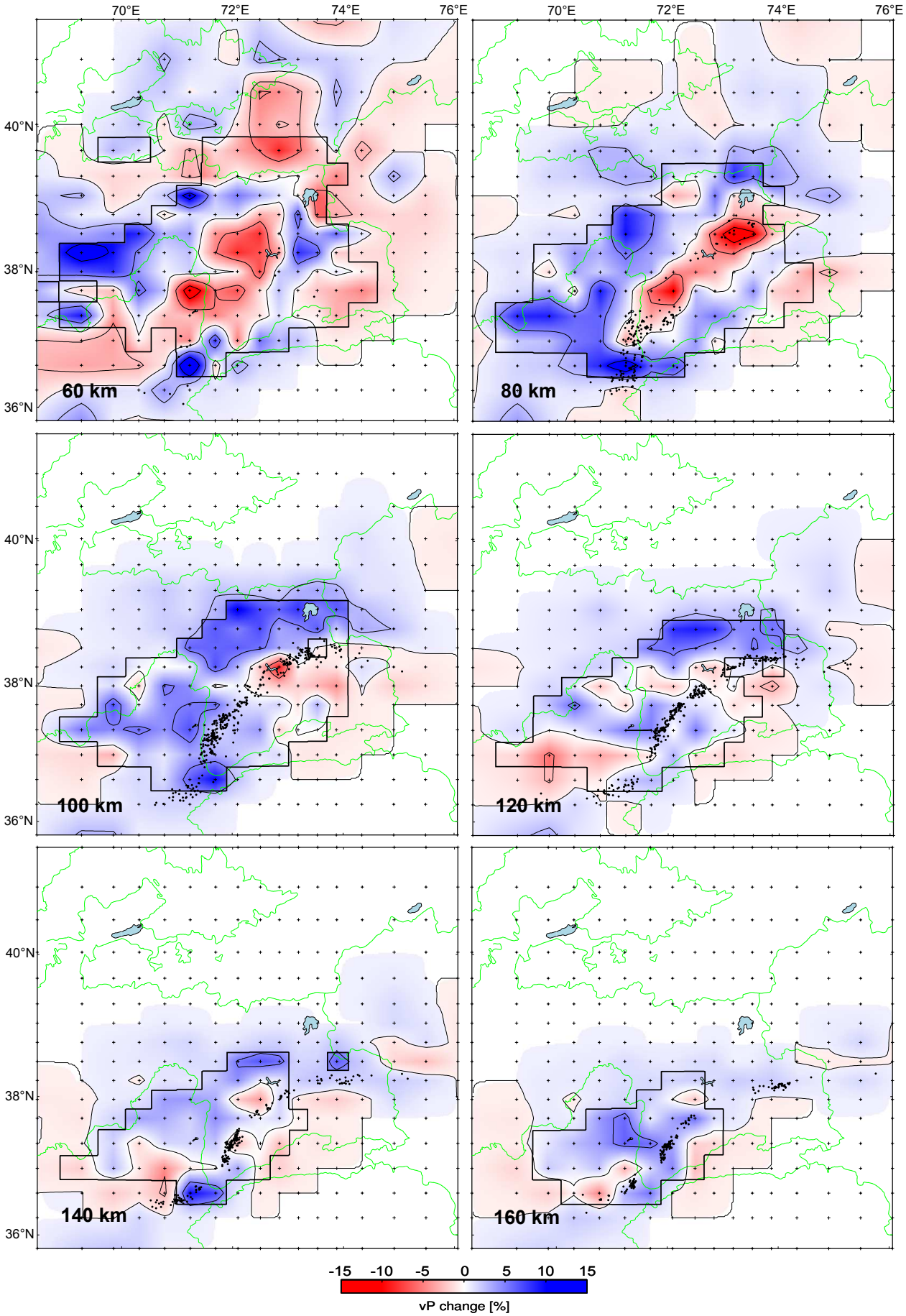
70°E
72°E
74°E
76°E
40°N
38°N
36°N
60 km
80 km
100 km
120 km
140 km
160 km
-15
-10
-5
0
5
10
15
vP change [%]

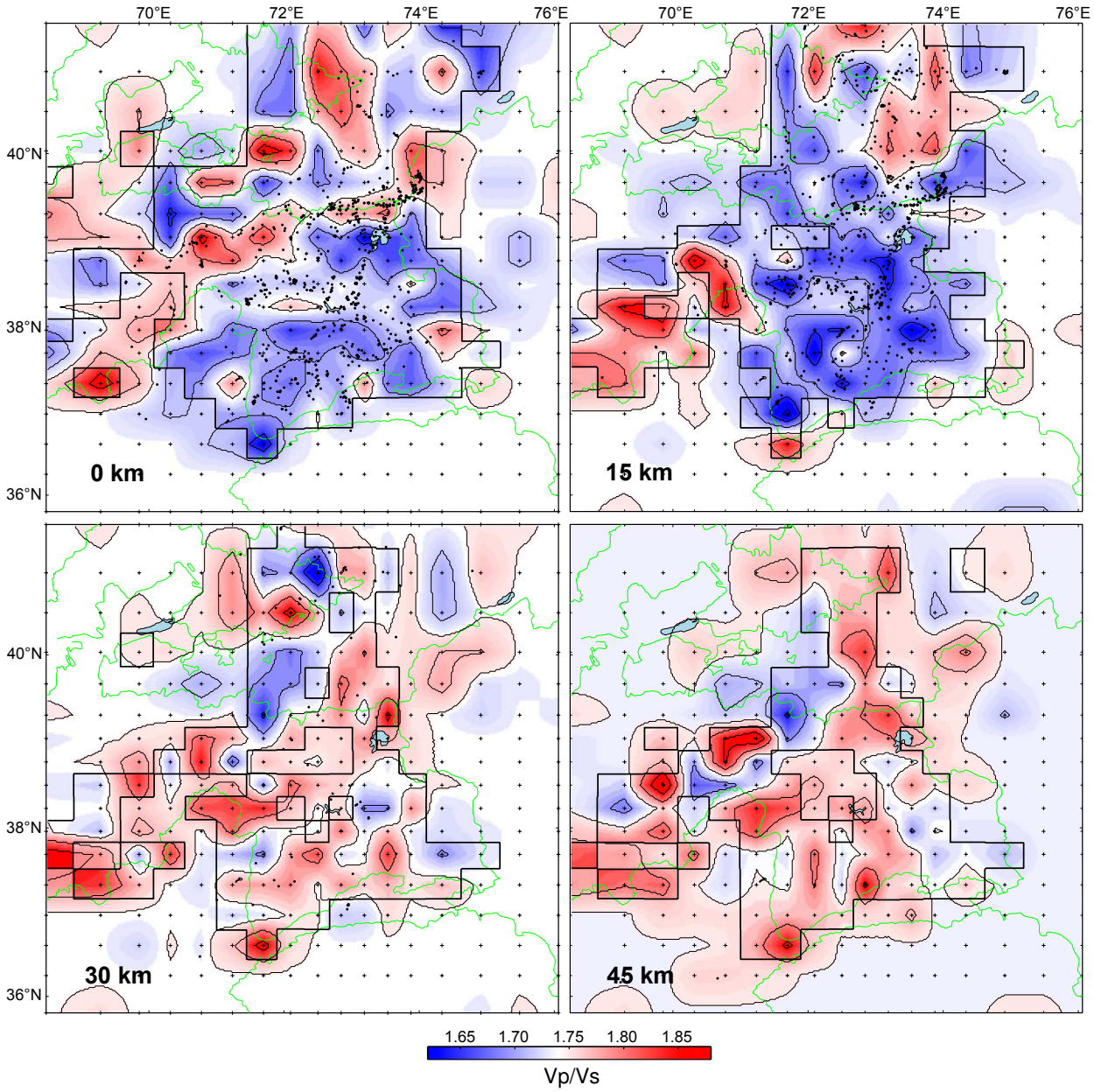

Figure 6.16.: Map view sections through the obtained v_p/v_s model at crustal depths. Chosen depth levels correspond to the location of grid nodes at depth. Regions inferred to have good resolution are encircled by the heavy black spread contour line, regions with presumably bad resolution are shown with weaker colors. Earthquake locations (relocated in the 3D model) from 10 above to 10 km below the shown depth level are displayed as black dots, green lines depict national boundaries.

low velocities are observed at greater depths, which appear to migrate into the slab. Hence, the upper slab boundary is not consistently outlined there. The mantle on the southeastern side of the Pamir slab shows velocities close to the starting model, i.e. 8.0-8.1 km/s, slightly faster in the west, indicating the presence of relatively undisturbed mantle material.

Intermediate-depth seismicity appears to be confined to the interface of the slab with the overlying mantle. This relationship breaks down with the presence of lower velocities well into the slab in profiles C-C' and D-D' of Figure 6.18, which leads to earthquake loci inside low-velocity material. This zone roughly corresponds to where seismicity thins out and becomes more narrowly confined in depth along strike of the Pamir seismic zone (see Figure 4.14). The updip end of seismic activity lies just below the slow spots or Moho bulge, actually consistently traces their lower boundary all along strike (Figure 6.18, e.g. profiles A-A', F-F').

At greater depths (>100 km), imaged velocities become more homogeneous, i.e. anomalies decrease in amplitude to less than ±5%. As resolution for the western Pamir is not observed to decrease in these depths (see amplitudes of recovered checkerboard pattern in Figure 6.5), this should be a real effect that could hint at thermal or chemical equilibration of the slab. The Pamir slab is, however, clearly imaged as a high-wavespeed anomaly to depths in excess of 200 km, with lower velocities to the southeast of it.

The Hindu Kush slab can not be resolved, since the entire network is located to the north and east of it. Rays from Hindu Kush deep seismicity, which should be confined to the slab's uppermost part, thus only travel very short distances in the slab. However, a zone of low mantle velocities is imaged immediately to the north of the Hindu Kush seismicity from depths of 120 km downwards, which in some depth sections appears to penetrate into the gap between Pamir and Hindu Kush seismicity.

6.4. Interpretation

6.4.1. Partial melting or aqueous fluids in the south Pamir middle crust

The observed middle crustal zone of anomalously low P velocities underlying the southern Pamir from a depth of 15 km onwards (see Figure 6.14) correlates well with an extended high-conductivity anomaly discovered with magnetotelluric (MT) deep sounding techniques on a north-south profile through the eastern Pamir by *P. Sass (pers. comm., 2012)*. The 5.75 km/s v_p contour line traces the conductivity anomaly remarkably well (see Figure 6.20). Since the depth resolution of the tomographic inversion is comparatively poor (nodes at 0 and 15 km depth, interpolation between), the position of the upper end of this body determined with MT should be considerably more precise. High heat flow values (up to 120 mW/m^2, see *Duschkov et al.*, 2001), which are corroborated by the abundance of hot springs in this area, set the southern Pamir apart from

Figure 6.17. *(following page)*: Map view sections of v_p/v_s at mantle depths. For an explanation of the different plot features, refer to Figure 6.16.

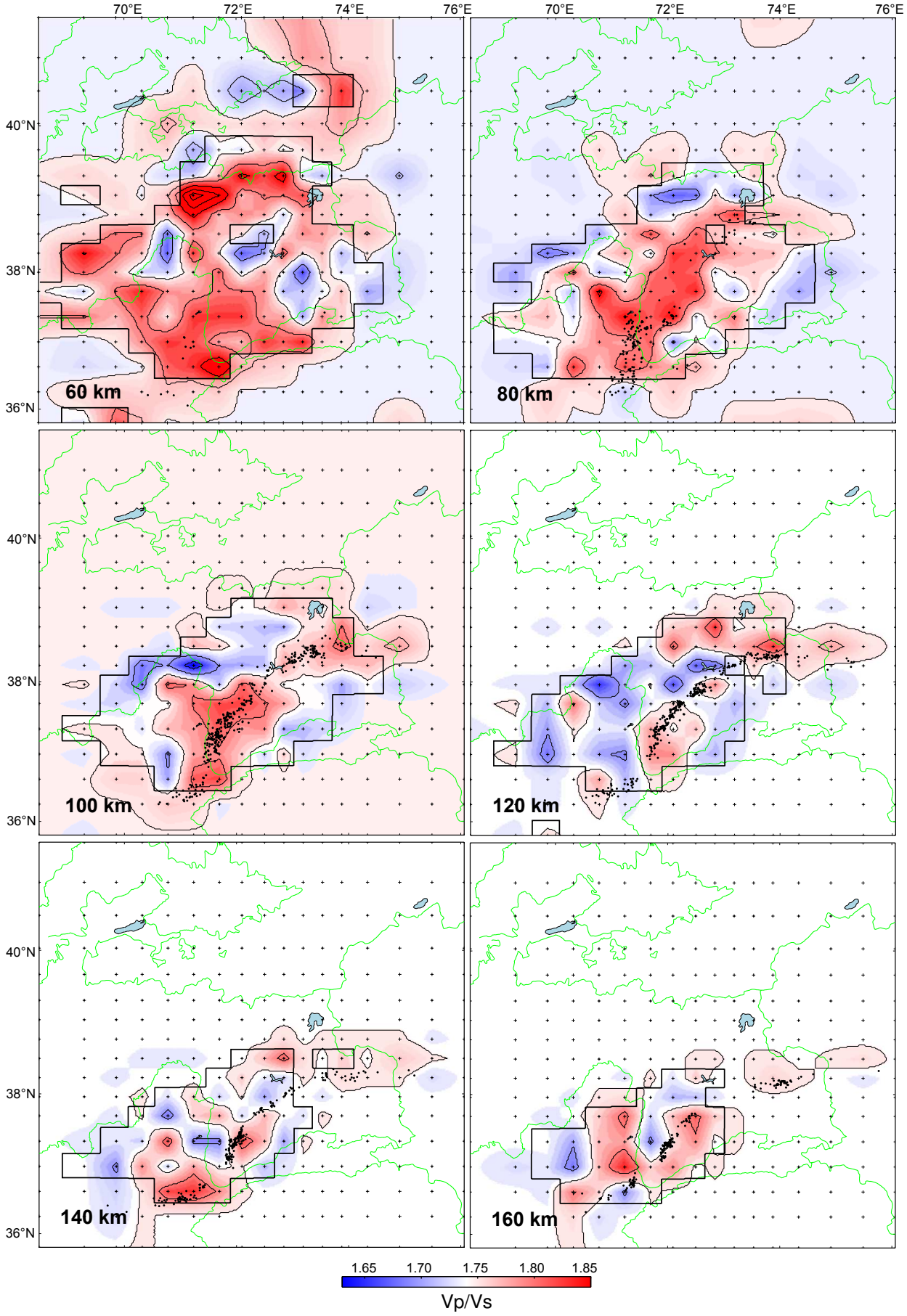
70°E
72°E
74°E
76°E
40°N
38°N
36°N
60 km
80 km
100 km
120 km
140 km
160 km
1.65
1.70
1.75
1.80
1.85
Vp/Vs

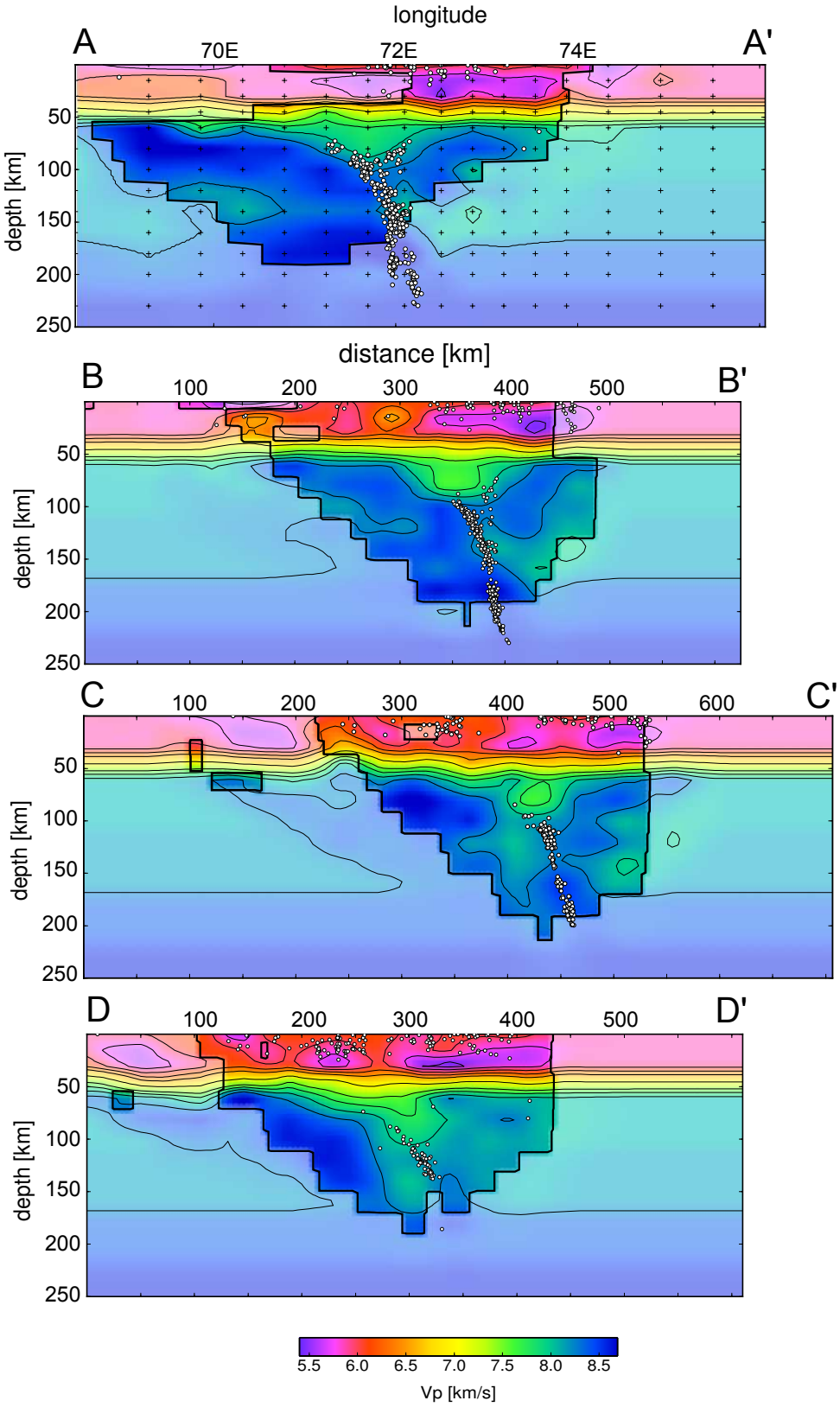

Figure 6.18.: Cross sections of absolute P velocity. Location of the profiles is shown in Figure 6.1. Heavy black line surrounds well resolved regions, according to the spread criterion (see Section 6.2.1). Hypocentral locations of earthquakes (relocations in the 3D model) are shown as white circles, black crosses mark grid nodes (only shown for longitudinal and latitudinal sections).

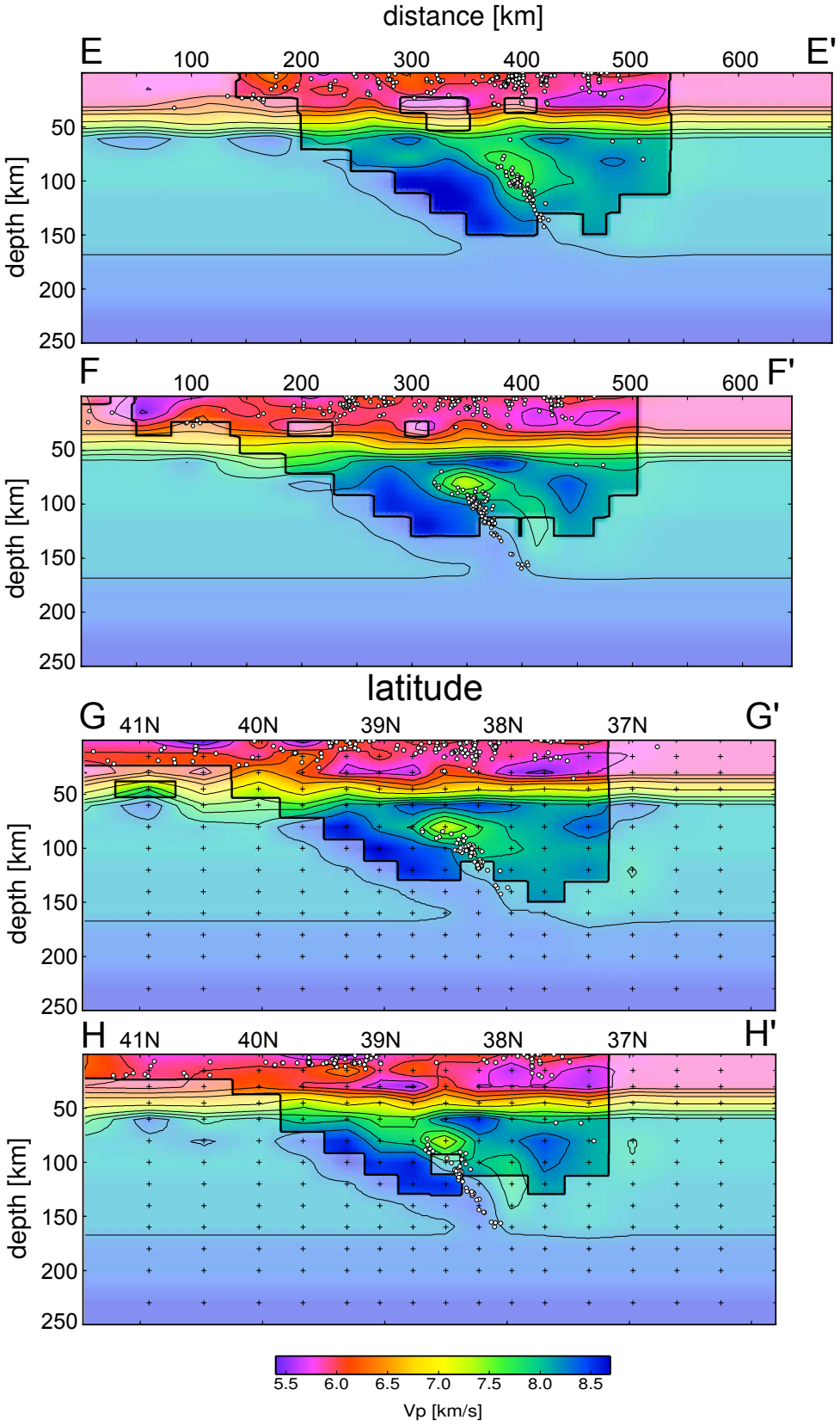

Figure 6.18.: Cross sections of absolute P velocity *(continued)*

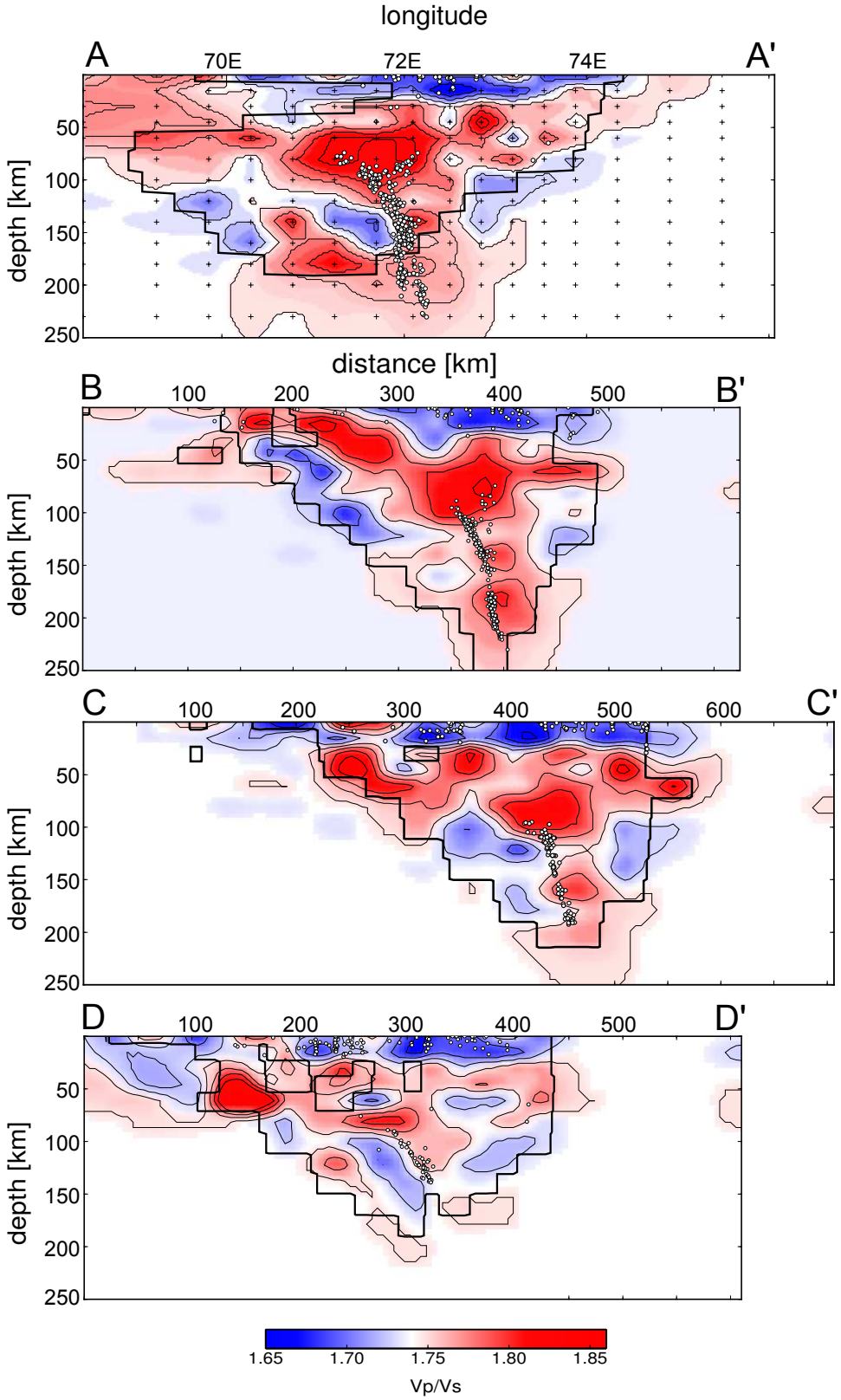

Figure 6.19.: Cross sections of v_p/v_s ratio. Location of the profiles is shown in Figure 6.1. Heavy black line surrounds well resolved regions, according to the spread criterion (see Section 6.2.1). Hypocentral locations of earthquakes (relocations in the 3D model) are shown as white circles, black crosses mark grid nodes (only shown for longitudinal and latitudinal sections).

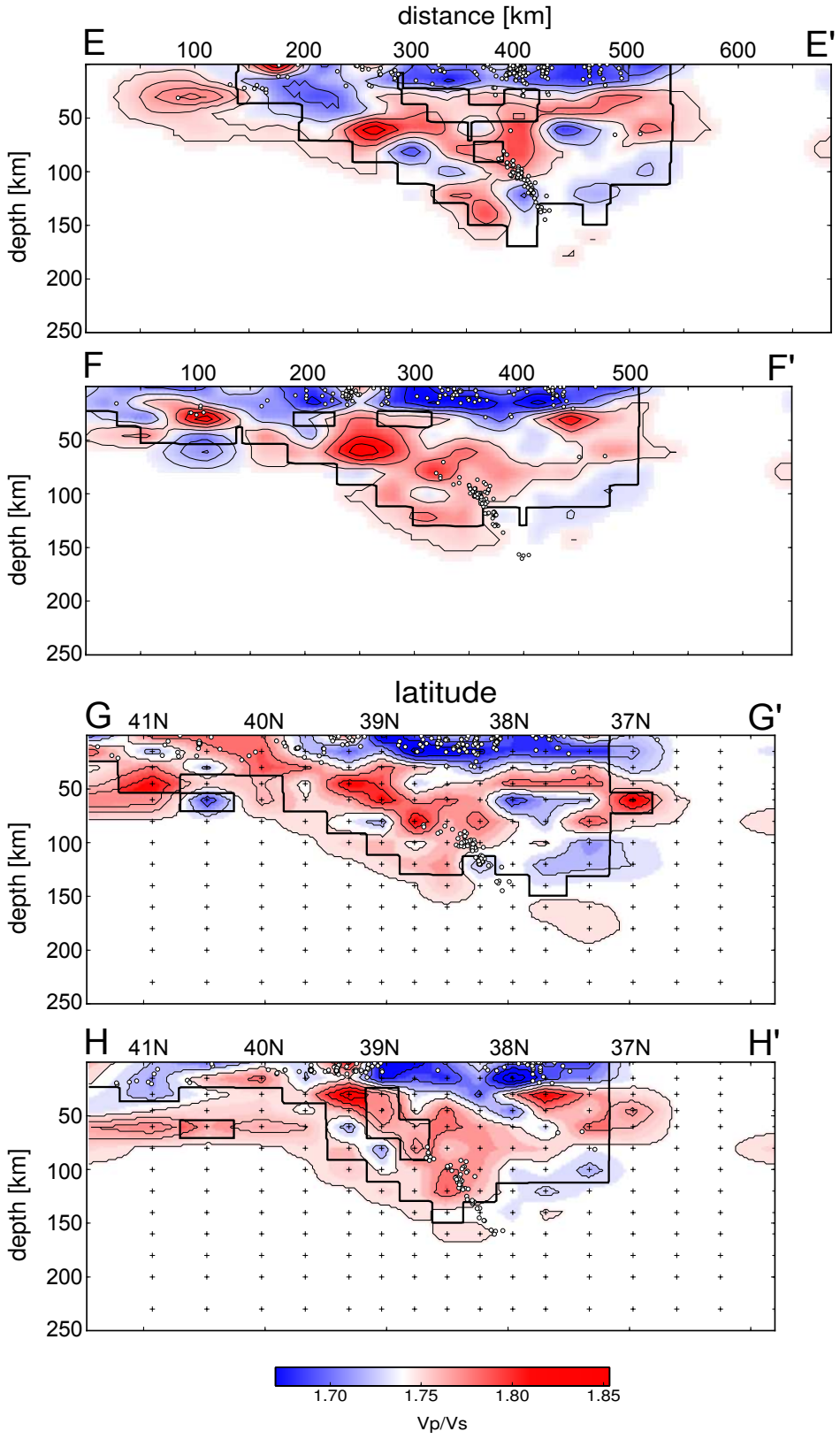

Figure 6.19.: Cross sections of v_p/v_s ratio *(continued)*

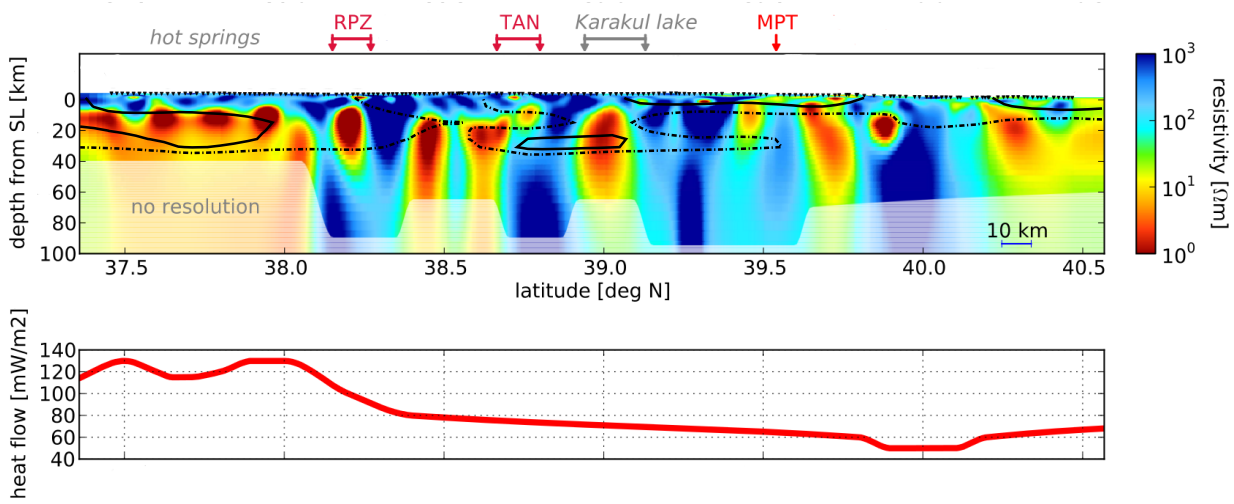

Figure 6.20.: *Upper subplot:* Results of 2D inversion of magnetotelluric data collected along the TIPAGE profile (*P. Sass, pers. comm., 2012*), displayed as resistivity anomalies. v_p contour lines of 5.75 km/s (solid lines) and 6.0 km/s (dashed lines) from this study are overlain. The imaged good conductor in the southern part of the profile correlates well with the middle crustal low-velocity zone found in this study, the upper end of this body appears to be at depths of 10-15 km. RPZ = Rushan-Pshart zone, TAN = Tanymas suture, MPT = Main Pamir Thrust
Lower subplot: Heat flow values from *Duschkov et al.* (2001), projected onto the same profile (*P. Sass, pers. comm., 2012*), show that elevated heat flow values of up to $>120\,mW/m^2$ are found in the southern Pamir.

its surroundings and correlate well with the position of the observed high-conductivity and low-velocity body. To the north, this anomalous region is bounded by the Rushan-Pshart zone (see Section 2.2), which is the suture separating southern from central Pamir.

Intriguingly, the lowest P velocities in the middle crust are found directly beneath the Shakhdara dome in the very southwestern Pamir (Figure 6.14). Since the exhumation of this migmatitic gneiss dome supposedly stopped only about 2 Ma ago (*Stübner et al.*, 2012), a remnant thermal signal related to the exhumation might still be detectable and could lower seismic velocities. Lithologically, slower-than-average values are not to be expected there. No MT data for this region are available, but as both heat flow and low seismic velocity anomalies cover the entire southern Pamir, I speculate that this likewise is the case for the middle crustal conductor.

The observed low velocities could be a temperature effect, consequence of the relative enrichment of radiogenic heat production in thick felsic crust and of mechanical friction during thickening, which should also have a thermal signature. However, the presence of a very good conductor (here: resistivity <10 Ωm) in the crust is hard to explain with a temperature increase alone, but has to imply the presence of fluids, either as partial melts or aqueous pore fluid (*Haak and Hutton*, 1986; *Schmeling*, 1986). However, the low values of v_p/v_s (<1.70) observed for the depth of 15 km (see Figure 6.16) appear to be rather badly compatible with this hypothesis, since fluids or partial melts are supposed to significantly increase v_p/v_s due to the fact that v_s is more strongly coupled to the shear modulus μ than v_p (e.g. *Stein and Wysession*, 2003). The retrieved low v_p/v_s values

at middle crustal depths can not be an artifact of lacking resolving power: the checkerboard test shows still fair resolution at these depths (Figure 6.6), and no downward smearing of shallower anomalies are observed in the synthetic test (Figures 6.9 and 6.10). The effect of fluid presence on v_p/v_s ratios is, however, less straightforward than previously indicated. Relative proportions of partial melt/fluids as well as the geometry and connectivity of pore space in the crustal rocks can largely influence obtained values (e.g. *Takei*, 2002). Hence, the presence of a moderate proportion of disconnected partial melt pockets in the pore space of felsic crust may not lead to a lowered v_p/v_s at all. The increase of v_p/v_s at 30 km could then indicate a change in the chemical composition of rocks, i.e. a transition towards more mafic lower crustal material (e.g. *Rudnick and Fountain*, 1995). The fact that crustal seismicity appears to exclusively occur at depths shallower than the upper end of the observed low-velocity body in the south Pamir (see Figure 4.10) is compatible with the assumption of the presence of partial melt. At p-T conditions allowing this, deformation should exclusively occur in the ductile regime.

The findings presented here appear to be highly similar to what was discovered in the framework of the INDEPTH project in southern Tibet (*Nelson et al.*, 1996), where the presence of mid-crustal partial melts was inferred from "bright spots" of very low velocities observed with seismic wide-angle reflection profiling (*Brown et al.*, 1996), together with the presence of highly conductive material at the same depths (*Chen et al.*, 1996). A similar highly conductive body at middle crustal depths has been found in the central Andes (*Schilling et al.*, 1997). Velocities in the Tibetan bright spots were found to be significantly lower than what is found in this study ($\leq$3.5 km/s for v_p), but such narrow, prominent reflectors should lead to a picture of smeared out, significantly higher velocities in a tomographic inversion with a grid spacing of 15 km with depth. *Makovsky and Klemperer* (1999) later interpreted project INDEPTH bright spots as representing the presence of about 10% aqueous fluids, not partial melts, based on amplitude modelling and petrophysical considerations. Modelled v_p/v_s values in this study are, interestingly, $\leq$1.70.

6.4.2. Deep subduction of continental crust

The tomographic images at mantle depths show a southward-dipping slab beneath the Pamir, that follows the arcuate geometry outlined by the earthquake hypocenters (see e.g. Figure 4.10). P wave velocities inside the slab are 3-5 % higher than for the surrounding mantle, not different to what is routinely observed in oceanic subduction zones (e.g. *Husen et al.*, 2000; *Schurr et al.*, 2006). This velocity contrast should be to first order due to significantly lower temperatures in the subducting slab. Considering, however, that the pre-Pamir basin most likely comprised continental shelf material (*Leith*, 1982), involved material might not be highly different anyway. v_p/v_s ratios of slab material appear to be lower than for the mantle material overlying the slab, but are rather diverse and patchy, so the slab is not imaged as a zone of uniform values. This might in part be due to the general low resolving capability of v_p/v_s inversion at mantle depths. Unlike for the Hindu Kush, which has been clearly imaged as a high-velocity region by many teleseismic or global studies (e.g. *Mellors et al.*, 1995; *Bijwaard et al.*, 1998; *Simmons et al.*, 2011), no such clear images exist for the region beneath the Pamir. The presence of a fast, southward dipping lithospheric slab can be inferred from images shown by *Koulakov and Sobolev* (2006), *Koulakov* (2011) and *Negredo et al.* (2007), but its geometry is generally not clearly defined. An arcuate high-velocity region, adjacent to lower velocities to its southeast, corroborating my findings, are discernible in the 75 km depth sections in *Koulakov and Sobolev* (2006, here also at 50 km) and

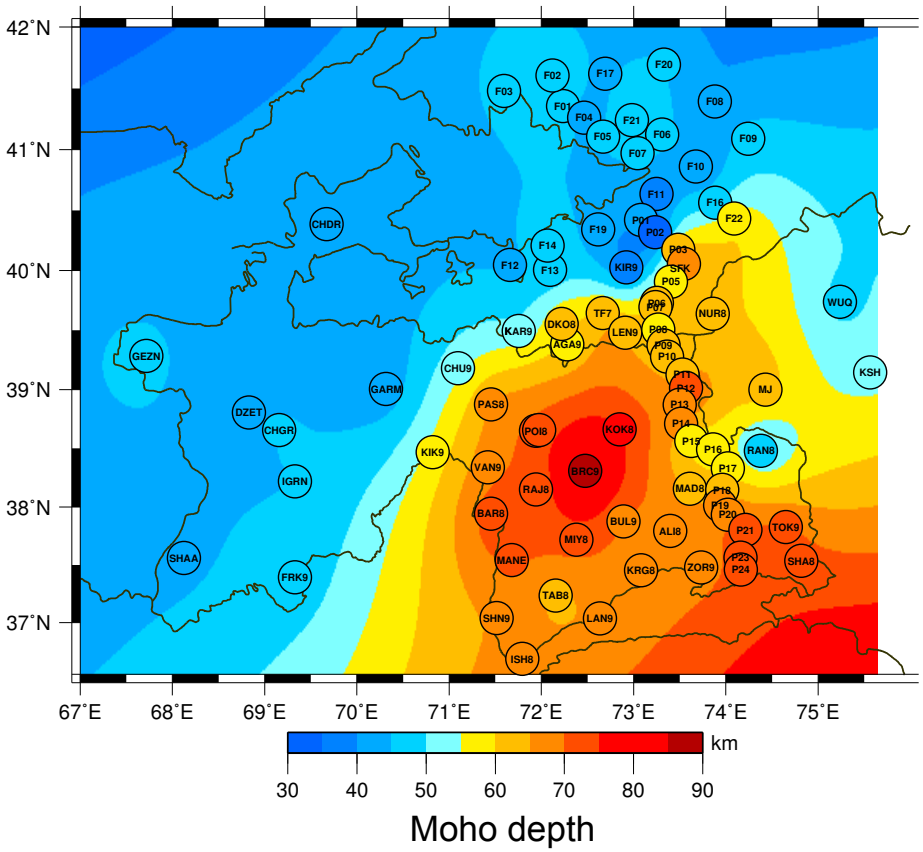

Figure 6.21.: Moho map compiled by *F. Schneider (pers. comm., 2012)*, applying the technique of *Zhu and Kanamori* (2000) for the shown stations. The map is a spline interpolation of point measurements beneath the stations, which are indicated by the color of the circle representing them, and agrees to a high degree with the Moho depths that can be inferred from seismic tomography (see Figure 6.14 and 6.15).

Koulakov (2011). However, due to the utilized methodology in all of these studies, no absolute velocities were obtained.

Very low P wave velocities are obtained directly above the slab in depths from 60-80 km, which consistently occur along strike of the slab, but show some variation in amplitude and appearance. The location and extent of low P wavespeeds below 60 km depth are to first order corroborated by a map of Moho depths throughout the Pamir compiled by *F. Schneider (pers. comm., 2012)* using the method of *Zhu and Kanamori* (2000) shown in Figure 6.21. They might also show up in the studies by *Koulakov and Sobolev* (2006) and *Koulakov* (2011). Retrieved velocities in these low-velocity structures are as low as 7.1-7.2 km/s. Taken together with results of synthetic tests (see Figures 6.5 and 6.8) that attest to an amplitude decrease of retrieved anomalies (caused by the damping) and the fact that a density increase with depth due to the higher confining pressure should also lead to an increase in seismic velocity (*Birch*, 1961), these might even be too slow for lower crustal material, but could hint at the incorporation of middle crustal rocks. v_p/v_s values in these anomalies are high, and taking into account the strong amplitude decrease by spatial smearing inherent in the tomographic reconstruction of v_p/v_s, probably very high ($\geq$1.90). Which conclusions in terms of lithology do these values above the slab allow? Table 6.1 shows a

Metastable

	granite	granodiorite	felsic gneiss	diorite	granulite	mafic gneiss	gabbro
H_2O [wt. %]	0.2	0.9	0.0	1.0	0.0	0.0	0.0
ρ $[g/cm^3]$	2.78	2.90	2.93	3.02	3.09	3.11	3.19
v_p [km/s]	6.33	6.45	6.75	6.82	7.37	7.47	7.57
v_s [km/s]	3.57	3.58	3.85	3.76	4.12	4.20	4.18
v_p/v_s	1.77	1.80	1.75	1.82	1.79	1.78	1.81

Equilibrated

	granite	felsic gneiss	diorite1	diorite2	Eclogitized granulite	mafic gneiss	gabbro
H_2O [wt. %]	0.7	0.8	0.5	0.9	0.7	0.0	0.1
ρ $[g/cm^3]$	3.06	3.22	3.26	3.32	3.44	3.56	3.50
v_p [km/s]	7.50	7.64	7.96	7.75	7.95	8.35	8.35
v_s [km/s]	4.19	4.27	4.49	4.34	4.41	4.65	4.69
v_p/v_s	1.79	1.79	1.77	1.79	1.80	1.79	1.78

Table 6.1.: Tables of seismic velocities computed for a number of crustal rock suites (*S. Angiboust, pers. comm., 2012*), using the method of *Hacker and Abers* (2004) and p-T conditions of 3.3 GPa and 700 °C. Values are shown for the metastable (i.e. mineral assemblage corresponding to crustal conditions) and fully equilibrated case. Rock compositions were either generically produced, by modelling with `PerpleX` (*Connolly*, 2005) or taken from petrological studies of exhumed ultrahigh-pressure rocks. Granulite and eclogitized granulite compositions from Bergen Arcs, Norway (*Boundy et al.*, 1992), reequilibrated Gabbro from Dabie Shan, China (*Zhang et al.*, 1996), Diorite2 from Sesia, Ivrea Zone, Italian Alps (*Pin and Sills*, 1986).

compilation of seismic velocities computed for different suites of crustal rocks at p-T conditions comparable to what the crustal material at depth should experience (3.3 GPa, 700 °C, temperature estimate from thermomechanical modeling, *J. Tympel, pers. comm., 2012*), using the method of *Hacker and Abers* (2004). The compositions for the different crustal rocks were either generically defined (using the code `PerpleX`, *Connolly*, 2005) or taken from petrological studies of exhumed ultra-high pressure rocks. Seismic velocities are shown for the metastable case, i.e. where the burial of the rocks occurred fast enough that they are out of equilibrium, and for the fully equilibrated case. The values show that no matter what source rock is assumed, P velocities for equilibrated material at these p-T-conditions are too high to fit to the observations. Moreover, strongly mafic compositions can be ruled out, since they show too high seismic velocties. Still, several metastable or partly equilibrated (values between metastable and equilibrated case) rock compositions could explain the obtained findings. v_p/v_s values for the computed scenarios are quite uniform and presumably lower than what is obtained for the imaged low-velocity zone. This might indicate fluid involvement there, which could in turn influence pertrological compositions and lower seismic velocities, making the conclusions just drawn invalid. In any case, v_p/v_s values for the different crustal rocks in Table 6.1 are very uniform, hence do not provide a means to discriminate between the various host lithologies.

Due to the event-station distribution, the Hindu Kush seismic zone cannot be decently imaged, but the low-velocity anomaly north of it, which appears from a depth of 120 km and that is also visible in *Koulakov and Sobolev* (2006), appears to be clearly resolved. Since it seems to

be penetrating the seismic gap between the Pamir and Hindu Kush seismic zones, which opens with depth (see Figure 4.15), this anomaly could be interpreted with asthenospheric return flow through this proposed "slab window" (*Thorkelson*, 1996).

Intermediate-depth seismicity beneath the Pamir appears to be confined to the upper edge of the subducting slab, which can also be observed for some classical ocean-continent subduction zones (e.g. *Schurr et al.*, 2006). No indication of a double seismic zone (*Brudzinski et al.*, 2007) is obtained here. However, the geometric relation between seismicity distribution and tomographic inversion results is fundamentally different from findings elsewhere. Sub-Moho seismic activity only starts below the low-velocity regions, actually the onset of seismicity traces the outline of these anomalies, i.e. it commences at or below the 7.75-8.0 km/s velocity isoline. Explanations for this observed behavior might be that either a change in the petrological composition coincides with these velocity isolines, or that p-T conditions only become favorable for the creation of intermediate-depth earthquakes at these depths.

A narrow low-velocity channel containing the mantle-depth seismicity was identified with receiver function analysis (*Schneider et al.*, 2012, *manuscript in preparation*) along the north-south profile through the eastern Pamir that was installed during the first year of the TIPAGE deployment (see Section 3). Overlaying their results with the tomographic images (see Figure 6.22) shows that the upper part of the low-velocity zone they obtain may correspond to the anomalously slow velocities seen directly above the slab, but that this low-velocity zone can be traced to greater depths to actually engulf the seismicity. An additional synthetic test was carried out in order to determine whether such a narrow channel (*Schneider et al.*, 2012, get a thickness of about 10 km) could be resolved with the tomographic inversion presented here. A scenario with a broad zone of low velocities (-10%) at 60-80 km depth, grading into a narrow (10 km wide) low-velocity channel, both overlying a fast (+5%) slab, is taken as input model, using a finer grid in this region for the forward calculation. The retrieval of these anomalies using the standard grid (see Figure 6.1) and all other settings of the v_p inversion procedure shows that whereas slab and the broader zone of low velocities are decently imaged, the narrow low-velocity channel can hardly be identified in the tomographic reconstruction. Hence, such a thin low-velocity zone can not be resolved with the data used here.

A combination of these findings leads to three possible scenarios:

1. *Stalled continental slab with attached oceanic material*
   The found velocity distribution could be interpreted with the transition of oceanic to continental material in a collision zone setting. In that case, the low-velocity channel containing the earthquakes would be oceanic crust, which for a slightly thickened oceanic platform or such is compatible with thickness estimates. Moreover, earthquakes inside this kind of material could be explained with dehydration embrittlement easier than if continental material is involved. The broader low-velocity anomalies in the uppermost mantle would represent the onset of continental crustal material that was pulled down by the negative buoyancy of the oceanic material attached to it. This would, however, require that oceanic material existed at the locus of today's Pamir until very recently, which I think unlikely (see e.g. Introduction). Moreover, this scenario implies that subduction in the Pamir would currently have to be stalled, i.e. convergence across the MPT should have vanished, which is not what is observed from both GPS (*Zubovich et al.*, 2010) and geomorphology (*Arrowsmith and Strecker*, 1999).

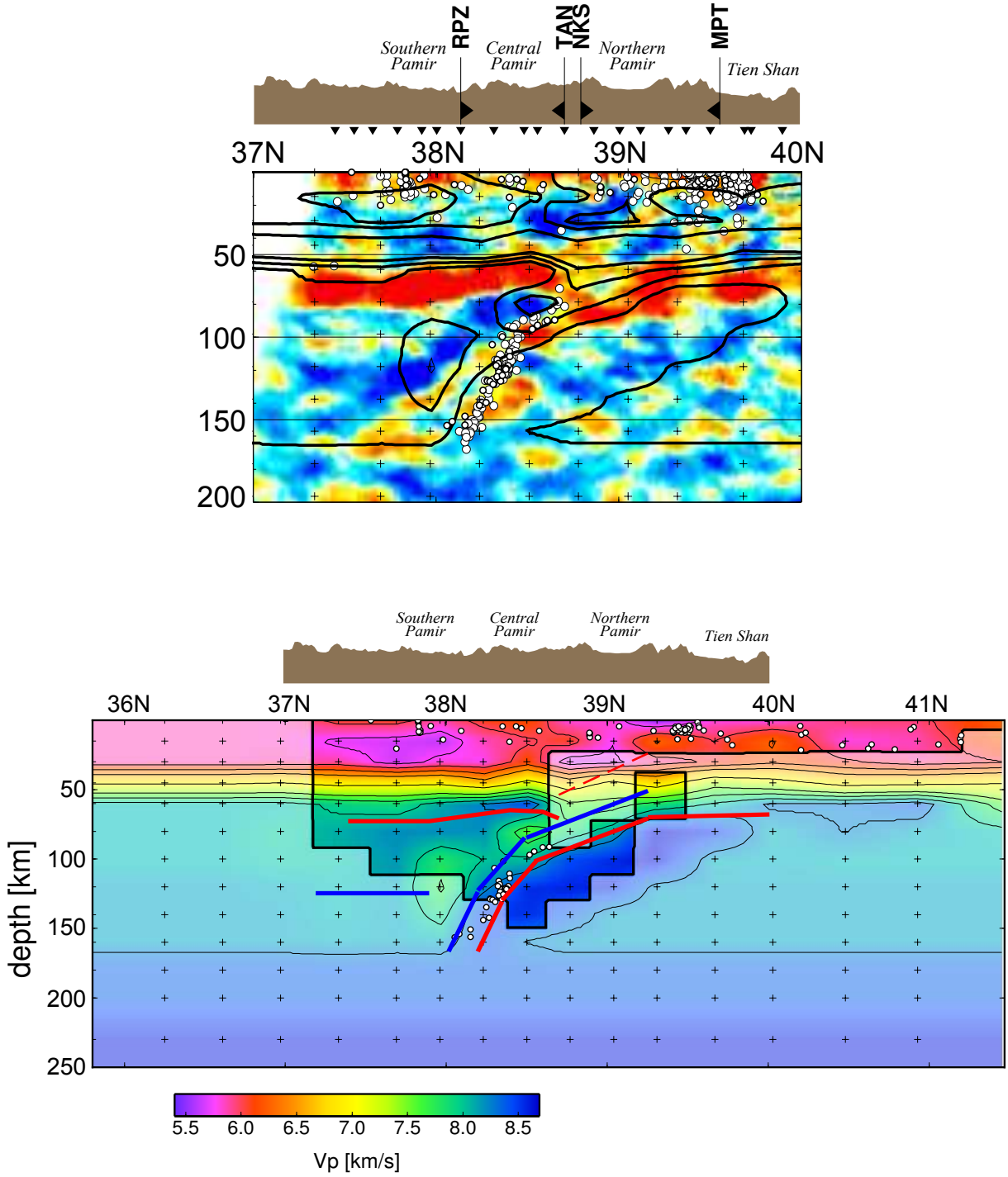

Figure 6.22.: (*upper subplot*:) Overlay of v_p contour lines from the tomographic study presented herein onto P-to-S receiver function results of *Schneider et al.* (2012). Their dipping converter in red clearly corresponds to the upper boundary of the Pamir slab. (*lower subplot*:) Interpreted converters (red lines indicate upward decrease of velocity, e.g. at the Moho, blue lines upward velocity increase) of *Schneider et al.* (2012) overlain onto tomographic cross section. The low-velocity channel discovered in this study is situated right on top of the Pamir slab and might be imaged as a much broader zone of lowered v_p

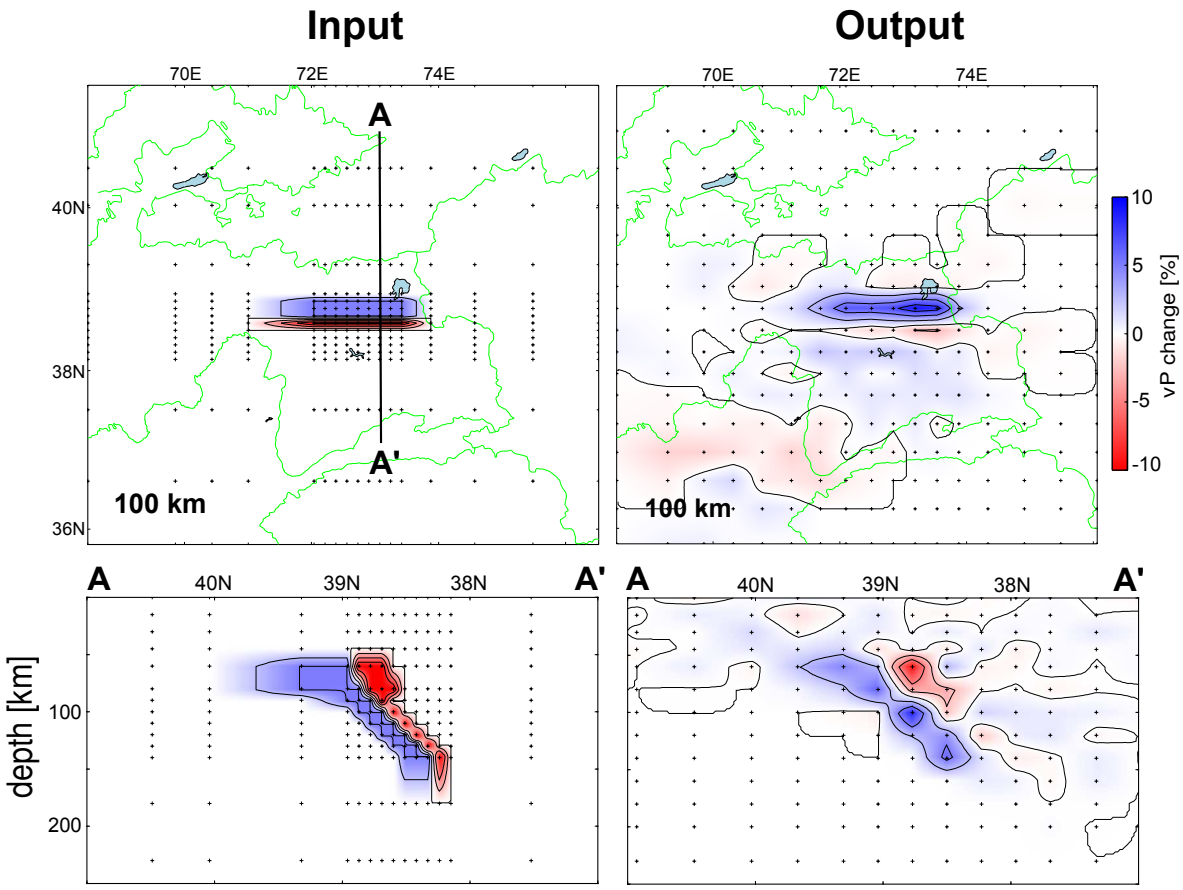

Figure 6.23.: Synthetic test for the retrieval of a narrow channel of low v_p on top of a high-v_p slab: Input model was defined on a grid severely refined around the region of interest, the retrieved velocity distribution on the coarser grid decently images the broader low-velocity zone at 60-80 km depth and the slab, but shows only very faint hints at the narrow low-velocity channel at greater depth. The obtained tomographic image would probably not be interpreted as a low-v_p channel overlying the slab.

2. *Deep subduction of continental lower crust with anomalous mantle wedge*
The presumably very high v_p/v_s values in combination with low P velocities observed at uppermost mantle depths throughout the Pamir could also be explained with a heavily serpentinized mantle wedge. Serpentinite has been shown to feature this combination of petrophysical parameters in laboratory experiments (*Christensen*, 1996). However, such a scenario leaves some open questions as to its genesis. Observed velocities are lower than for most oceanic mantle wedges, which would have to hint at a stronger degree of serpentinization, which occurs when peridotite, i.e. mantle material, is subjected to hydration (*Raleigh*, 1967). The necessary water would have to come from the subducting lower crust, which should be drier than a corresponding layer of oceanic crust, hence not be capable of effecting a stronger serpentinization. Moreover, the assumption that a highly serpentinized mantle wedge is responsible for the broad low-velocity zone overlying the Pamir slab can not explain the occurrence of "forking" of earthquake locations around this zone. Alternatively, low v_p and high v_p/v_s could also imply the presence of partially molten mantle material, although it is unclear if such low P velocities would be observed in this case. If intermediate-

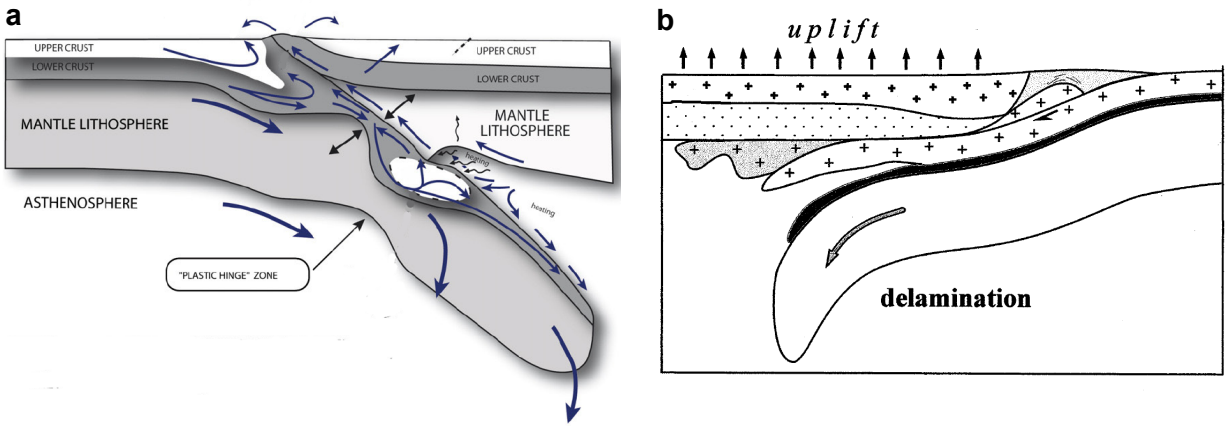

Figure 6.24.: Two conceptual models possibly applicable to processes beneath the Pamir: a) intracontinental subduction with entrainment of middle crustal material, which could later be exhumed. Lower crustal material is present to both sides of the middle crustal fragment and is subducted to greater depth as a narrow layer atop the mantle lithospheric slab (modified from *Burov and Yamato*, 2008).
b) Underthrusting of continental material, followed by delamination of mantle lithospheric and lower crustal material (modified from *Chemenda et al.*, 2000)

depth earthquakes are indeed confined to subducting lower crustal material (as inferred by *Schneider et al.*, 2012), then these would have to be mislocations, since no subducting lower crust can be present at the side of the mantle wedge that is further from the slab.

3. *Deep subduction of continental lower crust, entrainment of middle crustal material*
Ongoing subduction of continental lithosphere and lower crust entrains less dense middle crustal material, which is transported to sub-crustal depths but resists further recycling, will due to its low density probably be exhumed or transformed by mineral reactions eventually. These middle crustal fragments make up the aseismic, low-velocity and high-v_p/v_s zone in the shallowest mantle. The high v_p/v_s values might hint at dehydration reactions or partial melting. A rather thin layer of lower crustal material, possibly in part eclogitized, entrains these middle crustal fragments and forms a continuous layer on top of the subducting slab to greater depths. Due to the eclogitization of the mafic lower crustal material, it acquires the necessary negativ buoyancy for deep subduction (*Cloos*, 1993). This material hosts the intermediate-depth earthquakes, which explains the findings of their location within a narrow low-velocity zone as well as the apparent "forking" of the earthquake around the broader low-velocities here interpreted as middle crust, which was already observed in Chapter 4 (there termed "backthrust geometry"). A conceptual sketch of this scenario by *Burov and Yamato* (2008) is supplied in Figure 6.24a. An implication of this scenario is that it clearly favors subduction over a pure delamination setup, in which the entrainment of middle crustal material would be hard to explain. However, a process of overthrusting of the Pamir over its surroundings, followed by a delayed detachment of the underthrusted material (which is not a delamination *sensu stricto*), can be imagined in this context (see Figure 6.24b, taken from *Chemenda et al.*, 2000).

6.4.3. Where is underthrusted India?

The underthrusting of continental India under the Tibetan Plateau is one primary mode of how today's convergence between India and Eurasia is accommodated (see Section 2.1 or e.g. *Matte et al.*, 1997). The presence of Indian lithosphere beneath large parts of the Tibetan Plateau has been imaged with seismic tomography (*Tilmann et al.*, 2003; *Li et al.*, 2008a) and receiver functions (*Yuan et al.*, 1997; *Kosarev et al.*, 1999; *Nábelek et al.*, 2009; *Kind and Yuan*, 2010), showing a prominent zone of elevated wavespeeds at depths of about 100 to 250 km, indicative of a cold lithospheric slab. Mapping of the front of underthrusting India shows that it advances further north in the western part of Tibet, until it abuts against the lithosphere of the Tarim Basin (see Figure 6.25 and *Li et al.*, 2008a). This might be responsible for the recent acceleration (*Zubovich et al.*, 2010; *Sobel et al.*, 2011a) and clockwise rotation of the Tarim Basin, effecting further uplift of the Tien Shan (*Craig et al.*, 2012). Extrapolating the front of underthrusting India further west should make it reach well into the Pamir, possibly even as far north as the MPT. However, I do not see a clear high-velocity body that could potentially be associated with underthrusted India in my tomography results (Figures 6.15 and 6.18). South and east of the imaged Pamir slab, found uppermost mantle velocities are around 8-8.1 km/s, in accordance or only slightly above predictions from the global model *ak135* (*Kennett et al.*, 1995).

A review of regional tomographic studies of the Pamir-Hindu Kush proves inconclusive: no clear front of an Indian indenter at depth is imaged in *Koulakov and Sobolev* (2006) and *Koulakov* (2011), although the latter of these clearly shows elevated uppermost mantle velocities beneath most of the Tibetan plateau. In the images shown by *Negredo et al.* (2007) and *Bijwaard et al.* (1998), the entire Pamir-Hindu Kush region appears to be faster than the background model at depths between 100 and 250 km, again no clear Indian front is identifiable.

In the depth cut at 100 km in *Li et al.* (2008a) (see Figure 6.25, right), the fast material that characterizes underthrusting India all along the Himalaya and under southern Tibet terminates westward directly to the south of the Tarim Basin's western edge. A low-wavespeed anomaly characterizes the southern Pamir, north of which an arcuately shaped zone of high P velocities is imaged. Directly south of it, rather low uppermost mantle velocities prevail. Only farther south, directly at the continental suture, do high velocities possibly indicating Indian lithosphere at depth reoccur (Figure 6.25). At greater depths (*Li et al.*, 2008a), this arcuate anomaly penetrates further south, and the low velocities beneath the southern Pamir disappear. These results fit exceptionally well to what is obtained in the present study: the arcuately shaped high-velocity anomaly corresponds to the Pamir slab, which advances southwards with depth due to its dip direction, whereas lower velocities are found at mantle depths beneath the southern Pamir.

The absence of underthrusted India southwest of the Tarim Basin could be indicative of a relatively recent breakoff event that led to the recycling of previously underthrusted continental lithosphere into the mantle. The last oceanic remnants attached to Greater India are thought to have detached from the henceforth continental "slab" soon after the collision took place, and can still be imaged as high-velocity anomalies in the mantle (*Van der Voo et al.*, 1999). At least one break-off event of continental lithosphere is assumed to have ocurred since, which is often associated with the big change in deformation style throughout Tibet at about 25 Ma (e.g. *Maheo et al.*, 2002). Other studies favor a later date for this breakoff (10-20 Ma, e.g. *DeCelles et al.*, 2002).

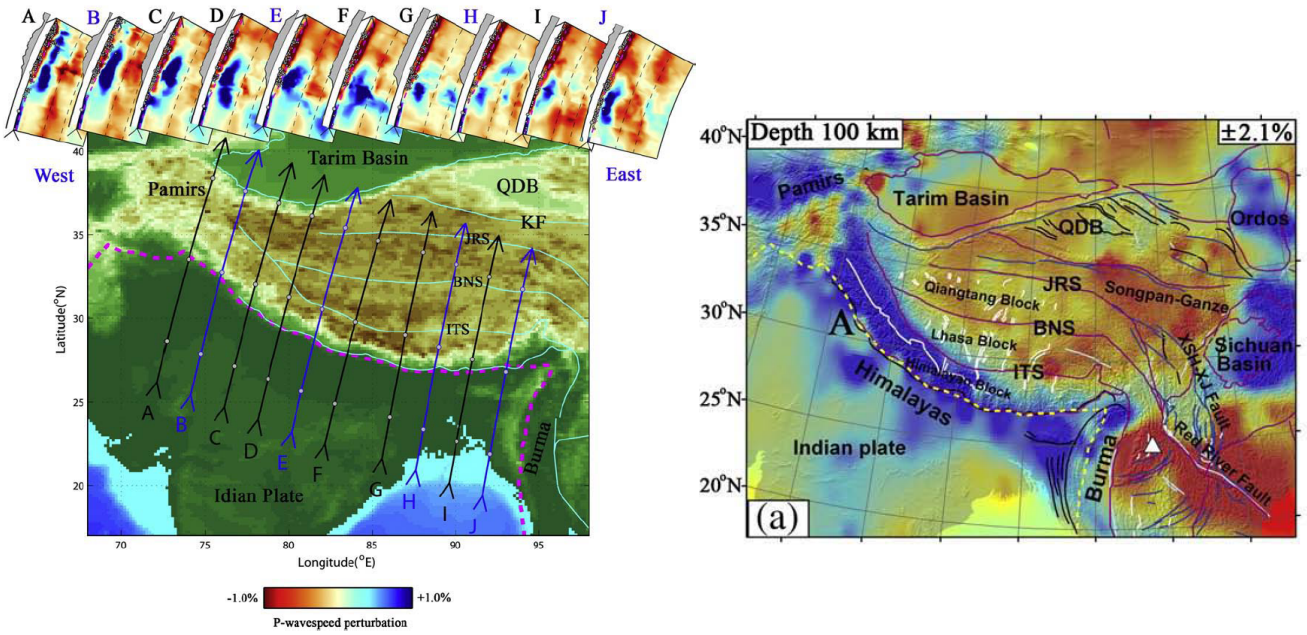

Figure 6.25.: Several cross sections (*left*) and depth section at 100 km depth (*right*) through the multiscale tomographic model of *Li et al.* (2008a) (Figures taken from said publication). Number in the upper right corner of the right subfigure indicate the maximum amplitude of tomographic anomalies in this depth section.

It is possible that either another, more recent breakoff event removed the westernmost part of underthrusting India, or that northward underthrusting ceased there because the relative motion of India and Eurasia was mostly taken up somewhere else (here: southward subduction in the Pamir), stalling the northward advancement of Indian lithosphere. Both of these possibilities require some kind of mechanical decoupling along strike of the slab. The following speculative scenarios can be invoked to explain the absence of underthrusted India beneath the Pamir:

1. In the case of a more recent breakoff, the apparent extent of underthrusting India to not more than 100 km north of the continental suture would require this event to have occurred significantly less than 10 Ma ago. This number emerges when assuming that only 1 cm/yr, i.e. less than a third of the total India-Eurasia convergence at this longitude, are accommodated by underthrusting. However, the obtained estimate has to be further reduced due to the fact that a slab breakoff would probably not reset the slab length to zero, but would leave a slab remnant of some length behind (*Duretz et al.*, 2012). Moreover, a breakoff exclusively occurring along such a small proportion of the entire along-strike length of the slab does not appear intuitive to me.

2. It is likewise possible that the main mode of convergence along the westermost part of the India-Eurasia collision changed from northward underthrusting of India to southward subduction of Eurasia north of the Pamir from the last breakoff event onwards. Taking today's convergence rate at the MPT of 10-15 mm/yr (*Zubovich et al.*, 2010) and a timing at 20-25 Ma of the last breakoff event, this leads to 200-375 km of southward subduction in the Pamir, which correlates well with slab lengths determined from teleseismic tomography (*Negredo et al.*, 2007; *Koulakov and Sobolev*, 2006) and earthquake locations (*Pegler and*

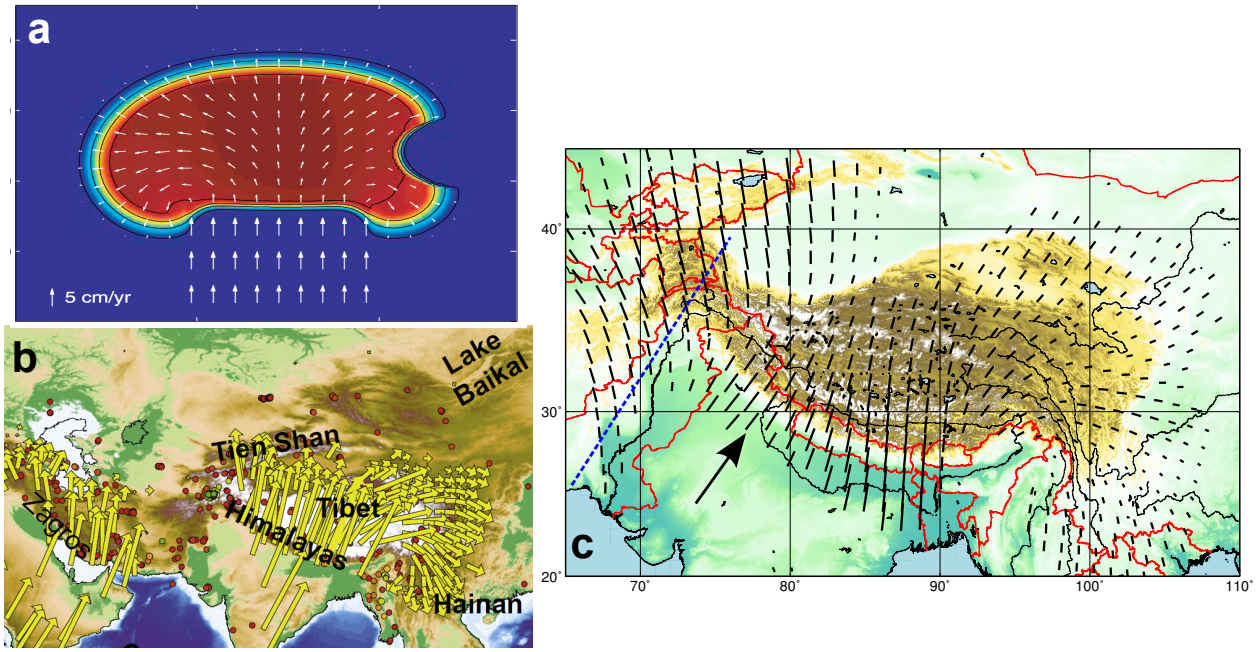

Figure 6.26.: **a:** Numerical simulation result of the indentation of a rigid India into plastic Eurasia (red), effecting a rotation of displacement vectors away from the indenter on the Eurasian side near the syntaxes (Figure taken from *Cook and Royden*, 2008)
b: Compilation of GPS diplacement vectors, showing India's NNE motion relative to Eurasia. Figure modified from *Becker and Faccenna* (2011). Plotted datasets from *Zhang et al.* (2004), *Gan et al.* (2007) and *ArRajehi et al.* (2010).
c: Orientation of principal compressive axes for the Himalaya-Tibet region, computed on a regular grid with the code `SSPX` (*Allmendinger et al.*, 2007; *Cardozo and Allmendinger*, 2009). Computations carried out by *M. Moreno (pers. comm., 2012)*, using GPS data of *Zhang et al.* (2004), *Mohadjer et al.* (2010) and *Zubovich et al.* (2010). Results show that the pure northward compression that constitutes the background deformation in the Pamir-Hindu Kush is likely an edge effect of the NNE-ward indentation of India into Eurasia. Dashed blue line traces the approximate western outline of the Indian indenter. Together with the principal direction of indentation (black arrow), this could lead to a constellation where underthrusted India has its westward termination around the western edge of the Tarim Basin.

Das, 1998, and this study, Chapter 4).

3. Alternatively, the lateral transition from fast to slow velocities shown in Figure 6.25 (right subplot) might mark the western end of the Indian indenter at depth. The Euler pole of India's current motion relative to Eurasia is located at 31.7°N, 17.3°E, i.e. due west of the collision (MORVEL data, *DeMets et al.*, 2010). This implies that India's motion contains a counterclockwise rotation component, which is expressed in convergence rates systematically higher for the eastern part of India (*Molnar and Stock*, 2009), today by about 1 cm/yr. The translative motion this rotation component is superimposed upon is not pure northward, but rather NNE, as evident from GPS (*Zhang et al.*, 2004; *Gan et al.*, 2007) and shown in Figure 6.26b. Likewise, India's trajectory before the collision with Eurasia is assumed to have been in a NNE direction (*Molnar and Stock*, 2009; *Zahirovic et al.*, 2012).

However, GPS vectors in the Pamir-Hindu Kush region show a general pure northward trend (*Mohadjer et al.*, 2010; *Zubovich et al.*, 2010), which could be explained as an edge effect of India's indentation into Eurasia. Principal compression axes for the India-Eurasia collision, calculated on a regularly spaced grid using the software `SSPX` (*Allmendinger et al.*, 2007; *Cardozo and Allmendinger*, 2009) by *M. Moreno (pers. comm., 2012)*, are shown in Figure 6.26c. It is clearly evident that whereas compression axes are north-south on the Indian plate in the very east (Bangladesh), they acquire an eastward component that increases westwards, thus makes the compression axes stay perpendicular to the arcuate strike of the Himalayan front. This tendency, which is mirrored by the fault plane solutions of earthquakes related to active Indian underthrusting (*Ni and Barazangi*, 1984), is a consequence of the counterclockwise rotation of India. Nearing the syntaxes, i.e. the edges of the indenter, compressive axes on the Eurasian side progressively turn outwards, away from the indenter, which is mirrored by the GPS vectors at least on the eastern edge of India (Figure 6.26b). This most likely represents the response of plastic Eurasia to the indentation of rigid, cratonic India, as illustrated in Figure 6.26a. Near the western syntaxis, the few available GPS stations are all within Eurasia, their motion might thus not reflect the indentation direction of India (compressive axes in northern Pakistan plotted in Figure 6.26c which point north-south are a result of interpolation, no data points are available there). I hence propose that the motion of India south of the western syntaxis is NNE-ward (black arrow in the figure), and the northward-directed GPS arrows on the Eurasian side of the collision north of the western syntaxis do not reflect a pure northward movement of India here, as e.g. claimed by *Larson et al.* (1999).

This would have profound consequences: the dashed blue line in Figure 6.26c roughly traces the western termination of the Indian indenter (see Figure 2.3) at the surface, which appears to be parallel with the direction of motion of its western part (black arrow). The prolongation of this line indicates that if the assumptions made are true, underthrusting India would probably pass by to the southeast of my study area and could never underlie the Pamir. However, this theory is highly speculative due to several uncertainties: the exact geometry of the Indian indenter is unclear, the plotting of the blue line in Figure 6.26c is based on the trace of the MFT, which is situated in sediments inside the Indian plate (see Figure 2.2). In the basement, India might easily penetrate further west.

7. Geodynamic Model

In this Chapter, I will try to integrate the obtained findings to a single geodynamic model that potentially explains tectonic processes active in the Pamir and Hindu Kush. This model (shown in Figure 7.1) is, of course, speculative and is surely not the only possible way to interpret the presented evidence. However, I hope it serves as a starting point fur further discussions, and that it will be falsified or modified based on data from other disciplines, such as structural geology, geochronology etc.

Based on the geometry outlined by the hypocentral locations of intermediate-depth earthquakes (Figure 4.10), in combination with tomography images (Figure 6.18), the deep structure beneath the Pamir can be clearly defined as a slab of continental Eurasian provenance. This slab dips due southward in the eastern Pamir, then describes a 90 ° arc to end up with a due eastward dip at its southwestern termination. Westwards, the Pamir slab appears to be continuous into the lithosphere underlying the Tajik Depression, which implies its eastward subduction, possibly also involving the crustal basement of the Tajik Depression. The western termination of the Pamir slab, together with its curvature, is probably linked to a change in the deformation field (see Figure 6.26c) imposed by the India-Eurasia collision at that longitude. Its eastern end appears to be predetermined by the change of crustal properties from the Tajik-Yarkand Basin into the Tarim Basin (*Sobel*, 1999), which instead of being underthrusted transfers deformation further north, into the Tien Shan.

The Pamir, penetrating northward into said Tajik-Yarkand Basin, overthrusted this former basin in a geometry resembling a quarter of a concentrically growing circle. The basement of the overthrusted basin most likely comprised continental shelf material (*Leith*, 1982). As such, it does not readily subduct into the mantle (*Cloos*, 1993) but instead underthrusted the Pamir in the same fashion India underthrusts Eurasia today (see Figure 2.2). Only significantly later did this underthrusted material begin to sink into the mantle, possibly driven by mineral phase transformations occurring as a consequence of the exposure to elevated p-T conditions (e.g. eclogitization of mafic lower crust, see *Kay and Kay*, 1993; *Xu et al.*, 2002). This scenario of underthrusting followed by "delamination" (which is different from delamination in the sense of *Bird*, 1979, see Figure 6.24b) would effect the along-arc extensive stresses within the slab that were shown to dominate in the Pamir slab in Chapter 5. An along-strike minimum in seismicity rate as well as depth extent of the earthquakes (around 73 °E) could be interpreted as ongoing vertical tear in the slab, propagating from bottom to top as would be expected as a consequence of the delamination (see reasoning in Section 5.5.2). A "classical" delamination scenario would not be compatible with the observed presence of upper or middle crustal material at mantle depths, whereas normal subduction is hard to reconcile with the along-arc extensive stress field in the Pamir slab.

During the process of ongoing continental underthrusting, the hingeline of which advances into the surrounding basins ("radial thrusting", see Figure 5.23 (4)), middle or upper crustal material is mostly scraped off and forms, as a series of stacked thrust sheets, the front of the Pamir

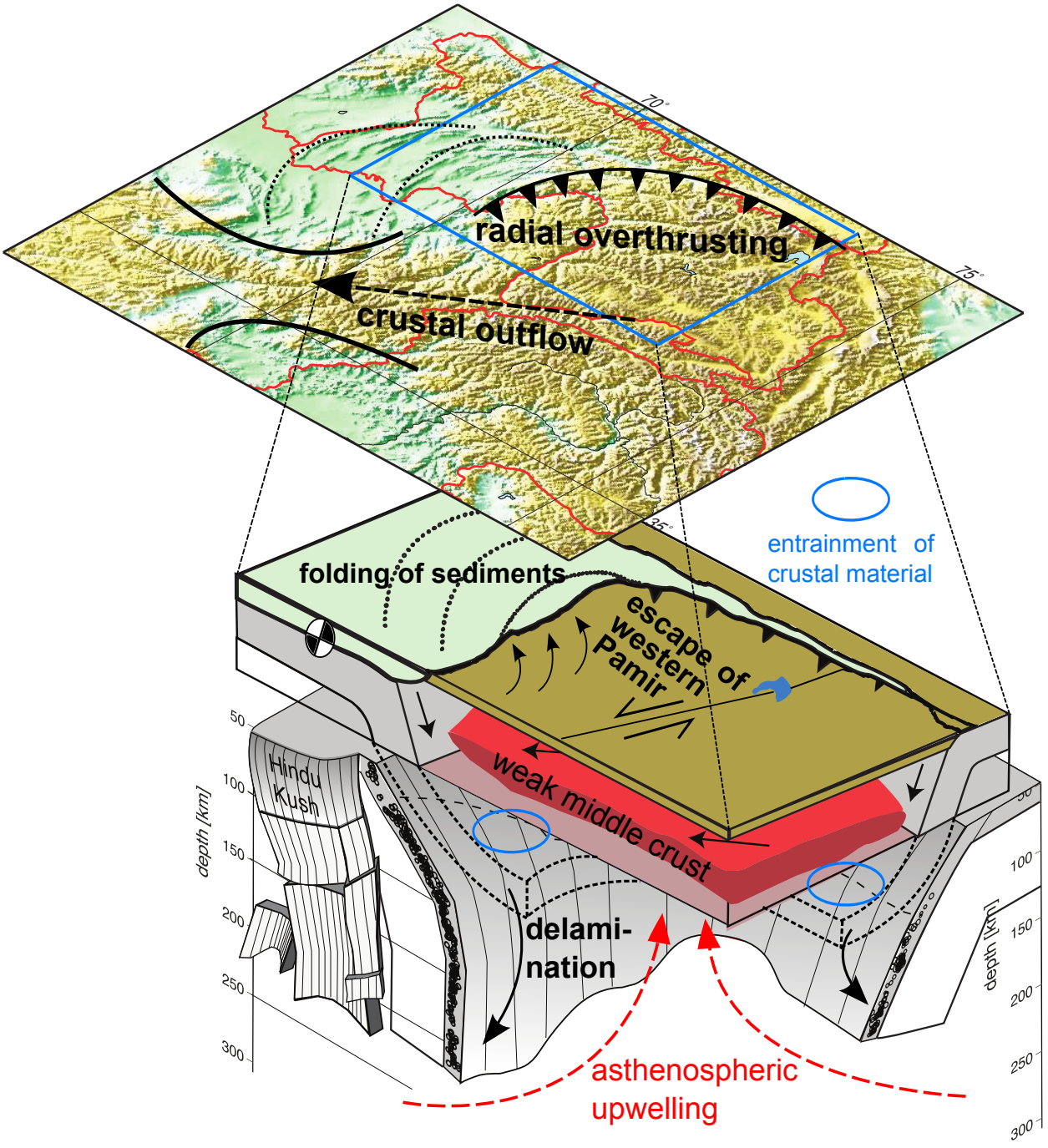

Figure 7.1.: Geodynamic model for the Pamir, summarizing processes described in the text.

Mountains. However, a smaller proportion is entrained in the process of underthrusting and is buried to greater depths, where it can be identified as an anomaly of extremely slow v_p in the uppermost mantle (Figure 6.15, upper right). Due to its buoyancy (*Molnar and Gray*, 1979), this material is not delaminated, but might either be exhumed or added to the continental crust in its further evolution. The lower crustal part of the underthrusted material, however, forms a narrow layer on top of the delaminating slab (imaged with receiver functions, see Figure 6.22) in which intermediate-depth seismicity occurs. Continental lower crust surrounding the entrained upper or middle crustal material is responsible for the forked geometry of earthquake locations at the updip end of the deep seismic zone (see Figure 6.18, profile A-A'). The actual mechanism generating intermediate-depth seismicity can only speculated about here, dehydration embrittlement promoted by the release of fluids from hydrous minerals contained in mafic lower crustal material seems the most likely candidate to me.

Ongoing delamination beneath the Pamir effects return flow of asthenospheric material into the vacated space, possibly also through the slab window between the Pamir and Hindu Kush seismic zones, which might be imaged by a low-velocity anomaly north of Hindu Kush seismicity at depths exceeding 120 km (see Figure 6.15). This upwelling, together with the removal of the dense "crustal root" (underthrusted material after phase transformation) would effect the uplift of the Pamir Plateau and elevated crustal temperatures in the southern Pamir. Lower seismic velocities and higher measured heat flow values in the southern Pamir (see Figure 6.20) can hence be explained. Steeper geotherms in the southern Pamir compared to further north are likewise indicated by a southward shallowing of the maximum seismogenic depth in the crust, which can be discerned by a careful look at the longitudinal profile in Figure 4.10. Another consequence of the delamination process should be extension in the upper plate, which would be maximum in a direction perpendicular to the strike of the delaminating structure. Due to the arcuate geometry of the proposed delamination, extension should occur in north-south as well as in east-west direction. This extension, together with the presence of a warm, weak and ductile middle crust, could have induced or at least facilitated the uplift of the south Pamir gneiss domes (*Schmidt et al.*, 2011; *Stübner et al.*, 2012). Current crustal tectonics in the northern Pamir are most likely a superposition of ongoing radial thrusting, i.e. north- and westward propagation of overthrusting, and a likely gravity-driven, distributed westward escape of the northwestern Pamir.

The high electrical conductivity of the middle and lower crust in the southern Pamir (Figure 6.20) is interpreted with the presence of partial melt, which could imply crustal channel flow, similar to what has been proposed for the region of the Eastern Himalayan Syntaxis (*Bai et al.*, 2010) or the entirety of East Tibet (*Clark and Royden*, 2000). On a topographic map, the western Hindu Kush appears like an outflow structure, fanning out to the southwest after passing through a "bottleneck" around 35.5 °N, 69.5 °E. Middle to lower crustal outflow, driven by gravitative forces due to the difference in altitude between Pamir Plateau and its surroundings to the southwest, could explain the presence of elevated topography in a region dominated by pure strike-slip tectonics.

The apparent lateral discontinuity of underthrusted India (see Figure 6.26b), which is clearly not present beneath the southern Pamir (Figure 6.18), necessitates the mechanical transfer of stress from the India-Eurasia collision through the Pamir crust to drive the underthrusting north of it. Although the Pamir crust seems to be in a rather weak state, thermomechanical modeling (*J. Tympel, pers. comm., 2012*) has shown that such a transfer is possible.

The provenance of the slab beneath the Hindu Kush could not be clarified in this work. Although

there are minor clues for a Eurasian origin, it remains questionable how the presence of this slab could be incorporated into the presented model. Further research has to be performed in order to get more constraints on velocities in and around the Hindu Kush slab.

8. Conclusions and Outlook

In this thesis, crustal and intermediate-depth seismicity of the Pamir-Hindu Kush occurring between 2008 and 2010 has been systematically catalogued, employing a specially designed automated processing chain. A subset of the obtained phase picks is utilized for tomographic inversion, inverting for the spatial distribution of v_p and v_p/v_s at depths of up to 200 km. Additionally, fault plane solutions are determined, combining the analysis of first motion polarities with a waveform inversion technique in order to maximize the number of earthquake for which a mechanism can be retrieved. Obtained results can be summarized as follows:

Crustal seismic activity is mostly observed around the northern and northwestern circumference of the Pamir and throughout the Pamir's west, whereas its eastern part appears to be nearly aseismic. Western an eastern Pamir seem to be separated by a seismically active, NNE-SSW striking lineament. Focal mechanisms throughout the western Pamir and even along most of the Main Pamir Thrust show a predominance of sinistral strike-slip events with northeast-southwest trending rupture planes. Compressive axes of Pamir earthquakes are mainly oriented north-south, but acquire an east-west component in the northwestern Pamir. Into the Tajik Depression, P axes are observed to further turn towards a pure east-west orientation. Earthquakes featuring a westward relative motion of the sediment cover with respect to the basement are found for the Tajik Depression, their depth corresponds well to the location of an evaporite décollement decoupling sediments and basement. Since deformation in salt should occur ductilely, these earthquakes are assumed to represent stick-slip motion in places where the salt layer is absent. The crust of the southern Pamir is found to be strong and brittle only in the uppermost 10-15 km, evident from a shallowing of the lower end of the seismogenic zone. Below, low seismic velocities and high electrical conductivity hint at the presence of partial melts, which could promote crustal outflow towards the southwest.

At mantle depths, seismicity outlines two distinct structures beneath the Pamir and Hindu Kush, separated by a gap that widens with depth. Across this gap, a 90 ° change of dip and strike direction occurs. Earthquakes in the Hindu Kush define a to first order subvertically northward dipping, east-west striking planar structure, which features considerable complexity, i.e. dip change along strike, segmentation into a shallower and a deeper part separated by a seismic gap at about 150 km depth and fragmentation of the lower part into several distinct, highly seismically active clusters. In contrast to this structural complexity, observed earthquake mechanisms of the Hindu Kush are remarkably uniform, consistently featuring downdip extension with nearly vertical T axes, P axes are oriented perpendicular to the strike of the structure.

The Pamir seismic zone, as outlined by hypocentral locations, defines an arc resembling the upper left quarter of a full circle. Earthquakes occur along narrow planes, which feature a dip angle of about 50 °, which steepens to (sub)vertical at depths greater than 150 km in the western part of the Pamir seismic zone. Observed earthquakes occur within a thin low-velocity zone overlying the subducting (or delaminating) Pamir slab. Directly above the upper end of intermediate-depth

seismicity, very low seismic velocities are found at mantle depths, which hint at the deep burial of middle crustal material. Earthquake mechanisms of deep Pamir events are more heterogeneous than in the Hindu Kush, but exhibit a tendency of along-arc extension, which is indicative of active bending of the slab.

Observed findings were interpreted in a model of continental underthrusting of the Tajik-Yarkand Basin under the Pamir, followed by delamination of lower crust and mantle lithosphere. Middle crustal material is entrained in the initial underthrusting, but not the later recycling into the mantle, whereas continental lower crust is subducted to greater depth as a seismogenic thin layer atop the mantle lithospheric slab. Asthenospheric return flow effected by this delamination causes high temperatures and middle crustal melting in the southern Pamir, which might lead to plastic flow of topography.

To further illuminate active tectonic processes in the Pamir and Hindu Kush, a teleseismic tomography study, utilizing the obtained recordings of distant earthquakes, could provide useful information about the depth extent of the Pamir slab, which can not be determined with the local earthquake tomography shown here. This knowledge could be useful for estimating a rough material budget, which could yield an indication of whether the proposed mechanism of underthrusting followed by delamination is valid or not. Moreover, to know whether or not the downdip end of seismicity coincides with the downdip end of the slab could provide insights for the mechanism behind the seismicity. In order to integrate findings from local and teleseismic tomographic studies, a joint inversion of both data sets could be attempted.

More information about the deep structure of the Hindu Kush is vital for the understanding of large-scale processes active in Central Asia. However, these can not be gleaned from a teleseismic tomography study utilizing the TIPAGE (or TIPTIMON) stations, since the network geometry, together with the predominance of teleseismic events from eastern directions, is far from ideal for sampling the Hindu Kush slab. This could be overcome either by the installation of stations in Afghanistan or by making use of source-receiver reciprocity in the teleseismic tomography (i.e. not using global events recorded by Pamir-Hindu Kush stations but Pamir-Hindu Kush events recorded by global stations, see *Koulakov and Sobolev*, 2006). The provenance of the Hindu Kush is a very important piece in the Central Asian tectonic puzzle.

As already mentioned in Section 5.5.1, a detailed GPS survey centered on the Main Pamir Thrust, retrieving a more precise value for current convergence across it, and likewise some idea about possible along-strike variation of convergence rates, would help to discriminate between different possible models for upper crustal deformation in the northern and western Pamir.

In order to clarify whether or not the proposed channel flow of middle and possibly lower crustal material from the southern Pamir into the western Hindu Kush might actually be occurring, a magnetotelluric study in the southwestern Pamir would be interesting (although probably logistically very challenging). It could thus be investigated if the found middle crustal conductor in the eastern Pamir continues all the way into the Pamir's west, as indicated by the continuity of low seismic wavespeeds.

Another important goal of future research should be the retrieval of exact petrophysical parameters, i.e. v_p, v_s and possibly density, for the crustal material at depth imaged beneath the Pamir with local earthquake tomography and receiver functions. The knowledge of the composition and state of this material is critical when attempting to explain the creation of intermediate-depth

seismicity in buried continental crustal rocks. Possible roads towards this goal are the modelling of guided waves travelling through the narrow low-velocity channel and the application of the method of *Lin and Shearer* (2007) for retrieving *in situ* v_p/v_s values.

Moreover, the automated phase picking and earthquake location procedure outlined in Chapter 4 should be re-applied to the Tajik Depression, using an adapted velocity model in order to quantify what proportion of events was actually missed due to the for this region grossly wrong averaged 1D model, and in order to get a better idea about the seismicity of this area.

A. Correction of Timing Errors

Digitizer logfiles were checked for prolonged GPS outages for all stations where these files were available (networks TI, TF, FH). Outages lasting longer than two weeks were listed (see Table A.1) and examined in more detail. For shorter periods of lacking GPS reception, the internal clocks of the dataloggers should be sufficiently precise to guarantee accurate timing.

A noise cross-correlation technique (roughly following the concept of *Sens-Schönfelder*, 2008) was applied for checking and, where necessary, correcting the timing of the listed stations. The main advantage of this approach over, for instance, using travel time differences of teleseismic events recorded by station pairs, is that it provides a continuous temporary evolution of the clock error rather than just point measurements of clock drift.

The nearest broadband station with flawless GPS reception was chosen as reference for each of the stations. The following preprocessing steps were applied (as in *Bensen et al.*, 2007):

1. downsampling to 20 Hz for accelerating the calculations. Even lower sampling frequencies were tried, but provided insufficient accuracy of resulting clock error estimates
2. instrument simulation: All traces were migrated to a Mark L4-3D 1Hz seismometer (the only short-period instrument involved)
3. demeaning and detrending of traces
4. bandpass filtering with a 2-corner Butterworth filter, corner frequencies 0.1 and 0.5 (as these values yielded the best results although being below the instrument's corner frequency)
5. amplitude normalization as defined in *Bensen et al.* (2007)

Subsequently, data were cross-correlated hourwise in the time domain (using a function from the software package ObsPy (*Beyreuther et al.*, 2010)). 24 hourly Green's Functions were combined to a daily stack for each of the three components. An example for nearly nine months of daily stacks for the station pair RAJ8-BAR8 (here: E component only) can be seen in Figure A.1.

It is evident from this Figure that the internal clock of station RAJ8, without GPS reception from day 93 onwards because the GPS cable had been chewn through by an animal, shows a clear drift relative to "true" GPS timing. The main maximum of the GF is, at the start of the time series, found at roughly 8 seconds time shift (this value is proportional to the inter-station distance) and begins to migrate to smaller values for days later than roughly 150 (see Figure A.1). This means that the internal clock of station RAJ8 went faster than the true time given by GPS at station BAR8.

To better resolve this clock drift, a monthly stack of GFs computed for the time before the GPS outage was used as reference trace, and the daily GFs were cross-correlated against it. Results from this procedure can be seen in Figure A.2, left image. A clear trend is already discernible

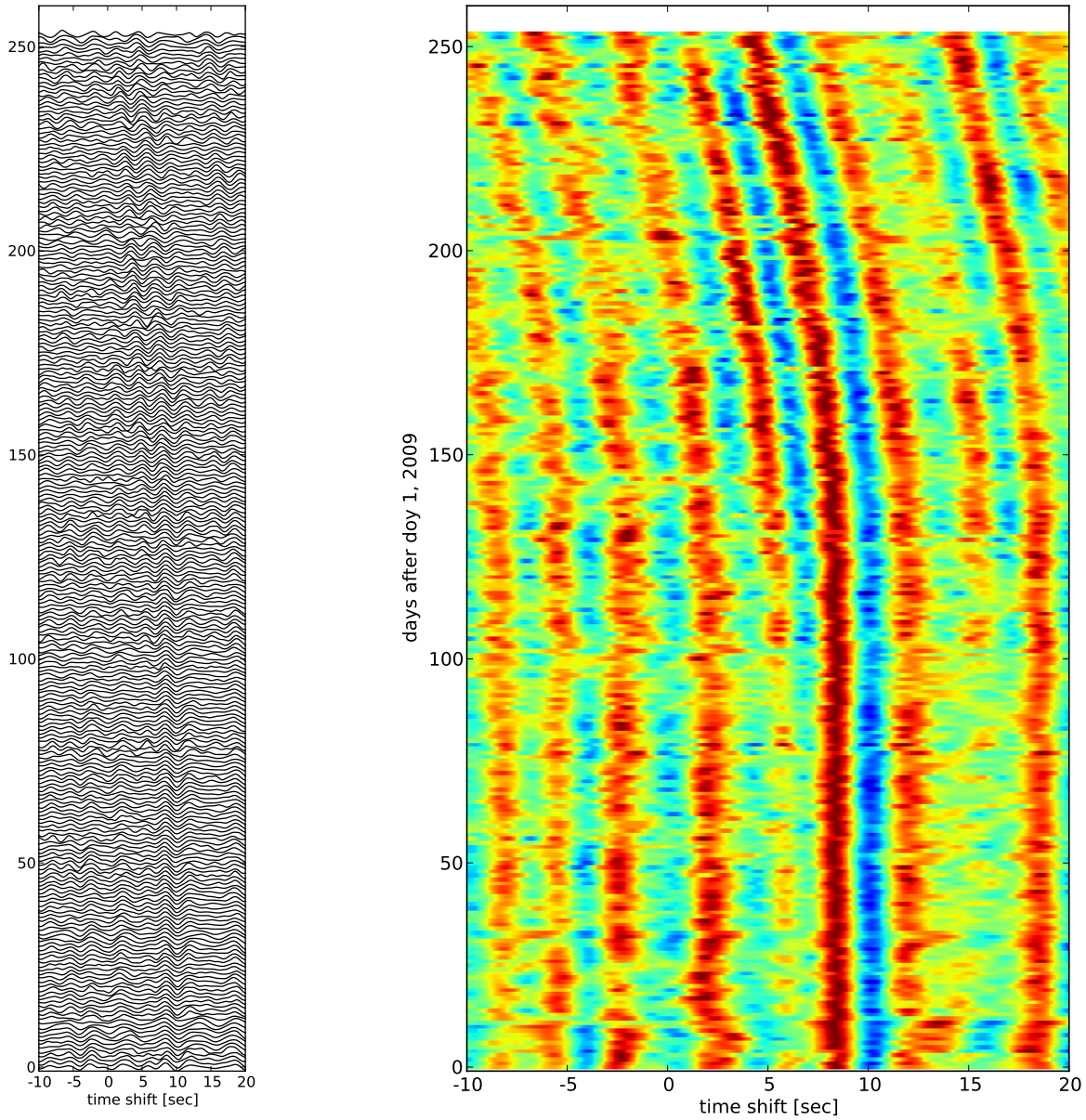

Figure A.1.: Green's functions retrieved through noise cross-correlation of E components from the station pair RAJ8 - BAR8. For a detailed description of processing steps applied refer to the text. GPS reception at station RAJ8 was lost at day 93, a drift of its clock is visible roughly from day 150 on. Both subfigures display the same Green's functions, only use a different visualization method. On the left, the traces are represented as wiggles, whereas they are shown color-coded in the right subfigure. Colors represent values of -1 (dark blue) to +1 (dark red) for the normalized traces.

station	GPS outage time (julian days)	duration (days)	correlation with	correction necessary?
MAD8	2008/230 - 2009/012	149	P15	no
	2009/059 - 2009/074	16	P15	no
	2009/175 - 2009/192	18	P15	no
	2009/220 - 2009/244	25	P15	no
RAJ8	2009/093 - 2009/254	162	BAR8	yes
P20	2009/140 - 2009/155	16	P21	no
POI8	2009/177 - 2009/193	17	BAR8	no
POI9	2009/277 - 2009/307	31	KOK8	no
TOK9	2009/251 - 2010/172	288	SHA8	yes
P07	2010/127 - 2010/194	68	P03	no
F16	2010/129 - 2010/159	31	F22	yes

Table A.1.: Summary of GPS reception outages of more than 14 days' duration

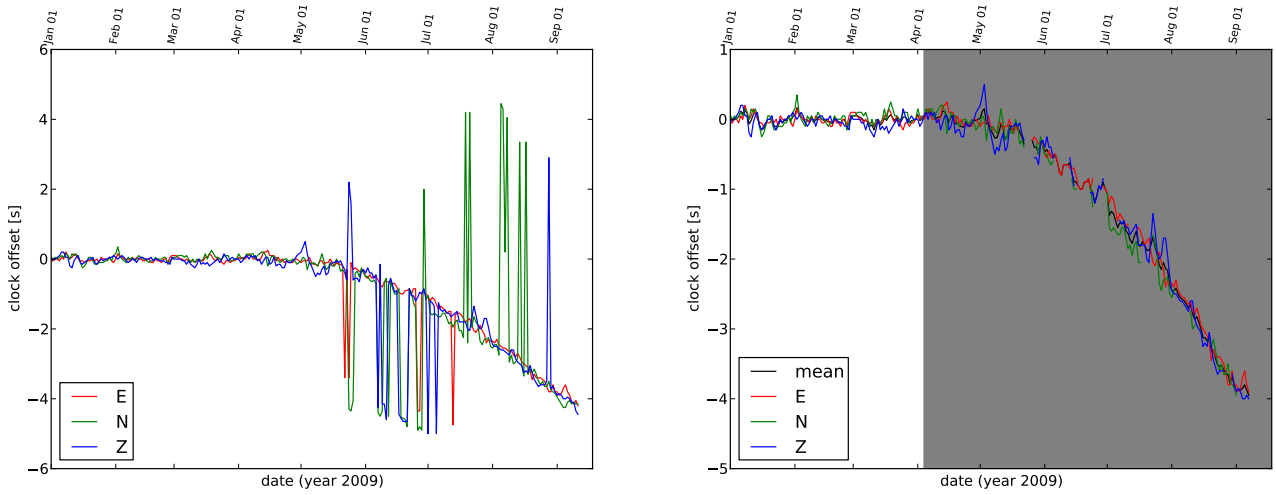

Figure A.2.: Cross-correlation of the obtained daily Green's functions to a reference trace, here a stack of the GFs of the first month, in which both stations had an operational GPS timing. Colors denote the different components.
(left) "Raw" traces: Sudden jumps indicate cycle skipping, i.e. a neighboring "wiggle" obtained a higher correlation coefficient than the "correct" one
(right) After despiking procedure (see text): Data points associated with cycle skipping were removed automatically (note the gaps in the various traces), the mean over all three components (if present) was calculated for each day in order to obtain a more robust estimate of the timing error. Grey shading indicates the time without GPS reception.

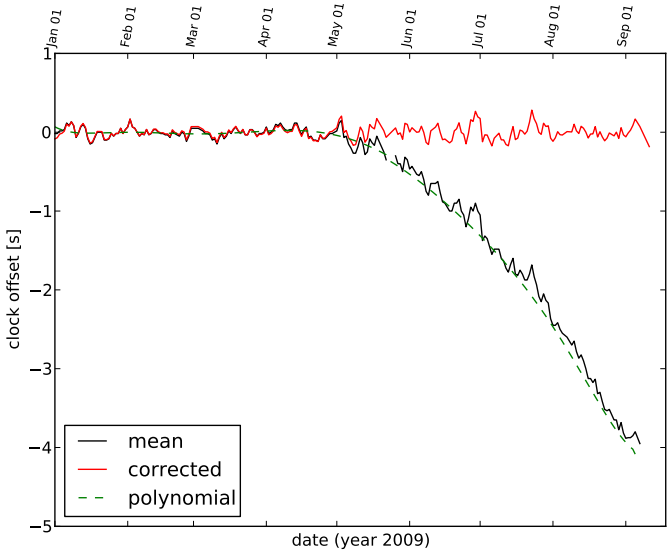

Figure A.3.: Mean curve from Figure A.2 (black) fitted by a third-order polynomial (dashed green). Subtracting the polynomial from this mean yields the curve shown in red, which robustly stays near a timing error of 0.

in this figure, but, especially towards later times, many sudden jumps in the offset values occur. These are due to cycle skipping, a peak/trough is wrongly correlated to a neighboring peak/trough in the other trace. These effects were somewhat suppressed in the left image by setting a maximum possible daily clock drift value. Moreover, a rather primitive despiking routine was used to get rid of erroneous time offsets caused by cycle skipping, causing the gaps in the traces of the right subfigure. The mean value over the three single components was judged to be more robust than any of the components alone, so it was used in the final correction procedure. A third-order polynomial was fitted to the encountered clock offset curve (see Figure A.3), values of which were utilized to correct the timing of daily traces by shifting the start time header values. Maximum total clock drift was slightly above four seconds.

The clock drift encountered for station TOK9 was considerably more rapid, TOK9's clock deviated from "true" GPS time by nearly one second per day (see Figure A.4. With GPS problems beginning only two days after installation, no robust reference trace could be computed for this station pair. Hence, TOK9 was not used in this study.

Station F16 exhibited a one minute time jump (see Figure A.5) that was also corrected. Other stations produced no measurable clock drift.

The applied correction for station RAJ8 should be capable to yield a timing uncertainty smaller than +-0.1 seconds.

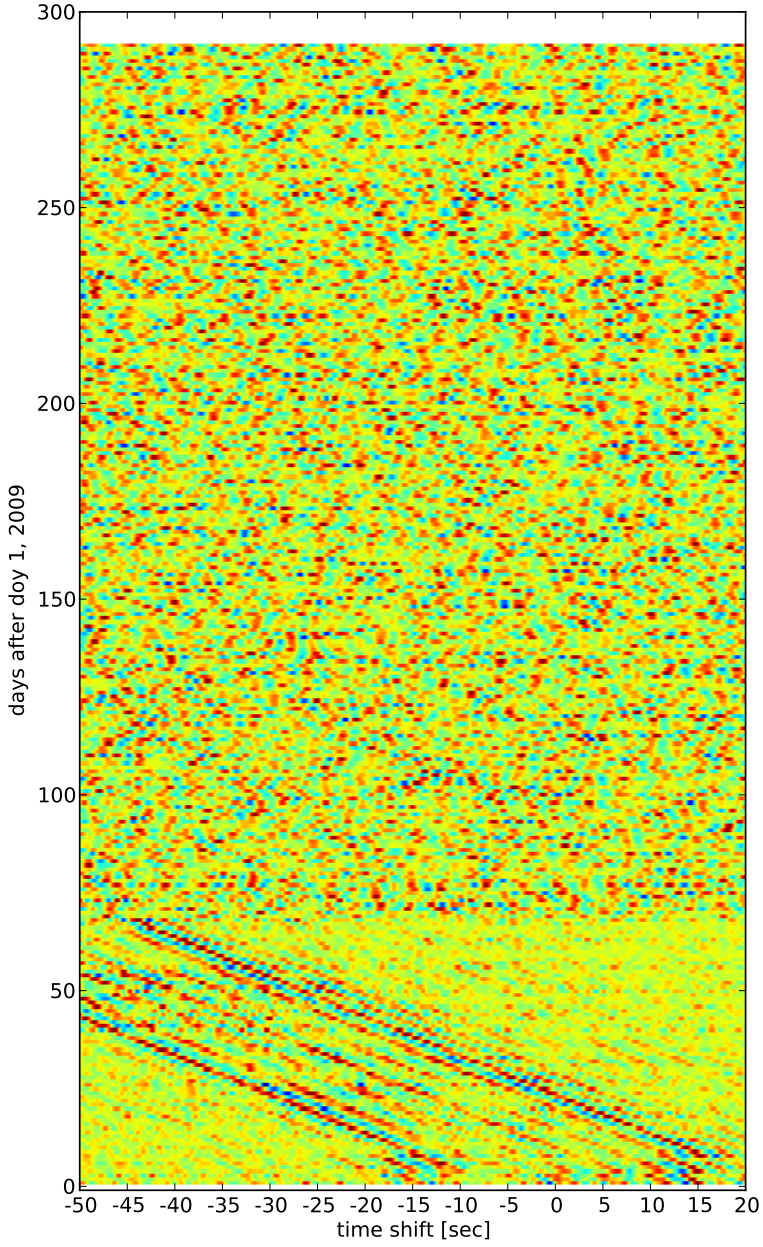

Figure A.4.: Retrieved Green's functions for station pair TOK9-SHA8. TOK9 was without GPS reception from the second day of recording. During the first few days, it repeatedly lost GPS reception and regained it, producing, even in these relatively short periods of GPS loss, comparatively big lag times (a lot bigger than they should be for this type of digitizer). From about day 6 onwards, GPS was finally lost, and the clock constantly drifted away from true GPS time by nearly one second per day.

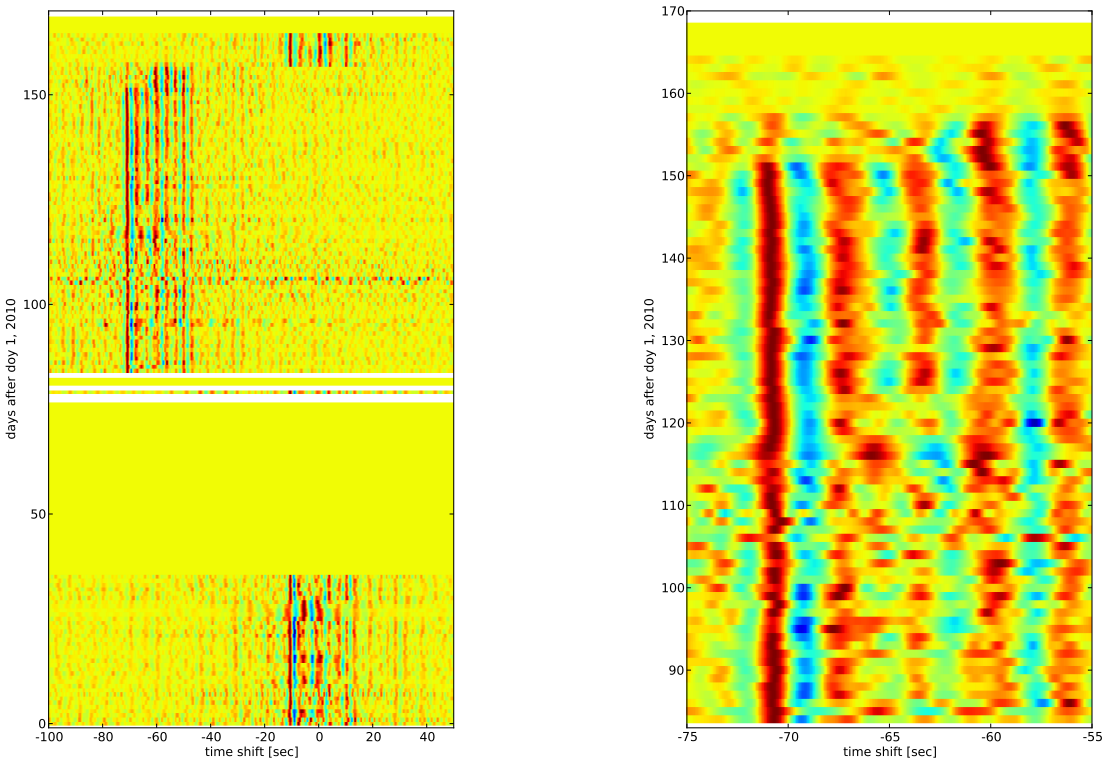

Figure A.5.: Retrieved Green's functions for station pair F16-F22.
(left) Whole time period, with the clearly visible deflection of 60 seconds from day 84 to day 158
(right) Zoom into the region where the true GPS outage occurred. No continuous drift super-imposed onto the 60 seconds jump is discernible.

B. Calibration of MPX

MPX uses a set of nine predictor variables to imitate the picking style of a human analyst (*Aldersons*, 2004). These variables are retrieved from the application of a calibration procedure with handpicked data, utilizing signal characteristics in the pick vicinity and multiple discriminant analysis (MDA). The predictor variables have to be adjusted to the data set and the human analyst, hence MPX should not be used "out of the box", but should be calibrated with a carefully handpicked (*Diehl et al.*, 2009a) benchmark data set. For a guideline to this calibration procedure, refer to *Diehl and Kissling* (2008).

A representative selection of 235 manually picked earthquakes comprising 9,178 P picks was used for this calibration of MPX. Assuming that the manual picks represent the true arrival time, "true weights" W_{true} based on the residual ϵ_{Pick} between handpick and MPX pick are defined for use in the MDA. Three slightly different schemes for the calculation of W_{true} were applied (see *Diehl and Kissling*, 2008), their performance is evaluated in the three confusion matrices in Figure B.1 (for an explanation of confusion matrices, refer to Figure 4.3). Based on these matrices, scheme TW2 was chosen as optimal, since it falsely upgrades significantly less picks than TW1, while not rejecting and downgrading as many arrivals as TW3. For the predictor variables determined for each of these weighting schemes, refer to Table B.1.

MPX comes with a set of predictor variables (Table B.1) determined for a dataset in the Dead Sea region (*Aldersons*, 2004). Application of this set of variables ("out of the box" use of MPX) leads to a markedly worse performance (see Figure B.1), where a larger amount of picks is falsely upgraded to high quality classes.

weighting scheme	quality class	Constant	WFStoN	GDStoN	GDAmpRatio	SigFmaxRa	DFAmpMax	CFRatio	PcAbove	PcBelow	CFNoiDev
Dead Sea	0	-23.260	0.860	-0.266	0.461	0.297	0.06068	-0.658	-2.252	0.185	10.120
	1	-24.030	0.887	-0.330	0.425	0.303	0.08187	-0.690	-2.246	0.235	10.430
	2	-23.060	0.891	-0.303	0.358	0.264	0.02194	-0.494	-2.329	0.241	10.310
	3	-28.630	0.993	-0.322	0.367	0.256	0.141	-0.419	-1.187	0.339	10.860
TW 1	0	-16.462	0.390	-0.563	0.649	0.302	-0.092	-0.259	-1.159	0.066	5.078
	1	-14.653	0.403	-0.475	0.503	0.277	-0.074	-0.342	-1.235	0.075	5.352
	2	-14.621	0.398	-0.518	0.538	0.264	-0.055	-0.294	-1.197	0.081	5.504
	3	-14.229	0.358	-0.583	0.640	0.233	-0.049	-0.240	-1.121	0.092	5.487
TW 2	0	-18.459	0.397	-0.598	0.743	0.310	-0.106	-0.133	-1.023	0.062	4.567
	1	-15.253	0.408	-0.492	0.539	0.296	-0.087	-0.325	-1.152	0.063	5.129
	2	-14.676	0.405	-0.523	0.552	0.266	-0.064	-0.292	-1.211	0.078	5.377
	3	-14.407	0.352	-0.592	0.658	0.237	-0.050	-0.224	-1.131	0.095	5.498
TW 3	0	-18.390	0.389	-0.612	0.764	0.308	-0.105	-0.128	-1.020	0.064	4.601
	1	-15.390	0.395	-0.530	0.584	0.305	-0.094	-0.315	-1.158	0.058	5.152
	2	-15.060	0.406	-0.489	0.541	0.280	-0.073	-0.339	-1.177	0.075	5.271
	3	-14.380	0.371	-0.567	0.619	0.246	-0.055	-0.242	-1.152	0.088	5.442

Table B.1.: Predictor variables used in the four different calibration schemes

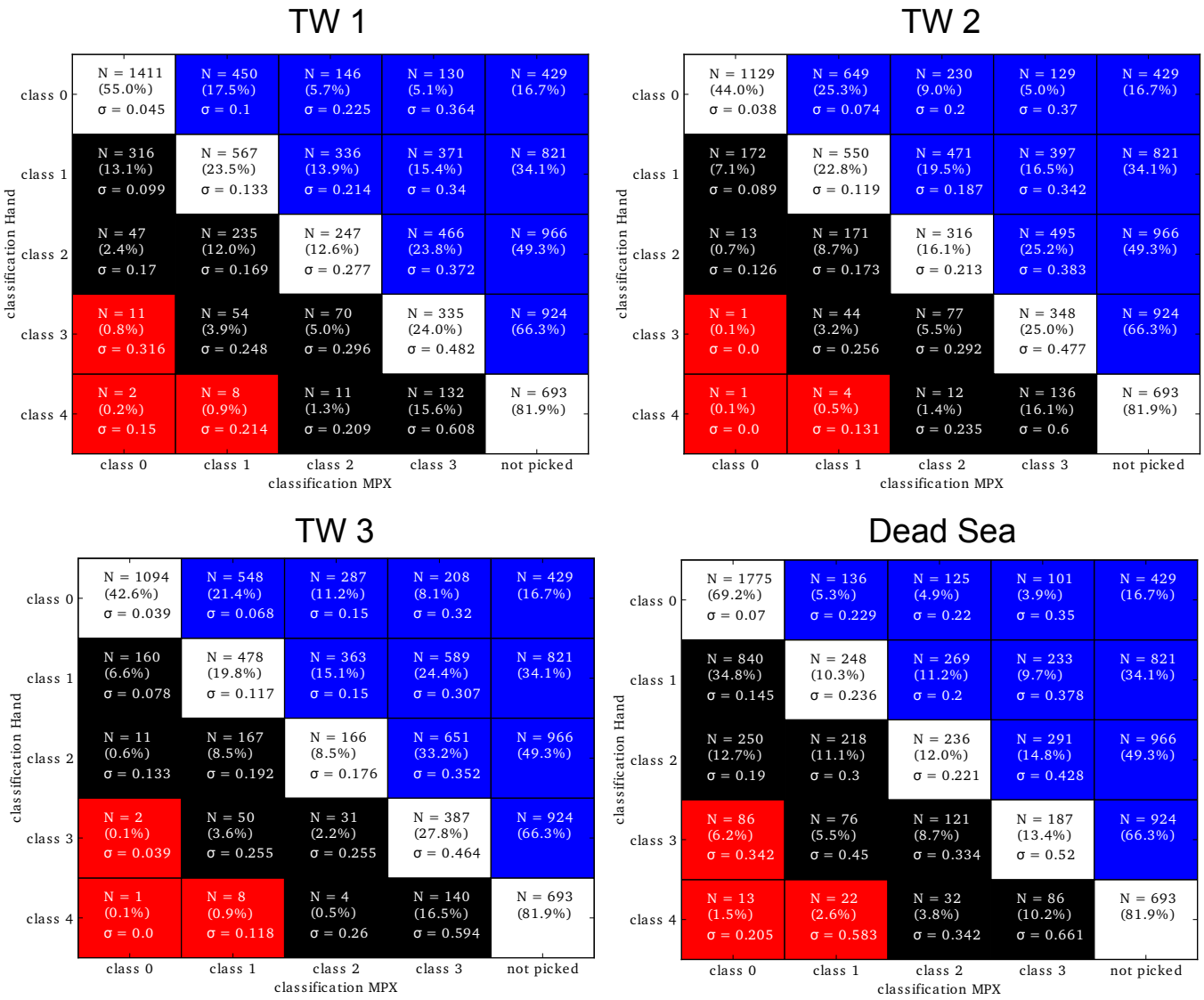

Figure B.1.: Comparison of confusion matrices with four different calibration schemes: TW 1 through TW 3 denote different calibration strategies (see text), Dead Sea shows uncalibrated usage of MPX with the supplied coefficients. For an explanation of confusion matrices, refer to Figure 4.3. The actual picked arrivals, both from MPX and performed manually, are the same for all sets, the only difference are the assigned weights. This means that the contents of each row in the confusion matrix are redistributed (only the last entry for onsets not identified by MPX stays the same). The goal is to have as few as possible entries in the black and especially the red fields, and the values for σ should be conforming to the formal weighting criteria as listed in Table 4.1. It is clearly discernible that the weighting scheme "Dead Sea" (and, to a lesser degree, also "TW 1"), falsely upgrades too many picks of high uncertainty and actual picking error into high quality classes.

C. Comparison of seismicity distribution to ISC, EHB and ZSSSR catalogs

Since only two years of data are investigated in the framework of this thesis, the question whether the imaged distribution of seismicity is representative of actual processes in the region is consequential. I herein try to get an idea if the long-term behavior of intermediate-depth seismicity differs from the picture I obtained in Chapter 4 by comparing my results to locations in existing global (EHB, ISC) catalogs and to a Soviet regional seismicity catalog.

The ISC catalog (*Bondár and Storchak*, 2011) is a global earthquake bulletin where earthquake locations, mostly done utilizing globally distributed stations, are collected. This catalog is frequently used as database for global or regional teleseismic tomography studies (e.g. *Koulakov and Sobolev*, 2006) and was used for the cross section plots in *Fan et al.* (1994). Between 1962 and 2010, 21,712 hypocentral locations for the Pamir-Hindu Kush area can be found in the ISC catalog.

The EHB catalog (*Engdahl et al.*, 1998) contains significantly fewer events than the ISC, but the locations, especially concerning hypocentral depths, should be of higher reliability through the relocation with use of depth phases. The global tomography study of *Li et al.* (2008b) used this catalog as primary data source. 2,284 Pamir-Hindu Kush events for the time interval 1960-2007 were extracted.

The so-called ZSSSR catalog for Tajikistan and surroundings (*Leith and Simpson*, 1986b; *Simpson et al.*, 1987), covering the years 1962 through 1985, contains 43,425 regional earthquake locations retrieved from a network of permanent regional seismograph stations. Unfortunately, only the origin times, locations and magnitudes, but apparently not the arrival times for the single stations survived the fall of the Soviet Union. Soviet energy classes K are translated to magnitudes with the empirical formula by *Rautian* (1960)

$$M = (K - 4)/1.8 \tag{C.1}$$

Locations in this catalog were performed on a grid, the grid spacing was apparently chosen to reflect the potential resolution dictated by the station geometry. For most deep events in the Pamir and Hindu Kush, the grid cells have a size $0.1° \times 0.1° \times 10$ km, whereas they are significantly smaller throughout the Tajik Depression and especially in the Garm region, which used to be the center of Soviet seismological investigations.

A comparison of these catalogs for the three cross sections through the Hindu Kush (Figures C.1, C.2 and C.3) shows that the ISC catalog exhibits by far the most scatter in locations. Moreover, it features several horizontal lines of earthquakes that reflect the fixing of hypocentral depths to certain standard values (most common: 33 km) for badly resolved events.

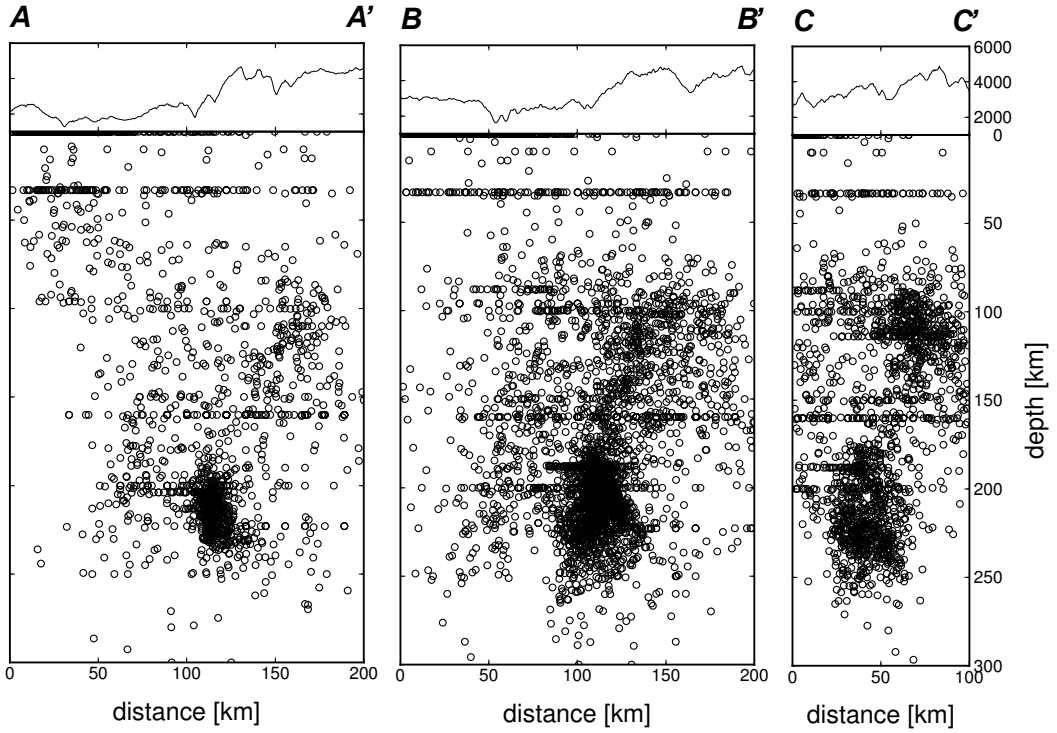

Figure C.1.: Cross sections through Hindu Kush events in the ISC catalog, between 1962 and 2010. For location and orientation of the shown profiles, refer to Figure 4.10.

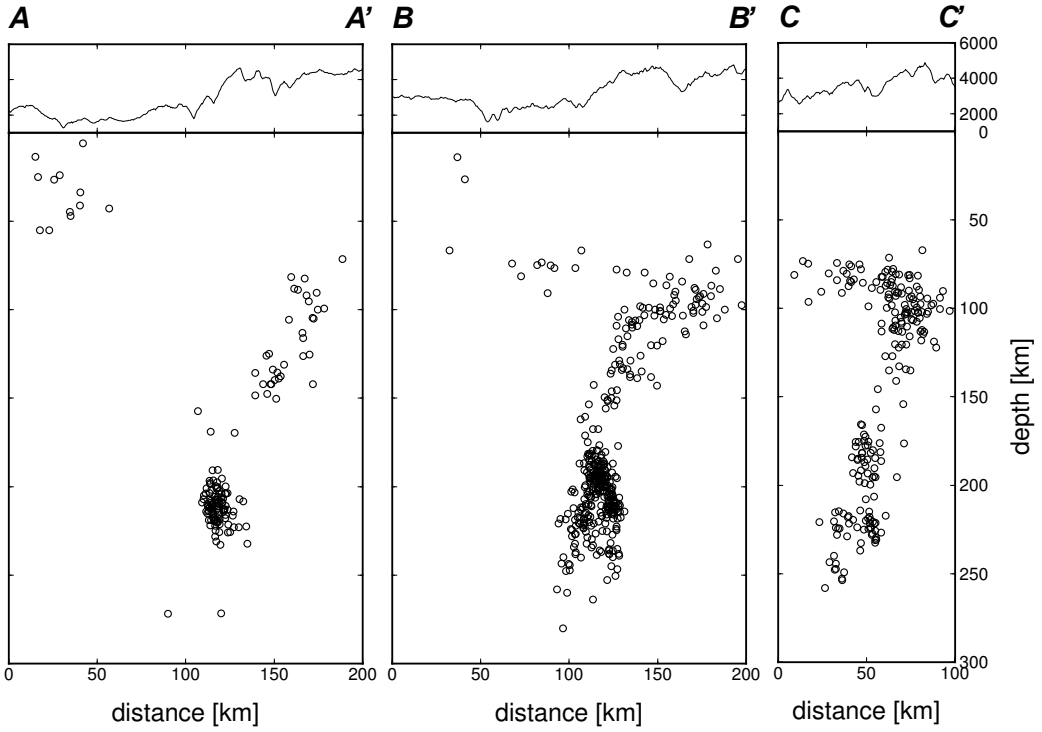

Figure C.2.: Cross sections through Hindu Kush events in the EHB catalog, between 1960 and 2007. For location and orientation of the shown profiles, refer to Figure 4.10.

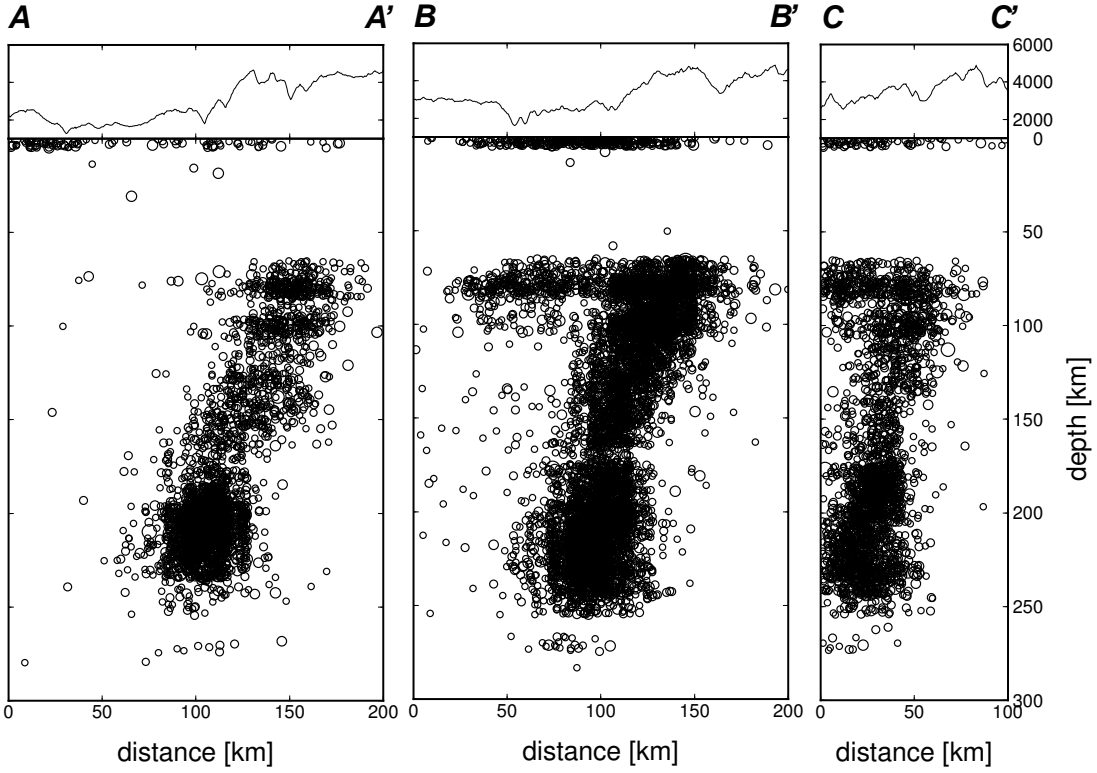

Figure C.3.: Cross sections through Hindu Kush events of the ZSSSR catalog, years 1962 through 1985. For imaging purposes, the grid-bound locations were perturbed in all three dimensions by adding random noise of a maximal amplitude that is half the grid cell size (i.e. filling out the cells). For location and orientation of the shown profiles, refer to Figure 4.10.

Even so, a number of features from the profiles in Figure 4.14 can be recognized here. The presence of an isolated, steeply southward dipping cluster of earthquakes at depth in cross section A-A' is evident in both EHB and ISC data, whereas the ZSSSR catalog rather shows a continuous structure extending from the Moho downwards. A general northward vergence of the Hindu Kush seismic zone, with the highest seismicity rates in its lower part, is shown by all three datasets.

Events from the EHB catalog appear to resolve more structural detail, the presence of two planar structures with opposite dip in cross section B-B' appears to confirm the results of Chapter 4. However, the presence of distinct subclusters for the deeper events of cross section C-C' is not resolved.

In general, outlined structures in the catalog data appear significantly broader than in Figure 4.14, which is to be expected of teleseismic locations (ISC, EHB) and, for the Soviet data, might reflect non-ideal network geometry, less precise analog data (e.g. concerning timing information) or a less advanced location procedure.

For intermediate-depth earthquakes in the Pamir, the ZSSSR catalog shows the best defined structures (Figures C.4, C.5 and C.6), which is probably due to station geometry, since the Soviets operated some permanent stations in the Pamir (e.g. Khorog, Murghab). The EHB catalog does not contain enough deep Pamir events (probably due to their generally small magnitudes) to

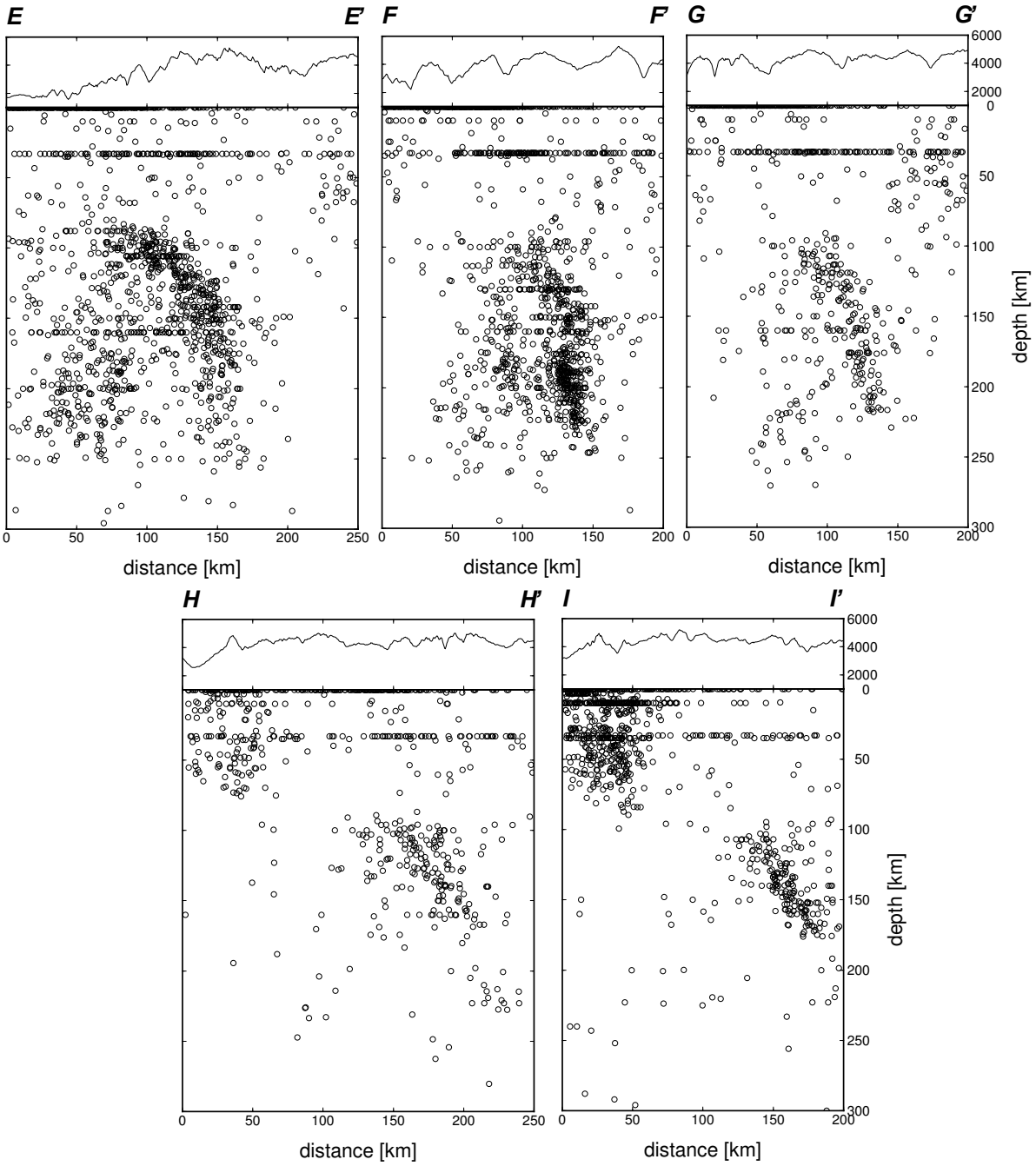

Figure C.4.: Cross sections through Pamir intermediate-depth events in the ISC catalog. For location and orientation of the shown profiles, refer to Figure 4.10.

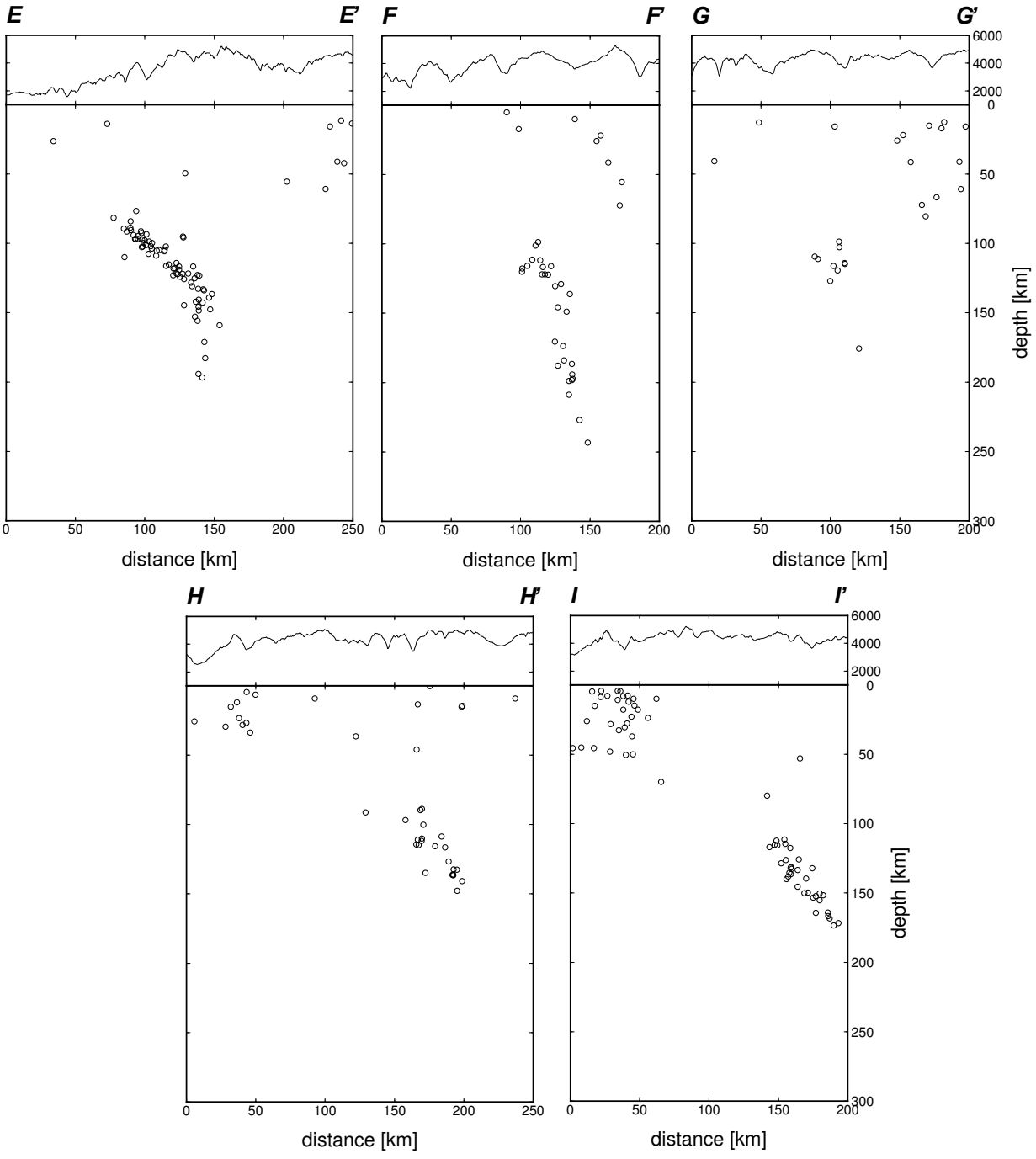

Figure C.5.: Cross sections through Pamir intermediate-depth events in the EHB catalog. For location and orientation of the shown profiles, refer to Figure 4.10.

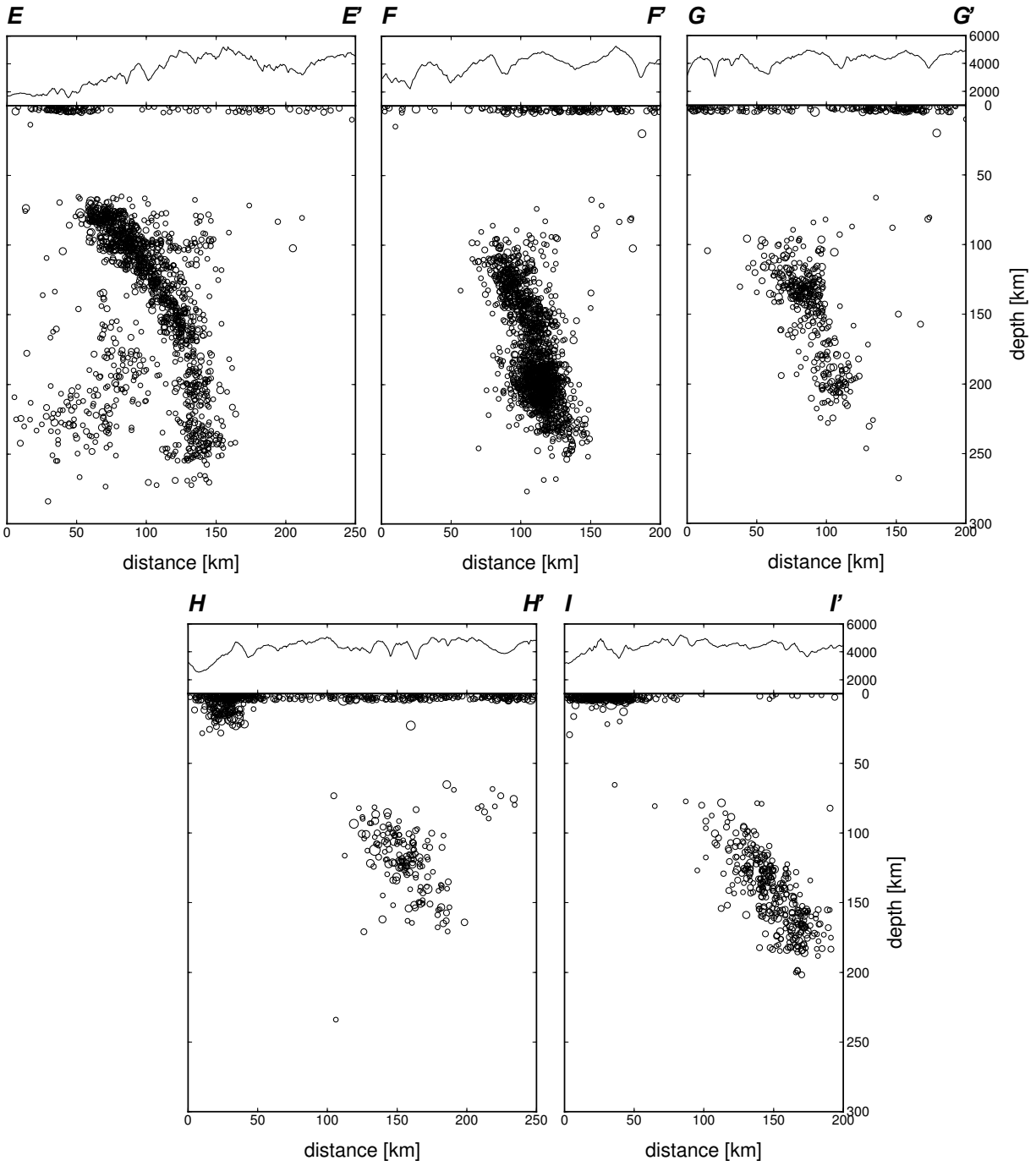

Figure C.6.: Cross sections through Pamir events of the ZSSSR catalog. For imaging purposes, the grid-bound locations were perturbed in all three dimensions by adding random noise of a maximal amplitude that is half the grid cell size (i.e. filling out the cells). For location and orientation of the shown profiles, refer to Figure 4.10.

effectively outline structures, whereas the ISC exhibits, again, significant scatter. Several key features of the seismicity distribution retrieved in this thesis are mirrored by these more long-term data: the eastward dip of the westernmost Pamir, the lower activity and vertical extent of the Pamir seismic zone in our profiles G-G' and H-H' and the apparent aseismic nature of the lower crust, among others, are clearly imaged in the ZSSSR data and can partly be identified in the ISC data. Again, outlined structures are broader than in my data, which reflects higher location uncertainties in the catalogs.

In conclusion, all of these catalog data appear to represent a blurred image of the structures shown in this study, which means that the two years of data decently well mirror the long-term behavior of these seismic zones.

D. List of all obtained earthquake mechanisms

Nr	Origin Time	Latitude	Longitude	Depth [km]	Centroid depth [km]	M_w	M_L	Plane 1 strike [o]	dip	rake	Plane 2 strike [o]	dip	rake	P axis strike [o]	dip	T axis strike [o]	dip	method
1	2008/08/02 21:23:35	37.936N	68.996E	20.53	24	3.83	4.5	14	59	-106	224	35	-65	247	71	116	13	RMT
2	2008/08/06 08:26:52	36.536N	70.424E	193.38	207	4.33	5.0	68	70	114	195	31	41	140	22	11	58	RMT
3	2008/08/06 13:27:44	36.373N	69.527E	74.52	141	3.98	4.6	49	56	130	172	51	46	112	3	17	57	RMT
4	2008/08/08 16:07:58	38.964N	71.391E	0.01	9	3.5	4.5	224	63	93	37	27	82	312	18	141	72	RMT
5	2008/08/17 17:58:21	38.637N	70.319E	7.36	4	3.97	4.5	357	90	-81	88	9	-179	276	44	79	44	RMT
6	2008/08/18 22:31:23	38.729N	70.518E	2.14	4	3.46	4.5	192	84	93	348	7	67	279	39	105	51	RMT
7	2008/08/18 23:07:56	38.773N	70.500E	2.94	6	3.77	4.5	191	79	87	26	11	105	284	34	98	56	RMT
8	2008/08/31 18:51:53	38.363N	73.141E	12.08	15	3.16	3.5	314	76	-146	214	57	-17	179	34	81	12	RMT
9	2008/09/01 04:24:33	37.405N	68.907E	34.42	15	5.04	5.4	175	55	111	321	40	63	250	8	137	71	RMT
10	2008/09/05 04:57:51	36.538N	71.260E	226.40	240	5.31	6.6	42	62	100	201	30	72	124	16	334	71	RMT
11	2008/09/06 05:47:38	36.490N	70.854E	188.36	204	5.76	6.9	246	67	84	80	23	103	340	22	145	67	RMT
12	2008/09/09 01:33:04	38.127N	73.941E	155.60	156	4.39	5.1	138	89	-39	229	51	-178	86	28	191	26	RMT
13	2008/09/11 17:27:55	39.258N	72.672E	13.23	15	4.01	4.4	213	62	65	77	37	128	320	14	80	64	RMT
14	2008/09/18 22:00:19	38.063N	69.165E	11.4	6	3.67	4.5	119	81	38	22	52	169	245	19	348	33	RMT
15	2008/09/20 02:54:35	38.251N	73.267E	127.17	129	5.18	5.6	91	67	-146	346	59	-27	311	40	217	5	RMT
16	2008/09/24 12:04:54	36.514N	70.927E	167.94	204	4.55	5.6	23	67	83	221	24	107	118	22	279	67	RMT
17	2008/09/24 17:59:30	36.030N	71.140E	60.51	78	5.12	5.6	251	56	130	15	50	46	314	3	219	58	RMT
18	2008/09/29 13:15:14	38.828N	70.248E	1.90	4	3.79	4.4	310	78	-50	54	41	-162	258	42	11	23	RMT
19	2008/10/05 08:28:16	38.867N	70.499E	0.1	9	3.88	4.5	194	69	81	38	23	112	291	23	89	65	RMT
20	2008/10/05 15:52:44	39.535N	73.817E	2.79	4	6.62	6.6	89	59	109	236	36	62	166	12	41	70	RMT
21	2008/10/05 16:11:04	39.514N	73.871E		9	5.37	5.3	210	54	57	78	47	127	323	4	60	63	RMT
22	2008/10/05 18:27:36	39.510N	73.793E	17.48	9	4.67	4.7	245	60	94	58	30	84	332	15	165	75	RMT
23	2008/10/05 18:34:32	39.521N	73.839E	13.72	9	4.03	4.2	75	55	70	288	40	117	179	8	294	71	RMT
24	2008/10/05 21:46:00	39.634N	73.981E		6	4.51	4.6	54	55	61	278	45	125	164	6	266	66	RMT
25	2008/10/06 06:09:01	39.606N	73.929E	10.32	6	3.63	4.0	55	50	58	278	50	122	166	0	257	66	RMT
26	2008/10/06 07:27:45	39.506N	73.825E	14.77	6	3.85	4.2	279	82	163	11	73	8	326	6	234	18	RMT
27	2008/10/06 07:50:26	39.540N	73.891E	6.07	4	4.40	4.3	233	88	64	139	26	176	346	38	119	41	RMT
28	2008/10/07 02:52:35	36.701N	71.445E	155.06	180	4.45	5.3	270	59	115	47	39	55	342	11	227	66	RMT
29	2008/10/07 15:06:40	39.642N	73.953E	14.20	4	4.01	3.9	262	58	108	51	37	64	339	11	215	71	RMT
30	2008/10/07 23:13:14	39.504N	73.784E	7.56	4	3.95	4.3	262	58	118	37	42	52	332	9	223	64	RMT
31	2008/10/08 13:19:00	39.605N	73.959E	9.26	6	3.85	4.0	22	74	71	254	25	140	127	27	267	57	RMT
32	2008/10/08 23:31:14	39.513N	73.820E	15.79	9	4.10	4.4	64	67	79	269	26	114	162	21	314	67	RMT
33	2008/10/09 03:13:40	39.516N	73.924E		9	4.42	4.8	316	81	-130	216	41	-14	190	40	76	25	RMT
34	2008/10/09 14:43:17	39.606N	73.967E	3.96	6	4.30	4.5	11	55	61	236	45	125	122	5	223	66	RMT
35	2008/10/11 02:01:43	39.614N	73.949E	13.62	4	3.97	4.0	263	57	110	49	38	62	339	10	218	70	RMT
36	2008/10/12 17:02:30	39.582N	73.970E	4.38	4	4.01	4.5	223	80	-47	323	44	-166	171	39	281	23	RMT
37	2008/10/13 08:07:41	36.189N	71.058E	41.31	108	5.17	5.3	32	56	56	262	47	130	145	5	245	62	RMT
38	2008/10/13 09:23:28	39.528N	73.868E	9.38	9	4.89	4.9	121	87	139	214	49	3	175	26	69	30	RMT
39	2008/10/13 16:05:19	39.506N	73.840E	6.74	9	5.02	5.3	87	67	120	211	37	41	155	17	37	58	RMT
40	2008/10/13 17:16:09	38.645N	70.328E	0.01	6	5.16	6.3	189	82	85	44	9	125	284	37	92	52	RMT
41	2008/10/18 09:28:58	39.519N	73.801E		6	4.37	4.5	68	81	72	312	20	153	173	34	318	51	RMT
42	2008/10/23 05:50:43	39.563N	74.018E		9	4.58	4.5	241	56	92	58	35	88	330	10	157	79	RMT
43	2008/10/26 01:28:53	36.490N	70.705E	187.03	216	5.69	6.0	96	73	99	248	19	64	179	27	19	61	RMT
44	2008/10/30 10:44:56	39.616N	73.468E	13.69	9	4.28	4.6	40	86	12	309	78	176	174	6	265	11	RMT
45	2008/11/04 14:22:21	39.600N	74.038E	9.82	9	4.41	4.4	32	57	66	251	40	122	139	9	252	68	RMT
46	2008/11/07 09:21:13	39.552N	74.032E	5.90	4	4.02	4.5	247	82	111	356	23	21	318	34	180	48	RMT
47	2008/11/08 01:30:40	39.588N	74.023E	4.91	9	4.13	4.3	47	46	89	228	44	91	138	1	299	89	RMT
48	2008/11/08 04:04:22	38.263N	68.740E	29.26	6	4.16	4.8	68	84	41	333	50	172	194	23	299	32	RMT
49	2008/11/09 19:22:44	39.495N	73.851E	6.66	6	4.03	4.4	228	53	67	84	43	118	334	5	80	71	RMT
50	2008/11/11 00:57:24	36.868N	70.030E	0.01	12	3.60	4.5	265	88	-132	173	42	-3	141	34	28	30	RMT
51	2008/11/13 20:52:04	39.609N	74.054E	5.03	9	4.17	4.3	39	53	71	249	42	113	142	6	252	74	RMT
52	2008/11/27 15:49:46	39.606N	74.040E	4.88	9	4.09	4.1	45	51	69	257	43	114	150	4	255	73	RMT
53	2008/12/03 18:26:21	38.971N	71.376E	13.00	12	3.79	4.5	219	71	57	102	37	147	333	19	90	52	RMT
54	2008/12/05 15:51:31	38.914N	70.719E	0.01	4	3.38	4.5	168	82	31	72	59	170	296	15	34	28	RMT
55	2008/12/06 22:05:50	37.150N	71.651E	103.73	129	4.46	4.8	177	74	77	35	21	127	277	28	69	59	RMT
56	2008/12/16 22:39:53	36.426N	71.176E	82.47	96	4.23	4.8	84	51	83	275	40	98	179	5	314	82	RMT
57	2008/12/20 14:31:43	38.907N	70.713E	0.01	4	3.86	4.2	352	79	-33	90	58	-166	306	31	45	14	RMT
58	2008/12/21 03:15:41	38.889N	70.719E	0.01	4	3.46	4.5	184	79	40	85	50	166	308	19	52	36	RMT
59	2008/12/21 22:38:32	36.095N	71.405E	78.44	87	4.82	5.1	243	53	126	13	50	52	309	2	215	62	RMT
60	2008/12/23 20:52:17	36.391N	70.822E	189.82	195	4.23	4.7	82	62	91	260	28	88	171	17	355	73	RMT
61	2008/12/27 13:38:51	37.492N	74.599E	0.01	9	3.77	4.5	324	61	-135	209	52	-38	181	51	85	6	RMT
62	2008/12/29 03:37:41	36.495N	71.063E	132.45	147	5.68	6.6	267	59	84	98	32	100	1	13	159	76	RMT
63	2008/12/30 03:09:28	36.541N	70.985E	185.78	183	4.06	4.5	79	66	80	282	26	111	177	20	330	68	RMT
64	2009/01/04 23:12:59	36.538N	70.962E	171.85	204	5.61	6.5	53	60	73	264	34	117	155	14	287	70	RMT
65	2009/01/16 12:35:48	39.421N	73.465E	14.58	4	3.92	4.4	358	80	-16	90	74	-170	313	18	45	4	RMT
66	2009/01/17 20:08:17	39.628N	73.464E	14.10	6	4.49	4.5	38	88	17	308	73	178	172	11	264	13	RMT
67	2009/01/25 19:13:01	37.025N	71.528E	88.00	105	4.12	4.6	136	77	122	245	34	23	201	26	79	48	RMT
68	2009/01/25 21:16:16	38.524N	72.174E	4.66	9	4.64	4.8	284	90	-180	194	90	0	149	1	59	0	RMT
69	2009/02/06 17:11:34	36.611N	70.975E	199.67	222	4.36	5.4	95	45	99	263	45	81	179	0	87	84	RMT
70	2009/02/16 23:13:53	38.761N	75.499E	23.4	15	4.21	5.1	341	86	73	238	18	166	87	38	233	47	RMT

Nr	Origin Time	Latitude	Longitude	Depth [km]	Centroid depth [km]	M_w	M_L	Plane 1 strike [◦]	dip	rake	Plane 2 strike [◦]	dip	rake	P axis strike [◦]	dip	T axis strike [◦]	dip	method
71	2009/02/17 16:39:56	36.677N	71.162E	194.32	228	4.26	4.9	195	50	79	33	41	103	293	4	49	80	RMT
72	2009/02/18 02:49:03	36.682N	71.057E	45.21	66	4.15	4.9	15	51	71	224	42	112	118	5	225	74	RMT
73	2009/02/19 08:04:04	36.754N	70.795E	271.17	285	4.33	4.6	71	67	119	196	37	42	140	17	21	58	RMT
74	2009/02/21 02:09:50	38.499N	72.194E	3.25	6	3.84	4.4	107	85	171	198	81	6	152	2	62	10	RMT
75	2009/02/26 07:50:48	38.312N	73.882E	124.21	144	4.70	5.2	255	54	75	100	39	110	356	7	116	75	RMT
76	2009/02/26 08:38:17	39.455N	73.831E	7.64	4	3.80	4.2	116	76	-157	20	68	-16	339	26	247	5	RMT
77	2009/02/26 09:04:54	39.462N	73.829E	11.64	9	3.88	4.0	19	78	14	286	77	167	153	1	243	18	RMT
78	2009/03/01 00:05:19	38.539N	72.171E	2.75	6	4.09	4.4	114	62	-138	2	54	-35	332	48	236	5	RMT
79	2009/03/03 14:22:12	38.137N	71.566E	8.71	6	4.96	5.2	333	62	-143	224	57	-34	190	45	98	3	RMT
80	2009/03/13 20:42:15	36.521N	71.252E	188.43	213	4.08	4.7	77	55	77	279	38	108	177	9	304	76	RMT
81	2009/03/24 09:03:37	36.664N	71.427E	135.39	153	4.41	4.9	13	79	37	275	54	166	139	16	240	34	RMT
82	2009/04/06 18:11:45	36.074N	70.743E	60.74	84	4.55	5.1	195	74	-32	295	60	-161	152	34	248	9	RMT
83	2009/04/09 16:34:29	36.561N	70.973E	159.86	177	4.63	5.4	46	83	-88	206	7	-110	319	52	134	38	RMT
84	2009/04/27 00:06:38	39.012N	75.198E	38.89	18	3.87	4.1	139	50	88	322	40	92	230	5	37	85	RMT
85	2009/04/29 04:42:21	36.045N	71.153E	75.50	78	4.35	5.1	21	52	57	247	49	125	134	2	227	65	RMT
86	2009/04/29 08:26:58	39.735N	73.975E	12.07	9	4.21	4.6	124	86	165	215	75	4	170	7	78	13	RMT
87	2009/04/29 20:10:53	36.612N	70.947E	199.94	243	4.20	4.9	251	55	49	127	51	133	8	2	101	58	RMT
88	2009/05/10 17:34:05	38.197N	67.567E		12	4.83	5.1	20	56	94	193	34	84	107	11	306	79	RMT
89	2009/05/17 11:57:58	36.637N	71.055E	212.50	243	4.65	6.1	342	76	114	101	28	32	53	27	281	53	RMT
90	2009/05/25 15:18:53	38.812N	70.617E	2.89	6	4.39	4.8	202	81	82	65	12	132	299	35	102	53	RMT
91	2009/05/25 23:27:02	39.524N	73.738E	10.91	4	3.98	4.0	91	73	88	279	17	98	183	28	357	62	RMT
92	2009/06/07 00:05:30	36.464N	70.166E	197.68	216	4.24	4.7	108	84	105	219	16	21	185	37	35	49	RMT
93	2009/06/14 04:34:17	38.981N	73.300E	14.53	24	3.38	3.8	121	74	134	227	47	23	180	17	74	43	RMT
94	2009/06/17 09:22:15	37.964N	69.798E	0.01	4	4.27	4.6	177	90	69	86	21	179	286	41	67	42	RMT
95	2009/06/21 13:46:01	36.429N	70.823E	173.96	210	4.53	5.0	39	68	73	258	27	126	141	21	282	63	RMT
96	2009/07/01 00:29:21	39.630N	73.456E	12.85	6	4.96	5.1	307	76	-161	212	71	-15	170	24	79	3	RMT
97	2009/07/02 23:50:49	37.404N	71.703E	98.52	120	4.70	5.0	36	86	-125	300	35	-7	275	39	154	32	RMT
98	2009/07/05 09:45:46	36.445N	71.188E	219.61	249	5.19	5.8	4	68	64	236	33	137	113	19	237	59	RMT
99	2009/07/07 16:00:46	38.884N	71.462E	1.00	12	3.78		138	51	-124	6	50	-55	343	64	252	1	RMT
100	2009/07/11 18:16:12	38.227N	72.535E	4.15	4	3.49	3.6	80	71	35	337	57	157	206	9	303	38	RMT
101	2009/07/12 19:32:21	38.358N	73.324E	107.98			3.9	139	80	-157	45	67	-11	4	23	90	9	HASH
102	2009/07/13 01:52:21	37.245N	71.948E	0.15	9	3.73	4.0	118	80	-160	24	70	-11	342	21	250	7	RMT
103	2009/07/17 05:42:37	37.327N	71.757E	18.9	9	3.59	4.0	307	82	-168	216	78	-9	172	14	81	2	RMT
104	2009/07/18 03:13:11	39.470N	73.793E	12.67	12	3.72	4.0	356	54	-81	160	37	-102	299	78	79	9	RMT
105	2009/07/21 04:33:16	37.327N	72.144E	181.67			3.6	219	61	145	328	60	34	94	1	3	44	HASH
106	2009/07/28 03:17:49	39.590N	74.029E	6.09	9	4.31	4.4	23	58	64	246	41	125	132	9	243	66	RMT
107	2009/07/29 22:57:43	38.345N	73.376E	111.35			3.5	332	62	138	85	54	36	210	5	295	49	HASH
108	2009/07/31 03:43:30	37.121N	71.414E	87.52	99	4.37	4.8	124	62	118	256	39	49	194	12	80	62	RMT
109	2009/08/03 19:28:33	38.062N	73.457E	155.13			4.2	138	42	147	254	69	53	190	16	121	52	HASH
110	2009/08/08 06:22:36	37.428N	72.187E	178.88			3.9	233	5	-146	109	87	-86	23	48	15	42	HASH
111	2009/08/14 14:46:11	37.901N	72.473E	96.81			4.5	62	44	127	196	56	60	307	7	51	64	HASH
112	2009/08/25 06:45:04	38.909N	70.651E	0.01	6	3.75	4.5	196	67	64	67	34	137	305	18	68	59	RMT
113	2009/08/26 07:26:38	38.962N	70.581E	17.36	6	4.68	4.6	170	77	37	70	54	163	296	15	36	35	RMT
114	2009/08/26 18:29:03	37.417N	72.197E	190.86			3.4	311	88	75	214	15	172	235	41	26	45	HASH
115	2009/08/27 04:06:09	39.516N	73.904E	5.18	4	4.06	4.2	112	65	134	225	50	34	172	9	71	49	RMT
116	2009/08/30 02:20:20	36.515N	71.249E	209.62	231	3.99	4.7	333	68	39	226	54	152	97	8	194	43	RMT
117	2009/08/31 02:34:10	38.210N	72.946E	99.97			3.1	274	72	155	12	66	20	144	4	232	30	HASH
118	2009/09/01 03:10:54	39.437N	73.710E	15.40	9	4.07	4.2	30	60	47	272	51	139	149	5	246	53	RMT
119	2009/09/04 16:16:55	37.436N	72.204E	174.17	207	4.23	4.6	121	88	-118	27	28	-4	4	40	235	37	RMT
120	2009/09/04 19:42:37	37.436N	72.120E	168.11			3.6	55	86	-95	286	6	-39	140	49	150	41	HASH
121	2009/09/05 18:54:57	39.132N	71.706E	0.2			3.6	255	53	137	14	57	46	134	2	227	54	HASH
122	2009/09/07 09:01:52	36.429N	70.748E	180.23	207	4.27	4.8	136	70	81	339	22	112	233	24	32	64	RMT
123	2009/09/11 20:09:46	37.286N	72.182E	212.93			3.3	69	85	-99	310	10	-29	149	49	167	39	HASH
124	2009/09/12 04:04:38	38.291N	73.657E	131.04			3.5	162	50	174	256	85	40	202	23	307	31	HASH
125	2009/09/12 17:42:06	37.277N	72.115E	133.88			4.1	148	63	123	273	42	43	215	12	105	58	HASH
126	2009/09/15 08:54:19	37.391N	72.139E	163.72			3.5	133	42	88	316	48	92	44	3	68	87	HASH
127	2009/09/19 04:17:56	36.461N	70.724E	178.91	213	5.00	4.5	106	75	89	288	15	92	196	30	15	60	RMT
128	2009/09/22 20:34:35	37.368N	72.063E	176.46			3.9	209	45	136	333	61	54	268	9	192	58	HASH
129	2009/09/22 22:44:40	41.014N	73.373E	24.91	9	3.49	3.8	29	57	101	190	35	74	112	11	332	76	RMT
130	2009/09/27 02:26:18	37.342N	72.155E	201.32			3.7	154	53	133	277	54	48	215	1	126	57	HASH
131	2009/09/27 12:07:46	39.475N	73.666E	15.43	12	3.65	4.0	78	71	100	229	22	64	160	25	3	63	RMT
132	2009/09/29 10:29:26	39.358N	72.378E	22.16			3.4	308	77	173	40	83	13	173	4	264	14	HASH
133	2009/10/01 22:20:18	38.140N	73.962E	157.68			3.9	213	48	-167	114	80	-43	244	36	170	21	HASH
134	2009/10/02 09:12:11	37.576N	72.302E	166.53			4.2	236	86	126	331	36	7	297	31	178	38	HASH
135	2009/10/04 07:53:40	37.896N	72.255E	96.15			3.0	274	38	-33	31	70	-123	261	53	145	19	HASH
136	2009/10/04 14:22:04	38.367N	73.373E	109.67			3.8	112	85	179	202	89	5	157	3	67	4	HASH
137	2009/10/06 19:50:26	37.236N	71.969E	143.16			3.5	38	62	-124	273	43	-44	259	58	332	11	HASH
138	2009/10/08 01:47:43	37.358N	72.037E	146.38			3.0	272	21	-36	36	78	-107	105	54	320	31	HASH
139	2009/10/11 17:57:25	38.317N	72.934E	12.26	9	3.78	4.4	135	86	-157	43	67	-4	1	19	267	13	RMT
140	2009/10/12 22:34:39	38.236N	73.006E	100.74			3.2	122	78	-169	30	79	-12	166	16	256	1	HASH

Nr	Origin Time	Latitude	Longitude	Depth [km]	Centroid depth [km]	M_w	M_L	Plane 1 strike [o]	dip	rake	Plane 2 strike [o]	dip	rake	P axis strike [o]	dip	T axis strike [o]	dip	method
141	2009/10/13 12:47:15	38.681N	70.848E	0.01	15	4.83	4.5	133	84	155	226	66	6	182	13	87	21	RMT
142	2009/10/14 04:22:37	38.280N	73.580E	124.94	141	3.95	4.5	294	74	129	43	42	25	356	19	244	46	RMT
								279	13	171	18	88	77	300	42	95	46	HASH
143	2009/10/15 08:01:34	38.288N	73.289E	117.75			4.2	111	80	169	203	79	10	157	1	67	15	HASH
144	2009/10/15 13:27:47	37.038N	71.048E	50.64	78	4.67	5.0	102	52	119	240	46	58	172	3	75	68	RMT
145	2009/10/16 14:24:01	39.742N	72.368E		15	3.30	3.7	99	64	-121	334	40	-43	324	58	211	14	RMT
146	2009/10/17 08:56:34	38.101N	73.572E	159.04			4.3	278	79	129	21	40	17	339	24	225	42	HASH
147	2009/10/18 09:18:53	37.509N	72.349E	182.95			3.4	351	63	-113	214	35	-53	41	64	98	15	HASH
148	2009/10/18 14:46:03	37.299N	72.026E	159.24			3.3	84	50	145	198	64	46	138	8	58	50	HASH
149	2009/10/20 06:14:59	39.330N	72.947E	0.2			4.3	100	66	-175	8	85	-24	141	20	236	13	HASH
150	2009/10/22 05:14:01	37.774N	72.489E	121.72			4.4	316	82	166	48	76	8	183	4	91	16	HASH
151	2009/10/22 19:51:24	36.443N	70.966E	165.07	189	6.09	6.7	248	47	79	84	44	102	346	2	89	81	RMT
152	2009/10/23 02:34:52	37.289N	72.139E	203.96			4.4	174	39	139	298	66	59	230	15	165	57	HASH
153	2009/10/23 16:45:53	38.518N	73.019E	87.28			4.4	102	86	162	193	72	4	149	10	56	16	HASH
154	2009/10/23 19:14:35	37.830N	72.543E	125.76			3.1	282	88	174	12	84	2	327	3	57	6	HASH
155	2009/10/26 18:36:18	39.401N	73.086E	0.2			3.4	111	82	-164	19	74	-8	336	17	244	5	HASH
156	2009/10/27 13:37:46	38.415N	73.211E	92.36			2.9	284	78	-146	186	57	-14	150	32	51	14	HASH
157	2009/10/27 22:49:00	38.243N	74.433E	147.47			3.2	129	68	127	245	42	34	193	15	83	52	HASH
158	2009/10/28 08:36:04	41.213N	73.511E	28.06	15	3.80	3.8	59	57	54	292	47	132	174	5	273	60	RMT
159	2009/10/28 17:38:12	36.460N	71.236E	216.16	228	4.30	5.2	260	48	116	44	48	64	332	0	241	71	RMT
160	2009/10/29 14:55:08	37.669N	72.156E	109.44			3.4	235	15	-91	56	75	-90	147	60	326	30	HASH
161	2009/10/29 17:44:32	36.407N	70.772E	184.83	222	6.20	6.6	118	69	99	275	23	68	202	23	44	65	RMT
162	2009/10/30 08:06:12	37.519N	72.447E	189.25			3.5	273	18	126	56	76	79	154	30	311	58	HASH
163	2009/10/30 21:51:30	37.542N	72.128E	125.87			3.6	282	15	-121	134	77	-82	54	57	37	32	HASH
164	2009/10/31 07:51:32	38.243N	73.907E	124.35			3.0	88	50	130	215	54	53	151	2	65	60	HASH
165	2009/11/02 02:30:32	38.347N	74.035E	111.01			3.8	100	29	72	300	63	100	23	17	232	71	HASH
166	2009/11/05 13:18:36	38.154N	73.872E	150.88			3.3	201	59	-160	100	73	-33	57	35	153	9	HASH
167	2009/11/07 00:41:37	38.087N	73.447E	152.93			4.3	297	48	-43	59	60	-129	276	56	176	7	HASH
168	2009/11/08 02:11:12	38.449N	69.659E	14.22	4	4.42	4.5	233	77	138	335	49	17	290	18	185	39	RMT
169	2009/11/10 08:27:39	37.576N	72.115E	119.42			3.2	36	80	-95	243	11	-64	300	55	130	35	HASH
170	2009/11/10 10:00:51	38.541N	73.614E	88.9			3.5	294	41	116	81	54	69	6	7	297	72	HASH
171	2009/11/10 22:25:03	37.459N	72.079E	131.59			2.6	334	27	-77	139	64	-97	35	71	54	19	HASH
172	2009/11/11 02:40:02	40.533N	73.092E	25.6	4	3.57	3.7	46	58	68	264	38	121	152	11	270	69	RMT
173	2009/11/11 22:28:51	37.418N	72.190E	178.15			3.5	342	58	76	187	35	111	82	12	216	73	HASH
174	2009/11/12 13:13:28	37.267N	72.151E	214.49			3.2	256	27	-156	144	79	-65	82	50	214	30	HASH
175	2009/11/12 15:17:01	38.517N	69.616E	16.61	9	4.01	4.1	237	85	158	329	68	6	285	11	191	19	RMT
176	2009/11/15 01:39:35	39.313N	72.734E	7.25			3.1	266	83	165	358	75	7	133	5	221	16	HASH
177	2009/11/15 01:56:19	39.375N	72.817E	9.55	6	4.45	4.6	180	76	25	84	66	165	310	7	44	27	RMT
								355	87	-31	87	59	-177	307	23	45	19	HASH
178	2009/11/19 00:12:49	37.502N	72.258E	182.94			3.7	199	5	-161	90	88	-85	5	46	355	43	HASH
179	2009/11/20 17:46:40	37.385N	72.159E	183.19			3.1	273	72	84	112	19	108	8	27	174	63	HASH
180	2009/11/22 01:08:16	37.732N	72.186E	107.17			3.7	158	48	168	256	81	43	200	21	306	36	HASH
181	2009/11/25 23:33:25	37.542N	72.002E	116.87			3.4	229	79	-150	133	61	-13	275	29	178	12	HASH
182	2009/11/27 14:16:51	38.099N	73.873E	159.81	192	4.21	4.9	342	53	53	214	51	129	98	1	190	61	RMT
								285	45	30	173	69	131	234	14	127	49	HASH
183	2009/11/27 22:41:25	38.108N	73.827E	166.41			4.4	215	50	-178	124	88	-40	252	28	177	26	HASH
184	2009/11/29 14:49:09	38.067N	73.459E	161.82			3.1	129	68	127	245	42	34	193	15	83	52	HASH
185	2009/11/29 22:19:15	37.259N	72.005E	148.50			4.3	260	43	121	41	54	64	329	6	254	69	HASH
186	2009/11/29 23:17:02	37.408N	72.185E	183.78			3.3	97	88	-87	221	4	-146	190	47	4	43	HASH
187	2009/11/30 12:05:56	37.777N	72.357E	116.52			3.5	62	57	-99	258	34	-76	125	76	158	12	HASH
188	2009/11/30 15:49:29	37.329N	72.096E	174.92			2.6	290	75	95	91	16	72	16	30	27	60	HASH
189	2009/12/01 13:32:11	37.437N	72.217E	180.23			4.1	142	84	170	233	80	6	188	3	277	11	HASH
190	2009/12/03 16:51:40	38.300N	73.273E	82.31			2.6	44	87	149	136	59	3	277	25	352	29	HASH
191	2009/12/04 20:16:07	37.638N	72.165E	113.49			3.0	74	77	-100	292	16	-53	151	57	172	31	HASH
192	2009/12/05 03:18:21	37.842N	72.695E	133.68			2.7	247	25	178	339	89	65	91	39	226	41	HASH
193	2009/12/05 05:31:27	37.658N	72.266E	106.29			3.6	250	72	-127	138	41	-28	119	49	7	19	HASH
194	2009/12/06 01:09:15	37.354N	72.075E	177.00			4.0	314	61	119	85	40	49	24	11	271	62	HASH
195	2009/12/08 02:20:56	37.820N	72.090E	93.70			2.8	58	72	-120	300	35	-33	112	53	170	21	HASH
196	2009/12/08 22:30:19	38.666N	69.807E	11.01	4	3.66	4.5	224	61	82	60	30	104	320	15	114	73	RMT
197	2009/12/10 21:43:51	38.346N	73.536E	112.87			3.8	283	63	121	50	40	45	351	13	239	59	HASH
198	2009/12/12 18:51:07	38.377N	74.197E	57.25			3.7	138	74	154	236	65	18	188	6	275	30	HASH
199	2009/12/13 08:58:15	37.431N	72.229E	184.24			3.3	274	84	94	60	7	56	0	39	8	51	HASH
200	2009/12/14 00:31:34	37.414N	72.203E	173.22			3.5	252	20	-142	126	78	-74	235	54	23	31	HASH
201	2009/12/15 15:28:16	37.886N	72.481E	114.97			3.2	3	66	-89	181	24	-92	95	69	92	21	HASH
202	2009/12/19 18:12:03	37.473N	72.279E	190.34			3.5	232	46	135	357	59	54	112	8	214	58	HASH
203	2009/12/20 06:20:02	37.448N	72.169E	168.93			3.0	268	8	-111	109	83	-87	203	52	197	37	HASH
204	2009/12/22 06:16:29	38.336N	73.173E	103.00			3.0	312	89	175	42	85	1	177	3	87	4	HASH
205	2009/12/22 18:34:04	37.286N	72.091E	76.38			2.8	251	33	160	358	79	59	113	27	236	46	HASH
206	2009/12/23 05:45:31	37.847N	72.422E	113.81			3.4	285	17	-51	65	77	-101	321	57	164	31	HASH
207	2009/12/25 13:45:54	37.496N	71.841E	107.73			3.1	1	51	-85	173	39	-96	301	83	87	6	HASH

Nr	Origin Time	Latitude	Longitude	Depth [km]	Centroid depth [km]	M_w	M_L	Plane 1 strike [o]	dip	rake	Plane 2 strike [o]	dip	rake	P axis strike [o]	dip	T axis strike [o]	dip	method
208	2009/12/25 16:26:49	37.622N	72.343E	159.19			3.9	252	36	118	39	59	71	142	12	267	70	HASH
209	2009/12/28 02:13:45	39.054N	71.627E	0.2			3.4	40	46	93	216	44	87	128	1	14	88	HASH
210	2009/12/29 07:23:37	37.297N	72.004E	144.02			3.7	93	79	-92	283	11	-80	180	56	185	34	HASH
211	2010/01/01 16:26:28	37.322N	72.057E	148.61			3.0	207	5	-176	113	90	-85	28	45	198	44	HASH
212	2010/01/02 02:15:04	38.288N	71.445E	7.52	6	5.30	5.6	343	60	-137	228	53	-38	199	50	104	4	RMT
213	2010/01/02 03:12:07	38.279N	71.475E	4.00	4	3.86	4.2	250	83	-24	343	66	-173	204	22	299	12	RMT
214	2010/01/04 06:42:26	37.507N	72.303E	179.76			3.5	275	45	166	15	80	46	317	22	246	38	HASH
215	2010/01/05 16:01:23	37.369N	72.107E	87.69			3.3	122	65	176	214	86	25	345	15	261	20	HASH
216	2010/01/06 06:42:01	37.555N	72.444E	183.44			3.3	282	31	-140	156	71	-65	279	57	228	22	HASH
217	2010/01/06 07:00:02	37.448N	72.215E	181.09			4.4	65	69	121	186	37	37	132	18	14	55	HASH
218	2010/01/06 08:02:09	38.270N	71.485E	6.96	4	3.90	4.3	231	63	-34	339	60	-148	194	43	285	2	RMT
219	2010/01/06 16:45:40	37.731N	72.419E	134.47			2.6	67	46	-95	254	44	-85	264	86	341	1	HASH
220	2010/01/07 10:24:45	37.549N	72.461E	192.30			3.5	206	30	180	296	90	60	233	38	179	38	HASH
221	2010/01/08 13:23:49	38.424N	73.848E	102.34	120	4.09	4.5	51	71	41	305	52	156	174	12	275	42	RMT
								67	62	70	285	34	123	172	15	299	67	HASH
222	2010/01/10 14:48:01	37.456N	72.042E	121.97			3.1	49	65	-138	298	53	-32	269	47	171	7	HASH
223	2010/01/12 07:12:41	38.901N	70.589E	0.01	6	3.64	4.5	198	65	58	74	40	139	311	15	65	57	RMT
224	2010/01/13 23:34:48	37.356N	72.125E	182.24			3.5	97	47	108	252	46	72	174	1	82	77	HASH
225	2010/01/18 19:36:52	37.294N	72.198E	210.43			3.7	119	27	112	275	65	79	193	19	164	68	HASH
226	2010/01/19 20:57:25	38.393N	73.276E	95.90			3.5	65	80	-120	318	31	-19	124	47	179	29	HASH
227	2010/01/21 15:10:02	37.679N	72.364E	143.68			3.3	237	63	-171	143	82	-27	277	25	193	13	HASH
228	2010/01/23 10:55:30	37.359N	72.126E	186.32			4.0	260	47	108	55	46	72	157	1	245	77	HASH
229	2010/01/23 16:07:42	36.528N	71.302E	64.31	81	4.50	4.9	231	77	81	88	15	125	329	32	130	57	RMT
230	2010/01/23 18:50:38	37.431N	72.197E	175.87			3.1	253	35	-100	85	56	-83	200	78	350	10	HASH
231	2010/01/24 17:41:05	37.247N	71.914E	160.78			3.6	195	80	127	298	38	16	257	26	140	43	HASH
232	2010/01/26 14:50:13	37.663N	72.445E	165.82			3.3	51	74	-101	266	19	-56	306	60	150	28	HASH
233	2010/01/26 17:44:53	37.449N	69.663E	22.03	36	3.78	4.3	197	87	-67	295	24	-172	130	44	266	37	RMT
234	2010/01/26 19:33:10	37.785N	72.386E	117.17			3.1	333	81	87	174	9	110	66	36	239	54	HASH
235	2010/01/27 05:19:46	37.104N	71.449E	85.53	105	4.32	4.7	25	70	36	281	56	156	150	9	247	39	RMT
236	2010/01/30 21:37:41	36.735N	71.058E	62.07	81	4.77	4.7	11	87	41	278	49	176	137	25	243	30	RMT
237	2010/01/31 21:19:15	38.570N	73.479E	87.58			3.5	299	67	153	40	65	25	170	1	259	35	HASH
238	2010/02/01 20:41:07	38.042N	73.055E	134.84			3.3	143	74	-160	47	71	-17	186	25	95	2	HASH
239	2010/02/03 01:04:32	38.267N	73.669E	118.21			3.9	136	36	135	265	65	63	195	16	315	60	HASH
240	2010/02/05 06:39:21	37.509N	72.384E	184.86			3.2	272	24	-143	147	76	-70	82	55	222	28	HASH
241	2010/02/07 16:19:24	38.312N	73.688E	118.65			4.4	79	19	48	303	76	103	22	30	50	57	HASH
242	2010/02/09 21:49:17	37.198N	72.145E	222.42			3.3	245	36	-159	138	78	-56	83	46	22	25	HASH
243	2010/02/13 16:37:32	39.380N	72.725E	10.66	6	4.10		294	86	137	28	47	5	349	26	242	32	RMT
								295	62	138	48	54	36	173	5	258	49	HASH
244	2010/02/14 20:32:43	39.693N	71.727E	10.90	6	4.09	4.2	239	72	-59	356	36	-148	186	53	306	21	RMT
245	2010/02/17 00:39:04	39.540N	75.045E	9.95	12	4.13	4.0	226	56	89	48	34	92	317	11	131	79	RMT
246	2010/02/21 02:05:18	38.217N	71.489E	6.77	6	3.60	4.0	56	65	29	313	64	152	184	0	274	37	RMT
247	2010/02/22 01:51:37	36.045N	70.630E	47.55	78	4.27	4.8	264	78	-90	85	12	-89	174	57	354	33	RMT
248	2010/02/22 22:11:05	37.431N	72.205E	184.40			3.5	259	24	120	47	69	77	146	23	297	64	HASH
249	2010/02/24 04:36:39	37.561N	72.261E	167.63			4.3	54	83	-105	300	17	-25	128	50	157	36	HASH
250	2010/02/24 11:18:15	39.497N	73.746E	17.16	6	4.10	4.2	262	83	64	157	27	164	13	33	145	46	RMT
251	2010/02/25 01:52:59	38.152N	73.862E	153.97			3.0	211	76	166	304	76	14	258	0	348	20	HASH
252	2010/02/26 03:53:26	37.445N	72.210E	181.38			4.1	54	75	-103	276	20	-50	127	58	154	29	HASH
253	2010/02/27 04:11:55	37.339N	72.056E	139.47			3.5	280	8	-72	82	82	-92	169	53	354	37	HASH
254	2010/02/28 13:31:07	37.474N	72.231E	171.46			4.9	288	41	-105	128	51	-77	92	79	29	5	HASH
255	2010/03/01 16:46:41	37.631N	72.631E	182.55			2.9	38	89	-167	308	77	-1	264	10	352	8	HASH
256	2010/03/02 01:55:38	42.573N	75.625E	22.72	9	4.82	5.6	300	75	-121	188	34	-27	176	50	54	24	RMT
257	2010/03/06 00:19:56	37.122N	72.962E	0.1	12	3.63	3.9	320	62	-141	210	56	-34	178	46	84	4	RMT
								139	74	-172	47	82	-16	2	17	274	6	HASH
258	2010/03/06 00:53:04	37.132N	72.945E	2.1	9	3.48	3.7	189	73	-26	287	65	-161	147	30	240	5	RMT
259	2010/03/08 08:07:57	38.276N	73.068E	99.07			3.1	45	69	130	158	44	31	107	15	359	49	HASH
260	2010/03/11 07:24:26	37.421N	72.170E	177.46	192	4.05	4.9	317	67	107	100	28	56	34	20	255	64	RMT
								285	86	67	185	23	169	215	37	173	45	HASH
261	2010/03/12 06:55:45	37.230N	72.010E	158.80			3.2	80	89	-98	343	8	-7	162	45	178	43	HASH
262	2010/03/12 07:04:52	37.349N	72.151E	191.06			4.1	238	48	137	0	60	51	117	7	217	56	HASH
263	2010/03/12 17:59:43	37.479N	71.815E	101.56			3.7	161	71	133	270	46	27	221	15	115	46	HASH
264	2010/03/15 00:16:29	37.421N	72.171E	177.31			3.0	12	78	-121	263	33	-22	249	48	126	26	HASH
265	2010/03/15 05:56:48	38.548N	72.156E	17.07	9	4.01	4.3	9	84	10	278	81	174	143	2	234	11	RMT
266	2010/03/17 11:06:59	38.575N	72.725E	10.12	6	3.54	3.8	124	86	-171	34	81	-4	349	9	259	3	RMT
								118	88	-152	27	62	-2	346	21	69	18	HASH
267	2010/03/17 16:38:09	37.664N	72.156E	112.06			3.0	340	89	-117	248	27	-2	45	40	94	38	HASH
268	2010/03/19 00:24:08	37.280N	71.929E	135.94			3.8	247	38	123	28	59	67	134	11	252	67	HASH
269	2010/03/21 19:18:47	37.274N	71.809E	116.83			2.8	33	48	-82	201	43	-99	3	83	117	3	HASH
270	2010/03/23 15:51:18	37.507N	74.606E	18.9	6	4.71	5.0	203	65	-34	310	59	-150	165	41	258	3	RMT
271	2010/03/24 16:32:29	37.806N	72.602E	118.45			3.2	258	24	-105	94	67	-83	197	67	359	22	HASH
272	2010/03/26 05:03:46	37.476N	72.306E	190.34			3.3	21	2	38	253	89	92	161	44	345	46	HASH

Nr	Origin Time	Latitude	Longitude	Depth [km]	Centroid depth [km]	M_w	M_L	Plane 1 strike [o]	dip	rake	Plane 2 strike [o]	dip	rake	P axis strike [o]	dip	T axis strike [o]	dip	method
273	2010/03/26 23:16:40	36.709N	71.364E	172.68	207	3.96	4.6	244	58	89	65	32	91	334	13	152	77	RMT
274	2010/03/27 16:35:54	38.147N	73.453E	142.81			4.0	103	64	-99	303	27	-72	174	70	20	19	HASH
275	2010/03/30 00:32:32	37.749N	72.458E	107.77			3.1	88	69	-94	279	21	-80	351	66	1	24	HASH
276	2010/03/30 02:28:16	37.974N	72.780E	122.36			3.7	74	72	161	170	72	19	122	0	32	26	HASH
277	2010/03/31 11:20:54	38.292N	73.888E	126.90			4.0	274	46	107	70	47	73	172	0	263	78	HASH
278	2010/04/01 07:13:47	38.588N	73.470E	81.23			2.8	108	86	-167	17	77	-4	153	12	62	6	HASH
279	2010/04/01 13:00:24	37.922N	72.462E	104.00			3.6	117	34	-142	354	70	-62	121	56	243	20	HASH
280	2010/04/01 22:47:07	37.285N	71.965E	139.61			3.2	284	28	-133	151	70	-70	270	60	45	22	HASH
281	2010/04/03 04:10:16	37.269N	72.188E	212.32			3.5	37	57	75	243	36	112	138	11	267	73	HASH
282	2010/04/04 10:37:51	38.319N	73.728E	122.59			4.2	175	42	-178	84	89	-48	208	33	320	31	HASH
283	2010/04/07 09:22:30	39.479N	73.297E	12.46	6	4.08	4.3	52	69	85	246	22	103	146	24	313	66	RMT
284	2010/04/07 14:54:07	37.406N	72.159E	175.61			3.3	115	78	-72	238	22	-145	227	54	190	31	HASH
285	2010/04/07 20:47:04	38.279N	73.040E	94.46			3.7	110	79	146	207	57	13	163	15	63	32	HASH
286	2010/04/07 21:12:50	38.090N	73.720E	162.33			3.0	147	76	131	253	43	21	207	20	97	44	HASH
287	2010/04/09 17:56:06	36.158N	69.557E	59.82	129	4.40	5.2	246	69	74	106	26	127	348	23	131	62	RMT
288	2010/04/10 20:05:43	37.424N	72.205E	173.56			3.5	262	38	166	3	81	53	302	27	238	41	HASH
289	2010/04/12 16:01:44	36.587N	70.967E	196.09	210	4.13	4.7	199	60	58	70	43	133	311	10	59	60	RMT
290	2010/04/14 17:34:16	37.550N	72.012E	118.02			2.9	278	30	-138	150	70	-67	272	58	223	22	HASH
291	2010/04/16 19:48:05	37.339N	72.152E	195.38			3.8	251	42	130	23	59	60	314	9	242	63	HASH
292	2010/04/19 11:33:31	37.422N	72.195E	180.28			3.0	269	37	-149	153	72	-57	102	52	39	20	HASH
293	2010/04/20 08:42:35	39.216N	72.269E	5.09			3.8	75	65	144	182	58	30	130	4	216	42	HASH
294	2010/04/20 10:58:27	38.223N	71.520E	0.01	4	3.97	4.5	228	64	-59	354	40	-136	183	59	295	13	RMT
295	2010/04/20 19:07:42	39.276N	72.488E	7.76	9	3.93	4.1	217	77	61	104	32	154	329	26	94	50	RMT
								205	63	20	106	72	152	157	6	64	32	HASH
296	2010/04/21 23:54:32	36.451N	71.427E	72.15	87	4.08	4.5	189	55	98	356	36	79	274	9	129	79	RMT
297	2010/04/22 09:08:47	38.666N	70.835E	0.01	12	3.82	4.5	128	79	151	224	62	13	179	12	82	28	RMT
298	2010/04/23 17:07:32	39.032N	72.511E	15.62	9	3.49	3.8	26	84	-41	121	50	-172	335	32	80	23	RMT
299	2010/04/24 10:36:15	37.338N	72.186E	195.90			3.5	122	59	133	241	51	41	183	5	87	54	HASH
300	2010/04/24 21:16:51	37.436N	72.220E	174.92			4.3	270	57	125	38	47	49	156	6	236	61	HASH
301	2010/04/26 06:02:32	37.305N	72.048E	150.97			3.5	264	31	-51	41	66	-111	278	63	146	19	HASH
302	2010/04/26 08:27:41	36.461N	70.730E	180.40	201	4.08	4.6	107	70	105	249	24	55	185	24	39	62	RMT
303	2010/04/27 00:07:11	39.614N	73.965E	4.88	12	4.17	4.4	41	79	26	306	64	168	171	10	266	26	RMT
304	2010/05/02 02:36:50	37.258N	72.082E	148.87			3.1	293	27	146	54	75	67	162	27	296	54	HASH
305	2010/05/03 09:02:29	37.772N	72.601E	129.43			3.3	177	69	-139	70	52	-27	40	43	120	10	HASH
306	2010/05/04 15:35:36	36.722N	71.314E	171.67	201	4.04	4.6	207	59	91	26	31	89	297	14	120	76	RMT
307	2010/05/06 17:24:03	37.333N	72.171E	197.24			3.0	174	23	153	289	80	69	36	32	176	51	HASH
308	2010/05/08 18:23:30	37.349N	72.131E	191.51			3.2	193	20	59	46	73	101	127	27	151	61	HASH
309	2010/05/08 21:42:05	37.432N	72.213E	170.26			3.8	237	29	-151	121	76	-64	61	52	191	27	HASH
310	2010/05/08 22:45:40	38.017N	72.932E	133.44			3.6	76	65	-169	341	80	-25	296	25	211	10	HASH
311	2010/05/09 13:03:10	37.734N	72.329E	121.00			3.4	143	71	128	256	42	29	206	17	95	49	HASH
312	2010/05/11 06:31:35	36.522N	71.087E	134.99	168	4.77	5.7	188	74	36	87	56	160	314	12	53	36	RMT
313	2010/05/11 07:17:08	37.436N	71.888E	112.36	114	4.24	4.7	32	88	-110	298	20	-4	283	43	140	40	RMT
314	2010/05/11 20:15:08	36.403N	69.883E	51.12	126	4.06	4.7	226	74	-29	325	62	-161	183	32	278	7	RMT
315	2010/05/11 22:58:30	41.431N	71.936E	28.21	18	4.26	5.1	68	56	88	251	34	92	160	11	332	79	RMT
316	2010/05/11 23:07:20	41.423N	71.940E	28.75	21	3.28	4.0	51	50	88	234	41	92	142	4	302	85	RMT
317	2010/05/12 09:08:07	37.438N	72.212E	178.53			4.0	209	7	-157	96	87	-84	13	47	0	42	HASH
318	2010/05/13 04:36:21	38.314N	73.819E	124.26	150	4.52	5.3	258	59	71	111	35	118	1	13	128	70	RMT
								282	60	120	53	41	49	351	10	241	62	HASH
319	2010/05/13 05:06:22	38.307N	73.872E	125.35			3.0	232	19	-109	72	72	-84	172	62	157	27	HASH
320	2010/05/13 12:54:53	36.709N	71.416E	156.88	192	4.45	5.2	181	53	90	1	37	90	271	8	92	82	RMT
321	2010/05/14 07:02:08	38.287N	71.458E	5.45	4	3.95	4.2	139	77	-148	41	58	-15	4	32	266	12	RMT
322	2010/05/14 07:59:40	38.232N	73.220E	125.47			3.9	250	55	-175	157	86	-35	288	27	29	21	HASH
323	2010/05/16 03:24:32	37.415N	72.165E	182.50			3.4	279	19	-41	48	78	-105	120	55	150	31	HASH
324	2010/05/16 17:47:38	38.281N	72.282E	78.41			3.3	135	60	-161	35	74	-31	172	34	268	9	HASH
325	2010/05/19 07:39:42	37.603N	72.050E	103.57			4.2	132	34	167	233	83	57	169	30	291	42	HASH
326	2010/05/21 01:37:02	37.339N	72.147E	182.68			3.0	215	18	-97	42	72	-88	136	63	311	27	HASH
327	2010/05/23 19:29:26	37.697N	72.397E	141.90			3.4	88	68	173	181	84	22	132	11	226	20	HASH
328	2010/05/23 20:01:12	37.274N	72.126E	205.81			3.7	137	55	125	266	48	51	203	4	106	62	HASH
329	2010/05/25 18:04:29	37.072N	71.563E	10.17			3.1	141	78	-168	48	78	-12	5	17	95	0	HASH
330	2010/05/25 20:34:19	37.398N	72.124E	176.40			3.4	151	71	-159	54	70	-20	13	28	102	1	HASH
331	2010/05/25 23:05:54	37.435N	72.217E	184.07			3.5	269	31	126	49	65	71	153	18	286	64	HASH
332	2010/05/27 05:38:19	38.247N	71.509E	6.27	6	4.00		13	64	-85	181	27	-101	295	71	99	19	RMT
333	2010/05/27 14:25:46	37.440N	72.169E	178.47			3.1	129	70	-135	20	48	-27	354	45	70	13	HASH
334	2010/05/30 01:36:52	37.086N	71.573E	9.02			3.5	359	34	-83	171	56	-95	244	78	84	11	HASH
335	2010/05/30 10:19:25	37.014N	71.250E	0.01	12	4.04	4.5	227	69	-24	326	68	-158	186	31	277	1	RMT
336	2010/05/30 13:53:51	36.333N	71.137E	76.61	96	4.19	4.5	59	89	82	321	8	171	157	43	322	46	RMT
337	2010/05/30 23:54:12	37.777N	69.740E	17.91	9	3.99	4.1	174	89	90	3	1	99	264	44	83	46	RMT
338	2010/05/31 00:22:07	37.731N	69.792E	12.17	4	4.46	4.5	359	88	-87	130	3	-139	272	47	87	43	RMT
339	2010/06/01 04:29:27	38.336N	73.641E	119.89			3.5	314	83	-167	222	77	-7	359	14	88	4	HASH
340	2010/06/02 16:41:29	38.206N	75.545E	158.41	153	4.28	4.5	334	67	100	130	25	68	57	21	263	67	RMT

Nr	Origin Time	Latitude	Longitude	Depth [km]	Centroid depth [km]	M_w	M_L	Plane 1 strike [o]	dip	rake	Plane 2 strike [o]	dip	rake	P axis strike [o]	dip	T axis strike [o]	dip	method
341	2010/06/04 11:49:41	36.526N	70.165E	196.83	216	5.06	4.5	102	81	111	213	23	23	174	33	35	50	RMT
342	2010/06/04 15:49:37	38.685N	70.387E	28.86			3.4	192	58	130	314	49	44	255	5	157	57	HASH
343	2010/06/08 07:30:29	37.276N	72.189E	206.37	231	4.06	5.2	247	76	107	15	22	41	323	29	178	56	RMT
344	2010/06/10 06:38:10	40.064N	74.464E		21	4.87	5.7	61	69	82	263	23	110	158	23	317	66	RMT
345	2010/06/10 20:19:03	37.429N	72.191E	181.53			3.3	45	83	119	147	30	14	111	32	344	44	HASH
346	2010/06/11 19:16:53	38.252N	72.897E	94.83			3.1	52	56	178	143	88	34	272	22	193	25	HASH
347	2010/06/12 11:24:52	37.410N	72.169E	180.85			4.1	257	46	167	356	81	45	119	22	47	37	HASH
348	2010/06/12 19:00:03	36.295N	71.147E	93.09	120	4.22	4.6	74	79	83	286	12	122	169	34	335	55	RMT
349	2010/06/14 12:09:01	37.663N	72.285E	133.83			3.1	64	79	-100	287	15	-48	142	55	162	33	HASH
350	2010/06/14 20:49:23	37.514N	71.805E	86.53			3.3	215	58	116	352	40	55	107	9	175	66	HASH
351	2010/06/15 23:39:11	38.580N	71.885E	23.83	9	4.11	4.5	156	55	-91	337	35	-89	64	80	246	10	RMT
352	2010/06/17 05:57:43	37.462N	72.329E	194.73			3.6	221	49	136	343	58	50	100	5	198	57	HASH
353	2010/06/17 08:06:35	39.215N	71.925E	0.01	6	3.53	4.5	204	63	76	52	30	115	304	17	87	69	RMT
354	2010/06/19 12:58:26	37.102N	71.585E	0.01	12	4.27	4.5	35	72	-43	142	49	-155	350	43	93	14	RMT
355	2010/06/19 14:41:58	37.124N	71.546E	0.1	6	4.20	4.5	23	72	-70	153	27	-136	321	58	97	24	RMT
356	2010/06/20 02:37:16	37.239N	72.121E	206.57			3.9	276	17	-101	107	73	-87	202	62	195	28	HASH
357	2010/06/22 10:22:33	38.312N	73.115E	93.32	117	4.12	4.7	15	82	-23	109	67	-171	330	22	64	10	RMT
								197	61	36	87	59	145	321	10	223	36	HASH
358	2010/06/24 23:48:33	36.626N	71.089E	41.23	81	4.50	4.6	63	62	81	261	29	107	159	17	313	71	RMT
359	2010/07/07 17:03:00	40.612N	72.462E	28.5	21	3.53	3.5	221	54	109	11	40	67	298	7	184	74	RMT

Table D.1.: Parameters of all earthquakes we obtained fault plane solutions for, the inversion type is indicated (HASH = from first motion polarities; RMT = from waveform inversion)

E. Profiles of v_p perturbations

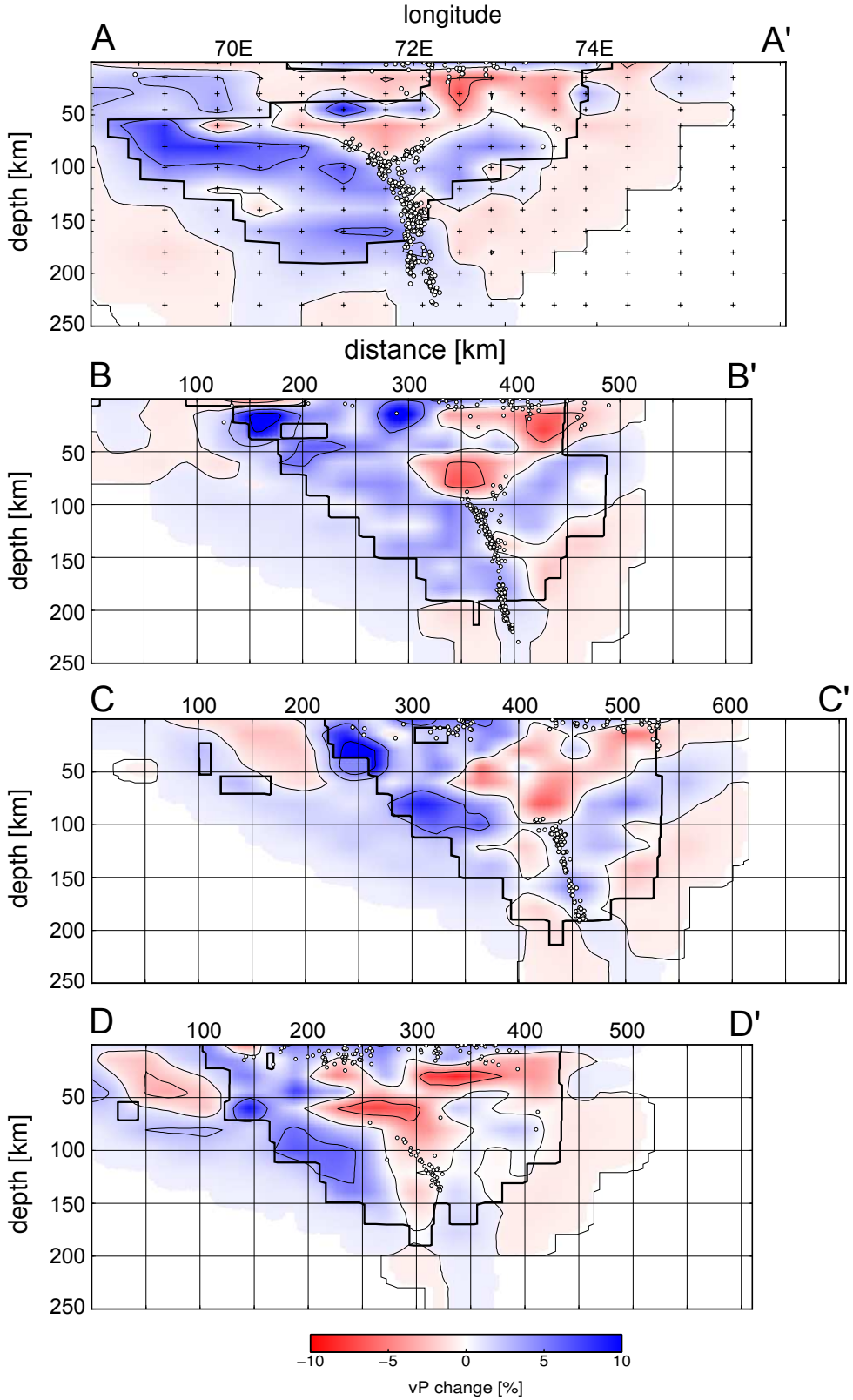

Figure E.1.: Profiles of relative change of P velocities compared to background model (see Figure 4.2). For the location of the profiles, refer to Figure 6.1.

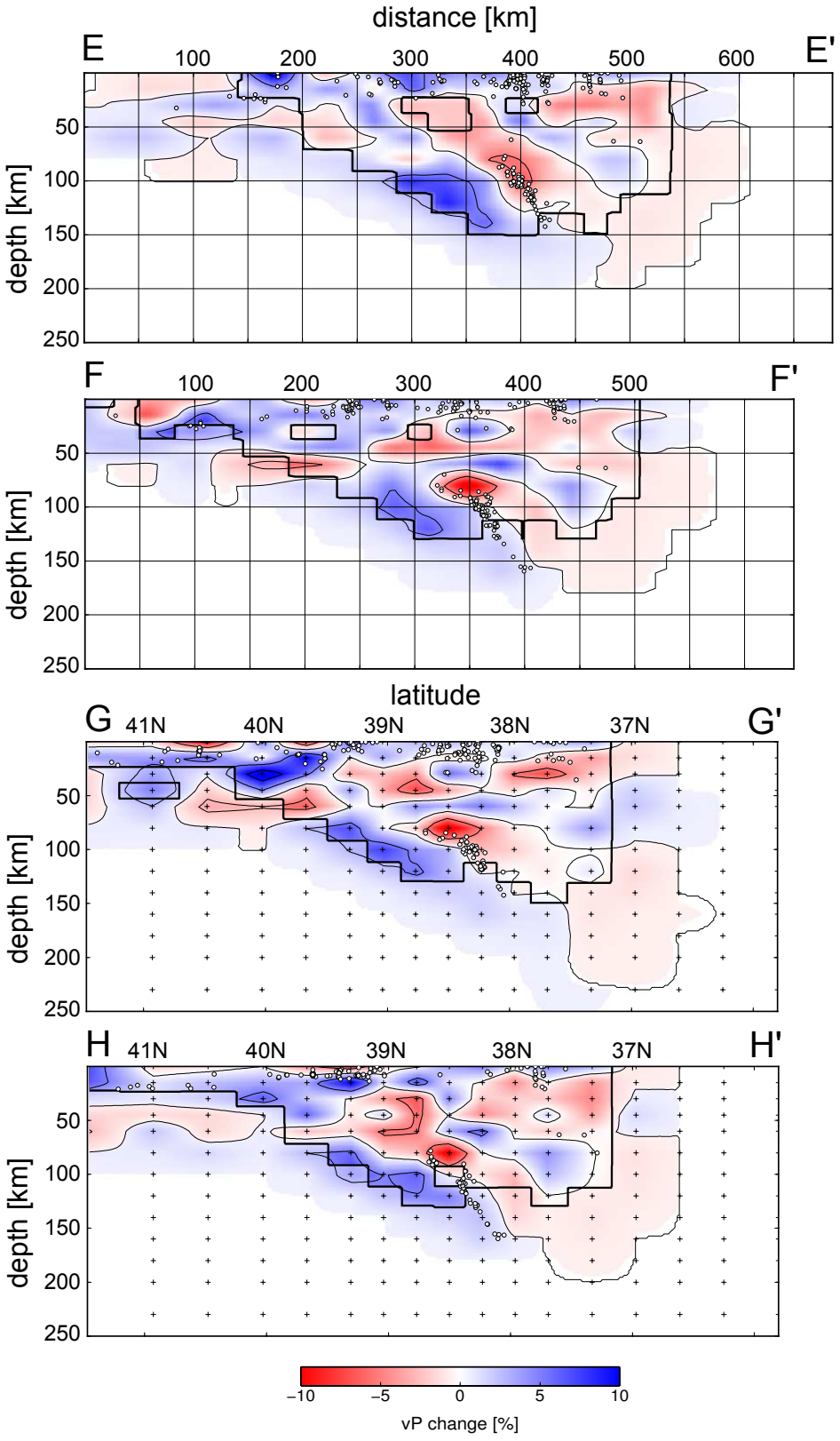

Figure E.1.: Profiles of relative P velocity change (*continued*)

Bibliography

Abdrakhmatov, K., S. Aldazhanov, B. Hager, M. Hamburger, T. Herring, K. Kalabaev, V. I. Makarov, P. Molnar, S. Panasyuk, M. Prilepin, R. Reilinger, I. Sadybakasov, B. Souter, Y. Trapeznikov, V. Tsurkov, and A. Zubovich (1996), Relatively recent construction of the Tien Shan inferred from GPS measurements of present-day crustal deformation rates, *Nature*, *384*, 450–453.

Abers, G., C. Bryan, and S. Roecker (1988), Thrusting of the Hindu Kush over the southeastern Tadjik Basin, Afghanistan: evidence from two large earthquakes, *Tectonics*, *7*(1), 41–56.

Aki, K., and W. Lee (1976), Determination of three-dimensional velocity anomalies under a seismic array using first P arrival times from local earthquakes - 1. A homogeneous initial model, *Journal of Geophysical Research*, *81*(23), 4,381–4,399.

Aki, K., and P. Richards (1980), *Quantitative Seismology: Theory and Methods*, 932 pp., W. H. Freeman, New York.

Aki, K., A. Christoffersson, and E. Husebye (1977), Determination of the three-dimensional seismic structure of the lithosphere, *Journal of Geophysical Research*, *82*(2), 277–296.

Aldersons, F. (2004), Toward a Three-Dimensional Crustal Structure of the Dead Sea region from Local Earthquake Tomography, Ph.D. thesis, Tel-Aviv University, Israel.

Ali, J. R., and J. C. Aitchison (2005), Greater India, *Earth-Science Reviews*, *72*(3-4), 169–188, doi:10.1016/j.earscirev.2005.07.005.

Allen, M. B., B. Windley, and Z. Chi (1993), Palaeozoic collisional tectonics and magmatism of the Chinese Tien Shan, central Asia, *Tectonophysics*, *220*, 89–115.

Allen, R. (1978), Automatic earthquake recognition and timing from single traces, *Bulletin of the Seismological Society of America*, *68*(5), 1521–1532.

Allmendinger, R., R. Reilinger, and J. Loveless (2007), Strain and rotation rate from GPS in Tibet, Anatolia, and the Altiplano, *Tectonics*, *26*(3), 1–18, doi:10.1029/2006TC002030.

ArRajehi, A., S. McClusky, R. Reilinger, M. Daoud, A. Alchalbi, S. Ergintav, F. Gomez, J. Sholan, F. Bou-Rabee, G. Ogubazghi, B. Haileab, S. Fisseha, L. Asfaw, S. Mahmoud, A. Rayan, R. Bendick, and L. Kogan (2010), Geodetic constraints on present-day motion of the Arabian Plate: Implications for Red Sea and Gulf of Aden rifting, *Tectonics*, *29*(3), TC3011, doi:10.1029/2009TC002482.

Arrowsmith, J. R., and M. Strecker (1999), Seismotectonic range-front segmentation and mountain-belt growth in the Pamir-Alai region, Kyrgyzstan (India-Eurasia collision zone), *Geological Society of America Bulletin*, *111*(11), 1665–1683, doi:10.1130/0016-7606(1999)111⟨1665:SRFSAM⟩2.3.CO;2.

Arroyo, I. G., S. Husen, E. R. Flueh, J. Gossler, E. Kissling, and G. E. Alvarado (2009), Three-dimensional P -wave velocity structure on the shallow part of the Central Costa Rican Pacific margin from local earthquake tomography using off- and onshore networks, *Geophysical Journal International*, *179*(2), 827–849, doi:10.1111/j.1365-246X.2009.04342.x.

Auden, J. B. (1974), Afghanistan-West Pakistan, *Geological Society, London, Special Publications*, *4*(1), 235–253, doi:10.1144/GSL.SP.2005.004.01.13.

Avouac, J., and P. Tapponnier (1993), Kinematic model of active deformation in central Asia, *Geophysical Research Letters*, *20*(10), 895–898.

Baer, M., and U. Kradolfer (1987), An automatic phase picker for local and teleseismic events, *Bulletin of the Seismological Society of America*, *77*(4), 1437–1445.

Bai, D., M. Unsworth, M. Meju, X. Ma, J. Teng, X. Kong, Y. Sun, J. Sun, L. Wang, C. Jiang, C. Zhao, P. Xiao, and M. Liu (2010), Crustal deformation of the eastern Tibetan plateau revealed by magnetotelluric imaging, *Nature Geoscience*, *3*(5), 358–362, doi:10.1038/ngeo830.

Bajolet, F., J. Galeano, F. Funiciello, M. Moroni, A. Negredo, and C. Faccenna (2012), Continental delamination: Insights from laboratory models, *Geochemistry Geophysics Geosystems*, *13*(1), 1–22, doi:10.1029/2011GC003896.

Bazhenov, M. (1986), Tectonics and paleomagnetism of structural arcs of the Pamir-Punjab syntaxis, *Journal of Geodynamics*, *5*(3-4), 383–396, doi:10.1016/0264-3707(86)90017-7.

Becker, T. W., and C. Faccenna (2011), Mantle conveyor beneath the Tethyan collisional belt, *Earth and Planetary Science Letters*, *310*(3-4), 453–461, doi:10.1016/j.epsl.2011.08.021.

Beloussov, V., N. Belyaevsky, A. Borisov, B. Volvosky, I. Volvosky, D. Resvoy, B. Tal-Visky, I. Khamrabaev, K. Kaila, H. Narain, A. Marussi, and J. Finetti (1980), Structure of the lithosphere along the deep seismic sounding profile: Tien Shan—Pamirs—Karakorum—Himalayas, *Tectonophysics*, *70*(3-4), 193–221, doi:10.1016/0040-1951(80)90279-6.

Benetatos, C., A. Kiratzi, C. Papazachos, and G. Karakaisis (2004), Focal mechanisms of shallow and intermediate depth earthquakes along the Hellenic Arc, *Journal of Geodynamics*, *37*(2), 253–296, doi:10.1016/j.jog.2004.02.002.

Bensen, G. D., M. Ritzwoller, M. P. Barmin, A. Levshin, F. Lin, M. P. Moschetti, N. M. Shapiro, and Y. Yang (2007), Processing seismic ambient noise data to obtain reliable broad-band surface wave dispersion measurements, *Geophysical Journal International*, *169*(3), 1239–1260, doi:10.1111/j.1365-246X.2007.03374.x.

Bernard, M., B. Shen-Tu, W. E. Holt, and D. M. Davis (2000), Kinematics of active deformation in the Sulaiman Lobe and Range, Pakistan, *Journal of Geophysical Research*, *105*, 13,253–13,279.

Beyreuther, M., R. Barsch, L. Krischer, T. Megies, Y. Behr, and J. Wassermann (2010), ObsPy: A Python Toolbox for Seismology, *Seismological Research Letters*, *81*(3), 530–533, doi:10.1785/gssrl.81.3.530.

Bijwaard, H., W. Spakman, and E. Engdahl (1998), Closing the gap between regional and global travel time tomography, *Journal of Geophysical Research*, *103*(B12), 30,055–30,078, doi:10.1029/98JB02467.

Billington, S., B. Isacks, and M. Barazangi (1977), Spatial distribution and focal mechanisms of mantle earthquakes in the Hindu Kush-Pamir region: A contorted Benioff zone, *Geology*, *5*(11), 699–704.

Birch, F. (1961), The velocity of compressional waves in rocks to 10 kilobars, part 2, *Journal of Geophysical Research*, *66*(7), 2199–2224.

Bird, P. (1979), Continental delamination and the Colorado Plateau, *Journal of Geophysical Research*, *84*(B13), 7561–7571.

Blisniuk, P. M., B. Hacker, J. Glodny, L. Ratschbacher, S. Bi, Z. Wu, M. McWilliams, and A. Calvert (2001), Normal faulting in central Tibet since at least 13.5 Myr ago., *Nature*, *412*, 628–632, doi:10.1038/35088045.

Bondár, I., and D. Storchak (2011), Improved location procedures at the International Seismological Centre, *Geophysical Journal International*, doi:10.1111/j.1365-246X.2011.05107.x.

Bouchon, M. (1982), The Complete Synthesis of Seismic Crustal Phases at Regional Distances, *Journal of Geophysical Research*, *87*(B3), 1735–1741, doi:10.1029/JB087iB03p01735.

Boundy, T. M., D. M. Fountain, and H. Austrheim (1992), Structural development and petrofabrics of eclogite facies shear zones, Bergen Arcs, western Norway: implications for deep crustal deformational processes, *Journal of Metamorphic Geology*, *10*(2), 127–146, doi:10.1111/j.1525-1314.1992.tb00075.x.

Bourgeois, O., P. Cobbold, D. Rouby, J. Thomas, and V. Shein (1997), Least squares restoration of Tertiary thrust sheets in map view, Tajik depression, central Asia, *Journal of Geophysical Research*, *102*(B12), 27,553–27,573.

Brookfield, M. (2001), The geology and petroleum potential of the North Afghan platform and adjacent areas (northern Afghanistan, with parts of southern Turkmenistan, Uzbekistan and Tajikistan), *Earth-Science Reviews*, *55*(1-2), 41–71, doi:10.1016/S0012-8252(01)00036-8.

Brown, L., W. Zhao, K. Nelson, M. Hauck, D. Alsdorf, A. Ross, M. Cogan, M. Clark, X. Liu, and J. Che (1996), Bright spots, structure, and magmatism in southern Tibet from INDEPTH seismic reflection profiling, *Science*, *274*, 1688–1690.

Brudzinski, M. R., C. Thurber, B. Hacker, and E. Engdahl (2007), Global prevalence of double Benioff zones., *Science*, *316*(5830), 1472–4, doi:10.1126/science.1139204.

Burov, E., and P. Yamato (2008), Continental plate collision, P–T–t–z conditions and unstable vs. stable plate dynamics: Insights from thermo-mechanical modelling, *Lithos*, *103*(1-2), 178–204, doi:10.1016/j.lithos.2007.09.014.

Burtman, V., and P. Molnar (1993), Geological and geophysical evidence for deep subduction of continental crust beneath the Pamir, *Tech. rep.*

Burtman, V., S. Skobelev, and P. Molnar (1996), Late Cenozoic slip on the Talas-Ferghana fault, the Tien Shan, central Asia, *Geological Society of America Bulletin*, *108*(8), 1004–1021.

Cardozo, N., and R. Allmendinger (2009), SSPX: A program to compute strain from displacement/velocity data, *Computers & Geosciences*, *35*(6), 1343–1357, doi:10.1016/j.cageo.2008.05.008.

Chatelain, J., S. Roecker, D. Hatzfeld, and P. Molnar (1980), Microearthquake seismicity and fault plane solutions in the Hindu Kush region and their tectonic implications, *Journal of Geophysical Research*, *85*(B3), 1365–1387.

Chemenda, A., J. Burg, and M. Mattauer (2000), Evolutionary model of the Himalaya-Tibet system: geopoem based on new modelling, geological and geophysical data, *Earth and Planetary Science Letters*, *174*(3-4), 397–409.

Chen, L., J. Booker, A. Jones, N. Wu, M. Unsworth, W. Wenbo, and T. Handong (1996), Electrically conductive crust in southern Tibet from INDEPTH magnetotelluric surveying, *Science*, *274*, 1694–1696.

Christensen, N. I. (1996), Poisson's ratio and crustal seismology, *Journal of Geophysical Research*, *101*(B2), 3139–3156, doi:10.1029/95JB03446.

Cichowicz, A. (1993), An automatic S-phase picker, *Bulletin of the Seismological Society of America*, *83*(1), 180–189.

Clark, M., and L. Royden (2000), Topographic ooze: Building the eastern margin of Tibet by lower crustal flow, *Geology*, *28*(8), 703–706, doi:10.1130/0091-7613(2000)028⟨0703:TOBTEM⟩2.3.CO;2.

Cloos, M. (1993), Lithospheric buoyancy and collisional orogenesis: Subduction of oceanic plateaus, continental margins, island arcs, spreading ridges, and seamounts, *Geological Society of America Bulletin*, *105*(6), 715–737, doi:10.1130/0016-7606(1993)105⟨0715:LBACOS⟩2.3.CO;2.

Cobbold, P., P. Davy, D. Gapais, E. Rossello, E. Sadybakasov, J. Thomas, J. Tondji Biyo, and M. De Urreiztieta (1993), Sedimentary basins and crustal thickening, *Sedimentary Geology*, *86*(1-2), 77–89.

Connolly, J. (2005), Computation of phase equilibria by linear programming: A tool for geodynamic modeling and its application to subduction zone decarbonation, *Earth and Planetary Science Letters*, *236*(1-2), 524–541, doi:10.1016/j.epsl.2005.04.033.

Cook, K. L., and L. Royden (2008), The role of crustal strength variations in shaping orogenic plateaus, with application to Tibet, *Journal of Geophysical Research*, *113*(B8), 1–18, doi:10.1029/2007JB005457.

Coutand, I., M. Strecker, J. R. Arrowsmith, G. Hilley, R. Thiede, A. Korjenkov, and M. Omuraliev (2002), Late Cenozoic tectonic development of the intramontane Alai Valley, (Pamir-Tien Shan region, central Asia): An example of intracontinental deformation due to the Indo-Eurasia collision, *Tectonics*, *21*(6), doi:10.1029/2002TC001358.

Coward, M., and R. Butler (1985), Thrust tectonics and the deep structure of the Pakistan Himalaya, *Geology*, *13*, 417–420.

Cowgill, E. (2010), Cenozoic right-slip faulting along the eastern margin of the Pamir salient, northwestern China, *Geological Society of America Bulletin*, *122*(1-2), 145–161, doi:10.1130/B26520.1.

Craig, T. J., A. Copley, and J. Jackson (2012), Thermal and tectonic consequences of India underthrusting Tibet, *Earth and Planetary Science Letters*, *353-354*, 231–239, doi:10.1016/j.epsl.2012.07.010.

Crawford, A. (1974), The Salt Range, the Kashmir syntaxis and the Pamir arc, *Earth and Planetary Science Letters*, *22*(4), 371–379.

Creager, K., and T. Boyd (1991), The geometry of Aleutian subduction: Three-dimensional kinematic flow model, *Journal of Geophysical Research*, *96*, 2293–2307.

Davis, D. M., and T. Engelder (1985), The role of salt in fold-and-thrust belts, *Tectonophysics*, *119*, 67–88.

de Lapparent, A. (1972), L'Afghanistan et la derive du continent indien (in French), *Rev. Geogr. Phys. Geol. Dyn*, *XIV*(4), 449–455.

DeCelles, P. G., D. Robinson, and G. Zandt (2002), Implications of shortening in the Himalayan fold-thrust belt for uplift of the Tibetan Plateau, *Tectonics*, *21*(6), 1–25, doi: 10.1029/2001TC001322.

DeMets, C., R. G. Gordon, and D. F. Argus (2010), Geologically current plate motions, *Geophysical Journal International*, *181*(1), 1–80, doi:10.1111/j.1365-246X.2009.04491.x.

Dewey, J., S. Cande, and W. Pitman (1989), Tectonic evolution of the India/Eurasia collision zone, *Eclogae Geologicae Helvetiae*, *82*(3), 717–734.

Di Stefano, R., F. Aldersons, E. Kissling, P. Baccheschi, C. Chiarabba, and D. Giardini (2006), Automatic seismic phase picking and consistent observation error assessment: application to the Italian seismicity, *Geophysical Journal International*, *165*(1), 121–134, doi: 10.1111/j.1365-246X.2005.02799.x.

Diehl, T. (2008), 3-D Seismic Velocity Models of the Alpine Crust from Local Earthquake Tomography, Ph.D. thesis, ETH Zürich.

Diehl, T., and E. Kissling (2008), Users Guide for MPX Picking System; Appendix D of T. Diehl's, Ph.D. thesis, ETH Zürich.

Diehl, T., E. Kissling, S. Husen, and F. Aldersons (2009a), Consistent phase picking for regional tomography models: application to the greater Alpine region, *Geophysical Journal International*, *176*(2), 542–554, doi:10.1111/j.1365-246X.2008.03985.x.

Diehl, T., N. Deichmann, E. Kissling, and S. Husen (2009b), Automatic S-Wave Picker for Local Earthquake Tomography, *Bulletin of the Seismological Society of America*, *99*(3), 1906–1920, doi:10.1785/0120080019.

Douglas, A. (1997), Bandpass filtering to reduce noise on seismograms: Is there a better way?, *Bulletin of the Seismological Society of America*, *87*(4), 770–777.

Ducea, M., V. Lutkov, V. Minaev, B. Hacker, L. Ratschbacher, P. Luffi, M. Schwab, G. Gehrels, M. McWilliams, J. Vervoort, and J. Metcalf (2003), Building the Pamirs: The view from the underside, *Geology*, *31*(10), 849, doi:10.1130/G19707.1.

Duretz, T., S. M. Schmalholz, and T. V. Gerya (2012), Dynamics of slab detachment, *Geochemistry Geophysics Geosystems*, *13*(3), doi:10.1029/2011GC004024.

Duschkov, A., Y. Shvartsman, and L. Sokolova (2001), Deep heat flow in the Tien Shan: Advances and drawbacks, *Geologia & Geofizika*, *42*(10), 1516–1531.

Eberhart-Phillips, D. (1986), Three-dimensional velocity structure in northern California Coast Ranges from inversion of local earthquake arrival times, *Bulletin of the Seismological Society of America*, *76*(4), 1025–1052.

Eberhart-Phillips, D. (1993), Local earthquake tomography: earthquake source regions, in *Seismic Tomography: Theory and Practice*, edited by H. Iyer and K. Hirahara, pp. 614–643, Chapman and Hall, London.

Eberhart-Phillips, D., and M. Reyners (1997), Continental subduction and three-dimensional crustal structure: The northern South Island, New Zealand, *Journal of Geophysical Research*, *102*(B6), 11,843–11,861, doi:10.1029/96JB03555.

Ekström, G., and E. Engdahl (1989), Earthquake source parameters and stress distribution in the Adak Island region of the central Aleutian Islands, Alaska, *Journal of Geophysical Research*, *94*, 15,499–15,519.

Engdahl, E., R. van der Hilst, and R. Buland (1998), Global teleseismic earthquake relocation with improved travel times and procedures for depth determination, *Bulletin of the Seismological Society of America*, *88*(3), 722–743.

Engelder, T. (1987), Joints and Shear Fractures in Rocks, in *Fracture Mechanics of Rock*, edited by B. Atkinson, Elsevier.

Evans, J., D. Eberhart-Phillips, and C. Thurber (1994), User's manual for simulps12 for imaging vp and vp/vs: A derivative of the "Thurber" tomographic inversion simul3 for local earthquakes and explosions, *Tech. rep.*, Open File Report 94-431, U.S. Geological Survey.

Fan, G., J. Ni, and T. Wallace (1994), Active tectonics of the Pamirs and Karakorum, *Journal of Geophysical Research*, *99*(B4), 7131–7160.

Feld, C. (2011), Seismotectonic Study of the Fergana Region (Southern Kyrgyzstan): Distribution and Kinematics of Local Seismicity, Master thesis, Freie Universität Berlin.

Gan, W., P. Zhang, Z.-K. Shen, Z. Niu, M. Wang, Y. Wan, D. Zhou, and J. Cheng (2007), Present-day crustal motion within the Tibetan Plateau inferred from GPS measurements, *Journal of Geophysical Research*, *112*(B8), 1–14, doi:10.1029/2005JB004120.

Geiger, L. (1910), Herdbestimmung bei Erdbeben aus den Ankunftszeiten, *K. Gesellschaft d. Wiss. Göttingen*, *4*, 331–349.

Gephart, J., and D. Forsyth (1984), An improved method for determining the regional stress tensor using earthquake focal mechanism data: application to the San Fernando earthquake sequence, *Journal of Geophysical Research*, *89*(B11), 9305–9320, doi:10.1029/JB089iB11p09305.

Gilbert, F. (1973), Derivation of Source Parameters from Low-Frequency Spectra, *Phil. Trans. R. Soc. Lond*, *Ser. A*(274), 369–371.

Gordon, S. M., P. Luffi, B. Hacker, J. Valley, M. Spicuzza, R. Kozdon, P. Kelemen, L. Ratschbacher, and V. Minaev (2012), The thermal structure of continental crust in active orogens: insight from Miocene eclogite and granulite xenoliths of the Pamir Mountains, *Journal of Metamorphic Geology*, *30*(4), 413–434, doi:10.1111/j.1525-1314.2012.00973.x.

Govers, R., and M. Wortel (2005), Lithosphere tearing at STEP faults: response to edges of subduction zones, *Earth and Planetary Science Letters*, *236*(1-2), 505–523, doi:10.1016/j.epsl.2005.03.022.

Göğüş, O. H., and R. N. Pysklywec (2008), Near-surface diagnostics of dripping or delaminating lithosphere, *Journal of Geophysical Research*, *113*(B11), 1–11, doi:10.1029/2007JB005123.

Gray, R., and R. N. Pysklywec (2012), Geodynamic models of mature continental collision: Evolution of an orogen from lithospheric subduction to continental retreat/delamination, *Journal of Geophysical Research*, *117*(B3), 1–14, doi:10.1029/2011JB008692.

Guillot, S. (2003), Reconstructing the total shortening history of the NW Himalaya, *Geochemistry Geophysics Geosystems*, *4*(7), doi:10.1029/2002GC000484.

Gutenberg, B., and C. Richter (1954), *Seismicity of the Earth and Associated Phenomena*, Princeton University Press, Princeton, NJ.

Haak, V., and R. Hutton (1986), Electrical resistivity in continental lower crust, *Geological Society, London, Special Publications*, *24*(1), 35–49, doi:10.1144/GSL.SP.1986.024.01.05.

Haberland, C., U. Abdybachaev, B. Schurr, H.-U. Wetzel, S. Roessner, A. Sarnagoev, S. Orunbaev, and C. Janssen (2011), Landslides in southern Kyrgyzstan: Understanding tectonic controls, *EOS Transactions*, *92*(20), 169–170, doi:10.1007/s11069-.

Hacker, B. (2003), Subduction factory 1. Theoretical mineralogy, densities, seismic wave speeds, and H 2 O contents, *Journal of Geophysical Research*, *108*(B1), 1–26, doi:10.1029/2001JB001127.

Hacker, B. (2005), Near-Ultrahigh Pressure Processing of Continental Crust: Miocene Crustal Xenoliths from the Pamir, *Journal of Petrology*, *46*(8), 1661–1687, doi:10.1093/petrology/egi030.

Hacker, B., S. Peacock, G. Abers, and S. G. Holloway (2003), Subduction factory 2. Are intermediate-depth earthquakes in subducting slabs linked to metamorphic dehydration reactions?, *Journal of Geophysical Research*, *108*(B1), doi:10.1029/2001JB001129.

Hacker, B. R., and G. Abers (2004), Subduction Factory 3: An Excel worksheet and macro for calculating the densities, seismic wave speeds, and H 2 O contents of minerals and rocks at pressure and temperature, *Geochemistry Geophysics Geosystems*, *5*(1), 1–7, doi:10.1029/2003GC000614.

Hamburger, M., D. Sarewitz, T. Pavlis, and G. Popandopulo (1992), Structural and seismic evidence for intracontinental subduction in the Peter the First Range, central Asia, *Bulletin of the Geological Society of America*, *104*(4), 397–408.

Hardebeck, J. L., and E. Hauksson (2001), Stress orientations obtained from earthquake focal mechanisms: what are appropriate uncertainty estimates?, *Bulletin of the Seismological Society of America*, *91*(2), 250–262.

Hardebeck, J. L., and A. Michael (2006), Damped regional-scale stress inversions: Methodology and examples for southern California and the Coalinga aftershock sequence, *Journal of Geophysical Research*, *111*(B11), 1–11, doi:10.1029/2005JB004144.

Hardebeck, J. L., and P. Shearer (2002), A New Method for Determining First-Motion Focal Mechanisms, *Bulletin of the Seismological Society of America*, *92*(6), 2264–2276, doi:10.1785/0120010200.

Haslinger, F., and E. Kissling (2001), Investigating effects of 3-D ray tracing methods in local earthquake tomography, *Physics of the Earth and Planetary Interiors*, *123*(2-4), 103–114, doi:10.1016/S0031-9201(00)00204-1.

Haslinger, F., E. Kissling, J. Ansorge, D. Hatzfeld, E. Papadimitriou, V. Karakostas, K. Makropoulos, H.-G. Kahle, and Y. Peter (1999), 3D crustal structure from local earthquake tomography around the Gulf of Arta (Ionian region, NW Greece), *Tectonophysics*, *304*(3), 201–218, doi:10.1016/S0040-1951(98)00298-4.

Hatzfeld, D., and P. Molnar (2010), Comparisons of the kinematics and deep structures of the Zagros and Himalaya and of the Iranian and Tibetan plateaus and geodynamic implications, *Reviews of Geophysics*, *48*, 1–48, doi:10.1029/2009RG000304.1.INTRODUCTION.

Hendrix, M., T. Dumitru, and S. A. Graham (1994), Late Oligocene-early Miocene unroofing in the Chinese Tian Shan: An early effect of the India-Asia collision, *Geology*, *22*(6), 487–490.

Hetényi, G., R. Cattin, F. Brunet, L. Bollinger, J. Vergne, J. Nábelek, and M. Diament (2007), Density distribution of the India plate beneath the Tibetan plateau : Geophysical and petrological constraints on the kinetics of lower-crustal eclogitization, *Earth and Planetary Science Letters*, *264*, 226–244, doi:10.1016/j.epsl.2007.09.036.

Hildebrand, P. R., S. Noble, M. P. Searle, R. Parrish, and Shakirullah (1998), Tectonic significance of 24 Ma crustal melting in the eastern Hindu Kush, Pakistan, *Geology*, *26*(10), 871–874.

Hildebrand, P. R., S. Noble, M. P. Searle, D. Waters, and R. Parrish (2001), Old origin for an active mountain range: Geology and geochronology of the eastern Hindu Kush, Pakistan, *Geological Society of America Bulletin*, *113*(5), 625–639, doi:10.1130/0016-7606(2001)113⟨0625:OOFAAM⟩2.0.CO;2.

Houseman, G., D. McKenzie, and P. Molnar (1981), Convective instability of a thickened boundary layer and its relevance for the thermal evolution of continental convergent belts, *Journal of Geophysical Research*, *86*(B7), 6115–6132.

Husen, S., E. Kissling, and E. R. Flueh (2000), Local earthquake tomography of shallow subduction in north Chile: A combined onshore and offshore study, *Journal of Geophysical Research*, *105*(B12), 28,183–28,198, doi:10.1029/2000JB900229.

Hutton, L., and D. Boore (1987), The ML scale in southern California, *Bulletin of the Seismological Society of America*, *77*(6), 2074–2094.

Isacks, B., and P. Molnar (1969), Mantle earthquake mechanisms and the sinking of the lithosphere, *Nature*, *223*, 1121–1124.

Ismail-Zadeh, A., L. Matenco, M. Radulian, S. Cloetingh, and G. F. Panza (2012), Geodynamics and intermediate-depth seismicity in Vrancea (the south-eastern Carpathians): Current state-of-the art, *Tectonophysics*, *530-531*, 50–79, doi:10.1016/j.tecto.2012.01.016.

John, T., S. Medvedev, L. H. Rüpke, T. B. Andersen, Y. Y. Podladchikov, and H. Austrheim (2009), Generation of intermediate-depth earthquakes byself-localizing thermal runaway, *Nature Geoscience*, *2*(2), 137–140, doi:10.1038/ngeo419.

Jost, M., and R. Herrmann (1989), A student's guide to and review of moment tensors, *Seismological Research Letters*, *60*(2), 37–57.

Julian, B., A. Miller, and G. Foulger (1998), Non-double-couple earthquakes 1. Theory, *Reviews of Geophysics*, *36*(4), 525–549.

Jung, H., H. Green, and L. F. Dobrzhinetskaya (2004), Intermediate-depth earthquake faulting by dehydration embrittlement with negative volume change, *Nature*, *428*, 545–549, doi:10.1038/nature02412.

Kay, R., and S. M. Kay (1993), Delamination and delamination magmatism, *Tectonophysics*, *219*(1-3), 177–189, doi:10.1016/0040-1951(93)90295-U.

Kelemen, P., and G. Hirth (2007), A periodic shear-heating mechanism for intermediate-depth earthquakes in the mantle, *Nature*, *446*, 787–790, doi:10.1038/nature05717.

Kennett, B., E. Engdahl, and R. Buland (1995), Constraints on seismic velocities in the Earth from traveltimes, *Geophysical Journal International*, *122*(1), 108–124, doi:10.1111/j.1365-246X.1995.tb03540.x.

Khan, S. D., D. J. Walker, S. Hall, K. C. Burke, M. T. Shah, and L. Stockli (2009), Did the Kohistan-Ladakh island arc collide first with India?, *Geological Society of America Bulletin*, *121*(3-4), 366–384, doi:10.1130/B26348.1.

Kind, R., and X. Yuan (2010), Seismic images of the biggest crash on Earth, *Science*, *329*(5998), 1479–1480, doi:10.1126/science.1191620.

Kind, R., X. Yuan, J. Saul, D. Nelson, S. V. Sobolev, J. Mechie, W. Zhao, G. Kosarev, J. Ni, U. Achauer, and M. Jiang (2002), Seismic images of crust and upper mantle beneath Tibet: evidence for Eurasian plate subduction., *Science*, *298*, 1219–1221, doi:10.1126/science.1078115.

Kirby, S., S. Stein, E. Okal, and D. Rubie (1996), Metastable mantle phase transformations and deep earthquakes in subducting oceanic lithosphere, *Reviews of Geophysics*, *34*(2), 261–306.

Kiser, E., M. Ishii, C. Langmuir, P. Shearer, and H. Hirose (2011), Insights into the mechanism of intermediate-depth earthquakes from source properties as imaged by back projection of multiple seismic phases, *Journal of Geophysical Research*, *116*(B6), B06,310, doi:10.1029/2010JB007831.

Kissling, E. (1988), Geotomography with local earthquake data, *Reviews of Geophysics*, *26*(4), 659–698.

Kissling, E., W. Ellsworth, D. Eberhart-Phillips, and U. Kradolfer (1994), Initial reference models in local earthquake tomography, *Journal of Geophysical Research*, *99*(B10), 19,635–19,646.

Klootwijk, C., J. Gee, J. Peirce, G. Smith, and P. McFadden (1992), An early India-Asia contact: paleomagnetic constraints from Ninetyeast Ridge, ODP leg 121, *Geology*, *20*(5), 395–398.

Knopoff, L., and M. Randall (1970), The compensated linear-vector dipole: a possible mechanism for deep earthquakes, *Journal of Geophysical Research*, *75*(26), 4957–4963.

Kosarev, G., R. Kind, S. V. Sobolev, X. Yuan, W. Hanka, and S. Oreshin (1999), Seismic Evidence for a Detached Indian Lithospheric Mantle Beneath Tibet, *Science*, *283*, 1306–1309, doi:10.1126/science.283.5406.1306.

Koulakov, I. (2009), Out-of-Network Events Can Be of Great Importance for Improving Results of Local Earthquake Tomography, *Bulletin of the Seismological Society of America*, *99*(4), 2556–2563, doi:10.1785/0120080365.

Koulakov, I. (2011), High-frequency P and S velocity anomalies in the upper mantle beneath Asia from inversion of worldwide traveltime data, *Journal of Geophysical Research*, *116*(B4), 1–22, doi:10.1029/2010JB007938.

Koulakov, I., and S. V. Sobolev (2006), A tomographic image of Indian lithosphere break-off beneath the Pamir-Hindukush region, *Geophysical Journal International*, *164*(2), 425–440, doi:10.1111/j.1365-246X.2005.02841.x.

Krumbiegel, C. (2011), The analysis of the 05/10/2008 Mw 6.7 Nura earthquake sequence on the Main Pamir Thrust, Diploma thesis, TU Bergakademie Freiberg, Germany.

Kuchai, V., and V. Trifonov (1977), Young left-lateral strike-slip along the zone of the Darvaz Fault (in Russian), *Geotektonika*, *3*, 91–105.

Kuge, K., and H. Kawakatsu (1993), Significance of non-double couple components of deep and intermediate-depth earthquakes: implications from moment tensor inversions of long-period seismic, *Physics of the Earth and Planetary Interiors*, *75*, 243–266.

Kulagina, M., A. Lukk, and B. Kulagin (1974), Block structure of the earth's crust of Tadjikstan, in *Searches for precursors of earthquakes in prediction polygons*, pp. 70–84, Moscow, Nauka.

Küperkoch, L., T. Meier, J. Lee, W. Friederich, and E. Working Group (2010), Automated determination of P -phase arrival times at regional and local distances using higher order statistics, *Geophysical Journal International*, pp. 1159–1170, doi:10.1111/j.1365-246X.2010.04570.x.

Lacassin, R., F. Valli, N. Arnaud, P. Leloup, J. L. Paquette, L. Haibing, P. Tapponnier, M.-L. Chevalier, S. Guillot, G. Maheo, and X. Zhiqin (2004), Large-scale geometry, offset and kinematic evolution of the Karakorum fault, Tibet, *Earth and Planetary Science Letters*, *219*(3-4), 255–269, doi:10.1016/S0012-821X(04)00006-8.

Larson, K., R. Bürgmann, R. Bilham, and J. Freymueller (1999), Kinematics of the India-Eurasia collision zone from GPS measurements, *Journal of Geophysical Research*, *104*(B1), 1077–1093.

Le Pichon, X., M. Fournier, and L. Jolivet (1992), Kinematics, topography, shortening, and extrusion in the India-Eurasia collision, *Tectonics*, *11*(6), 1085–1098.

Lee, W., and J. Lahr (1975), Hypo71 (revised): A computer program for determining hypocenter, magnitude, and first motion pattern of local earthquakes, *US Geol. Surv. Open File Report*, *75-311*, 1–113.

Leech, M. (2001), Arrested orogenic development: eclogitization, delamination, and tectonic collapse, *Earth and Planetary Science Letters*, *185*, 149–159.

Leith, W. (1982), Rock assemblages in central Asia and the evolution of the southern Asian margin, *Tectonics*, *1*(3), 303–318.

Leith, W., and W. Alvarez (1985), Structure of the Vakhsh fold-and-thrust belt, Tadjik SSR: Geologic mapping on a Landsat image base, *Bulletin of the Geological Society of America*, *96*(7), 875–885.

Leith, W., and D. Simpson (1986a), Earthquakes related to active salt doming near Kulyab, Tadjikistan, USSR, *Geophysical Research Letters*, *13*(10), 1019–1022.

Leith, W., and D. Simpson (1986b), Seismic domains within the Gissar-Kokshal seismic zone, Soviet central Asia, *Journal of Geophysical Research*, *91*(B1), 689–699.

Levander, A., B. Schmandt, M. S. Miller, K. Liu, K. E. Karlstrom, R. S. Crow, C.-T. A. Lee, and E. D. Humphreys (2011), Continuing Colorado plateau uplift by delamination-style convective lithospheric downwelling., *Nature*, *472*, 461–465, doi:10.1038/nature10001.

Lévěque, J.-J., L. Rivera, and G. Wittlinger (1993), On the use of the checker-board test to assess the resolution of tomographic inversions, *Geophysical Journal International*, *115*(1), 313–318, doi:10.1111/j.1365-246X.1993.tb05605.x.

Li, C., R. van der Hilst, A. Meltzer, and E. Engdahl (2008a), Subduction of the Indian lithosphere beneath the Tibetan Plateau and Burma, *Earth and Planetary Science Letters*, *274*(1-2), 157–168, doi:10.1016/j.epsl.2008.07.016.

Li, C., R. van der Hilst, E. Engdahl, and S. Burdick (2008b), A new global model for P wave speed variations in Earth's mantle, *Geochemistry Geophysics Geosystems*, *9*(5), doi:10.1029/2007GC001806.

Lin, G., and P. Shearer (2007), Estimating Local Vp/Vs Ratios within Similar Earthquake Clusters, *Bulletin of the Seismological Society of America*, *97*(2), 379–388, doi:10.1785/0120060115.

Lister, G., B. Kennett, S. Richards, and M. Forster (2008), Boudinage of a stretching slablet implicated in earthquakes beneath the Hindu Kush, *Nature Geoscience*, *1*(3), 196–201, doi:10.1038/ngeo132.

Lomax, A., J. Virieux, P. Volant, and C. Berge (2000), Probabilistic earthquake location in 3D and layered models: Introduction of a Metropolis-Gibbs method and comparison with linear locations, in *Advances in Seismic Event Location*, edited by C. Thurber and N. Rabinowitz, pp. 101–134, Kluwer, Amsterdam.

Lorinczi, P., and G. Houseman (2009), Lithospheric gravitational instability beneath the Southeast Carpathians, *Tectonophysics*, *474*(1-2), 322–336, doi:10.1016/j.tecto.2008.05.024.

Lukk, A., S. Yunga, V. Shevchenko, and M. Hamburger (1995), Earthquake focal mechanisms, deformation state, and seismotectonics of the Pamir-Tien Shan region, Central Asia, *Journal of Geophysical Research*, *100*(B10), 20,321–20,343.

Maheo, G., S. Guillot, J. Blichert-Toft, Y. Rolland, and A. Pecher (2002), A slab breakoff model for the Neogene thermal evolution of South Karakorum and South Tibet, *Earth and Planetary Science Letters*, *195*(1-2), 45–58.

Makovsky, Y., and S. Klemperer (1999), Measuring the seismic properties of Tibetan bright spots: Evidence for free aqueous fluids in the Tibetan middle crust, *Journal of Geophysical Research*, *104*(B5), 10,795–10,825, doi:10.1029/1998JB900074.

Mattauer, M. (1986), Intracontinental subduction, crust-mantle decollement and crustal-stacking wedge in the Himalayas and other collision belts, *Geological Society, London, Special Publications*, *19*(1), 37–50, doi:10.1144/GSL.SP.1986.019.01.02.

Matte, P., M. Mattauer, J. Olivet, and D. Griot (1997), Continental subductions beneath Tibet and the Himalayan orogeny: a review, *Terra Nova*, *9*, 264–270.

McKenzie, D. (1969), The relation between fault plane solutions for earthquakes and the directions of the principal stresses, *Bulletin of the Seismological Society of America*, *59*(2), 591–601.

Mechie, J., X. Yuan, B. Schurr, F. Schneider, C. Sippl, L. Ratschbacher, V. Minaev, M. Gadoev, I. Oimahmadov, U. Abdybachaev, B. Moldobekov, S. Orunbaev, and S. Negmatullaev (2012), Crustal and uppermost mantle velocity structure along a profile across the Pamir and southern Tien Shan as derived from project TIPAGE wide-angle seismic data, *Geophysical Journal International*, *188*, 385–407, doi:10.1111/j.1365-246X.2011.05278.x.

Mellors, R. J., G. Pavlis, M. Hamburger, H. J. Al-Shukri, and A. Lukk (1995), Evidence for a high-velocity slab associated with the Hindu Kush seismic zone, *Journal of Geophysical Research*, *100*(B3), 4067–4078, doi:10.1029/94JB02642.

Michael, A. (1984), Determination of stress from slip data: faults and folds, *Journal of Geophysical Research*, *89*(B13), 517–526.

Michael, A. (1987), Use of focal mechanisms to determine stress: a control study, *Journal of Geophysical Research*, *92*(B1), 357–368.

Michael, A. (1991), Spatial variations in stress within the 1987 Whittier Narrows, California, aftershock sequence: New techniques and results, *Journal of Geophysical Research*, *96*(B4), 6303–6319.

Michelini, A., and T. McEvilly (1991), Seismological studies at Parkfield. I. Simultaneous inversion for velocity structure and hypocenters using cubic B-splines parameterization, *Bulletin of the Seismological Society of America*, *81*(2), 524–552.

Miller, A., G. Foulger, and B. Julian (1998), Non-double-couple earthquakes 2. Observations, *Reviews of Geophysics*, *36*(4), 551–568.

Mohadjer, S., R. Bendick, A. Ischuk, S. Kuzikov, A. Kostuk, U. Saydullaev, S. Lodi, D. Kakar, A. Wasy, M. A. Khan, P. Molnar, R. Bilham, and A. Zubovich (2010), Partitioning of India-Eurasia convergence in the Pamir-Hindu Kush from GPS measurements, *Geophysical Research Letters*, *37*(4), 1–6, doi:10.1029/2009GL041737.

Molnar, P., and D. Gray (1979), Subduction of continental lithosphere: some constraints and uncertainties, *Geology*, *7*(1), 58–62.

Molnar, P., and J. M. Stock (2009), Slowing of India's convergence with Eurasia since 20 Ma and its implications for Tibetan mantle dynamics, *Tectonics*, *28*(3), 1–11, doi:10.1029/2008TC002271.

Molnar, P., and P. Tapponnier (1975), Cenozoic tectonics of Asia: effects of a continental collision, *Science*, *189*(4201), 419–426.

Molnar, P., P. England, and J. Martinod (1993), Mantle dynamics, uplift of the Tibetan Plateau, and the Indian monsoon, *Reviews of Geophysics*, *31*(4), 357–396.

Monsalve, G., A. Sheehan, V. Schulte-Pelkum, S. Rajaure, M. R. Pandey, and F. Wu (2006), Seismicity and one-dimensional velocity structure of the Himalayan collision zone: Earthquakes in the crust and upper mantle, *Journal of Geophysical Research*, *111*(B10), 1–19, doi:10.1029/2005JB004062.

Murphy, M., V. Sanchez, and M. Taylor (2010), Syncollisional extension along the India-Asia suture zone, south-central Tibet: Implications for crustal deformation of Tibet, *Earth and Planetary Science Letters*, *290*(3-4), 233–243, doi:10.1016/j.epsl.2009.11.046.

Nábelek, J. (1984), Determination of earthquake source parameters from inversion of body waves, Ph.D. thesis, Massachusetts Institute of Technology.

Nábelek, J., and G. Xia (1995), Momenttensor analysis using regional data: Application to the 25 March, 1993, Scotts Mills, Oregon, Earthquake, *Geophysical Research Letters*, *22*(1), 13–16.

Nábelek, J., G. Hetényi, J. Vergne, S. Sapkota, B. Kafle, M. Jiang, H. Su, J. Chen, B.-S. Huang, and HiClimb-Team (2009), Underplating in the Himalaya-Tibet collision zone revealed by the Hi-CLIMB experiment, *Science*, *325*, 1371–1374, doi:10.1126/science.1167719.

Negredo, A., A. Replumaz, A. Villaseñor, and S. Guillot (2007), Modeling the evolution of continental subduction processes in the Pamir–Hindu Kush region, *Earth and Planetary Science Letters*, *259*(1-2), 212–225, doi:10.1016/j.epsl.2007.04.043.

Neil, E., and G. Houseman (1997), Geodynamics of the Tarim Basin and the Tian Shan in central Asia, *Tectonics*, *16*(4), 571–584.

Nelson, K., W. Zhao, L. Brown, J. Kuo, J. Che, X. Liu, S. Klemperer, Y. Makovsky, R. Meissner, J. Mechie, R. Kind, F. Wenzel, J. Ni, J. Nabelek, C. Leshou, H. Tan, W. Wei, A. Jones, J. Booker, M. Unsworth, W. Kidd, M. Hauck, D. Alsdorf, A. Ross, M. Cogan, C. Wu, E. Sandvol, and M. Edwards (1996), Partially Molten Middle Crust Beneath Southern Tibet: Synthesis of Project INDEPTH Results, *Science*, *274*, 1684–1688.

Ni, J., and M. Barazangi (1984), Seismotectonics of the Himalayan collision zone: Geometry of the underthrusting Indian plate beneath the Himalaya, *Journal of Geophysical Research*, *89*(B2), 1147–1163.

Nikolaev, V. G. (2002), Afghan-Tajik depression: Architecture of sedimentary cover and evolution, *Russian Journal of Earth Sciences*, *4*(6), 399–421, doi:10.2205/2002ES000106.

Nolet, G. (2008), *A Breviary of Seismic Tomography*, 344 pp., Cambridge University Press, Cambridge, UK.

Nowroozi, A. (1971), Seismo-tectonics of the Persian plateau, eastern Turkey, Caucasus, and Hindu-Kush regions, *Bulletin of the Seismological Society of America*, *61*(2), 317–341.

Paige, C. C., and M. Saunders (1982), LSQR: An Algorithm for Sparse Linear Equations and Sparse Least Squares, *ACM Transactions on Mathematical Software*, *8*(1), 43–71, doi:10.1145/355984.355989.

Patriat, P., and J. Achache (1984), India–Eurasia collision chronology has implications for crustal shortening and driving mechanism of plates, *Nature*, *311*, 615–621.

Pavlis, G., and J. Booker (1980), The mixed discrete-continuous inverse problem: application to the simultaneous determination of earthquake hypocenters and velocity structure, *Journal of Geophysical Research*, *85*, 4801–4810.

Pavlis, G., and S. Das (2000), The Pamir-Hindu Kush seismic zone as a strain marker for flow in the upper mantle, *Tectonics*, *19*(1), 103–115.

Pegler, G., and S. Das (1998), An enhanced image of the Pamir-Hindu Kush seismic zone from relocated earthquake hypocentres, *Geophysical Journal International*, *134*(2), 573–595, doi: 10.1046/j.1365-246x.1998.00582.x.

Pin, C., and J. D. Sills (1986), Petrogenesis of layered gabbros and ultramafic rocks from Val Sesia, the Ivrea Zone, NW Italy: trace element and isotope geochemistry, *Geological Society, London, Special Publications*, *24*(1), 231–249, doi:10.1144/GSL.SP.1986.024.01.21.

Prevot, R., D. Hatzfeld, S. Roecker, and P. Molnar (1980), Shallow Earthquakes and Active Tectonics in Eastern Afghanistan, *Journal of Geophysical Research*, *85*(B3), 1347–1357, doi: 10.1029/JB085iB03p01347.

Raleigh, C. B. (1967), Tectonic Implications of Serpentinite Weakening, *Geophysical Journal of the Royal Astronomical Society*, *14*, 113–118, doi:10.1111/j.1365-246X.1967.tb06229.x.

Randall, M., and L. Knopoff (1970), The mechanism at the focus of deep earthquakes, *Journal of Geophysical Research*, *75*(26), 4965–4976.

Rautian, T. (1960), Earthquakes energy, in *Methods of Detailed Investigation of Seismicity*, edited by J. Reznichenko, pp. 75–113, Acad. U.S.S.R., Moscow.

Rawlinson, N., and M. Sambridge (2003), Seismic traveltime tomography of the crust and lithosphere, *Advances in Geophysics*, *46*, 81–197.

Rawlinson, N., S. Pozgay, and S. Fishwick (2010), Seismic tomography: A window into deep Earth, *Physics of the Earth and Planetary Interiors*, *178*(3-4), 101–135, doi:10.1016/j.pepi.2009.10.002.

Reasenberg, P., and D. Oppenheimer (1985), FPFIT, FPPLOT and FPPAGE: Fortran computer programs for calculating and displaying earthquake fault-plane solutions, *Tech. rep.*, US Geological Survey Open File Report, 85-739.

Reigber, C., G. Michel, R. Galas, D. Angermann, J. Klotz, J. Chen, A. Papschev, R. Arslanov, V. Tzurkov, and M. Ishanov (2001), New space geodetic constraints on the distribution of deformation in Central Asia, *Earth and Planetary Science Letters*, *191*(1-2), 157–165, doi: 10.1016/S0012-821X(01)00414-9.

Reiter, K., N. Kukowski, and L. Ratschbacher (2011), The interaction of two indenters in analogue experiments and implications for curved fold-and-thrust belts, *Earth and Planetary Science Letters*, *302*(1-2), 132–146, doi:10.1016/j.epsl.2010.12.002.

Replumaz, A., and P. Tapponnier (2003), Reconstruction of the deformed collision zone Between India and Asia by backward motion of lithospheric blocks, *Journal of Geophysical Research*, *108*(B6), doi:10.1029/2001JB000661.

Robinson, A. (2009), Geologic offsets across the northern Karakorum fault: Implications for its role and terrane correlations in the western Himalayan-Tibetan orogen, *Earth and Planetary Science Letters*, *279*(1-2), 123–130, doi:10.1016/j.epsl.2008.12.039.

Robinson, A., A. Yin, C. Manning, T. M. Harrison, S.-H. Zhang, and X.-F. Wang (2004), Tectonic evolution of the northeastern Pamir: Constraints from the northern portion of the Cenozoic Kongur Shan extensional system, western China, *Geological Society of America Bulletin*, *116*(7), 953, doi:10.1130/B25375.1.

Robinson, A., A. Yin, C. Manning, T. M. Harrison, S.-H. Zhang, and X.-F. Wang (2007), Cenozoic evolution of the eastern Pamir: Implications for strain-accommodation mechanisms at the western end of the Himalayan-Tibetan orogen, *Bulletin of the Geological Society of America*, *119*(7), 882–896, doi:10.1130/B25981.1.

Roecker, S. (1982), Velocity structure of the Pamir-Hindu Kush region: possible evidence of subducted crust, *Journal of Geophysical Research*, *87*(B2), 945–959.

Roecker, S., O. Soboleva, I. Nersesov, A. Lukk, D. Hatzfeld, J. Chatelain, and P. Molnar (1980), Seismicity and fault plane solutions of intermediate depth earthquakes in the Pamir-Hindu Kush region, *Journal of Geophysical Research*, *85*(B3), 1358–1364.

Roecker, S., B. Tucker, J. King, and D. Hatzfeld (1982), Estimates of Q in central Asia as a function of frequency and depth using the coda of locally recorded earthquakes, *Bulletin of the Seismological Society of America*, *72*(1), 129–149.

Rudnick, R. (1995), Making continental crust, *Nature*, *378*, 571–578.

Rudnick, R., and D. M. Fountain (1995), Nature and composition of the continental crust: a lower crustal perspective, *Reviews of Geophysics*, *33*(3), 267–309.

Sambridge, M. (1990), Non-linear arrival time inversion: constraining velocity anomalies by seeking smooth models in 3-D, *Geophysical Journal International*, *102*(3), 653–677, doi: 10.1111/j.1365-246X.1990.tb04588.x.

Satyabala, S. P., Z. Yang, and R. Bilham (2012), Stick–slip advance of the Kohat Plateau in Pakistan, *Nature Geoscience*, *5*(2), 147–150, doi:10.1038/ngeo1373.

Schilling, F. R., G. M. Partzsch, H. Brasse, and G. Schwarz (1997), Partial melting below the magmatic arc in the central Andes deduced from geoelectromagnetic field experiments and laboratory data, *Physics of the Earth and Planetary Interiors*, *103*(1-2), 17–31, doi:10.1016/S0031-9201(97)00011-3.

Schmeling, H. (1986), Numerical models on the influence of partial melt on elastic, anelastic and electrical properties of rocks. Part II: electrical conductivity, *Physics of the Earth and Planetary Interiors*, *43*(2), 123–136, doi:10.1016/0031-9201(86)90080-4.

Schmidt, J., B. Hacker, L. Ratschbacher, K. Stübner, M. Stearns, A. Kylander-Clark, J. M. Cottle, A. Alexander, G. Webb, G. Gehrels, and V. Minaev (2011), Cenozoic deep crust in the Pamir, *Earth and Planetary Science Letters*, *312*(3-4), 411–421, doi:10.1016/j.epsl.2011.10.034.

Schneider, F., X. Yuan, B. Schurr, J. Mechie, C. Sippl, C. Haberland, V. Minaev, I. Oimahmadov, M. Gadoev, N. Radjabov, U. Abdybachaev, S. Orunbaev, and S. Negmatullaev (2012), Ongoing subduction of Eurasian continental crust beneath the Pamir constrained by teleseismic converted waves, *Manuscript in preparation.*

Schultz-Ela, D., M. Jackson, and B. Vendeville (1993), Mechanics of active salt diapirism, *Tectonophysics*, *228*(3-4), 275–312, doi:10.1016/0040-1951(93)90345-K.

Schurr, B. (2000), Seismic structure of the Central Andean subduction zone from local earthquake data, Ph.D. thesis, Freie Universität Berlin.

Schurr, B., A. Rietbrock, G. Asch, R. Kind, and O. Oncken (2006), Evidence for lithospheric detachment in the central Andes from local earthquake tomography, *Tectonophysics*, *415*(1-4), 203–223, doi:10.1016/j.tecto.2005.12.007.

Schwab, M., L. Ratschbacher, W. Siebel, M. McWilliams, V. Minaev, V. Lutkov, F. Chen, K. Stanek, B. Nelson, W. Frisch, and J. Wooden (2004), Assembly of the Pamirs: Age and origin of magmatic belts from the southern Tien Shan to the southern Pamirs and their relation to Tibet, *Tectonics*, *23*(4), doi:10.1029/2003TC001583.

Searle, M. P. (1996), Geological evidence against large-scale pre-Holocene offsets along the Karakoram Fault: Implications for the limited extrusion of the Tibetan plateau, *Tectonics*, *15*(1), 171–186, doi:10.1029/95TC01693.

Sengör, A., B. Natal'in, and V. Burtman (1993), Evolution of the Altaid tectonic collage and Palaeozoic crustal growth in Eurasia, *Nature*, *364*, 299–307.

Sens-Schönfelder, C. (2008), Synchronizing seismic networks with ambient noise, *Geophysical Journal International*, *174*(3), 966–970, doi:10.1111/j.1365-246X.2008.03842.x.

Shin, T.-C. (1993), The calculation of local magnitude from the simulated Wood-Anderson seismograms of the short-period seismograms in the Taiwan area, *Terrestrial, Atmospheric and Oceanic Sciences*, *4*(2), 155–170.

Simmons, N., S. Myers, and G. Johannesson (2011), Global-scale P wave tomography optimized for prediction of teleseismic and regional travel times for Middle East events: 2. Tomographic inversion, *Journal of Geophysical Research*, *116*(B4), B04,305, doi:10.1029/2010JB007969.

Simpson, D., P. Richards, and A. Lerner-Lam (1987), Regional network: Seismicity of Asia and frequency-dependent Q, *Tech. rep.*, Air Force Geophysics Laboratory, New York.

Sippl, C., B. Schurr, X. Yuan, J. Mechie, F. Schneider, M. Gadoev, I. Oimahmadov, C. Haberland, U. Abdybachaev, V. Minaev, S. Negmatullaev, and N. Radjabov (2012), Origin and geometry of the Pamir-Hindu Kush zone of intermediate-depth earthquakes from local seismicity data, *Journal of Geophysical Research - in review.*

Sobel, E. (1999), Basin analysis of the Jurassic–Lower Cretaceous southwest Tarim basin, northwest China, *Geological Society of America Bulletin*, *111*(5), 709–724.

Sobel, E., and T. Dumitru (1997), Thrusting and exhumation around the margins of the western Tarim basin during the India-Asia collision, *Journal of Geophysical Research*, *102*(B3), 5043–5063, doi:10.1029/96JB03267.

Sobel, E., L. Schoenbohm, J. Chen, R. Thiede, D. Stockli, M. Sudo, and M. Strecker (2011a), Late Miocene–Pliocene deceleration of dextral slip between Pamir and Tarim: Implications for Pamir orogenesis, *Earth and Planetary Science Letters*, *304*(3-4), 369–378, doi:10.1016/j.epsl.2011.02.012.

Sobel, E., L. Schoenbohm, J. Chen, R. Thiede, D. Stockli, and M. Sudo (2011b), Slab Rollback and Subduction Erosion Model for the North Pamir - Alai Intracontinental Subduction Zone, *American Geophysical Union, Fall Meeting 2011, abstract #T51J-05.*

Sobel, E., J. Chen, L. Schoenbohm, R. Thiede, D. Stockli, M. Sudo, and M. Strecker (2012), Oceanic-style subduction controls late Cenozoic deformation of the Northern Pamir Orogen, *Earth and Planetary Science Letters*, *in review.*

Spakman, W., and R. Hall (2010), Surface deformation and slab–mantle interaction during Banda arc subduction rollback, *Nature Geoscience*, *3*(8), 562–566, doi:10.1038/ngeo917.

Stauder, W. (1968), Tensional character of earthquake foci beneath the Aleutian Trench with relation to sea-floor spreading, *Journal of Geophysical Research*, *73*(24), 7693–7701, doi:10.1029/JB073i024p07693.

Steffen, R., H. Steffen, and G. Jentzsch (2011), A three-dimensional Moho depth model for the Tien Shan from EGM2008 gravity data, *Tectonics*, *30*(5), 1–19, doi:10.1029/2011TC002886.

Stein, S., and M. Wysession (2003), *An Introduction to Seismology, Earthquakes and Earth Structure*, 498 pp., Blackwell Publishing.

Strecker, M., W. Frisch, M. Hamburger, L. Ratschbacher, S. Semiletkin, A. Zamoruyev, and N. Sturchio (1995), Quaternary deformation in the eastern Pamirs, Tadzhikistan and Kyrgyzstan, *Tectonics*, *14*(5), 1061–1079.

Strecker, M., G. Hilley, J. R. Arrowsmith, and I. Coutand (2003), Differential structural and geomorphic mountain-front evolution in an active continental collision zone: The northwest Pamir, southern Kyrgyzstan, *Bulletin of the Geological Society of America*, *115*(2), 166–181.

Stübner, K., L. Ratschbacher, D. Rutte, R. Gloaguen, V. Minaev, K. Stanek, and M. Wiesinger (2012), The Giant Shakhdara migmatitic gneiss dome, Pamir, India – Asia collision zone, I : Geometry and kinematics, *Tectonics*, *in review.*

Stump, B., and L. Johnson (1977), The determination of source properties by the linear inversion of seismograms, *Bulletin of the Seismological Society of America*, *67*(6), 1489–1502.

Styron, R., M. Taylor, and K. Okoronkwo (2010), Database of active structures from the Indo-Asian Collision, *EosTransactions*, *91*(20), 181–182, doi:10.1130/GES00217.1.Wessel.

Tahirkheli, R., M. Mattauer, F. Proust, and P. Tapponnier (1979), The India Eurasia suture zone in northern Pakistan: synthesis and interpretation of recent data at plate scale, in *Geodynamics of Pakistan*, edited by A. Farah and K. DeJong, pp. 125–130, Geological Survey of Pakistan, Quetta.

Takanami, T., and G. Kitagawa (1988), A new efficient procedure for the estimation of onset times of seismic waves, *Journal of Physics of the Earth*, *36*(6), 267–290.

Takei, Y. (2002), Effect of pore geometry on Vp/Vs: From equilibrium geometry to crack, *Journal of Geophysical Research*, *107*(B2).

Tapponnier, P., and P. Molnar (1979), Active faulting and Cenozoic tectonics of the Tien Shan, Mongolia, and Baykal regions, *Journal of Geophysical Research*, *84*(B7), 3425–3459.

Tapponnier, P., M. Mattauer, F. Proust, and C. Cassaigneau (1981), Mesozoic ophiolites, sutures, and large-scale tectonic movements in Afghanistan, *Earth and Planetary Science Letters*, *52*(2), 355–371.

Tapponnier, P., G. Peltzer, A. L. Dain, R. Armijo, and P. Cobbold (1982), Propagating extrusion tectonics in Asia: New insights from simple experiments with plasticine, *Geology*, *10*, 611–616.

Tapponnier, P., X. Zhiqin, F. Roger, B. Meyer, N. Arnaud, G. Wittlinger, and Y. Jingsui (2001), Oblique stepwise rise and growth of the Tibet plateau., *Science*, *294*, 1671–1677, doi:10.1126/science.105978.

Thomas, J., H. Perroud, P. Cobbold, M. Bazhenov, V. Burtman, A. Chauvin, and E. Sadybakasov (1993), A Paleomagnetic Study of Tertiary Formations From the Kyrgyz Tien-Shan and Its Tectonic Implications, *Journal of Geophysical Research*, *98*(B6), 9571–9589, doi:10.1029/92JB02912.

Thomas, J., A. Chauvin, D. Gapais, M. Bazhenov, H. Perroud, P. Cobbold, and V. Burtman (1994), Paleomagnetic evidence for Cenozoic block rotations in the Tadjik depression (Central Asia), *Journal of Geophysical Research*, *99*(B8), 15,141–15,160.

Thorkelson, D. J. (1996), Subduction of diverging plates and the principles of slab window formation, *Tectonophysics*, *255*(1-2), 47–63, doi:10.1016/0040-1951(95)00106-9.

Thurber, C. (1983), Earthquake Locations and Three-Dimensional Crustal Structure in the Coyote Lake Area, Central California, *Journal of Geophysical Research*, *88*(B10), 8226–8236.

Thurber, C. (1993), Local earthquake tomography: Velocities and vp/vs-theory, in *Seismic Tomography: Theory and Practice*, edited by H. Iyer and K. Hirahara, pp. 563–583, Chapman and Hall, London.

Thurber, C., and D. Eberhart-Phillips (1999), Local earthquake tomography with flexible gridding, *Computers &Geosciences*, *25*, 809–818.

Thurber, C., and W. Ellsworth (1980), Rapid solution of ray tracing problems in heterogeneous media, *Bulletin of the Seismological Society of America*, *70*(4), 1137–1148.

Tilmann, F., J. Ni, and INDEPTH-III-SeismicTeam (2003), Seismic Imaging of the Downwelling Indian Lithosphere Beneath Central Tibet, *Science*, *300*, 1424–1427.

Toomey, D., and G. Foulger (1989), Tomographic inversion of local earthquake data from the Hengill-Grensdalur central volcano complex, Iceland, *Journal of Geophysical Research*, *94*(B12), 17,497–17,510.

Toussaint, G., E. Burov, and J. Avouac (2004), Tectonic evolution of a continental collision zone: A thermomechanical numerical model, *Tectonics*, *23*(TC6003), 1–24, doi:10.1029/2003TC001604.

Treloar, P. J., and M. Coward (1991), Indian plate motion and shape: constraints on the geometry of the Himalayan orogen, *Tectonophysics*, *191*(3-4), 189–198.

Trifonov, V. (1978), Late Quaternary tectonic movements of western and central Asia, *Bulletin of the Geological Society of America*, *89*(7), 1059–1072.

Um, J., and C. Thurber (1987), A fast algorithm for two-point seismic ray tracing, *Bulletin of the Geological Society of America*, *77*(3), 972–986.

Van der Voo, R., W. Spakman, and H. Bijwaard (1999), Tethyan subducted slabs under India, *Earth and Planetary Science Letters*, *171*(1), 7–20, doi:10.1016/S0012-821X(99)00131-4.

van Hinsbergen, D., P. Kapp, G. Dupont-Nivet, P. C. Lippert, P. G. DeCelles, and T. Torsvik (2011), Restoration of Cenozoic deformation in Asia and the size of Greater India, *Tectonics*, *30*(5), 1–31, doi:10.1029/2011TC002908.

van Hinsbergen, D., P. C. Lippert, G. Dupont-Nivet, N. McQuarrie, P. V. Doubrovine, W. Spakman, and T. Torsvik (2012), Greater India Basin hypothesis and a two-stage Cenozoic collision between India and Asia, *Proceedings of the National Academy of Sciences*, doi: 10.1073/pnas.1117262109.

von Seggern, D. H. (2009), Direct Empirical Estimation of Arrival-Time Picking Error from Waveform Cross-Correlations, *Bulletin of the Seismological Society of America*, *99*(5), 2749–2758, doi:10.1785/0120080304.

Waldhauser, F., and W. Ellsworth (2000), A Double-Difference Earthquake Location Algorithm: Method and Application to the Northern Hayward Fault, California, *Bulletin of the Seismological Society of America*, *90*(6), 1353–1368, doi:10.1785/0120000006.

Wellman, H. (1966), Active wrench faults of Iran, Afghanistan and Pakistan, *Geologische Rundschau*, *55*(3), 716–735.

Wessel, P., and F. Smith (1998), New, improved version of Generic Mapping Tools released, *EOS Transactions*, *79*(47), 579–579, doi:10.1029/98EO00426.

Withers, M., R. Aster, C. Young, J. Beiriger, M. Harris, S. Moore, and J. Trujillo (1998), A comparison of select trigger algorithms for automated global seismic phase and event detection, *Bulletin of the Seismological Society of America*, *88*(1), 95–106.

Wittlinger, G., J. Vergne, P. Tapponnier, V. Farra, G. Poupinet, M. Jiang, H. Su, G. Herquel, and A. Paul (2004), Teleseismic imaging of subducting lithosphere and Moho offsets beneath western Tibet, *Earth and Planetary Science Letters*, *221*(1-4), 117–130, doi:10.1016/S0012-821X(03)00723-4.

Wittlinger, G., V. Farra, G. Hetényi, J. Vergne, and J. Nábelek (2009), Seismic velocities in Southern Tibet lower crust: a receiver function approach for eclogite detection, *Geophysical Journal International*, *177*(3), 1037–1049, doi:10.1111/j.1365-246X.2008.04084.x.

Xu, J.-F., R. Shinjo, M. J. Defant, Q. Wang, and R. P. Rapp (2002), Origin of Mesozoic adakitic intrusive rocks in the Ningzhen area of east China: Partial melting of delaminated lower continental crust?, *Geology*, *30*(12), 1111–1114, doi:10.1130/0091-7613(2002)030⟨1111:OOMAIR⟩2.0.CO;2.

Yang, Y., and M. Liu (2002), Cenozoic deformation of the Tarim plate and the implications for mountain building in the Tibetan Plateau and the Tian Shan, *Tectonics*, *21*(6), 1–17, doi: 10.1029/2001TC001300.

Yin, A. (2010), Cenozoic tectonic evolution of Asia: A preliminary synthesis, *Tectonophysics*, *488*(1-4), 293–325, doi:10.1016/j.tecto.2009.06.002.

Yin, A., and T. M. Harrison (2000), Geologic Evolution of the Himalayan-Tibetan Orogen, *Annual Review of Earth and Planetary Sciences*, *28*(1), 211–280, doi:10.1146/annurev.earth.28.1.211.

Yuan, X., J. Ni, R. Kind, J. Mechie, and E. Sandvol (1997), Lithospheric and upper mantle structure of southern Tibet from a seismological passive source experiment, *Journal of Geophysical Research*, *102*(B12), 27,491–27,500.

Zahirovic, S., R. D. Müller, M. Seton, N. Flament, M. Gurnis, and J. Whittaker (2012), Insights on the kinematics of the India-Eurasia collision from global geodynamic models, *Geochemistry Geophysics Geosystems*, *13*(4), doi:10.1029/2011GC003883.

Zandt, G., H. Gilbert, T. J. Owens, M. Ducea, J. Saleeby, and C. H. Jones (2004), Active foundering of a continental arc root beneath the southern Sierra Nevada in California., *Nature*, *431*, 41–46, doi:10.1038/nature02847.

Zhang, P.-Z., Z.-K. Shen, M. Wang, W. Gan, R. Bürgmann, P. Molnar, Q. Wang, Z. Niu, J. Sun, J. Wu, S. Hanrong, and Y. Xinzhao (2004), Continuous deformation of the Tibetan Plateau from global positioning system data, *Geology*, *32*(9), 809–812, doi:10.1130/G20554.1.

Zhang, R., J. Liou, and C. Tsai (1996), Petrogenesis of a high-temperature metamorphic terrane: a new tectonic interpretation for the north Dabieshan, central China, *Journal of Metamorphic Geology*, *14*, 319–333.

Zhao, W., P. Kumar, J. Mechie, R. Kind, R. Meissner, Z. Wu, D. Shi, H. Su, G. Xue, M. Karplus, and F. Tilmann (2011), Tibetan plate overriding the Asian plate in central and northern Tibet, *Nature Geoscience*, *4*(12), 1–4, doi:10.1038/ngeo1309.

Zhu, L., and H. Kanamori (2000), Moho depth variation in southern California from teleseismic receiver functions, *Journal of Geophysical Research*, *105*(B2), 2969–2980.

Zubovich, A., X. Wang, Y. G. Scherba, G. Schelochkov, R. Reilinger, C. Reigber, O. I. Mosienko, P. Molnar, W. Michajljow, V. I. Makarov, J. Li, S. Kuzikov, T. Herring, M. Hamburger, B. Hager, Y. Dang, V. D. Bragin, and R. T. Beisenbaev (2010), GPS velocity field for the Tien Shan and surrounding regions, *Tectonics*, *29*(6), 1–23, doi:10.1029/2010TC002772.

List of Figures

List of Tables

Acknowledgments

First and foremost, my thanks go to my supervisor (not on the paper, but in reality) Dr. Bernd Schurr, who guided and supported this work a lot, and was always available for questions or discussions. He supplied countless ideas and frequently provided sound advice, without which this thesis would not be what it is (whatever that may be).
Profs. Rainer Kind and Frederik Tilmann are acknowledged for official supervision duty, the latter likewise for serving as primary referee for this thesis.
Many thanks go to my colleagues of GFZ Section 3.1 for hosting and enduring me for three years. Sofia Kufner, Karsten Reiter and, again, Bernd Schurr are thanked for reading and providing comments on (large) parts of this manuscript.
Drs. Marcos Moreno, Samuel Angiboust as well as Felix Schneider, Paul Sass, Jens Tympel, Daniel Rutte and Lukasz Gagala provided information and/or figures that were used in this thesis.
Fellow sufferer Francisca Albert is thanked for fellow suffering, and for help with a figure.
I acknowledge all institutes and organizations that supplied seismic data for this work: the Central Asian Institute for Applied Geosciences (Sagynbek Orunbaev), PMP International (Sobit Negmatullaev), the Earthquake Administration of Xingjiang Uygur Autonomous Region in China (He Rui and L. Pingren) as well as the IRIS consortium.
Without the excellent work of the field crews, foreign scientists and collaborators, drivers and diggers on the various (crazy) campaigns in the rough environs of Tajikistan and Kyrgyzstan, this work would not have been possible. Moreover, the overwhelming friendliness and hospitality of the populace of these countries, together with the stunning landscapes (and the combination of bad roads and worse cars) made these trips adventures to be remembered.
Instruments were provided by GIPP Potsdam.
A big thanks go to the entire TIPAGE team for fruitful discussions on several workshops that sparked or developed numerous ideas (and likewise discarded stupid ones). Moreover, I wish to thank Profs. Onno Oncken and Alan Levander, Drs. Kamil Ustaszewski, Tobias Diehl, Dietrich Lange as well as Karsten Reiter and Christoph von Hagke for interesting and important discussions.
Prof. Jean-Phillipe Avouac pointed out one interesting publication that I would probably never have found myself.
Claudia Krumbiegel, Margit Wieprich and Christian Feld acted as "human analysts", manually picking seismic arrival times for comparison with my automatic scheme. Gesa Becker checked and corrected the first motion polarities that were used for the retrieval of fault plane solutions in Chapter 5. Sergey Evseev is thanked for his gOcad visualization.
Many of the figures were compiled with `GMT` (*Wessel and Smith*, 1998), obspy (http://obspy.org *Beyreuther et al.*, 2010) was used for various data handling purposes.
Deutsche Forschungsgesellschaft provided funding for the first two years and entertainment/suspense for the last year of this study.

Erklärung

Hiermit versichere ich, dass ich die vorliegende Dissertation ohne unzulässige Hilfe Dritter und ohne Benutzung anderer als der angegebenen Literatur angefertigt wurde. Die Stellen der Arbeit, die anderen Werken wörtlich oder inhaltlich entnommen sind, wurden durch entsprechende Angaben der Quellen kenntlich gemacht. Diese Arbeit hat in gleicher oder ähnlicher Form noch keiner Prüfungsbehörde vorgelegen.

Berlin, Dezember 2012

Curriculum Vitae

For reasons of data protection,
the curriculum vitae is not included in the online version